On photoplethysmography artifact reduction and applications

On photoplethysmography artifact reduction and applications

PROEFSCHRIFT

ter verkrijging van de graad van doctor aan de Technische Universiteit Eindhoven, op gezag van de rector magnificus prof.dr.ir. F.P.T. Baaijens, voor een commissie aangewezen door het College voor Promoties, in het openbaar te verdedigen op dinsdag 6 september 2016 om 16:00 uur

door

Ralph Wilhelm Christianus Gemma Rosa Wijshoff

geboren te Sittard

Dit proefschrift is goedgekeurd door de promotor en de samenstelling van de promotiecommissie is als volgt:

voorzitter:	prof.dr.ir. A.B. Smolders
1^{e} promotor:	prof.dr. R.M. Aarts
copromotor:	dr.ir. M. Mischi
leden:	dr. J. Allen (Newcastle University)
	prof.dr.ir. W. Steenbergen (Universiteit Twente)
	prof.dr.ir. F.N. van de Vosse (TU Eindhoven)
	prof.dr.ir. P.F.F. Wijn (TU Eindhoven)
adviseur:	dr. G.J. Noordergraaf (Elisabeth-Tweesteden Ziekenhuis Tilburg & Radboud UMC Nijmegen)

Het onderzoek dat in dit proefschrift wordt beschreven is uitgevoerd in overeenstemming met de TU/e Gedragscode Wetenschapsbeoefening.

On photoplethysmography artifact reduction and applications

Ralph Wijshoff

Doctorate committee:

prof.dr. R.M. Aarts	TU Eindhoven, promotor
dr.ir. M. Mischi	TU Eindhoven, copromotor
prof.dr.ir. A.B. Smolders	TU Eindhoven, chairman
dr. J. Allen	Newcastle University
prof.dr.ir. W. Steenbergen	Universiteit Twente
prof.dr.ir. F.N. van de Vosse	TU Eindhoven
prof.dr.ir. P.F.F. Wijn	TU Eindhoven
dr. G.J. Noordergraaf	Elisabeth-Tweesteden Ziekenhuis Tilburg & Radboud UMC Nijmegen

NL Agency
Ministry of Economic Affairs, Agriculture and Innovation

This work was supported by NL Agency, IOP Photonic Devices, IPD083359 HIP, Hemodynamics by Interferometric Photonics.

Cover design: Romy van Geffen, Echt, the Netherlands.
Reproduction: CPI Koninklijke Wöhrmann, Zutphen, the Netherlands.

A catalogue record is available from the Eindhoven University of Technology Library. ISBN: 978-90-386-4113-3.

Summary

On photoplethysmography artifact reduction and applications

Photoplethysmography (PPG) is a non-invasive and easy-to-use optical technology which is nowadays widely applied to monitor the cardiovascular and respiratory systems. By emitting light through tissue, PPG can measure variations in tissue blood-volume via the resulting variations in optical absorption and scattering. PPG is mostly used in the application of pulse oximetry where cardiac-induced variations in a red and a near-infrared PPG signal are used to measure pulse rate (PR) and peripheral arterial functional-hemoglobin oxygen-saturation (SpO_2). The use of PPG is currently also spreading in ambulatory settings. PPG is for instance applied in optical heart rate watches. Ambulatory PPG measurements could also be valuable for the detection of epileptic seizures and atrial fibrillation. Ambulatory oximetry measurements could be of relevance for improved management of long-term oxygen-therapy.

PPG signals are highly susceptible to motion. Motion artifacts in PPG signals are spurious fluctuations which complicate the detection of the cardiac component. Motion artifacts can be caused by motion of the PPG sensor relative to the skin, acceleration-induced sloshing of blood, and deformation of the illuminated tissue volume by dynamic variations in sensor contact-pressure. Furthermore, motion can cause the PPG sensor to variably loose contact with the skin, which can cause variations in the amount of ambient light reaching the photodiode.

This thesis deals with the processing and analysis of PPG signals which have been corrupted by motion artifacts. We focused on applications where motion artifacts are (quasi-)periodic and could therefore be modeled and removed. Motion artifacts were estimated via motion reference signals. Quasi-periodic motion artifacts can occur during activities of daily living (ADL) and are relevant in cardiopulmonary exercise testing (CPX) and cardiopulmonary resuscitation (CPR). We furthermore focused on explicitly removing the motion artifacts to recover artifact-reduced PPG signals for further beat-to-beat analysis.

We first investigated artifacts caused by motion of the PPG sensor relative to the skin (Chapter 2). We developed a convenient method to measure relative sensor motion via a laser diode and self-mixing interferometry (SMI). Via SMI, the monitor diode of a laser diode could measure the Doppler frequency-shift of laser-light which was back-scattered by a moving object and re-entered the laser cavity. The motion of the laser diode could be derived from the Doppler frequencies. Via SMI we could conveniently use a single component as a light source for the PPG measurement and as a sensor for the relative motion measurement. We also developed an in-vitro skin perfusion phantom to investigate the effect of relative sensor motion on PPG signals. We used a laser diode as PPG light source to illuminate the perfusion phantom, and we generated artifacts in-vitro by dynamically varying the distance between the laser diode and the PPG photodiode. We showed that SMI could accurately measure displacement of the laser diode relative to the diffusely-scattering skin phantom. In-vitro, we found good correlation between the laser displacement and the resulting artifacts.

Subsequently, we performed a study on healthy volunteers to test SMI-derived relative sensor motion in a more realistic scenario (Chapter 3). Red and near-infrared PPG signals were measured on the forehead of healthy volunteers with a commercially available PPG sensor. Quasi-periodic motion artifacts were generated by walking on a treadmill. We measured sensor motion relative to the skin by augmenting the PPG sensor with a laser diode and using SMI. For comparison, we positioned an accelerometer on top of the PPG sensor to measure head motion. Both motion measurements were used to estimate the fundamental frequency of motion. We found that the accelerometer outperformed the SMI measurement by providing a motion reference signal which had a better signal-to-noise ratio and more consistently contained a frequency component at the fundamental frequency of motion. This may have been the result of limited relative sensor motion. We therefore recommend using an accelerometer to obtain a motion reference signal in this scenario. We furthermore used these data to develop a generic algorithm to estimate and remove the motion artifacts from the measured PPG signals (Chapter 3). The resulting artifact-reduced PPG signals provided more stable measurements of inter-beat-intervals and SpO_2, which can be of relevance for applications in ADL, CPX and CPR.

We have also investigated the potential value of using PPG during CPR. The goal of CPR is achieving return of spontaneous circulation (ROSC). Detection of ROSC involves assessing whether the heart has resumed beating, which is typically performed by manual palpation. Manual palpation is unreliable, time-consuming and interrupts the chest compressions. As a result, manual palpation can lead to long interruptions in the chest compressions, which reduce the compression-generated blood flow and can thereby negatively impact CPR outcome. An objective, non-invasive and easy-to-use method which can support the detection of ROSC, preferably during compressions, would therefore be a valuable asset.

In a pre-clinical automated-CPR study we found that PPG can potentially detect when the heart resumes beating during CPR (Chapter 4). PPG could detect

absence and presence of a spontaneous pulse in few-second pauses in compressions and during ongoing compressions. When the spontaneous pulse rate and compression rate were different, PPG could detect the spontaneous pulse rate.

Based on the pre-clinical data, we developed an algorithm to detect cardiogenic output in a PPG signal during CPR, intended to support clinicians in detecting ROSC (Chapter 5). The algorithm could estimate and reduce the compression component in the PPG signal, to recover a compression-reduced PPG signal which contained an estimate of the underlying spontaneous pulse component. Visual inspection of such a signal can support detecting whether the heart has resumed beating and, if so, whether the heart is beating at regular intervals. The algorithm could track the spontaneous pulse rate via spectral analysis of the compression-reduced PPG signal. The algorithm could also detect a pronounced decrease in the baseline of the PPG signal, which occurred when the heart resumed beating and was presumably caused by a redistribution of blood volume to the periphery. Detection of a decrease in the baseline accommodated for coinciding spontaneous pulse rate and compression rate, at which occurrence the compression reduction algorithm and the spectral analysis could not be used to detect cardiogenic output. The algorithm indicated cardiogenic output when a spontaneous pulse rate or a pronounced decrease in the baseline were detected. The indication of cardiogenic output by the algorithm showed good agreement with the occurrence of ROSC as annotated by clinicians. Therefore, we concluded that the algorithm may support clinicians in the detection of ROSC during CPR.

PPG-based support for ROSC detection may offer improvements in CPR. Objective detection of the absence of cardiogenic output could shorten or prevent unnecessary interruptions in compressions for ROSC assessment. This can increase the fraction of time that compressions are delivered during CPR to generate blood flow, and may therefore increase the chance of achieving ROSC. Objective detection of the presence of cardiogenic output could guide stopping CPR, which may reduce refibrillation which is associated with sustained compressions on a beating heart. Detection of the presence of cardiogenic output could also guide administration of vasopressors, which may have detrimental effects if administered when the heart has just resumed beating.

Contents

1 Introduction **1**

1.1 Photoplethysmography and pulse oximetry 2
1.2 The PPG signal 4
1.3 Oxygen saturation 6
1.3.1 Theoretical determination of oxygen saturation 6
1.3.2 Practical determination of oxygen saturation 8
1.3.3 Oxygen saturation levels 9
1.4 Applications 9
1.4.1 Pulse rate and pulse interval 9
1.4.2 Heart rate variability and pulse rate variability 9
1.4.3 Heart rate turbulence and pulse rate turbulence 10
1.4.4 Pulse arrival time and pulse transit time 10
1.4.5 Ambulatory oximetry monitoring 10
1.4.6 Cardiopulmonary exercise testing 11
1.4.7 Cardiopulmonary resuscitation 11
1.4.7.1 Introduction to CPR 11
1.4.7.2 PPG and pulse oximetry during CPR 13
1.5 Motion artifact handling 14
1.5.1 Origins of motion artifacts in PPG 14
1.5.2 Recovery of artifact-reduced PPG signals 15
1.5.3 Motion-robust extraction of parameters 15
1.5.4 Detection of artifact-free PPG signal segments 16
1.6 Scope and objectives of the thesis 16
1.6.1 Scope 17
1.6.2 Objectives of Part I 17
1.6.3 Objectives of Part II 18

1.7 Thesis outline 18

Part I Motion artifact reduction in photoplethysmography 21

2 In-vitro model for reduction of motion artifacts in photoplethysmography using relative sensor motion 23
2.1 Introduction 25
2.2 Methods A: Experimental setup 27
2.2.1 Skin perfusion phantom 27
2.2.2 Measurement setup 29
2.2.3 In-vitro PPG measurements 31
2.3 Methods B: Displacement measurement 32
2.3.1 SMI signal structure 33
2.3.2 Determination of displacement 36
2.3.3 Accuracy analysis 39
2.3.4 Validation 41
2.4 Methods C: Artifact reduction algorithm 42
2.4.1 PPG signal model 42
2.4.2 Motion artifact estimation and reduction 44
2.4.3 In-vitro artifact reduction 46
2.5 Results 47
2.5.1 In-vitro PPG measurements 47
2.5.2 Displacement measurement 49
2.5.2.1 Doppler signals 49
2.5.2.2 Accuracy 51
2.5.3 In-vitro artifact reduction 52
2.6 Discussion 54
2.6.1 In-vitro PPG measurements 54
2.6.2 Displacement measurement 56
2.6.3 In-vitro artifact reduction 57
2.7 Conclusions 58

3 Generic algorithm for reduction of quasi-periodic motion artifacts in photoplethysmography 59
3.1 Introduction 61
3.2 Methods A: Experiment and measurements 62
3.3 Methods B: Artifact reduction algorithm 65
3.3.1 Relative sensor motion 65
3.3.2 Accelerometry 66
3.3.3 Preprocessing 66
3.3.4 Measurement of the step rate 66
3.3.5 Estimation and reduction of motion artifacts 69
3.4 Methods C: Performance evaluation 70
3.4.1 Motion references 70

3.4.2 R-peak detection . . . 71
3.4.3 Pulse detection . . . 71
3.4.4 Inter-beat intervals . . . 72
3.4.5 Oxygen saturation . . . 72
3.5 Results . . . 73
3.5.1 Motion artifact references . . . 73
3.5.2 Motion artifact reduction . . . 73
3.6 Discussion . . . 82
3.7 Conclusions . . . 84

Part II Photoplethysmography in cardiopulmonary resuscitation 85

4 Detection of a spontaneous pulse via photoplethysmography during pre-clinical automated cardiopulmonary resuscitation 87
4.1 Introduction . . . 89
4.2 Methods . . . 90
4.2.1 Study design . . . 90
4.2.2 Anesthesia and management . . . 91
4.2.3 Instrumentation and monitoring . . . 91
4.2.4 Experimental protocol . . . 92
4.2.5 Data analysis . . . 93
4.3 Results . . . 93
4.3.1 Spontaneous pulse during ventilation pauses . . . 93
4.3.2 Spontaneous pulse during chest compressions . . . 96
4.3.3 Trend of relative PPG amplitude . . . 96
4.4 Discussion . . . 96
4.5 Conclusions . . . 101

5 Photoplethysmography-based algorithm for detection of cardiogenic output during cardiopulmonary resuscitation 103
5.1 Introduction . . . 105
5.2 Methods . . . 106
5.2.1 Experimental measurements . . . 106
5.2.2 Overview of the algorithm . . . 107
5.2.3 Determination of compression characteristics . . . 107
5.2.4 Reduction of the compression component . . . 110
5.2.4.1 Harmonic model . . . 110
5.2.4.2 Evaluation . . . 112
5.2.5 Spectrum estimation . . . 112
5.2.5.1 Autoregressive (AR) model . . . 112
5.2.5.2 Model order . . . 113
5.2.6 Spectral analysis . . . 114
5.2.6.1 Signal presence . . . 114
5.2.6.2 PR detection . . . 115

5.2.6.3 Evaluation 117
5.2.7 Detection of blood volume redistribution to the periphery . 117
5.2.8 Indicator of cardiogenic output 118
5.2.9 Validation of the indicator 118
5.3 Results 119
5.3.1 Determination of compression characteristics 119
5.3.2 Reduction of the compression component 121
5.3.3 AR model order 124
5.3.4 Spectral analysis 124
5.3.5 Detection of blood volume redistribution to the periphery . 127
5.3.6 Validation of the indicator 127
5.4 Discussion 129
5.5 Conclusions 131

6 General discussion and future directions for research 133
6.1 Artifact reduction in PPG 133
6.2 PPG in CPR 136

Bibliography 141

Acknowledgements 161

About the author 163

List of publications 165

CHAPTER 1

Introduction

This chapter provides a general background on photoplethysmography and pulse oximetry. Furthermore, the scope and outline of the thesis are described.

1.1 Photoplethysmography and pulse oximetry

Photoplethysmography (PPG) is a non-invasive and easy-to-use optical technology which is nowadays widely applied in medical practice and during activities of daily living (ADL) to monitor the cardiovascular and respiratory systems [6, 10, 88, 146, 156, 177]. A PPG signal is obtained by emitting light through tissue and detecting the amount of light which has propagated through the tissue. PPG can measure variations in blood volume in the illuminated tissue, because this causes variations in optical absorption and scattering, which results in variations in the PPG signal [10, 105, 146]. PPG is mostly used in the application of pulse oximetry, where cardiac-induced variations in a red and a near-infrared (IR) PPG signal are used to measure pulse rate (PR) and oxygen saturation (SpO_2) [10, 88, 105, 146, 191]. The oxygen saturation is the fraction of hemoglobin molecules in the red blood cells carrying oxygen [19, 105, 191]. The oxygen saturation influences the absorption of red and near-IR light, which is used by pulse oximeters to determine SpO_2 [19,105,191]. Nowadays, a relatively new application of PPG is the measurement of PR during sports, e.g., by incorporating a PPG measurement in a watch and obtaining green PPG signals from the wrist [177].

PPG is related to plethysmography, which is the measurement of pulsatile tissue volume [146]. Plethysmography stems from the Greek word "plethysmos" which means "to increase" [163]. Plethysmography directly measures pulsatile tissue volume, e.g., by measuring variations in the circumference of an extremity [146]. In PPG, light is applied to perform a similar but not equivalent measurement [146]. The variations in the PPG signal cannot be quantitatively related to the variations in blood volume in the illuminated tissue [146].

A PPG measurement is typically performed by emitting light through skin using a light emitting diode (LED) and measuring the amount of light that has propagated through the skin using a photodiode [10,19,88,105,177,191]. The LED and photodiode can be configured opposite of each other to perform a transmissive measurement through, e.g., a fingertip [88,146,191]. This is illustrated in Fig. 1.1.

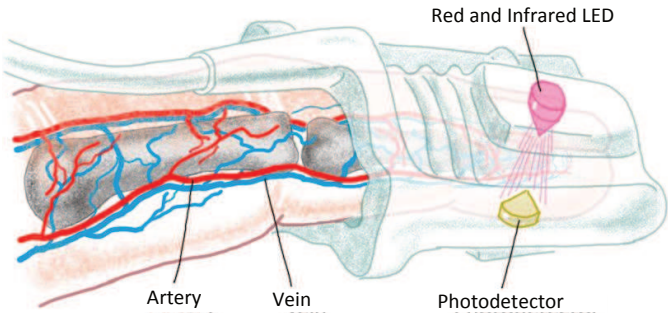

Figure 1.1: Schematic representation of a transmissive finger pulse oximetry clip. This drawing has been made by Mr Henny Herps. LED: light emitting diode.

Alternatively, the LED and photodiode can be configured next to each other to perform a reflective measurement through, e.g., the skin on the forehead [24, 191] or the wrist [170, 177].

Figure 1.2 illustrates PPG signals acquired from the fingertip (Fig. 1.2a) and the forehead (Fig. 1.2b), using red and near-IR light. The cardiac-induced increases in the microvascular arterial blood volume can be recognized as periodic decreases in the PPG signal [10, 105, 146]. This is illustrated during the periods of rest in Fig. 1.2. The PR can be directly derived from the cardiac-induced variations in the PPG signal, either in the time domain [118] or the frequency domain [155].

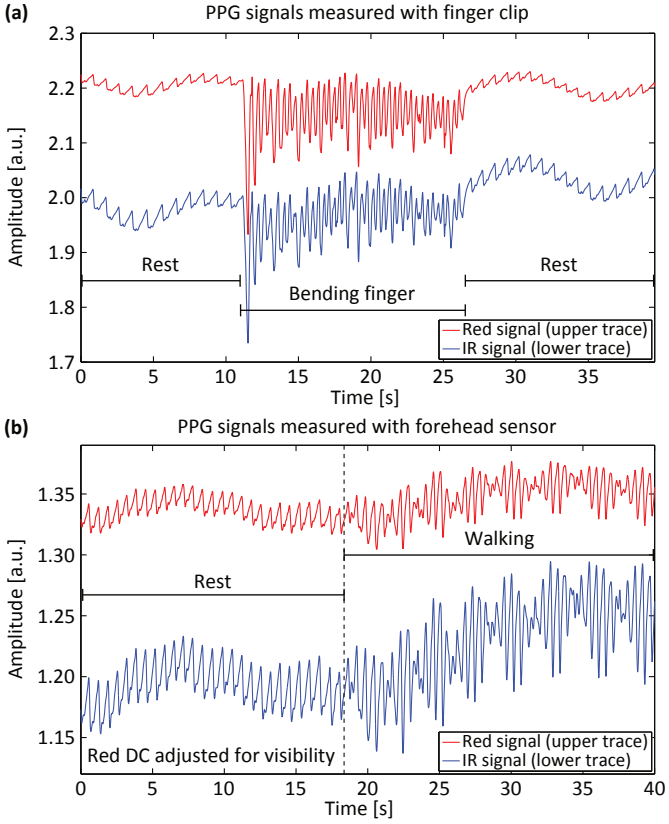

Figure 1.2: Illustration of PPG signals and the influence of motion on these signals. (a) PPG signals obtained using a transmissive finger clip. The motion artifacts were caused by repetitive slight bending of the finger. (b) PPG signals obtained using a reflective forehead sensor. Walking caused the motion artifacts. DC: direct current; IR: infrared; PPG: photoplethysmography.

Cardiac-induced variations in the PPG signal can be subtle. The peak-to-valley amplitude of the cardiac pulse in the PPG signal is often expressed as a percentage of the average detected light power [105, 191, 206]. Weak cardiac pulses in the PPG signal can have peak-to-valley amplitudes as small as about 0.1%, typical pulses have peak-to-valley amplitudes between 1% and 5%, and strong pulses can have peak-to-valley amplitudes as large as about 10% of the average detected light power [24, 105, 123, 140, 191, 206].

PPG signals are highly susceptible to motion [10, 14, 140, 177]. This is also illustrated in Fig. 1.2, where Fig. 1.2a shows motion artifacts in finger PPG signals caused by finger bending, and Fig. 1.2b shows motion artifacts in forehead PPG signals caused by walking. Here, bending of the finger has a larger effect on the PPG signal than walking has.

Research on PPG was already conducted early in the twentieth century. In 1937, transmissive PPG signals were measured by Alrick Hertzman, who used a light bulb and a photocell to perform measurements on the fingers, toes and nasal septum of healthy volunteers [70, 71]. Alrick Hertzman also performed reflective measurements, comparing PPG signals obtained from various sites such as the fingertips, hands, toes, forehead, ears and the side of the nose [72]. Between 1940 and 1942, Glenn Millikan developed a dual-wavelength-PPG light-weight ear oxygen-meter for aviation, which he called an "oximeter" [108, 161]. In 1948, Earl Wood and J.E. Geraci added an inflatable balloon to the ear oximeter of Glenn Millikan, with which the ear could be made bloodless for initial zero setting [108, 161]. These oximeters where "non-pulse" oximeters [206]. Pulse oximetry has been invented by Takuo Aoyagi in 1972 [11, 108, 162]. To determine oxygen saturation, Takuo Aoyagi introduced using the cardiac-induced variations in red and near-IR PPG signals, which were assumed to solely result from local variations in arterial blood volume. This removed the requirement of an individual calibration prior to each measurement. The use of pulse oximeters has widely expanded in hospitals [10, 88, 108]. Pulse oximetry has been standard of care in the operating room since 1990, and in the recovery room since 1992 [19].

1.2 The PPG signal

In pulse oximetry, PPG signals are commonly modeled using the Beer-Lambert law [11, 19, 58, 105, 191]. The Beer-Lambert law describes the absorbance of a monochromatic electromagnetic wave when travelling through a homogeneous medium containing a uniformly distributed absorber. When assuming that all light propagates through tissue with pulsating arterial blood, i.e., there is no optical shunt of light passing through tissue without pulsating arterial blood, the detected light power can be described as

$$P_d(t) = P_0 \exp\left(-A_{\mathrm{BL}}(\lambda, t) - \Delta A_a(\lambda, t)\right), \tag{1.1}$$

with $P_d(t)$ [W] the power of the detected light, P_0 [W] the power of the emitted light, and $A(\lambda, t)$ [-] the absorbance of light by tissue, which depends on the wavelength λ [m] of the emitted light and varies over time t [s]. The detected light power $P_d(t)$ is the basis of the PPG signal. In (1.1) the absorbance of light has been split in two components. The first absorbance, $A_{\mathrm{BL}}(\lambda, t)$, describes the constant absorbance by skin pigmentation, fat, muscle, bone and the average arterial and venous blood volumes in the illuminated tissue, plus the absorbance by slowly-varying variations of the blood volume in the illuminated tissue [19,191]. The second absorbance, $\Delta A_a(\lambda, t)$, describes the cardiac-induced variations in arterial blood volume in the illuminated tissue. Because $\Delta A_a(\lambda, t)$ is small, in first order (1.1) can be approximated by

$$P_d(\lambda, t) \approx P_0 \exp\left(-A_{\mathrm{BL}}(\lambda, t)\right)\left(1 - \Delta A_a(\lambda, t)\right). \tag{1.2}$$

In practice, PPG signals are measured using a photodiode and a transimpedance amplifier (TIA) [10,191]. The photodiode converts the detected light power $P_d(\lambda, t)$ into a current, and the TIA converts the photodiode current into a voltage. Therefore, the measured PPG signal is proportional to the responsivity of the photodiode and the gain of the TIA. The measured PPG signal, $v_d(\lambda, t)$ [V], can be expressed as

$$v_d(\lambda, t) = G_{\mathrm{TIA}} R_{\mathrm{PD}}(\lambda) P_d(\lambda, t), \tag{1.3}$$

with TIA gain G_{TIA} [V/A] and photodiode responsivity $R_{\mathrm{PD}}(\lambda)$ [A/W].

Expressions (1.1) through (1.3) show that the amplitude of the cardiac-induced component in the detected PPG signal is proportional to the emitted light power, P_0, the attenuation by the baseline absorbance of the tissue and the average blood volume in the tissue, $\exp(-A_{\mathrm{BL}}(t))$, the photodiode responsivity, $R_{\mathrm{PD}}(\lambda)$, and the TIA gain, G_{TIA}. Therefore, the measured PPG signal is often normalized by its baseline, to remove the dependency on the emitted light power, the average absorbance, the photodiode and the TIA [191, 206]. The normalized measured PPG signal, $v_n(\lambda, t)$ [-], can be expressed as

$$v_n(\lambda, t) = \frac{v_d(\lambda, t)}{G_{\mathrm{TIA}} R_{\mathrm{PD}}(\lambda) P_0 \exp\left(-A_{\mathrm{BL}}(\lambda, t)\right)} \approx 1 - \Delta A_a(\lambda, t). \tag{1.4}$$

Expressions (1.1) through (1.4) show that an increase in the illuminated blood volume leads to a decrease in the detected light power and measured PPG signal, i.e., the PPG signal is inversely related to the illuminated blood volume. Patient monitors therefore typically show an inverted version of the PPG signal, to facilitate interpreting the PPG signal time-trace as variations in blood volume in the illuminated tissue [10, 116, 146].

The low-frequency variation of the PPG signal baseline, $\exp\left(-A_{\mathrm{BL}}(\lambda, t)\right)$, is caused by low-frequency variation in the average blood volume in the illuminated tissue. This can have several origins. Baseline variations can result from variations

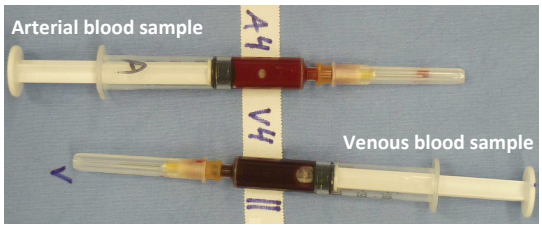

Figure 1.3: Picture of arterial (top) and venous (bottom) blood samples. The arterial blood is oxygen-rich and therefore has a bright red color. The venous blood is oxygen-poor and therefore has a dark red color. These samples were drawn during the pre-clinical study which is described in Chapter 4.

in blood flow through the microvasculature caused by variations in sympathetic tone or local autoregulation [10, 122, 125, 146]. Baseline variations can also be attributed to thermoregulation to maintain a constant body temperature [10], which is the main function of the cutaneous circulation [92]. Respiration causes variation in the baseline of the PPG signal via respiratory-induced variations in intra-thoracic pressure, which influence the venous return flow from the periphery to the heart [5, 6, 10, 116, 146, 163]. Finally, a baseline variation can result from a variation in hydrostatic pressure, which causes a redistribution of blood volume [116, 146].

1.3 Oxygen saturation

1.3.1 Theoretical determination of oxygen saturation

Oxygen is transported throughout the body by hemoglobin molecules, which reside inside erythrocytes or red blood cells [19, 182, 191]. Hemoglobin molecules can reversibly bind oxygen [19, 191]. Hemoglobin with oxygen bound is called oxyhemoglobin, indicated by HbO_2. Hemoglobin without oxygen bound is called deoxyhemoglobin or reduced hemoglobin, indicated by Hb. Hemoglobin is the main light-absorbing component in blood [19, 105]. When considering only the hemoglobin species which are functional in oxygen transport, i.e., Hb and HbO_2 [19, 191], the variation in arterial blood absorbance, $\Delta A_a(\lambda, t)$, can be expanded into two terms as

$$\Delta A_a(\lambda, t) = \left(\varepsilon_{\mathrm{HbO_2}}(\lambda) c_{\mathrm{HbO_2}} + \varepsilon_{\mathrm{Hb}}(\lambda) c_{\mathrm{Hb}}\right) \delta l(t), \tag{1.5}$$

with $\varepsilon_{\mathrm{HbO_2}}$ [$\mathrm{M^{-1}m^{-1}}$] and $\varepsilon_{\mathrm{Hb}}$ [$\mathrm{M^{-1}m^{-1}}$] the molar extinction coefficients of HbO_2 and Hb, respectively, $c_{\mathrm{HbO_2}}$ [M] and c_{Hb} [M] the concentrations of HbO_2 and Hb, respectively, and $\delta l(t)$ [m] the variation in the optical path length through arterial blood caused by the cardiac-induced variation in arterial blood volume.

The normalized measured PPG signal can now be expressed as

$$v_n(\lambda, t) \approx 1 - \left(\varepsilon_{\mathrm{HbO_2}}(\lambda) c_{\mathrm{HbO_2}} + \varepsilon_{\mathrm{Hb}}(\lambda) c_{\mathrm{Hb}}\right) \delta l(t). \tag{1.6}$$

Expression (1.6) shows that the amplitude of the cardiac component in the normalized PPG signal depends on the amount of oxygen bound to hemoglobin in the arterial blood, i.e., on the concentrations $c_{\mathrm{HbO_2}}$ and c_{Hb}, when it holds that $\varepsilon_{\mathrm{HbO_2}}(\lambda) \neq \varepsilon_{\mathrm{Hb}}(\lambda)$. This is the case when using red and near-IR light, with the exception of the isosbestic wavelength at about 805 nm [19,105,191]. Red light is absorbed less by HbO_2 than by Hb. That is, HbO_2 has a bright red color, and Hb has a dark red color, as illustrated by the oxygen-rich arterial and oxygen-poor venous blood samples in Fig. 1.3. The opposite holds for near-IR light, which is absorbed more by HbO_2 than by Hb. Therefore, when illuminating tissue with red and near-IR light, the amplitude of the cardiac pulse will be smaller in the normalized red PPG signal than in the normalized near-IR PPG signal when blood is oxygen-rich, and the amplitude of the cardiac pulse will be larger in the normalized red PPG signal than in the normalized near-IR PPG signal when blood is oxygen-poor. The amplitude of the cardiac pulse will be about equal in the normalized red and near-IR PPG signals at an oxygen saturation of approximately 80%, depending on the wavelengths used [19, 104, 140, 191]. This is the measurement principle used by a pulse oximeter to determine oxygen saturation from a red and a near-IR PPG signal [19, 105, 191].

SpO_2 [%] as measured by pulse oximeters is the peripheral arterial functional-hemoglobin oxygen-saturation, and can be expressed as [19, 191]

$$\mathrm{SpO_2} = 100 \times \frac{[\mathrm{HbO_2}]}{[\mathrm{Hb}] + [\mathrm{HbO_2}]} \ [\%], \tag{1.7}$$

where the square brackets indicate concentrations. Introducing (1.7) in (1.6) gives

$$v_n(\lambda, t) \approx 1 - \left(\varepsilon_{\mathrm{HbO_2}}(\lambda)\mathrm{SpO_2} + \varepsilon_{\mathrm{Hb}}(\lambda)\left(1 - \mathrm{SpO_2}\right)\right) c_{\mathrm{THb}} \delta l(t), \tag{1.8}$$

where the total hemoglobin concentration, c_{THb} [M], was assumed a sum of the oxyhemoglobin and deoxyhemoglobin concentrations, $c_{\mathrm{THb}} = c_{\mathrm{HbO_2}} + c_{\mathrm{Hb}}$ [19,191]. By performing measurements at two wavelengths, (1.8) can theoretically be solved for SpO_2. When considering a red and a near-IR PPG signal, in which a cardiac pulse has a peak-to-valley amplitude of AC_{rd} and AC_{ir}, and an average level of DC_{rd} and DC_{ir}, respectively, the ratio-of-ratios, ρ [-], can be determined,

$$\rho = \frac{AC_{\mathrm{rd}}/DC_{\mathrm{rd}}}{AC_{\mathrm{ir}}/DC_{\mathrm{ir}}} = \frac{\left(\varepsilon_{\mathrm{HbO_2}}(\lambda_{\mathrm{rd}})\mathrm{SpO_2} + \varepsilon_{\mathrm{Hb}}(\lambda_{\mathrm{rd}})\left(1 - \mathrm{SpO_2}\right)\right) \Delta l_{\mathrm{rd}}}{\left(\varepsilon_{\mathrm{HbO_2}}(\lambda_{\mathrm{ir}})\mathrm{SpO_2} + \varepsilon_{\mathrm{Hb}}(\lambda_{\mathrm{ir}})\left(1 - \mathrm{SpO_2}\right)\right) \Delta l_{\mathrm{ir}}}, \tag{1.9}$$

where λ_{rd} [m] and λ_{ir} [m] are the wavelengths of the red and near-IR light, respectively. The division by the average level in the first ratio in (1.9) normalizes the cardiac pulses in the PPG signals by their baselines, so (1.8) can be applied. The numerator and denominator of the second ratio in (1.9) have been obtained

via (1.8), and taking the difference between the maximum of the PPG signal at diastole and the minimum of the PPG signal at systole. Therefore, Δl_{rd} and Δl_{ir} are the differences between the maximum optical path length at systole and the minimum optical path length at diastole, for red and near-IR, respectively. The total hemoglobin concentration, c_{THb}, has canceled in the second ratio in (1.9). By assuming that the variations in optical path length through arterial blood caused by a cardiac pulse are equal for red and near-IR, i.e., $\Delta l_{\mathrm{rd}} = \Delta l_{\mathrm{ir}}$, (1.9) can be solved for $\mathrm{SpO_2}$ [19, 191]:

$$\mathrm{SpO_2} = \frac{\varepsilon_{\mathrm{Hb}}(\lambda_{\mathrm{rd}}) - \varepsilon_{\mathrm{Hb}}(\lambda_{\mathrm{ir}})\rho}{(\varepsilon_{\mathrm{Hb}}(\lambda_{\mathrm{rd}}) - \varepsilon_{\mathrm{HbO_2}}(\lambda_{\mathrm{rd}})) - (\varepsilon_{\mathrm{Hb}}(\lambda_{\mathrm{ir}}) - \varepsilon_{\mathrm{HbO_2}}(\lambda_{\mathrm{ir}}))\,\rho}. \tag{1.10}$$

Expression (1.10) shows how $\mathrm{SpO_2}$ can be theoretically determined from a measured ratio-of-ratios ρ.

1.3.2 Practical determination of oxygen saturation

The theoretical expression for $\mathrm{SpO_2}$ in (1.10) does not hold in practice. The assumption that the cardiac-induced variation in optical path length is equal for red and near-IR does not hold because of scattering effects [19, 174, 191]. The absorbtion of light by hemoglobin in red blood cells is not constant but varies throughout the cardiac cycle, because of variations in the orientation and distribution of the red blood cells as a function of blood flow velocity [96, 191]. The assumption of monochromatic light does not hold for LEDs, which have bandwidths between 20 and 50 nm [19,104,191]. Therefore, commercially available pulse oximeters determine $\mathrm{SpO_2}$ via an empirically determined calibration curve to correct for the deviations from theory [19, 124, 191], e.g., via

$$\mathrm{SpO_2} = a + b\rho + c\rho^2, \tag{1.11}$$

in which a [%], b [%] and c [%] are the calibration constants.

Commercial pulse oximeters are typically calibrated for a range between 70% and 100%, because the calibration data is obtained from healthy volunteers who are desaturated by breathing hypoxic gas mixtures [19, 88]. Calibration is performed by fitting the calibration curve, which is a function of the measured ratio-of-ratios ρ, to $\mathrm{SaO_2}$, the arterial oxygen saturation as measured by CO-oximetry in a drawn blood sample [88, 105, 124, 191]. In this way, manufacturers often report to achieve a difference between $\mathrm{SpO_2}$ and $\mathrm{SaO_2}$ which is smaller than 2% on average, with a standard deviation smaller than 3% [77].

Other inaccuracies in $\mathrm{SpO_2}$ can arise when, e.g., performing a dual-wavelength $\mathrm{SpO_2}$ measurement with blood containing dysfunctional hemoglobins such as methemoglobin or carboxyhemoglobin, thereby violating the assumption that only functional hemoglobins are present [19, 88, 191].

1.3.3 Oxygen saturation levels

The interpretation of SpO_2 levels is patient group specific. Here, a number of examples is presented. Normally, SpO_2 should vary between about 97% and 100%, readings of 95% are considered clinically acceptable, levels of 90% are considered to rise a warning sign, and levels below 90% are considered to indicate hypoxemia [32, 182]. For neonates in the neonatal intensive care unit (NICU), an SpO_2 level above 90% is targeted, but below 95%, because higher SpO_2 levels may lead to retinopathy of prematurity (ROP) [185]. In post-resuscitation care, an arterial blood oxygen saturation between 94% and 98% is recommended, to prevent the potential harm caused by hyperoxemia [41].

1.4 Applications

This section lists a number of applications of PPG and pulse oximetry, which are performed under conditions of motion, or where artifact-free PPG waveforms are required for beat-to-beat analysis of the PPG signal.

1.4.1 Pulse rate and pulse interval

In ADL, the use of PPG has been researched to detect PR changes in patients with epilepsy [183]. Changes in PR can occur before, during or after the seizure [184]. Detection of changes in PR can be used to warn a caregiver for a potentially dangerous situation, or to monitor the occurrences of seizures for therapy improvement, as seizures may remain unnoticed by the patient [107]. PPG has been incorporated in sports watches to perform PR measurements during exercise [170,177]. Beat-to-beat analysis of PPG signals acquired from the wrist has been researched as a practical screening tool to detect atrial fibrillation (AF) [23,45]. AF is asymptomatic in about one third of the patients [26]. Early detection of AF is important for the prevention of, e.g., stroke and further progression of AF [26].

1.4.2 Heart rate variability and pulse rate variability

Heart rate variability (HRV) quantifies the variations in the R-peak to R-peak intervals in an electrocardiography (ECG) signal, excluding ectopic beats [2, 9, 103, 180]. HRV contains information on the control of the heart rate by the sympathetic and parasympathetic branches of the autonomic nervous system, and the ability of the heart to respond to this control [2, 9, 103, 180]. Reduced HRV has prognostic value in patients who suffered from a myocardial infarction [2], and reduced HRV can provide an early indication of autonomic neuropathy in diabetic patients [2, 143]. Research on healthy volunteers has shown that a surrogate measure of HRV may be provided by pulse rate variability (PRV) derived from the beat-to-beat intervals in PPG signals [53, 101, 159]. However, PRV tends

to overestimate HRV in the respiratory frequency band caused by respiratory-induced variations in pulse transit time [159].

1.4.3 Heart rate turbulence and pulse rate turbulence

Heart rate turbulence (HRT) is another more specific measurement of variability in heart rate with prognostic value [18]. HRT refers to the early acceleration and late deceleration in heart rate following a ventricular premature beat. HRT indirectly assesses the baroreflex, where blunted or absent HRT can indicate a reduced baroreflex. HRT can be useful for risk stratification after a myocardial infarction, and monitoring of disease progression in heart failure, which may facilitate guiding therapy [18]. A surrogate of HRT may be derived from a PPG signal, called pulse rate turbulence (PRT) [54].

1.4.4 Pulse arrival time and pulse transit time

Pulse arrival time (PAT) is the delay between the R-peak in the ECG signal and the corresponding cardiac pulse in the PPG signal [168, 169, 214]. The PAT is defined as

$$\mathrm{PAT} = \mathrm{PEP} + \mathrm{PTT}, \tag{1.12}$$

where PEP stands for pre-ejection period and PTT stands for pulse transit time [48, 167, 168, 214]. The PEP is the time between the R-peak in the ECG signal and the moment at which the aortic valve opens. The PEP corresponds to the isovolumetric contraction of the heart [92]. During this time, the heart muscle is contracting to build up pressure while the pressure in the ventricles is still lower than the pressure in the lung artery and the aorta. During this phase the blood volume in the ventricles is constant. The PTT is the actual travel-time of the pulse between the moment at which the aortic valve opens and the moment at which the pulse is detected at the peripheral measurement site.

PTT can be considered a surrogate measure of pulse wave velocity (PWV) [167–169, 214], where a higher PWV leads to a shorter PTT and vice versa. An increased PWV is associated with an increased arterial stiffness, and is considered to predict cardiovascular risk [48, 121, 166, 168]. PTT may furthermore be used to track changes in blood pressure [48, 167, 168], which may facilitate continuous ambulatory blood pressure monitoring for, e.g., improved diagnosis and treatment of hypertension [14, 22, 167].

1.4.5 Ambulatory oximetry monitoring

Ambulatory oximetry monitoring (AOM) is becoming more widely used, e.g., to obtain temporal SpO_2 patterns of patients with chronic lung disease (CLD) during ADL [44]. AOM may improve screening for the need for long-term oxygen

therapy (LTOT) [37,44]. Currently, LTOT is prescribed based on periodical clinical examinations, such as the six-minute walk test [37,44]. However, the amount of oxygen needed during ADL may not be correctly determined during the clinical examinations [27,37,44]. The temporal SpO_2 patterns obtained during AOM can provide insight in desaturations during ADL, which could allow more effective management of supplemental oxygen treatment, by titration of the supplemental oxygen to the needs of the patient [17, 37, 44, 218]. AOM can also facilitate monitoring patient compliance with the home oxygen recommendations [17,37].

1.4.6 Cardiopulmonary exercise testing

Cardiopulmonary exercise testing (CPX) provides information on the simultaneous response of the cardiovascular and respiratory systems to the metabolic needs of skeletal muscles via exercise of increasing intensity [16,49]. During CPX, exercise is typically performed on a stationary bicycle or a treadmill. CPX has diagnostic and prognostic value in the evaluation of patients with heart failure or unexplained dyspnea [16,49]. SpO_2 measured during CPX can support identifying a pulmonary limitation to exercise, as suggested by a decrease in SpO_2 of more than 5% compared to the SpO_2 level at rest [16, 49]. CPX has also been widely used to assess the performance of athletes [16, 49]. Motion can affect the SpO_2 measurements during CPX, e.g., causing false positive desaturations [16, 49].

1.4.7 Cardiopulmonary resuscitation

The use of PPG during cardiopulmonary resuscitation (CPR) is addressed in Chapters 4 and 5 in Part II of this thesis. Therefore, this section first provides a more extended introduction to CPR (Section 1.4.7.1), and then addresses the use of PPG and pulse oximetry during CPR (Section 1.4.7.2).

1.4.7.1 Introduction to CPR

CPR is the emergency procedure for people suffering from a cardiac arrest [41,97, 120, 165]. During CPR, chest compressions are delivered to artificially generate circulation of blood, and ventilations are given to supply blood with oxygen. Chest compressions can be delivered either manually or with an automated mechanical device [173]. The goal of CPR is to achieve return of spontaneous circulation (ROSC). When ROSC has been achieved, the heart of the patient has resumed beating and generates a spontaneous circulation which is life-sustaining. CPR can be stopped after achieving ROSC.

Figure 1.4 presents a simplified schematic of the 30:2 CPR protocol, which is described in detail in [41, 97, 120, 165]. As shown by the schematic, CPR is delivered in 2-min blocks, in which series of thirty chest compressions are alternated by two ventilations. That is, these 2-min blocks have a 30:2 compression-ventilation ratio. A compression rate of 100 to 120 min^{-1} is targeted. During the ventilations,

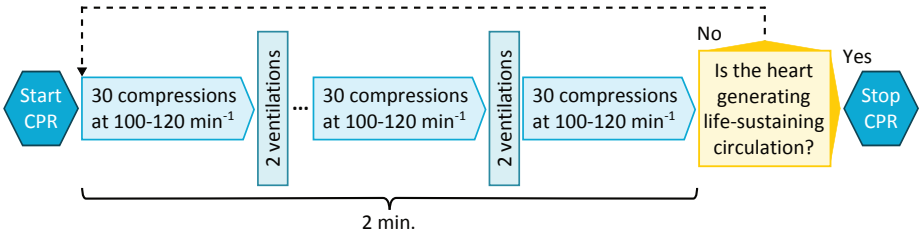

Figure 1.4: Simplified schematic of the 30:2 CPR protocol. CPR is delivered in 2-min blocks, in which series of thirty compressions are alternated by two ventilations. A compression rate of 100 to 120 min^{-1} is targeted. During the ventilations, compressions are stopped. At the end of each 2-min block, clinicians determine whether the heart of the patient has resumed beating and, if so, whether the heart generates a spontaneous circulation which is life-sustaining. If this is the case, CPR can be stopped, otherwise a new 2-min block of 30:2 CPR is initiated. This protocol is described in detail in [41, 97, 120, 165]. CPR: cardiopulmonary resuscitation.

compressions are stopped. At the end of each 2-min block, clinicians determine whether ROSC has been achieved. If so, CPR can be stopped. If ROSC has not been achieved, a new 2-min block of CPR is initiated. International guidelines state that interruptions of the compressions for assessment of ROSC should last no longer than 10 s [41, 97, 120, 165].

The 30:2 CPR protocol is typically followed when applying mouth-to-mouth or bag-mask ventilation. Once a patient has been intubated for ventilations, compressions are not paused for ventilations any longer, but are uninterruptedly delivered during a 2-min block of CPR [41, 97, 120, 165]. Ventilations are then given during ongoing compressions targeting a ventilation rate of about 10 min^{-1} [41, 97, 120, 165].

High-quality CPR requires the minimization of interruptions of the chest compressions, the delivery of adequate compressions at a rate of 100 to 120 min^{-1} with a depth of at least 5 cm, and a full recoil of the chest between compressions [126]. The use of CPR devices which give feedback on the quality of the delivered compressions is recommended [126].

Determining whether a patient has achieved ROSC comprises of the assessment of the electrical as well as the mechanical activity of the heart [41, 97, 120, 165]. The electrical activity of the heart is assessed via the ECG rhythm. If the ECG rhythm shows fibrillation or asystole, the heart cannot generate any output and it is clear that CPR should be continued. If the ECG signal looks organized with R-peaks, this is considered a potentially perfusing rhythm. An organized ECG signal does not imply that the heart has resumed contracting and generates output. Presence of an organized ECG signal while the heart has not resumed contracting with output is called pulseless electrical activity (PEA). PEA occurs frequently. PEA has been reported in about 49% of cases of in-hospital cardiac arrest [127], and in about 21% of cases of out-of-hospital cardiac arrest [145].

Therefore, if an organized ECG signal is observed, a pulse check is performed to determine whether the heart is actually contracting and generating output. In current clinical practice, pulse checks are typically performed by manual palpation at the neck, groin or wrist.

Manual palpation is known to be unreliable and time-consuming, and requires interruption of the chest compressions [43, 113, 129, 178]. Manual palpation can take significantly longer than the 10 s recommended for ROSC assessment, especially when a spontaneous pulse is absent [43, 178]. As a result, manual palpation can lead to long interruptions in the chest compressions, which reduce the compression-generated blood flow and can thereby negatively impact CPR outcome [21, 30, 36, 204].

Methods exist for more objective and more continuous assessment of ROSC. These methods are for instance monitoring of end-tidal CO_2 [39, 139], invasive blood pressure [133, 151], or central venous oxygen saturation [150], which can also be applied during compressions. However, measurement of end-tidal CO_2 requires intubation, and measurement of invasive blood pressure and central venous oxygen saturation require placement of catheters with associated risks for the patient. Trans-thoracic impedance (TTI) measurements [100, 149, 153] and near-infrared spectroscopy (NIRS) [79, 134, 160] are non-invasive methods, but TTI is strongly influenced by compressions and NIRS may respond slowly upon ROSC. Doppler ultrasound is being researched as a non-invasive method to detect pulse absence and presence in the carotid artery, but this technique is sensitive to a correct placement over the carotid artery and is strongly influenced by chest compressions [89,213]. The more objective methods are less practical in use during CPR or cannot be used during ongoing compressions. Therefore, an objective, rapid, non-invasive and easy-to-use method to detect presence or absence of a spontaneous pulse, especially during compressions, would be valuable to support ROSC detection.

1.4.7.2 PPG and pulse oximetry during CPR

Initially, pulse oximetry systems have been used experimentally during CPR to obtain feedback on the chest compression rate [208]. Some researchers considered the presence of a pulsatile PPG signal during chest compressions to be an indication of adequate compressions [59, 208], or reported the use of oxygen saturation readings during CPR [59, 119]. However, during CPR the pulsations in the PPG signal may result from compression-induced motion artifacts, for which reason the PPG signal may not provide an indication of the adequacy of the chest compressions and the oxygen saturation measurement may be unreliable during chest compressions [112, 146]. Furthermore, pulse absence detection by pulse oximeters is delayed, requiring 8 to 10 s of asystole, for which reason decision making during CPR based on a pulse oximeter is not recommended [112]. Pulse oximetry has been reported to be useful during respiratory arrest [171].

Chapters 4 and 5 in Part II of this thesis address the use of PPG during CPR to support detection of ROSC. More recent developments in the use of PPG during CPR are addressed in Section 6.2.

1.5 Motion artifact handling

This section first discusses origins of motion artifacts in PPG signals in Section 1.5.1, and then presents several approaches to handle the motion artifacts. The approaches have been subdivided in three categories. Section 1.5.2 presents methods which remove motion artifacts to recover an artifact-reduced PPG signal for further analysis. Section 1.5.3 presents methods designed for reliable extraction of a specific parameter from a motion-corrupted PPG signal, despite the presence of motion artifacts. Section 1.5.4 presents methods to distinguish artifact-free and artifact-corrupted segments in PPG signals, which can be used to determine whether segments can be, e.g., either analyzed directly or excluded from further analysis.

1.5.1 Origins of motion artifacts in PPG

Motion can cause additional spurious fluctuations in PPG signals, referred to as motion artifacts, which complicate detection of the cardiac pulses. Figure 1.2 shows examples of motion artifacts in PPG signals. Motion artifacts can have several origins. Motion can cause the PPG sensor to move with respect to the skin [10, 33, 65, 66, 72, 108], which results in changes in the illuminated tissue volume, but also in changes in the optical coupling between the LEDs, the tissue and the photodiode [65,66,105]. Pure optical coupling artifacts are multiplicative in nature and can be modeled as variations in P_0 in (1.1) [65, 66, 105]. The acceleration forces of motion can cause variations in venous blood volume in the illuminated tissue volume, sometimes called sloshing of venous blood [33, 57, 109, 137, 140, 211]. The additional variations in the PPG signal caused by sloshing can be modeled by introducing a second time-varying absorbance term in the exponent of (1.1), which in first order can be approximated as an additive motion artifact in (1.2) [57, 211]. Tissue deformation by dynamic variations in sensor contact pressure also leads to additional spurious fluctuations in the PPG signal [14,33,65,66,109,140,177,179]. Furthermore, the sensor can variably loose proper contact with the skin due to motion, which can cause variations in the amount of ambient light reaching the photodiode [14,65,188]. In (1.1), this can be modeled as an additive term next to the light-absorption described by the Beer-Lambert law [65]. The challenge of handling motion artifacts arises from their large magnitude compared to the cardiac component as well as from their occurrence at frequencies in the physiological range causing overlap with PR frequencies [14, 109, 140].

Motion does not necessarily lead to spurious fluctuations in the PPG signal which are comparable to cardiac pulses. Variations in hydrostatic pressure, e.g.,

as a result of raising or lowering the hand with the PPG sensor, leads to large variations in blood volume in the illuminated tissue volume, which shows up as large variations in the baseline of the PPG signal [66, 116, 146]. Motion-induced variations in the baseline can be incorporated in $A_{\mathrm{BL}}(t)$ in (1.1) and have a multiplicative effect on the amplitude of the cardiac component in the PPG signal.

1.5.2 Recovery of artifact-reduced PPG signals

Removal of motion artifacts to recover artifact-reduced PPG signals has been researched extensively. Various generic approaches exist for removal of additive periodic motion artifacts using correlation cancellation with an accelerometer as a motion reference [34, 51, 64, 90, 138, 205]. In these approaches, the artifact is estimated by applying a finite impulse response (FIR) filter to a single reference signal and updating all FIR-coefficients over time. However, quadrature reference signals would be preferred here, so only two coefficients are needed per frequency and undesired frequency-shifted components cancel in the estimate [56, 193]. Wavelength-independent multiplicative optical-coupling artifacts can be removed from a PPG signal by normalization by a second PPG signal obtained at a different wavelength [65, 66, 135]. However, this requires a revised calibration for SpO_2. Motion artifacts in a reflective green PPG signal can also be reduced by subtracting a red PPG signal simultaneously recorded from the same site [217]. Artifact-reduced PPG signals can further be recovered using a synthetic reference for the cardiac pulse waveform [33], deriving artifact references from the measured PPG signals [144, 212], applying a signal decomposition method [47, 83, 87, 157], or averaging several consecutive pulses [91]. However, the approaches without an additional motion measurement provide a segmented recovery of the artifact-reduced PPG signal, require a reliable PR measurement or a clean data segment prior to the artifact reduction, or need to detect the individual cardiac pulses in the corrupted PPG signal.

1.5.3 Motion-robust extraction of parameters

Methods have also been developed focussing on the extraction of averaged physiological parameters from motion-corrupted PPG signals. PR has been determined from the PPG signal frequency spectrum using an accelerometer to identify the motion frequencies [50, 158, 215, 216]. In [158], an artifact-reduced PPG signal time-trace is also reconstructed, but the reconstruction is window-based, and uses per window a single PR selected from the PPG frequency spectrum. PR has also been determined from the PPG signal frequency spectrum after artifact removal with a notch filter at the motion frequency as measured via the photodiode with the LEDs switched off [188]. A combined approach of motion artifact removal and motion artifact detection is presented in [82]. Here, PR is determined by analysis of the frequency spectrum of the presumable cardiac com-

ponent in the PPG signal which has been obtained by signal decomposition or by correlation cancellation with an accelerometry-derived reference signal, or by analysis of the frequency spectrum of a clean segment identified in the measured PPG signal. Motion-robust SpO_2 measurements have been obtained by discriminating cardiac-induced arterial and motion-induced venous components based on their different amplitude ratios in the red and near-IR PPG signals [57, 211]. PR and SpO_2 can also be measured more reliably by using the smoothed pseudo Wigner-Ville distribution [210].

Current commercial algorithms have mainly been designed to extract average PR and SpO_2 measurements and do not use an explicit measurement of motion to reduce the motion artifacts in the PPG signals, such as the Philips FAST-SpO_2 algorithm [78, 80] or the Masimo SET® algorithm [42, 57].

1.5.4 Detection of artifact-free PPG signal segments

Recovery of an artifact-reduced PPG signal or analysis of an artifact-corrupted PPG signal may not be feasible when the signal-corruption is too strong or correlated with the spontaneous pulse component [1,35,95]. Therefore, approaches have been developed to detect artifact-free segments in a PPG signal. The artifact-free segments can be analyzed directly, and the the artifact-corrupted segments can be excluded from further analysis. In cases where motion artifacts can be reduced, distinguishing artifact-free and artifact-corrupted segments can determine when artifact reduction is needed, to improve the efficiency of the artifact reduction and to avoid any unnecessary distortion of the artifact-free segment introduced by the artifact reduction [29, 87]. Artifact-free segments could be detected using morphological properties of the pulses in the PPG signal [1, 29, 35, 95], or by using higher-order statistics and phase relationships between spectral components [87].

The simultaneous use of multiple PPG channels and exploitation of the spatial diversity and the different responses to motion of these channels is another approach to possibly obtaining moderately-corrupted PPG segments during motion [109, 189]. In [109, 189], a custom-built sensor with radially-symmetric configured PPG channels was used to simultaneously measure multiple PPG signals on the forehead during motion. The response to motion was different across the PPG channels, which allowed for the selection of the least-corrupted PPG signal during motion. A template-based algorithm was shown to be able to select the least-corrupted PPG signal with the best correlation with the template, in order to improve PR measurements [189].

1.6 Scope and objectives of the thesis

This thesis consists of two parts. Part I deals with the general problem of motion artifact reduction in PPG. Part II deals with the use of PPG in CPR and the handling of motion artifacts as a result of chest compressions. This section first

presents the overall scope of the thesis in Section 1.6.1, and then presents the objectives of Part I and Part II of the thesis in Sections 1.6.2 and 1.6.3, respectively.

1.6.1 Scope

This thesis deals with the processing and analysis of PPG signals which have been corrupted by motion artifacts. We focused on applications where motion artifacts are (quasi-)periodic and could be modeled. Motion artifact estimates were obtained by using additional sensors to generate a motion reference signal. We focused on explicitly removing the motion artifacts to recover an artifact-reduced PPG signal for further application-specific beat-to-beat analysis. Furthermore, we only considered reflective PPG measurements, because these are not restricted to transilluminable body sites, and are therefore more widely applicable than transmissive PPG measurements [10, 63, 110, 177, 191]. Out of scope are non-contact remote or imaging PPG measurements [176, 187, 194].

We recognize that (quasi-)periodic motion artifacts are a specific subset of motion, and that in clinical practice most motion artifacts are irregular in nature [179]. Nevertheless, handling of (quasi-)periodic motion artifacts can be relevant for ADL, CPX, and CPR. CPR is especially relevant in this thesis, as the second half of the thesis addresses the use of PPG during CPR. Furthermore, (quasi-)periodic motion artifacts are of interest because algorithms may falsely detect them as a PR component [34].

1.6.2 Objectives of Part I

Part I starts with addressing a more fundamental aspect of the origin of motion artifacts. Motion artifacts in PPG signals can have several origins, as described in Section 1.5.1. We hypothesized that motion artifacts correlate with motion of the PPG sensor relative to the skin, which is considered one of the artifact origins. If this hypothesis holds true, relative sensor motion could be used as an artifact reference signal, capturing a different type of motion than that measured by, e.g., an accelerometer. To be able to test this hypothesis, our first objectives were (1) the development of a convenient method to measure sensor motion relative to the skin, and (2) the development of a basic in-vitro skin perfusion phantom to investigate the relationship between relative sensor motion and the resulting artifacts in a controlled laboratory environment. This is described in Chapter 2. Our next objective was to investigate to which extent a PPG sensor moves relative to the skin in a more realistic scenario. Therefore, we augmented a commercially available forehead PPG sensor with the developed method to measure relative sensor motion, and performed measurements with the customized PPG sensor on healthy volunteers while they were walking on a treadmill. This is covered in Chapter 3.

Various generic approaches have been developed for the removal of additive periodic motion artifacts using correlation cancellation with an accelerometer as

a motion reference as outlined in Section 1.5.2. In these approaches, the artifact is estimated by applying a FIR filter to a single reference signal and updating all FIR-coefficients over time. However, quadrature reference signals would be preferred here, so only two coefficients are needed per frequency leading to a short filter, and undesired frequency-shifted components cancel in the artifact estimate [56, 193]. A second objective in Chapter 3 was therefore the development of a generic algorithm which constructs a basis of quadrature reference signals from a measured motion reference signal for the estimation and removal of (quasi-)periodic motion artifacts. As many artifact reduction approaches make use of accelerometers, a third objective of Chapter 3 was to compare the performance of relative sensor motion and accelerometry-derived head motion as artifact reference signals.

1.6.3 Objectives of Part II

The use of PPG has also been researched in the context of CPR. As explained in Section 1.4.7.1, pulse checks during CPR are typically performed by manual palpation, which is unreliable, time-consuming and interrupts the chest compressions. Therefore, an objective, rapid, non-invasive and easy-to-use means to support pulse detection during CPR, preferably during ongoing compressions, would be a valuable asset. We investigated PPG in a pre-clinical automated-CPR study with the objective to determine its potential to detect absence and presence of a spontaneous pulse in pauses and during compressions. This is described in Chapter 4.

Our next objective was to develop an algorithm which can detect cardiogenic output in the PPG signal during CPR, in pauses and during compressions. The goal of the algorithm was to support clinicians in decision making during CPR by showing whether or not the heart has resumed beating with output. Our first goal for the algorithm was to recover a compression-reduced PPG signal by reducing the compression component. Such a signal could directly show the clinician whether a spontaneous pulse component is present and, if so, whether the spontaneous pulse intervals are regular or irregular. Our second goal for the algorithm was the determination of an indicator of cardiogenic output, which could show whether or not the algorithm detected a spontaneous cardiac component in the PPG signal. The indicator was meant to facilitate interpretation of the compression-reduced PPG signal. This algorithm is described in Chapter 5.

1.7 Thesis outline

This thesis consists of two parts. Part I deals with the general problem of motion artifact reduction in PPG. Part II deals with the use of PPG in CPR and the handling of motion artifacts as a result of chest compressions. Each part consists

of two chapters. These chapters are based on published peer-reviewed journal papers and are self-contained.

In Part I, Chapter 2 describes an in-vitro study conducted to determine the correlation between motion of a PPG sensor relative to the skin and the resulting artifacts in a PPG signal. For this purpose, a skin perfusion phantom was developed to mimic reflective PPG signals in the laboratory. The distance between the PPG light source and the photodetector was varied dynamically to introduce motion artifacts in the PPG signal. The PPG light source was a laser diode, which we also used to measure displacement via self-mixing interferometry (SMI) [3, 40, 136]. When the laser diode was translated relative to the perfusion phantom, back-scattered laser-light was Doppler-shifted. The Doppler frequency could be measured by the monitor diode of the laser diode, when the Doppler-shifted laser-light re-entered the laser cavity. Displacement could be derived from the measured Doppler frequencies. Via the laser diode we could use a single compact component as a light source for the PPG measurement and as a sensor for the displacement measurement. Results showed that SMI allowed for accurate measurement of the laser displacement relative to the diffusely-scattering skin phantom. Further, we used the SMI-derived displacement as a reference signal in a correlation canceler. The artifacts in the in-vitro PPG signal could be estimated and reduced by adaptively scaling the measured displacement with a single coefficient. Good correlation between the laser displacement and the motion artifacts was found in the laboratory setup. This work has been published in [J4].

The SMI-based measurement of relative sensor motion was further investigated in a study on healthy volunteers, and was used as a motion reference signal in an artifact-reduction algorithm as presented in Chapter 3. The developed algorithm was generic and reduced quasi-periodic motion artifacts in a PPG signal in order to recover an artifact-reduced PPG signal for beat-to-beat analysis. The algorithm could be of relevance during ADL, CPX, and CPR. The algorithm was developed based on PPG signals measured on the forehead of healthy volunteers while they were walking on a treadmill to induce quasi-periodic motion artifacts. Two measurements of motion were added to the forehead PPG sensor, from which artifact reference signals were derived for comparison. The forehead sensor was augmented with a laser diode to measure sensor motion relative to the skin via SMI using the method described in Chapter 2. An accelerometer was positioned on top of the forehead sensor to measure head motion. The algorithm tracked the step rate in each of the motion reference signals. The motion artifacts were modeled by a harmonic series of quadrature components with frequencies related to the tracked step rate. Subtracting the modeled artifacts from the measured PPG signal resulted in an artifact-reduced PPG signal which could provide a more stable measurement of inter-beat-intervals and SpO_2. For the quasi-periodic motion generated on the treadmill, the accelerometry-derived reference signal was shown to be superior to the SMI-derived reference signal in terms of signal-to-noise ratio and the consistency in providing to the algorithm a frequency component at the step rate. This may have been the result of limited relative sensor motion. We

therefore recommend the use of an accelerometer to obtain a motion reference signal in this scenario. This work has been published in [J1].

In Part II, Chapter 4 describes a pre-clinical automated-CPR study, where the potential of PPG to detect absence and presence of a spontaneous pulse during CPR was investigated. The results showed that PPG could detect absence and presence of a spontaneous pulse during CPR, both in pauses and during ongoing compressions. When the spontaneous pulse rate and the compression rate were different, PPG could also measure the spontaneous pulse rate during compressions. This work has been published in [J3].

Motivated by the results reported in Chapter 4, an algorithm was developed to detect cardiogenic output in a PPG signal during CPR. This algorithm is presented in Chapter 5, and was developed based on the pre-clinical data presented in Chapter 4. The algorithm recovered a compression-reduced PPG signal by subtracting a modeled compression component from the measured PPG signal. Analogous to Chapter 3, the compression component was modeled by a harmonic series of quadrature components with frequencies related to the compression rate. The compression rate was determined from the trans-thoracic impedance (TTI) signal which is measured between the defibrillation pads and commonly available in defibrillators. The compression-reduced PPG signal could directly show absence or presence of an underlying spontaneous pulse component. The algorithm also determined an indicator of cardiogenic output by detecting a spontaneous pulse rate, or a pronounced decrease in the baseline of the PPG signal. A spontaneous pulse rate could be tracked in the compression-reduced PPG signal via spectral analysis, if the spontaneous pulse was present and occurred at a rate different from the compression rate. A pronounced decrease could be detected in the baseline of the PPG signal, when the heart of the animal resumed beating during CPR, presumably caused by a redistribution of blood volume to the periphery. Detection of a decrease in the baseline accommodated for coinciding spontaneous pulse rate and compression rate, at which occurrence the compression reduction algorithm and the spectral analysis could not be used to detect cardiogenic output. The indication of cardiogenic output by the algorithm showed good agreement with the occurrence of ROSC as annotated by clinicians. Therefore, we concluded that this algorithm may support clinical decision making during CPR, by showing during the CPR process when the heart resumes beating with output. This work has been published in [J2].

A general discussion and conclusions with future directions for research are presented in Chapter 6.

Part I

Motion artifact reduction in photoplethysmography

CHAPTER 2

In-vitro model for reduction of motion artifacts in photoplethysmography using relative sensor motion

This chapter is based on

R.W.C.G.R. Wijshoff, M. Mischi, J. Veen, A.M. van der Lee, and R.M. Aarts, "Reducing motion artifacts in photoplethysmograms by using relative sensor motion: Phantom study," *Journal of Biomedical Optics*, vol. 17, no. 11, pp. 117007-1 - 117007-15, Nov. 2012.

Abstract

Introduction: Photoplethysmography (PPG) signals are highly susceptible to motion, which hampers deriving information from the waveform. Part of the motion artifacts are considered to result from sensor-tissue motion and sensor deformation. We hypothesized that these motion artifacts correlate with movement of the PPG sensor relative to the skin. To test our hypothesis, our objective was to remove sensor-motion artifacts in a PPG signal with a correlation canceler, which used sensor motion as the artifact reference signal.

Methods: We developed a skin-perfusion phantom with a diffusely-scattering skin phantom to measure in-vitro PPG signals. Optical motion artifacts were introduced in the in-vitro PPG signals by translating the PPG light source with respect to the PPG photodiode. As PPG light source we used a laser diode, in order to measure displacement via self-mixing interferometry (SMI). This allowed us to use a single component as light source as well as artifact reference measurement. Via SMI, we measured the motion-induced Doppler-shift, from which we derived the laser displacement. The SMI-derived displacement measurement was validated by comparison with a commercial laser Doppler vibrometer (LDV). We estimated and removed the motion artifacts in the in-vitro PPG signals by using a correlation canceler, which scaled the laser displacement by a single coefficient to estimate the motion artifacts. The coefficient was estimated via a least mean-squares algorithm.

Results: Translation of the laser diode was accurately measured via SMI, with an error on the order of 10^{-6} m compared to the LDV measurement. The optical motion artifacts were estimated accurately by scaling the SMI-derived displacement measurement by a single coefficient. This resulted in a significant reduction of the optical motion artifacts in the in-vitro PPG signals.

Conclusions: Displacement over a diffusely scattering surface can be accurately measured via SMI. In-vitro, optical motion artifacts can be accurately estimated and removed by scaling the laser displacement by a single coefficient. This proved our hypothesis true in-vitro. Although good results have been obtained using the in-vitro setup, in-vivo measurements are required to determine the true potential of the use of sensor displacement as a means to reduce motion artifacts in PPG signals.

2.1 Introduction

Pulse oximeters are nowadays widely applied in clinical practice to measure peripheral arterial functional-hemoglobin oxygen-saturation (SpO_2) and pulse rate (PR) [137]. Pulse oximeters derive these data from photoplethysmography (PPG) signals. PPG signals are obtained by illuminating the skin and measuring the intensity of the light that has propagated through the skin in a transmissive or planar configuration, the latter being referred to as a reflective PPG sensor. Transmissive sensors are for instance used on the finger or the earlobe. Reflective sensors are for instance used on the forehead of a patient. PPG signals show periodic decreases as a result of cardiac-induced increases in tissue microvascular arterial blood volume. PR can be directly obtained using this periodicity [105]. By measuring two PPG signals at different wavelengths, commonly red and near-infrared (IR), SpO_2 can be determined. Because blood oxygen saturation determines the color of the blood, SpO_2 can be determined from the ratio of the DC-normalized amplitudes of the cardiac-induced pulses in both PPG signals [191].

Though in clinical practice PPG signals are mostly used to measure SpO_2 and PR, their morphology conveys rich information about the cardiovascular status [115], sympathetic tone [116,146,163] and respiration [5,10,102,116]. Additionally, heart rate variability (HRV) can be determined from PPG signals [102, 123], and the arrival or transit time of the cardiac-induced pulses in PPG signals can be used to monitor changes in blood pressure or arterial compliance [10,146]. Furthermore, PPG signals are highly susceptible to patient and sensor-tissue motion, which can distort PPG signals and derived data [10, 102, 137, 175]. Therefore, to enable reliable extraction of beat-to-beat information from PPG morphology, an improved PPG motion artifact reduction is required which cleans up the PPG signal waveform.

Current commercial algorithms have mainly been designed to extract average SpO_2 and PR and do not use an explicit measurement of motion to reduce the motion artifacts in the PPG signals, such as the Philips FAST-SpO_2 algorithm [78, 80] or the Masimo SET® algorithm [42, 57]. Also in scientific literature, several different approaches to reduce motion artifacts in PPG signals have been investigated. The main approaches are illustrated in the following examples. For a ring-shaped PPG sensor that measures transmissive and reflective PPG signals, the reflective PPG signal has been suggested as a reference for the motion artifacts to clean up the transmissive PPG signal [14]. In an earpiece PPG sensor, a notch filter at the motion frequency removed the motion artifacts from the PPG signals. The motion frequency was determined from the photodiode signal with the LEDs switched off, as sensor-tissue motion caused a variation in the amount of ambient light reaching the photodiode [188]. Accelerometers have been applied as well to obtain a reference for the motion artifacts in a correlation canceler [90], also combined with the Laguerre expansion [52]. Furthermore, sensor-coupling motion artifacts have been removed by equalizing a transmissive PPG signal by a second transmissive PPG signal measured at a different wavelength [65, 66]. Lastly, the

influence of motion on SpO_2 measurements can be reduced by using wavelets [4], the smoothed pseudo Wigner-Ville distribution [210], and multiple colors [12].

In this chapter, we propose a motion artifact reduction method to clean up the PPG signal, in order to enable reliable extraction of beat-to-beat information from the cleaned PPG signal waveform. Different from other methods, we propose to measure motion of the PPG sensor with respect to the skin, and use the measured relative sensor motion as a reference signal for the motion artifacts [197]. Motion artifacts in PPG signals are presumably caused by hemodynamic effects, tissue deformation, and sensor movement and deformation [10, 65, 66, 105, 137]. We hypothesized that a large part of these motion artifacts correlate with relative sensor motion. When the sensor moves with respect to the skin, spurious fluctuations occur in the PPG signal as a result of variations in light coupling and the probed tissue volume, e.g., changes in the shunt light which does not probe pulsatile blood volume [65, 66, 105]. We expected that an estimate of these motion artifacts can be derived from a measure of relative sensor motion in order to remove these artifacts from the PPG signals. Moreover, by deriving motion artifacts from relative sensor motion, one can possibly obtain insight in the relative contribution of these artifacts to the total artifact that results from motion.

We furthermore focus on the use of reflective PPG sensors. Reflective PPG sensors are potentially more widely applicable than transmissive sensors, as reflective sensors are not restricted to transilluminable body sites [10]. On central sites, such as the forehead, reflective sensors have been shown to measure desaturation events earlier than finger sensors as a result of a shorter circulation transit time [24, 28]. Also, PPG measurements on the forehead suffer to a lesser extent from vasoconstrictive responses [24], and motion artifacts [209].

We built an in-vitro skin-perfusion phantom in a laboratory setup to develop a method to measure relative sensor motion, and to investigate the influence of sensor motion on PPG signals. We describe the skin-perfusion phantom and the setup in Section 2.2. In the setup, we used a single laser diode as both a light source for the PPG measurements and as a sensor to measure displacement. Optical motion artifacts were generated in the setup by translating the laser diode with respect to the PPG photodiode. The laser diode measured relative sensor motion via self-mixing interferometry (SMI), as explained in Section 2.3. When the sensor moved with respect to the skin phantom and the backscattered laser light re-entered the laser cavity, its Doppler shift could be determined via the monitor diode of the laser diode. Relative sensor motion was subsequently determined from the Doppler phase. Using SMI is practical, because this method is compact and self-aligning, and can therefore be integrated in a PPG sensor. In Section 2.4 we describe how we used the SMI displacement measurement as a reference for the motion artifacts in a least mean-squares (LMS) algorithm [68]. In this algorithm, an estimate of the motion artifacts was derived from the SMI displacement measurement, and was subtracted from the distorted in-vitro PPG signal to reduce the motion artifacts and to retrieve the mimicked cardiac component. The obtained in-vitro PPG signals, the accuracy of the SMI displacement

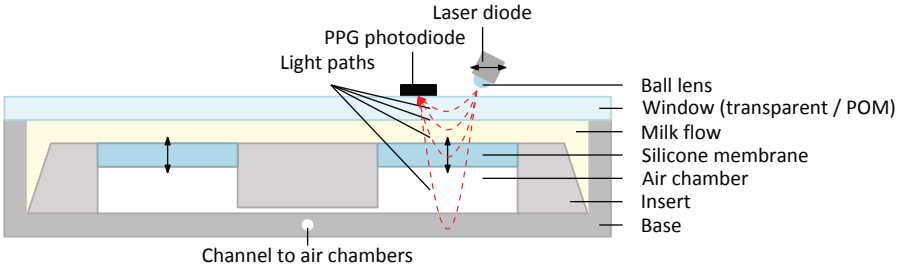

Figure 2.1: Cross-sectional view of the flow cell containing the insert with silicone membranes (not to scale). The dashed arrows indicate different light paths that contribute to the PPG signal. The solid arrows indicate motion of the membranes to mimic changing blood volume and motion of the laser diode to generate artifacts in the PPG signal. POM: polyoxymethylene (Delrin®); PPG: photoplethysmography.

measurement, and the performance of the artifact reduction approach are presented in Section 2.5 and discussed in Section 2.6, and conclusions are presented in Section 2.7.

2.2 Methods A: Experimental setup

An in-vitro setup was built to study whether it is possible to remove motion artifacts from a PPG signal by using relative sensor motion as an artifact reference, and to develop a method to measure relative sensor motion. The setup contained a flow cell that mimicked skin perfusion, as described in Section 2.2.1. The measurement setup in which the flow cell was used is described in Section 2.2.2. Section 2.2.3 describes how the in-vitro PPG measurements were obtained.

2.2.1 Skin perfusion phantom

To be able to measure PPG signals in-vitro, a flow cell was made that modeled cardiac-induced blood volume changes in the skin. Figure 2.1 shows a cross-sectional view of the flow cell, Fig. 2.2a shows the components of the flow cell, and Fig. 2.2b shows the assembled flow cell in the setup. Two different inserts were made that went into the base of the flow cell. Both inserts defined a rectangular flow channel that was 170 mm long and 34.7 mm wide. In both inserts, half of the flow channel was 0.5 mm deep and half was 1 mm deep, with an abrupt change in depth in the middle, as shown in Fig. 2.2a. In this study, PPG signals were only measured over the 1 mm deep channel. One insert defined a rigid flow channel, and the other insert contained two 29.7 mm by 45.8 mm silicone membranes to realize a flexible flow channel (Fig. 2.2a). Below the membranes, the insert contained air filled chambers, which were connected to ambient air via a channel in the base. Either a transparent or a polyoxymethylene (POM, Delrin®) window

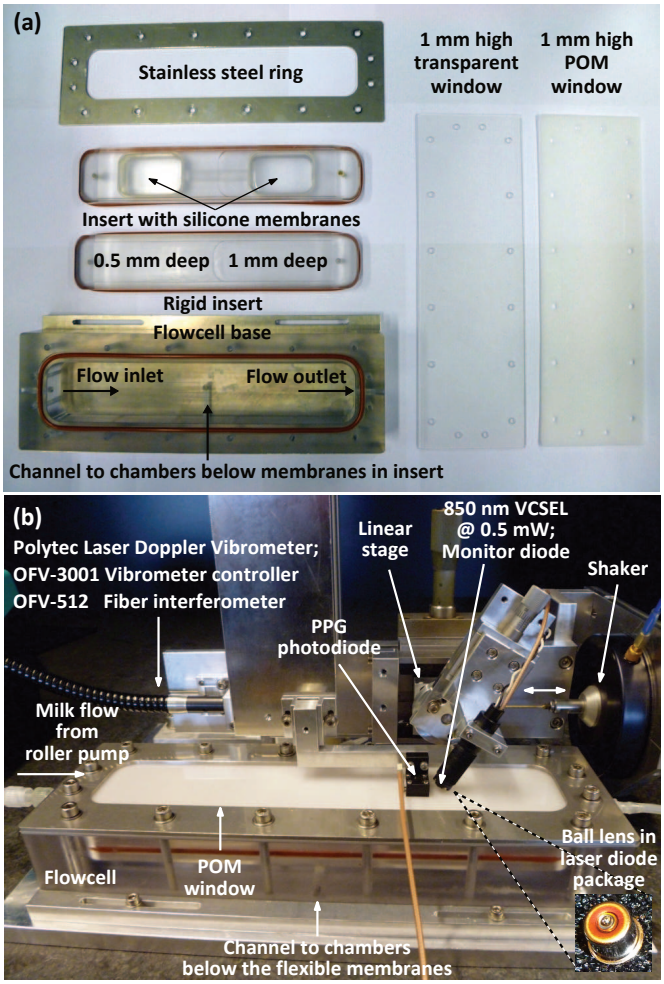

Figure 2.2: (a) The components of the flow cell that was developed as a skin-perfusion phantom. The inserts go into the base of the flow cell and define the flow channel. The top of the flow channel is closed off by either a transparent or a POM window. (b) The assembled flow cell in the experimental setup built to measure PPG signals distorted by optical motion artifacts. Optical motion artifacts were generated by translating the laser diode on the linear stage with respect to the PPG photodiode. The linear stage was driven by a shaker. The laser Doppler vibrometer was used as a reference measurement for the SMI-derived displacement measurement. POM: polyoxymethylene (Delrin®); PPG: photoplethysmography; SMI: self-mixing interferometry; VCSEL: vertical-cavity surface-emitting laser-diode.

of 1 mm high was mounted on top of the base and the insert to close off the flow channel. The window was fixed via a stainless steel ring, as shown in Fig. 2.2b.

Because the pulsatility in the PPG signal originates from the dermis, the flow channel was closed off by a 1 mm high POM skin phantom [7, 25, 147]. A diffuse scattering POM window was used as a skin phantom, because the optical properties of POM are similar to skin [186]. The POM window modeled the optical shunt caused by light that does not propagate through pulsating blood, as illustrated by the topmost dashed arrow in Fig. 2.1 [105, 147]. A transparent window was used to determine the contribution of the optical shunt through the POM skin phantom to the in-vitro PPG signal.

Because the topmost layers of the skin contain a dense network of capillaries and microvessels, blood flow was modeled by a thin layer of flow [25,147]. By using the insert with the silicone membranes, a flexible flow channel was obtained that enabled mimicking blood volume changes. A pulsatile flow caused the flexible membranes to bend downward upon increases in pressure in the channel, thus locally increasing the volume of the flow channel, as indicated in Fig. 2.1. The insert with the rigid flow channel was used to verify that the volume increase indeed was the origin of the pulse in the modeled PPG signal.

Finally, we used milk to mimic blood, as milk and blood contain light scattering particles of comparable size [99]. In blood, erythrocytes scatter light, which have a typical diameter of about 8 μm [62]. In milk, fat globules scatter light, which have a diameter between about 1 μm and 10 μm with an average of 4 μm [111]. Furthermore, also in reflective measurements the cardiac-induced pulsatile component in the PPG signal mainly results from increases in light attenuation [58, 146]. Any increase in directly backscattered light as a result of increased blood volume is usually negligible compared to the increased absorption of light returning from deeper tissue, for source-detector distances of approximately 1 cm [58, 146]. Therefore, because milk hardly absorbs light at 850 nm, a small amount of a water-soluble black dye was added to the milk as an absorber [141].

2.2.2 Measurement setup

The setup in Fig. 2.2b was used to measure in-vitro PPG signals and generate optical motion artifacts. An 850 nm VCSEL (Vertical-Cavity Surface-Emitting Laser-Diode, $\lambda_0 = 850$ nm) with an internal monitor diode was used to illuminate the flow cell (ULM-Photonics GmbH, Philips, Ulm, Germany). A roller pump with three rollers generated a pulsatile milk flow, which resulted in a varying milk volume in the flow cell. The photodiode on top of the window of the flow cell ("PPG photodiode" in Fig. 2.1 and 2.2b) measured a PPG signal when the laser diode illuminated the flow cell. The distance between the laser spot on the window of the flow cell and the center of the photodiode was approximately 1 cm. The laser diode was attached to a linear stage, which was driven by a shaker. In this way, the shaker could translate the laser diode to generate motion artifacts in the PPG signal as a result of a dynamically changing emitter-detector distance. Artifacts

resulted because the change in emitter-detector distance altered the optical shunt through the POM window and changed the depth at which the light probed the perfusion phantom (Fig. 2.1) [147]. In practice, these effects result from sensor deformation or when the whole PPG sensor translates over inhomogeneous tissue.

We also used the laser diode to measure displacement by means of SMI. To be able to measure displacement using SMI, sufficiently strong optical feedback into the laser diode was required. Therefore, the laser beam was focused on the window of the flow cell via the ball lens that was integrated in the laser diode package. A close-up of the laser diode package with integrated ball lens is shown bottom right in Fig. 2.2b. This compact component was used to be able to readily integrate it in a real sensor later on. The distance between the ball lens and the window was approximately 2 mm, resulting in a distance of about $L_o \approx 4$ mm between the laser diode and the window. The angle between the laser beam and the surface normal of the flow cell was set to 30°. To verify the SMI displacement measurement, a reference displacement measurement was obtained by a laser Doppler vibrometer (LDV) (Polytec, Waldbronn, Germany). Here the OFV-3001 Vibrometer Controller was used combined with the OFV-512 Fiber Interferometer. The LDV directly measured the translation of the linear stage to which the laser diode was attached (Fig. 2.2b). By limiting the displacement of the linear stage to 1280 μm, the LDV had a resolution of 0.32 μm.

A laser driver controlled the injection current of the laser diode. An optical output power of 0.5 mW was obtained at a DC current of 1.63 mA. The DC level of the monitor diode of the laser diode was visually inspected to confirm that the optical output power of the laser diode did not change during the measurements. To enable measuring the direction of motion via SMI, the laser injection current was amplitude modulated (see Section 2.3). A 40-kHz AC-current with an amplitude of 158 μA was superimposed to the DC current. The choice for the AC-amplitude had two consequences, as explained in the last paragraph of Section 2.3.1. First, it resulted in good-quality Doppler signals around the 40 kHz modulation frequency and its 80 kHz harmonic, which were needed for the displacement measurement. Second, it minimized the Doppler signals in the baseband, which reduced distortion in the PPG signal as the laser diode was also used as the light-source of the PPG measurement. The laser driver generated the 40-kHz AC-current from a 40-kHz AC voltage that was provided by a function generator (33250A 80 MHz Function / Arbitrary Waveform Generator, Agilent Technologies, Inc., Santa Clara, California, USA). For the 850-nm VCSEL that was used, the lasing wavelength dependency on the injection current was specified to be 0.4 nm/mA (specified by ULM-Photonics GmbH, Philips, Ulm, Germany). The modulation induced wavelength change, $\Delta\lambda_m$ [m], thus was approximately $\Delta\lambda_m \approx 63$ pm, giving $\Delta\lambda_m/\lambda_0 \approx 7 \cdot 10^{-5}$.

The PPG photodiode and monitor diode currents were amplified by transimpedance amplifiers to obtain the voltages $v_{\mathrm{PD}}(t)$ and $v_{\mathrm{MD}}(t)$, respectively, with time t [s]. The PPG photodiode and monitor diode voltages, and the LDV signal were band-limited to 100 kHz and recorded at 200 kHz by a 16-bit digital data ac-

Table 2.1: Overview of the types of measurements performed using the setup in Fig. 2.2 to analyze the in-vitro PPG signal.

Measurement	Window	Flow channel	Flow
Case 1	POM	Rigid	Milk
Case 2	POM	Flexible	Milk
Case 3	POM	Flexible	Milk with black dye
Case 4	Transparent	Flexible	Milk with black dye

POM: polyoxymethylene (Delrin®); PPG: photoplethysmography.

quisition card (DAQ) (NI USB-6259, National Instruments, Austin, Texas, USA). A LabVIEW® (National Instruments, Austin, Texas, USA) program controlled the DAQ. The LabVIEW® program also generated the signal that was sent out by the DAQ and amplified to control the shaker. Finally, a 10-MHz input clock-signal for the function generator was derived from the 20-MHz clock signal of the DAQ, to make sure that only one clock was used in the measurement system.

2.2.3 In-vitro PPG measurements

In-vitro PPG signals were obtained by illuminating the perfusion phantom using the laser diode and measuring the PPG photodiode signal, $v_{\mathrm{PD}}(t)$, as shown in Fig. 2.1 and 2.2b. The signal $v_{\mathrm{PD}}(t)$ was sampled by the DAQ giving the digitized signal $v_{\mathrm{PD}}[n]$. We obtained the raw PPG signal $ppg[n]$ from $v_{\mathrm{PD}}[n]$ by applying to $v_{\mathrm{PD}}[n]$ a second-order zero-phase Butterworth low-pass filter with a 100-Hz 3-dB cut-off frequency followed by down-sampling to 250 Hz, and applying a fourth-order zero-phase Butterworth low-pass filter with a 30-Hz 3-dB cut-off frequency.

As listed in Table 2.1, we performed four types of measurements to determine the influence of the silicone membranes, the water-soluble black dye, and the POM window on the in-vitro PPG signals. In all four cases, the roller-pump was used at 20 rounds per minute (RPM) to generate a pulsatile flow, thus simulating a PR of 60 beats per minute (BPM). In the first three cases, the channel was closed off by the POM window, and in the fourth case the channel was closed off by the transparent window. Furthermore, in all cases we measured the deflection of the window via SMI. Here, the angle θ between the laser beam and the direction of motion equaled 30°, because the window deflection was approximately an upward directed motion. We measured the window deflection, to determine whether pulsatile milk volume in the channel enabled by the silicone membranes indeed was the main contributor to the simulated pulse in the in-vitro PPG signal.

As shown in Table 2.1, in case one we measured a pulsatile milk flow through the insert with the rigid channel. In case two, we measured a pulsatile milk flow through the insert with the silicone membranes. Cases one and two were used to verify that the change in milk volume in the flexible channel represented the dominant contribution to the simulated pulse amplitude of the PPG signal. In case

three, we measured a pulsatile flow of milk with a water-soluble black dye through the insert with the silicone membranes. We used case three to determine whether the added dye caused decreases in the measured PPG signal upon increases in the milk volume in the channel. In case four, we performed similar measurements as in case three, except that we used a transparent window, to determine whether the POM window resulted in an optical shunt.

2.3 Methods B: Displacement measurement

We measured displacement with a laser diode by making use of SMI. SMI is observed when a laser diode illuminates an object such that part of the light backscattered by the object re-enters the cavity of the laser diode. The backscattered light interferes with the standing wave inside the laser cavity, thus changing the emitted optical lasing frequency and power [136]. Moreover, when light re-enters the cavity that has been backscattered by a moving object, a beat frequency $f_d(t)$ [Hz] equal to the Doppler shift is observed in the optical power,

$$f_d(t) = \frac{v_o(t)\cos(\theta)}{\lambda(t)/2}, \tag{2.1}$$

with time t [s], object velocity $v_o(t)$ [m/s], angle θ [rad] between the velocity vector of the object and the laser beam, and lasing wavelength $\lambda(t)$ [m]. The component of the displacement of the object in the direction of the laser beam follows by equating each full cycle in the optical power to half of the emitted wavelength.

However, only counting the number of cycles in the optical power does not reveal the direction of motion, because in this case one uses the absolute value of the velocity of the object. Without directional information the displacement measurement can have a frequency twice as high as the displacement itself (frequency doubling as a result of using the absolute value of the velocity). This complicates its use to correct motion artifacts in PPG signals which are caused by variations in sensor position. Therefore, displacement should be measured such that the direction is taken into account as well.[1] When using SMI, the direction of motion can be determined either from the shape of the interference pattern in the optical power, or by modulating the emitted wavelength. At moderate levels of optical feedback, the interference pattern is sawtooth shaped. In this case the direction of motion determines whether the fast edge of the sawtooth is directed upwards or downwards [3, 55, 85]. However, if the direction of motion is determined from the fast edge of the sawtooth shaped interference pattern, the level of optical feedback

[1] Note that with a single laser diode one can only determine whether the net motion in three dimensions is directed towards or away from the laser beam. Because the three-dimensional motion is projected onto a single axis only, it is not possible to determine the exact direction of motion in three-dimensional space. Moreover, any motion orthogonal to the laser beam is not observed at all. These can be limitations of the current configuration.

is required to exceed some threshold to guarantee proper functioning of the displacement measuring method. That is, sawtooth shaped interference patterns are only observed at moderate levels of optical feedback. At (very) weak levels of optical feedback the interference pattern is sinusoidally shaped. In this application though, the level of optical feedback can be (very) weak, thus not exceeding the required threshold to obtain sawtooth shaped interference patterns. This is because the level of optical feedback is linearly related to both the reflectivity of the illuminated object and the distance from the laser diode to the object [3, 55, 85, 136]. Because skin diffusely scatters the light and because the optical properties of skin are highly variable, in some conditions weak backscattering from the skin can lead to (very) weak optical feedback. In addition, the distance between the skin and the laser diode will only be on the order of millimeters. For these reasons, we prefer to use a method that can also observe the direction of motion at (very) weak feedback levels. This is accomplished by amplitude modulation of the laser injection current, which induces a wavelength modulation. In this case the direction of motion can be recovered by using two spectral Doppler components of the SMI signal, as explained in the next sections. The structure of the SMI signal is explained in Section 2.3.1. Section 2.3.2 explains how displacement is determined from the SMI signal, and the accuracy of the obtained displacement measurement is analyzed in Section 2.3.3. In Section 2.3.4 we explain how we validated our SMI-based displacement measurement.

2.3.1 SMI signal structure

The Doppler frequency in the optical power was measured by the internal monitor diode of the laser diode. The monitor signal, $v_{\mathrm{MD}}(t)$ [V], was obtained from the monitor diode current $i_{\mathrm{MD}}(t)$ [A] via a transimpedance amplifier with gain Z [V/A], and can be expressed as [3, 40, 55, 61, 85]

$$v_{\mathrm{MD}}(t) = Z i_{\mathrm{MD}}(t) \tag{2.2}$$

$$= ZR\left[P_{\mathrm{DC}} + \Delta P_m \sin(\omega_m t + \phi_m)\right]\left[1 + m(t)\cos(\phi_{\mathrm{ext}}(t))\right], \tag{2.3}$$

in which R [A/W] is the responsivity of the monitor diode, P_{DC} [W] is the DC optical power, and ΔP_m [W] is the amplitude of the AC optical power as a result of the modulation of the laser injection current at modulation frequency ω_m [rad/s] with initial phase ϕ_m [rad]. The second factor between square brackets describes the fluctuations in optical power caused by optical feedback. Here $m(t)$ [-] is the modulation depth which depends on the level of optical feedback. We assumed the modulation depth to be time-dependent, because speckle effects cause the level of optical feedback to vary over time [55]. Lastly, phase $\phi_{\mathrm{ext}}(t)$ [rad] is the interferometric phase of the light that re-enters the laser cavity, which contains the displacement information of the object. Because $\Delta P_m / P_{\mathrm{DC}} \ll 1$ and $m(t) < 1$, we approximated (2.3) by

$$v_{\mathrm{MD}}(t) \approx ZR\left\{P_{\mathrm{DC}} + \Delta P_m \sin(\omega_m t + \phi_m) + m(t) P_{\mathrm{DC}} \cos\left(\phi_{\mathrm{ext}}(t)\right)\right\}. \tag{2.4}$$

The phase change of the external cavity, $\phi_{\text{ext}}(t)$, can be further expressed as the phase change as a result of the distance L_o [m] traveled between the laser diode and the object, plus the Doppler phase change as a result of object motion:

$$\phi_{\text{ext}}(t) = \frac{4\pi L_o}{\lambda(t)} + 2\pi \int_0^t f_d(\xi) d\xi. \tag{2.5}$$

The emitted wavelength, $\lambda(t)$, contained two time-varying components, which can be expressed as

$$\lambda(t) = \lambda_0 + \Delta\lambda_m \sin(\omega_m t + \phi_m) + \lambda_{\text{fb}}(t), \tag{2.6}$$

where the first term is the average emitted wavelength, the second term is the wavelength modulation caused by the amplitude modulation of the injection current, and the third term is the fluctuation of the emitted wavelength caused by the time-varying optical feedback. As $\Delta\lambda_m/\lambda_0 \ll 1$ and $\Delta\lambda_{\text{fb}}(t)/\lambda_0 \ll 1$, the cosine term in (2.4) can be approximated by

$$\begin{aligned}
\cos\left(\phi_{\text{ext}}(t)\right) \approx & \cos\left(\frac{4\pi L_o}{\lambda_0}\left(1 - \frac{\Delta\lambda_m}{\lambda_0}\sin(\omega_m t + \phi_m) - \frac{\Delta\lambda_{\text{fb}}(t)}{\lambda_0}\right) + \right. \\
& \left. \frac{4\pi\cos(\theta)}{\lambda_0}\int_0^t v_o(\xi)d\xi - \frac{8\pi\cos(\theta)}{\lambda_0}\frac{\Delta\lambda_m}{\lambda_0}\frac{v_{o\max}}{\omega_m} - \frac{\lambda_0}{2\pi L_o}C\right) \qquad (2.7) \\
\approx & \cos\left(\frac{4\pi L_o}{\lambda_0}\left(1 - \frac{\Delta\lambda_m}{\lambda_0}\sin(\omega_m t + \phi_m) - \frac{\Delta\lambda_{\text{fb}}(t)}{\lambda_0}\right) + \right. \\
& \left. \frac{4\pi\cos(\theta)}{\lambda_0}\int_0^t v_o(\xi)d\xi\right) \qquad (2.8) \\
= & \cos\left(\phi_d(t)\right)\cos\left(\phi_0\sin\left(\omega_m t + \phi_m\right)\right) + \\
& \sin\left(\phi_d(t)\right)\sin\left(\phi_0\sin\left(\omega_m t + \phi_m\right)\right), \qquad (2.9)
\end{aligned}$$

in which

$$\phi_d(t) = \frac{4\pi L_o}{\lambda_0}\left(1 - \frac{\Delta\lambda_{\text{fb}}(t)}{\lambda_0}\right) + \frac{4\pi\cos(\theta)}{\lambda_0}\int_0^t v_o(\xi)d\xi, \tag{2.10}$$

$$\phi_0 = \frac{4\pi L_o \Delta\lambda_m}{\lambda_0^2}. \tag{2.11}$$

The one but last term of the argument in (2.7) is the upper bound of the effect of modulation on the integral of the Doppler frequency, in which $v_{o\max}$ [m/s] is the maximum object velocity. The upper bound was obtained by integrating over half of the modulation period. This term would equal zero when integrating over a full modulation period. This term was neglected in (2.8), because both $\Delta\lambda_m/\lambda_0 \ll 1$ and $v_{o\max}/\omega_m \ll 1$. Furthermore, the last term of the argument in (2.7) is an approximation of the effect of the feedback induced wavelength variation on the integral of the Doppler frequency, in which C [-] is the optical feedback parameter

[85, 136]. This approximation was obtained by using that $\Delta\lambda_{\mathrm{fb}}(t)$ varies with the Doppler frequency, just as the light intensity in the laser cavity [3], and integrating over half of a Doppler period. In addition, we used that the maximum feedback induced wavelength variation equals $\Delta\lambda_{fb\,\max} = \pm(\lambda_0^2 C)/(4\pi L_o)$, which was derived from the laser phase condition that included the effect of feedback, and by using the optical feedback parameter C [85, 136]. Also this term was neglected in (2.8), because $\lambda_0/L_o \ll 1$ and because $C < 1$ in the (very) weak feedback regime [55].

Via real-valued variations of the Jacobi-Anger expansion, we obtained a first order approximation of (2.9). By using the relationship $J_{-k}(\zeta) = (-1)^k J_k(\zeta)$ for the Bessel function of the first kind of order k, the following expression can be obtained for the Jacobi-Anger expansion [38]:

$$e^{j\zeta \sin\Omega} = \sum_{k=-\infty}^{\infty} J_k(\zeta) e^{jk\Omega} \tag{2.12}$$

$$= J_0(\zeta) + 2\sum_{k=1}^{\infty} J_{2k}(\zeta)\cos(2k\Omega) + 2j\sum_{k=1}^{\infty} J_{2k-1}(\zeta)\sin((2k-1)\Omega). \tag{2.13}$$

By using $\zeta = \phi_0$ and $\Omega = \omega_m t + \phi_m$ in the first order approximations of the real and imaginary parts of (2.13) for $\cos(\phi_0 \sin(\omega_m t + \phi_m))$ and $\sin(\phi_0 \sin(\omega_m t + \phi_m))$ in (2.9), respectively, and substituting this result in (2.4), the monitor diode signal can be expressed as a sum of signals in the baseband, around the modulation frequency, and around the second harmonic of the modulation frequency:

$$\begin{aligned} v_{\mathrm{MD}}(t) \approx & ZR\{P_{\mathrm{DC}} + \Delta P_m \sin(\omega_m t + \phi_m) + \\ & m(t) P_{\mathrm{DC}} \cos(\phi_d(t)) [J_0(\phi_0) + 2J_2(\phi_0)\cos(2(\omega_m t + \phi_m))] + \\ & m(t) P_{\mathrm{DC}} \sin(\phi_d(t)) [2J_1(\phi_0)\sin(\omega_m t + \phi_m)]\}. \end{aligned} \tag{2.14}$$

Equation (2.14) shows that light backscattered into the laser cavity by a moving object yields Doppler signals with a phase $\phi_d(t)$ as in (2.10). As modulation of the laser injection current causes the Doppler phase $\phi_d(t)$ to appear both in a sine and a cosine, the Doppler phase can be recovered conveniently by unwrapping the arctangent of the ratio of the sine and the cosine. Moreover, (2.14) shows that $\cos(\phi_d(t))$ appears both in the baseband and around the second harmonic of the modulation frequency. We used the $\cos(\phi_d(t))$ term around the second harmonic to measure displacement, because of its better signal-to-noise rate (SNR) compared to the baseband signal, given the $1/f$ noise characteristic of the monitor diode and the electronics, and mains interference.

Moreover, (2.14) shows that the Doppler signals in the baseband, around the modulation frequency, and around the second harmonic of the modulation frequency are proportional to $J_0(\phi_0)$, $J_1(\phi_0)$ and $J_2(\phi_0)$, respectively. Therefore, as illustrated by the Bessel functions in Fig. 2.3, a proper choice of ϕ_0 results in Doppler signals with a large amplitude around the modulation frequency and its

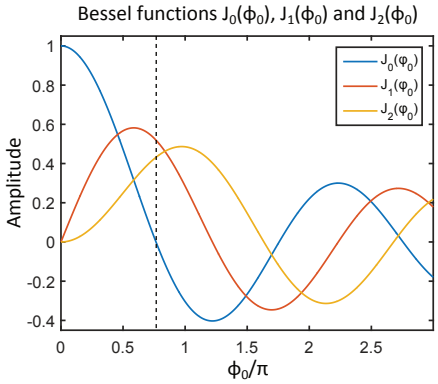

Figure 2.3: Bessel functions $J_0(\phi_0)$, $J_1(\phi_0)$ and $J_2(\phi_0)$ which scale the Doppler signals in the baseband, around the modulation frequency and around the second harmonic of the modulation frequency, respectively. The dashed vertical line indicates the choice of ϕ_0 which minimized the Doppler signals in the baseband.

second harmonic, and a small amplitude in the baseband. The latter is advantageous in this study, because we also used the laser diode to measure the PPG signal. By reducing the amplitude of the Doppler signals in the baseband, we could improve the SNR of the PPG signal. The preferred ϕ_0 equaled approximately 0.77π rad, at which phase $J_0(\phi_0)$ was approximately 0, as indicated by the dashed vertical line in Fig. 2.3. As (2.11) shows, we could obtain the preferred ϕ_0 by adjusting modulation depth $\Delta\lambda_m/\lambda_0$, which was proportional to the AC component of the laser injection current. Moreover, (2.11) shows that the modulation depth required to obtain the preferred ϕ_0 depends on the distance L_o between the laser diode and the object. Because L_o was constant in the in-vitro setup, the required modulation depth was not a time-varying parameter in this study. By using $\phi_0 = 0.77\pi$ rad, $L_o \approx 4$ mm, and $\lambda_0 = 850$ nm in (2.11), the required modulation depth was found to be approximately $\Delta\lambda_m/\lambda_0 \approx 4 \cdot 10^{-5}$. This also confirmed the validity of the assumption that $\Delta\lambda_m/\lambda_0 \ll 1$.

As explained in Section 2.2.2, we applied amplitude modulation at 40 kHz to the laser injection current with an AC-amplitude of 158 μA, resulting in $\Delta\lambda_m/\lambda_0 \approx 7 \cdot 10^{-5}$. We determined this amplitude experimentally, by inspecting the baseband Doppler signals on a spectrum analyzer while adjusting the AC-amplitude. The deviation between $\Delta\lambda_m/\lambda_0$ found experimentally and theoretically, can be explained by the inaccuracies in the specified laser diode parameters, the estimate of L_0 and the estimate of the laser injection current AC-amplitude.

2.3.2 Determination of displacement

We determined the displacement of the laser diode retrospectively using the digitized monitor diode signal as acquired by the DAQ. Therefore, as of this section,

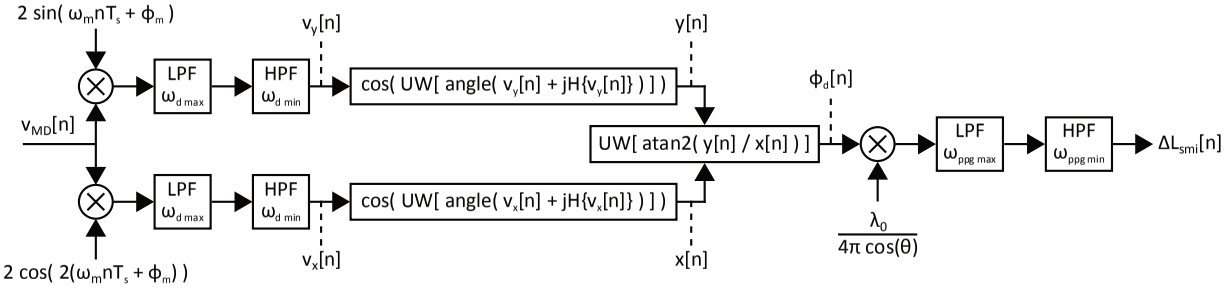

atan2(.)	four-quadrant arctangent	HPF	high-pass filter	θ	angle between laser-beam and velocity-vector	$v_{x,y}$	baseband Doppler signals
ΔL_{smi}	displacement measurement	LPF	low-pass filter			$\omega_{d\ max,\ min}$	max / min Doppler frequency
ϕ_d	Doppler phase	λ_0	average laser wavelength	T_s	sample time	ω_m	laser modulation frequency
ϕ_m	laser modulation phase	PPG	photoplethysmography	UW[.]	phase unwrapping	$\omega_{ppg\ max,\ min}$	max / min PPG signal frequency
H{.}	Hilbert transform	SMI	self-mixing interferometry	v_{MD}	monitor diode signal	x, y	normalized Doppler signals

Figure 2.4: Block diagram describing the displacement measurement $\Delta L_{\mathrm{smi}}[n]$ [m] as determined from the monitor diode signal $v_{\mathrm{MD}}[n]$ [V]. Band-limited baseband Doppler signals $v_x[n]$ [V] and $v_y[n]$ [V] were obtained by demodulation, followed by applying an LPF and an HPF. These signals were subsequently normalized by applying the Hilbert transform $H\{\cdot\}$ and using the unwrapped phase of the resulting analytical signals in a cosine, resulting in the normalized baseband Doppler signals $x[n]$ [-] and $y[n]$ [-]. Here, UW[·] indicates phase unwrapping. The Doppler phase $\phi_d[n]$ [rad] was then obtained from these signals by applying a four-quadrant arctangent implementation, atan2(·), to the ratio of $y[n]$ and $x[n]$, and unwrapping the resulting phase. Finally, the displacement measurement, $\Delta L_{\mathrm{smi}}[n]$ [m], was obtained by equating each phase change of 2π rad in $\phi_d[n]$ to a displacement of half a wavelength, $\lambda_0/2$, and correcting for the angle θ between the laser beam and the direction of motion. Here, λ_0 [m] is the average wavelength of the emitted laser-light. The bandwidth of $\Delta L_{\mathrm{smi}}[n]$ was adjusted to the bandwidth of the band-pass filtered PPG signal, $ppg_{\mathrm{ac}}[n]$, by the LPF and HPF at the end of the signal processing chain. HPF: high-pass filter; LPF: low-pass filter; PPG: photoplethysmography.

we will consider digital signals, with discrete-time index n and sample time T_s [s]. We indicated the digitized monitor diode signal by $v_{\mathrm{MD}}[n]$.

The block diagram in Fig. 2.4 describes how we determined displacement from the digitized monitor diode signal, $v_{\mathrm{MD}}[n]$. As a first step to track the Doppler phase $\phi_d[n]$, the Doppler signals were demodulated and band-pass filtered (BPF) to obtain baseband signals:

$$\begin{aligned} v_y[n] &= 2\ \mathrm{BPF}\left\{v_{\mathrm{MD}}[n]\sin\left(\omega_m n T_s + \phi_m\right)\right\} \\ &= 2ZRm[n]P_{\mathrm{DC}}J_1\left(\phi_0\right)\sin\left(\phi_d[n]\right) \\ &= A_y[n]\sin\left(\phi_d[n]\right), \end{aligned} \tag{2.15}$$

$$\begin{aligned} v_x[n] &= 2\ \mathrm{BPF}\left\{v_{\mathrm{MD}}[n]\cos\left(2(\omega_m n T_s + \phi_m)\right)\right\} \\ &= 2ZRm[n]P_{\mathrm{DC}}J_2\left(\phi_0\right)\cos\left(\phi_d[n]\right) \\ &= A_x[n]\cos\left(\phi_d[n]\right), \end{aligned} \tag{2.16}$$

in which $A_y[n]$ [V] and $A_x[n]$ [V] are the time-varying amplitudes of the baseband Doppler signals, respectively. The carriers required for demodulation were reconstructed in MATLAB® (MathWorks, Natick, Massachusetts, USA), by determining the phase ϕ_m that yielded maximum correlation between a 40-kHz sine and the monitor diode signal. The resulting phase ϕ_m was subsequently used to construct a locked 80-kHz cosine (2.14). Band-pass filtering was implemented as a low-pass filter (LPF) followed by a high-pass filter (HPF). We used a twelfth-order zero-phase Butterworth LPF with a 3-dB cut-off frequency at the maximum Doppler frequency of $\omega_{d\,\max}/(2\pi) = 15$ kHz. We created an HPF to remove the DC and low-frequency components by subtracting the output of a second-order zero-phase Butterworth LPF with a 3-dB cut-off frequency at $\omega_{d\,\min}/(2\pi) = 10$ Hz. The LPF and HPF respectively set the higher and lower limits of the speed of motion that could be measured by the system. The expression for the Doppler frequency (2.1) shows that this system could track velocities between about 8.5 μm/s and 12.75 mm/s, which we expected to be sufficient for the intended application.

Second, the demodulated Doppler signals $v_y[n]$ and $v_x[n]$ were normalized to be able to accurately track $\phi_d[n]$. Normalization made use of the Hilbert transform, as indicated by $H\{\cdot\}$. As the ideal Hilbert transform equals $+j$ for negative frequencies and $-j$ for positive frequencies [142], it follows that

$$v_y[n] + jH\left\{v_y[n]\right\} = A_y[n]e^{-j\pi/2}e^{j\phi_d[n]}, \tag{2.17}$$

$$v_x[n] + jH\left\{v_x[n]\right\} = A_x[n]e^{j\phi_d[n]}. \tag{2.18}$$

By substituting the phase of these analytical signals in a cosine, we obtained the normalized baseband Doppler signals $y[n]$ [-] and $x[n]$ [-],

$$y[n] = \cos\left(\mathrm{unwrap}\left[\ \angle\left(\ v_y[n] + jH\left\{v_y[n]\right\}\ \right)\ \right]\right) = \sin(\phi_d[n]), \tag{2.19}$$

$$x[n] = \cos\left(\mathrm{unwrap}\left[\ \angle\left(\ v_x[n] + jH\left\{v_x[n]\right\}\ \right)\ \right]\right) = \cos(\phi_d[n]), \tag{2.20}$$

in which unwrap removes the discontinuities in the radian phase by adding multiples of $\pm 2\pi$, and $\angle$ indicates the angle of a complex number.

Finally, displacement of the laser diode was reconstructed by tracking the phase $\phi_d[n]$ (2.10), which we obtained by unwrapping the arctangent of the ratio of $y[n]$ and $x[n]$. Considering the one-dimensional motion in the in-vitro setup, displacement $\Delta L_{\text{smi}}[n]$ [m] could be determined from phase $\phi_d[n]$ by equating each phase change of 2π rad to a displacement of half a wavelength $\lambda_0/2$, and correcting for the angle θ between the laser beam and the direction of motion,

$$\Delta L_{\text{smi}}[n] = \text{BPF}\left\{\frac{\lambda_0}{4\pi\cos(\theta)}\text{unwrap}\left[\text{atan2}\left(\frac{y[n]}{x[n]}\right)\right]\right\} \tag{2.21}$$

$$= \text{BPF}\left\{\frac{L_o}{\cos(\theta)}\left(1-\frac{\Delta\lambda_{\text{fb}}[n]}{\lambda_0}\right)+T_s\sum_{k=0}^{n}v_o[k]\right\}, \tag{2.22}$$

in which atan2$(\cdot)$ refers to a four-quadrant arctangent implementation which takes into account in which quadrant $y[n]$ and $x[n]$ are located. Also this BPF was implemented as an LPF followed by an HPF (Fig. 2.4). The BPF was used to create an artifact reference signal with the same bandwidth as the PPG signal, and was therefore the same BPF as we used to band-limit the PPG signal. First a second-order zero-phase Butterworth low-pass filter with a 100-Hz 3-dB cut-off frequency was applied, followed by down-sampling to 250 Hz. We then used a fourth-order zero-phase Butterworth LPF with a 3-dB cut-off frequency at $\omega_{\text{ppg max}}/(2\pi) = 30$ Hz, which accommodated the highest harmonic frequencies expected in the PPG signal. The LPF avoided introducing additional noise to the PPG signal, when using $\Delta L_{\text{smi}}[n]$ as an artifact reference in a correlation canceler (Section 2.4.2). Subsequently we created an HPF to remove the DC and low-frequency components by subtracting the output of a Butterworth LPF which was second-order and zero-phase and had a 3-dB cut-off frequency at $\omega_{\text{ppg min}}/(2\pi) = 0.3$ Hz. The cut-off at 0.3 Hz accommodated the lowest expected PR. The HPF removed any baseline drift in $\Delta L_{\text{smi}}[n]$.

2.3.3 Accuracy analysis

In practice, the demodulated Doppler signals $v_y[n]$ and $v_x[n]$ ((2.15) and (2.16)) are perturbed by additive noise terms, caused by shot noise, thermal noise, and quantization noise. We investigated the influence of these noise terms on the accuracy of the displacement measurement method in this section.

We expressed the additive noise terms in $v_y[n]$ and $v_x[n]$ as summations,

$$v_{yn}[n] = A_y[n]\sin\left(\phi_d[n]\right) + \sum_i A_{yn\_i}[n]\cos(\phi_{yn\_i}[n]), \tag{2.23}$$

$$v_{xn}[n] = A_x[n]\cos\left(\phi_d[n]\right) + \sum_i A_{xn\_i}[n]\cos(\phi_{xn\_i}[n]), \tag{2.24}$$

in which $A_{yn\_i}[n]$ and $A_{xn\_i}[n]$ are the amplitudes of the noise terms in $v_{yn}[n]$ and $v_{xn}[n]$, respectively, and $\phi_{yn\_i}[n]$ and $\phi_{xn\_i}[n]$ are the phases of the noise terms in $v_{yn}[n]$ and $v_{xn}[n]$, respectively. We determined the following first-order Taylor approximations of the normalized demodulated Doppler signals around $A_{yn\_i} = 0$ and $A_{xn\_i} = 0$, by assuming an SNR > 1:

$$\begin{aligned} y_n[n] &= \cos\left(\text{unwrap}\left[\angle\left(v_{yn}[n] + jH\left\{v_{yn}[n]\right\}\right)\right]\right) \\ &\approx \sin\left(\phi_d[n] + \frac{3}{2}\sum_i \frac{A_{yn\_i}[n]}{A_y[n]}\right), \end{aligned} \tag{2.25}$$

$$\begin{aligned} x_n[n] &= \cos\left(\text{unwrap}\left[\angle\left(v_{xn}[n] + jH\left\{v_{xn}[n]\right\}\right)\right]\right) \\ &\approx \cos\left(\phi_d[n] + \frac{3}{2}\sum_i \frac{A_{xn\_i}[n]}{A_x[n]}\right). \end{aligned} \tag{2.26}$$

Next, we determined a first-order Taylor approximation of the displacement measurement $\Delta L_{\text{smi}}[n]$ containing these noise sources, by using (2.25) and (2.26) for $y[n]$ and $x[n]$ in (2.21), respectively, and once more assuming an SNR > 1:

$$\begin{aligned} \Delta L_{\text{smi\_}n}[n] =& \text{BPF}\left\{\frac{\lambda_0}{4\pi\cos(\theta)}\cdot\right. \\ & \left.\text{unwrap}\left[\text{atan2}\left(\frac{\sin\left(\phi_d[n] + \frac{3}{2}\sum_i \frac{A_{yn\_i}[n]}{A_y[n]}\right)}{\cos\left(\phi_d[n] + \frac{3}{2}\sum_i \frac{A_{xn\_i}[n]}{A_x[n]}\right)}\right)\right]\right\} \end{aligned} \tag{2.27}$$

$$\begin{aligned} \approx& \text{BPF}\left\{\frac{L_o}{\cos(\theta)} + T_s\sum_{k=0}^{n} v_o[k] - \frac{L_o}{\lambda_0}\frac{\Delta\lambda_{\text{fb}}[n]}{\cos(\theta)} + \right. \\ & \left.\frac{\frac{3}{2}\frac{\lambda_0}{4\pi\cos(\theta)}}{1+\tan^2(\phi_d[n])}\cdot\left[\sum_i \frac{A_{yn\_i}[n]}{A_y[n]} + \tan^2(\phi_d[n])\sum_i \frac{A_{xn\_i}[n]}{A_x[n]}\right]\right\} \end{aligned} \tag{2.28}$$

$$\begin{aligned} \leq& \text{BPF}\left\{\frac{L_o}{\cos(\theta)} + T_s\sum_{k=0}^{n} v_o[k] + \frac{\lambda_0}{4\pi\cos(\theta)}C + \right. \\ & \left.\frac{\frac{3}{2}\lambda_0}{4\pi\cos(\theta)}\cdot\max_n\left[\sum_i \frac{A_{yn\_i}[n]}{A_y[n]} + \sum_i \frac{A_{xn\_i}[n]}{A_x[n]}\right]\right\}. \end{aligned} \tag{2.29}$$

The change in wavelength as a result of optical feedback, $\Delta\lambda_{\text{fb}}[n]$, in (2.28) was replaced in (2.29) by upper bound $-(\lambda_0^2 C)/(4\pi L_o)$, which was obtained using the lasing condition and optical feedback parameter C [136]. Equation (2.29) shows the upper bound of two additive noise terms which distort the displacement measurement, for SNR > 1. The first noise term results from the change in emitted optical wavelength due to optical feedback and was replaced by upper bound $(\lambda_0 C)/(4\pi\cos(\theta))$. Because we expected only (very) weak feedback regimes in

this application, we used that the feedback parameter $C < 1$ [136]. Therefore, we expected this error term to have a magnitude on the order of $(\lambda_0 C)/(4\pi\cos(\theta)) \sim 10^{-8}$ - 10^{-7} m. The second noise term, being a result of shot noise, thermal noise, and quantization noise, was inversely proportional to the SNR of the Doppler signals. For SNR > 1, we also expected this term to have a magnitude on the order of 10^{-8} - 10^{-7} m. Because we assumed sensor displacement to be on the order of 10^{-4} - 10^{-3} m, these error sources introduced a negligibly small error of roughly 0.1‰ - 1‰, as long as the SNR > 1. However, speckle could cause the amplitude of the Doppler signals to become very small, resulting in an SNR < 1, in which case the contribution of the second noise term would not be negligible any longer. Destructive speckle interference can occur when the surface roughness of the illuminated object is such that the backscattered contributions of the laser light cancel at the laser. This phenomenon cannot be prevented. Therefore, we expected destructive speckle interference to be the dominant cause of inaccuracies in the displacement measurement, but the exact impact would depend on the illuminated surface. In case of SNR < 1, the derived expressions (2.25) through (2.29) do not hold any longer.

Furthermore, inaccuracies in the displacement measurement (2.29) were also caused by not exactly knowing the average emission wavelength λ_0 and the angle θ between the laser beam and the direction of motion, as shown by the factor $\lambda_0/(4\pi\cos(\theta))$ which converts the Doppler phase to a displacement in (2.27). The emission wavelength of the 850 nm VCSEL was specified with an accuracy of 10 nm (specified by ULM-Photonics GmbH, Philips, Ulm, Germany), which thus could result in a displacement error of approximately 1%. Fluctuations in the emission wavelength as a result of modulation and optical feedback were negligible. Modulation of the injection current resulted in minor wavelength variations on the order of 10^{-11} m (see Section 2.2.2 and 2.3.1). Moreover, (2.28) and (2.29) indicate that optical feedback only changed the wavelength by at most $(\lambda_0^2 C)/(4\pi L_o) \sim 10^{-12}$ m. The inaccuracy $\delta\theta$ in the angle θ resulted in a displacement error of $(\tan(\theta)/\cos(\theta))\delta\theta \approx 3.5{\cdot}\delta\theta$ for $\theta/(2\pi) = 60°$, which equaled approximately 6% for $\delta\theta/(2\pi) = 1°$. The effect of the inaccuracy in the angle θ thus dominated the effect of wavelength inaccuracy. However, these inaccuracies are both constant scaling effects on the amplitude of the displacement measurement. Exactly measuring the absolute displacement is not relevant in the context of PPG motion artifact reduction. In this context, it is most important to accurately measure the dynamic variations of the sensor displacement.

2.3.4 Validation

We determined a conservative estimate of the SNR of the baseband Doppler signals to quantify the effect of speckle on the SNR of the Doppler signals. We determined the instantaneous amplitude of the baseband Doppler signals with noise, by using the magnitude of the Hilbert transform of $v_{yn}[n]$ (2.23) and $v_{xn}[n]$ (2.24), which we indicated by $H_{yn}[n]$ and $H_{xn}[n]$, respectively. We determined

background noise signals $n_y[n]$ and $n_x[n]$ in the signal bands around 40 kHz and 80 kHz, respectively, by applying the demodulation scheme in Fig. 2.4 to the monitor diode signal $v_{\mathrm{MD}}[n]$ which was measured when the laser diode did not experience any optical feedback. This condition was obtained by placing black foam approximately 4 cm in front of the ball lens. We measured the background noise signal for 30 s. We obtained conservative SNR estimates by dividing the signal amplitudes by three times the root mean-square (RMS) value of the background noise:

$$\mathrm{SNR}_y[n] = \frac{H_{yn}[n]}{3 \cdot \mathrm{RMS}(n_y[n])}, \tag{2.30}$$

$$\mathrm{SNR}_x[n] = \frac{H_{xn}[n]}{3 \cdot \mathrm{RMS}(n_x[n])}. \tag{2.31}$$

Here we assumed that the estimated background noise levels remained constant during the measurement of the Doppler signals.

We validated the displacement measurement $\Delta L_{\mathrm{smi}}[n]$ by comparison to the reference LDV measurement, which we indicated by $\Delta L_{\mathrm{ref}}[n]$. The SMI displacement measurement contained a scaling error due to inaccuracies in λ_0 and θ, as explained at the end of Section 2.3.3. We accounted for the scaling error by introducing a factor γ [-]. The scaling error was estimated by determining the scaling factor γ which minimized the mean squared-error between $\gamma\Delta L_{\mathrm{smi}}[n]$ and $\Delta L_{\mathrm{ref}}[n]$. After correction for the scaling error in $\Delta L_{\mathrm{smi}}[n]$, we determined the error with the reference LDV measurement as $\Delta L_{\mathrm{err}}[n] = \gamma\Delta L_{\mathrm{smi}}[n] - \Delta L_{\mathrm{ref}}[n]$.

2.4 Methods C: Artifact reduction algorithm

First, as described in Section 2.4.1, we coarsely modeled the PPG signal using the Beer-Lambert law, to determine the influence of changes in channel volume and emitter-detector distance on the measured PPG signal. Because a first-order model of the PPG signal showed that the artifacts were additive and proportional to the displacement of the laser diode, we used the displacement of the laser diode as an artifact reference in an LMS-based correlation canceler to reduce the optical motion artifacts in the corrupted PPG signal, as described in Section 2.4.2. Finally, Section 2.4.3 describes how we assessed the performance of the artifact reduction algorithm in the in-vitro setup.

2.4.1 PPG signal model

Figure 2.1 illustrates the contribution of different light paths to the signal that is detected by the PPG photodiode. As indicated from top to bottom by the four dashed arrows in Fig. 2.1, laser light that reached the PPG photodiode could be roughly considered to have propagated through the window directly, through the window and the milk, through the window, the milk and the membrane, or it was

backscattered by the base of the flow cell. To obtain a coarse model of the PPG signal $ppg[n]$, we used these four light paths in the Beer-Lambert law, which is commonly employed in pulse oximetry [58, 105, 191]:

$$\begin{aligned} ppg[n] \approx A_0 \{ & \exp\left[-\alpha_w l_w(L_{ed}[n])\right] + \exp\left[-2\alpha_w l_{wm} - \alpha_m l_m(L_{ed}[n], V_m[n])\right] \\ & + \exp\left[-2\alpha_w l_{wm} - 2\alpha_m l_{ms}(L_{ed}[n], V_m[n]) - \alpha_s l_s(L_{ed}[n], V_m[n])\right] \\ & + \exp\left[-2\alpha_w l_{wm} - 2\alpha_m l_{ms}(L_{ed}[n], V_m[n]) - 2\alpha_s l_{sb}(L_{ed}[n], V_m[n])\right. \\ & \left. -\alpha_b l_b(L_{ed}[n])\right]\}, \end{aligned} \tag{2.32}$$

in which A_0 [V] is proportional to the emitted light intensity, α [m^{-1}] is the extinction coefficient, l [m] is the optical path length, $L_{ed}[n]$ [m] is the emitter-detector distance, $V_m[n]$ [m^3] is the milk volume in the channel, and subscripts w, wm, m, ms, s, sb and b stand for window, from window to milk, milk, from milk to silicone, silicone, from silicone to base, and base, respectively. The first exponent in (2.32) describes the optical shunt through the window. The optical path through the window was a function of emitter-detector distance. The second exponent describes light that propagated through the window and the milk. The factor two in the first term of the exponent indicates that the light traveled through the window twice. The optical path length through the milk was a function of emitter-detector distance and milk volume in the channel. Both an increase in emitter-detector distance and an increase in milk volume extended the path through the milk. The third exponent describes light that traveled back to the photodiode via the silicone membrane. In this exponent the optical paths via the milk to the silicone and through the silicone were a function of emitter-detector distance and milk volume. The emitter-detector distance influenced the path that photons had to travel via the milk and through the silicone membrane to reach the photodiode. An increase in milk volume increased the optical path through the milk, and changed the shape of the membrane influencing the path through the membrane. The fourth exponent describes light that was backscattered by the base of the flow cell. The third term in this exponent describes light propagating via the silicone membrane to the base. The path through the silicone depended on emitter-detector distance, because this distance influenced the path that photons had to travel through the membrane to reach the photodiode via the base. Furthermore, this light path depended on milk volume, because an increase in milk volume deformed the membrane. The last term in this exponent describes the optical path that light traveled through the base of the flow cell before it was backscattered towards the photodiode. The distance that detected photons had traveled through the base depended on the emitter-detector distance.

To obtain more insight in the direct relationship between laser motion and the detected PPG signal, we determined a Taylor approximation of (2.32). The approximation around the stationary condition in which both milk volume and emitter-detector distance were constant, equals

$$ppg[n] \approx A_0 \{c_0 - c_1 \Delta V_m[n] - c_2 \Delta L_{ed}[n] - c_3 \Delta L_{ed}[n] \Delta V_m[n]\}, \tag{2.33}$$

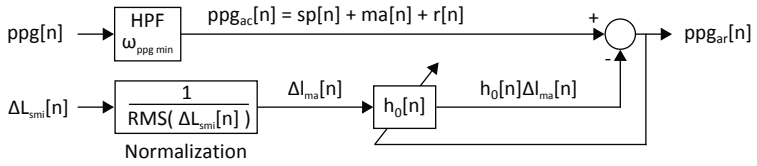

Figure 2.5: LMS structure used to estimate and remove the motion artifact, $ma[n]$, from the PPG signal, $ppg[n]$, in order to recover an artifact-reduced PPG signal, $ppg_{\mathrm{ar}}[n]$. The baseline of the PPG signal $ppg[n]$ was removed by applying an HPF with a 3-dB cut-off frequency at $\omega_{\mathrm{ppg\,min}}$, yielding $ppg_{\mathrm{ac}}[n]$. We modeled $ppg_{\mathrm{ac}}[n]$ as a sum of a simulated pulse component, $sp[n]$, a motion artifact, $ma[n]$, and residual noise, $r[n]$. The motion artifact was estimated by using the zero-mean laser displacement $\Delta L_{\mathrm{smi}}[n]$ as an artifact reference. The displacement was normalized by its RMS value to obtain $\Delta l_{\mathrm{ma}}[n]$. The LMS filter had a single adaptive coefficient $h_0[n]$ to scale $\Delta l_{\mathrm{ma}}[n]$ in order to estimate the artifact. Subtracting artifact estimate $h_0[n]\Delta l_{\mathrm{ma}}[n]$ from $ppg_{\mathrm{ac}}[n]$ resulted in the artifact-reduced output signal, $ppg_{\mathrm{ar}}[n]$. HPF: high-pass filter; LMS: least mean-squares; PPG: photoplethysmography; RMS: root mean-square.

in which c_0 [-], c_1 [m^{-3}], c_2 [m^{-1}] and c_3 [m^{-4}] are proportionality constants, $\Delta V_m[n]$ [m^3] is a small time-varying variation in milk volume in the channel, and $\Delta L_{ed}[n]$ [m] is a small time-varying deviation of the emitter-detector distance caused by the shaker action. This approximation shows that the time-varying part of the PPG signal $ppg[n]$ could be modeled as a sum of a simulated pulse component proportional to the variation in milk volume, $-c_1\Delta V_m[n]A_0$, an artifact due to motion of the laser diode proportional to the variation in emitter-detector distance, $-c_2\Delta L_{ed}[n]A_0$, and an artifact proportional to the product of the variations in milk volume and the emitter-detector distance, $-c_3\Delta L_{ed}[n]\Delta V_m[n]A_0$.

2.4.2 Motion artifact estimation and reduction

Based on the Taylor approximation in (2.33), which described the influence of laser motion on the PPG signal, an LMS algorithm [68] was used in a first attempt to reduce the motion artifacts in the PPG signal. If the LMS algorithm succeeded in reducing the motion artifacts by using the laser displacement as an artifact reference, this proved correlation between the displacement measurement and the artifacts, at least in the in-vitro setup. All inputs to the LMS algorithm were down-sampled to 250 Hz.

Figure 2.5 shows the LMS algorithm which estimated and removed the motion artifact, $ma[n]$, from the PPG signal, $ppg[n]$, in order to recover an artifact-reduced PPG signal, $ppg_{\mathrm{ar}}[n]$. The primary input was the band-pass filtered PPG signal, $ppg_{\mathrm{ac}}[n]$, which we obtained by applying an HPF to $ppg[n]$. We constructed the HPF by first applying to $ppg[n]$ a Butterworth LPF, which was second-order and zero-phase and had a 3-dB cut-off frequency at $\omega_{\mathrm{ppg\,min}}/(2\pi) = 0.3$ Hz, and then subtracting the output of this LPF from $ppg[n]$. Based on the

Taylor approximation in (2.33), we modeled $ppg_{\mathrm{ac}}[n]$ as a sum of a simulated cardiac pulse component, $sp[n]$, a motion artifact, $ma[n]$, and residual noise, $r[n]$,

$$ppg_{\mathrm{ac}}[n] = sp[n] + ma[n] + r[n]. \tag{2.34}$$

Here, $sp[n]$ is proportional to the second term in (2.33), and $ma[n]$ is proportional to the third plus fourth terms in (2.33). The secondary input of the LMS algorithm was the artifact reference signal, for which we used the zero-mean laser displacement $\Delta L_{\mathrm{smi}}[n]$, and which we obtained by applying the same LPF and HPF as were applied to the PPG signal (Fig. 2.4 and Section 2.3.2). The displacement was first normalized by its RMS value to obtain $\Delta l_{\mathrm{ma}}[n]$ [-]. The RMS value was determined over the entire length of the recording of length N_{rec} samples,

$$\Delta l_{\mathrm{ma}}[n] = \frac{\Delta L_{\mathrm{smi}}[n]}{\sqrt{\frac{1}{N_{\mathrm{rec}}}\sum_{k=0}^{N_{\mathrm{rec}}-1}\Delta L_{\mathrm{smi}}^2[k]}}. \tag{2.35}$$

The motion artifact was subsequently estimated by scaling $\Delta l_{\mathrm{ma}}[n]$ by $h_0[n]$ [V], which was the adaptive coefficient of the LMS algorithm. The LMS algorithm filter-order therefore was $N_f = 1$. We used only a single filter coefficient, because displacement of the laser diode was measured directly, and no mechanical transfer function was expected between the laser displacement and the resulting optical effect. Displacement of the laser diode furthermore directly affected the optical path through the flow cell, no hysteresis and memory effects were expected. Furthermore, the first-order Taylor approximation of $ppg[n]$ (2.33) shows two additive artifacts proportional to the variations in emitter-detector distance. Although the second additive artifact in (2.33) also varies with variations in milk volume $\Delta V_m[n]$, this could be accounted for by adapting $h_0[n]$ over time in presence of a simulated pulse $sp[n]$. Therefore, we expected to obtain a good first-order estimate of the optical artifacts by adaptively scaling the laser displacement by a single filter coefficient. Subtracting artifact estimate $h_0[n]\Delta l_{\mathrm{ma}}[n]$ from $ppg_{\mathrm{ac}}[n]$ resulted in the artifact-reduced output signal $ppg_{\mathrm{ar}}[n]$,

$$ppg_{\mathrm{ar}}[n] = ppg_{\mathrm{ac}}[n] - h_0[n]\Delta l_{\mathrm{ma}}[n]. \tag{2.36}$$

The optimal coefficient $h_0[n]$ for motion artifact reduction was determined by iteratively minimizing the power of output signal $ppg_{\mathrm{ar}}[n]$ [68]:

$$\min_{h_0} ppg_{\mathrm{ar}}^2[n] = \min_{h_0} \left(ppg_{\mathrm{ac}}[n] - h_0[n]\Delta l_{\mathrm{ma}}[n]\right)^2, \tag{2.37}$$

$$h_0[n+1] = h_0[n] - \mu\nabla_{h_0} ppg_{\mathrm{ar}}^2[n] = h_0[n] + 2\mu \cdot ppg_{\mathrm{ar}}[n]\Delta l_{\mathrm{ma}}[n], \tag{2.38}$$

with step-size parameter μ. We used step-size parameter $\mu = 0.01$, which we determined experimentally. The minimum power of the output signal was determined by successively taking steps in the opposite direction of its gradient, $\nabla_{h_0} ppg_{\mathrm{ar}}^2[n]$, with step-size μ. When $h_0[n]$ had converged, the minimum output power was found and $ppg_{\mathrm{ar}}[n]$ did not contain any information anymore that

correlated with $\Delta l_{\mathrm{ma}}[n]$. Ideally, after convergence, only the simulated pulse component and residual noise remained, $sp[n] + r[n]$, which would imply high correlation between $\Delta l_{\mathrm{ma}}[n]$ and the motion artifact $ma[n]$, and no correlation between $\Delta l_{\mathrm{ma}}[n]$ and the simulated pulse $sp[n]$.

2.4.3 In-vitro artifact reduction

We assessed the reduction of motion artifacts in-vitro using the following setup. All PPG signals were measured using milk containing the water-soluble black dye, the insert with the silicone membranes, and the POM window. We generated the motion artifacts by moving the laser diode on the linear stage with respect to the PPG photodiode, as shown in Fig. 2.1 and 2.2b. The laser diode was moved randomly by steering the shaker with a 0.5-10 Hz band-pass filtered white noise sequence.

First we measured pure optical motion artifacts, $ma[n]$, without a simulated cardiac pulse, $sp[n]$, by moving the laser diode over the perfusion phantom with the flow channel filled with a stationary volume of milk containing the black dye (roller pump switched off). So here we measured $ppg_{\mathrm{ac}}[n] = ma[n] + r[n]$. This experiment showed the correlation between the laser displacement, $\Delta L_{\mathrm{smi}}[n]$, and the optical motion artifacts, $ma[n]$, without the additional complication of a simulated cardiac pulse component, $sp[n]$, interfering with the process of estimating $h_0[n]$. That is, in this case $\Delta V_m[n]$ in (2.33) equaled zero.

Second we measured optical motion artifacts, $ma[n]$, corrupting a simulated cardiac pulse, $sp[n]$, by moving the laser diode over the perfusion phantom with a pulsatile flow of milk containing the black dye. The roller pump was set at 20 RPM to generate the pulsatile flow, where $sp[n]$ simulated a PR of 60 BPM. So here we measured $ppg_{\mathrm{ac}}[n] = sp[n] + ma[n] + r[n]$. In this case $\Delta V_m[n]$ in (2.33) was not zero any longer, which resulted in a motion artifact proportional to the product of the variations in milk volume and emitter-detector distance, as shown by the fourth term in (2.33). In the second case, we also measured a reference PPG signal, $ppg_{\mathrm{ref}}[n]$, by having the same pulsatile milk flow while keeping the laser diode stationary. So here we measured $ppg_{\mathrm{ref-ac}}[n] = sp[n]+r[n]$, with $ppg_{\mathrm{ref-ac}}[n]$ obtained by applying the same LPF and HPF as were applied to obtain $ppg_{\mathrm{ac}}[n]$. The reference PPG signal, $ppg_{\mathrm{ref-ac}}[n]$, was synchronized with the motion-corrupted PPG signal, $ppg_{\mathrm{ac}}[n]$, by determining the lag at which maximum correlation between these signals was achieved.

We assessed the reduction of the motion artifact, $ma[n]$, as achieved by the LMS algorithm by comparing the waveforms of the artifact-corrupted PPG signal, $ppg_{\mathrm{ac}}[n]$, the artifact-reduced PPG signal, $ppg_{\mathrm{ar}}[n]$, and the reference PPG signal, $ppg_{\mathrm{ref-ac}}[n]$. We quantified the reduction of the artifacts, Q [dB], via

$$Q = 10 \cdot \log \left(\frac{\sum_{k=0}^{N_{rec}-1} \left(ppg_{\mathrm{ar}}[k] - ppg_{\mathrm{ref-ac}}[k] \right)^2}{\sum_{k=0}^{N_{rec}-1} \left(ppg_{\mathrm{ac}}[k] - ppg_{\mathrm{ref-ac}}[k] \right)^2} \right). \tag{2.39}$$

In the case of pure optical motion artifacts, we used $ppg_{\mathrm{ref-ac}}[n] = 0$ to determine the artifact reduction Q.

For the measurements performed for artifact reduction, we also retrospectively visually inspected the baseline of the monitor diode signal, $v_{\mathrm{MD}}[n]$. We did this to determine whether the optical output power of the laser diode remained constant during motion, as any fast fluctuations in optical power of the laser diode would lead to multiplicative motion artifacts in the measured PPG signal. To extract the baseline of the monitor diode signal, we first applied to $v_{\mathrm{MD}}[n]$ a second-order zero-phase Butterworth LPF with a 100-Hz 3-dB cut-off frequency, followed by downsampling to 250 Hz, and we then applied a fourth-order zero-phase Butterworth LPF with a 3-dB cut-off frequency at 30 Hz.

2.5 Results

2.5.1 In-vitro PPG measurements

In-vitro PPG signals were measured in four different ways to determine the influence of the silicone membranes, the water-soluble black dye, and the POM window, as explained in Section 2.2.3 and listed in Table 2.1. The first three types of measurements are illustrated in Fig. 2.6. The solid blue curves are the measured in-vitro PPG signals, $ppg[n]$, and the dashed green curves are the POM-window deflections as measured via SMI and (2.21) with $\theta = 30°$. An offset was added to the zero-mean deflection measurement such that its minimum was 0 μm.

In case one, a pulsatile milk flow went through the insert with the rigid channel (Fig. 2.6a). In case two, a pulsatile milk flow went through the insert with the silicone membranes (Fig. 2.6b). In case three, a pulsatile milk flow with water-soluble black dye went through the insert with the silicone membranes (Fig. 2.6c). Case one resulted in a PPG signal with a 5.5 mV peak-to-peak amplitude, and a window deflection of approximately 55 μm upward (Fig. 2.6a). Case two resulted in a PPG signal with a 13 mV peak-to-peak amplitude, and here the DC level increased by approximately 100 mV compared to case one. Furthermore, the window moved upward by only 23 μm (Fig. 2.6b). In cases one and two, the PPG signal $ppg[n]$ was in phase with the window deflection. In case three, however, the PPG signal $ppg[n]$ was in antiphase with the window deflection (Fig. 2.6c). The increased absorption in case three furthermore lowered the PPG signal peak-to-peak amplitude to 11 mV and its DC level to 268 mV. In case three, the amplitude of the PPG signal equaled approximately 4% of its DC level.

The fourth measurement was carried out using the transparent window. Compared to the transparent window, the POM window caused a decrease in the DC level and the amplitude of the PPG signal. The decrease in amplitude resulted from additional attenuation (2.32). Moreover, in combination with milk, the POM window introduced an optical shunt, because the amplitude of the PPG signal decreased by a larger factor than its DC level did (2.32).

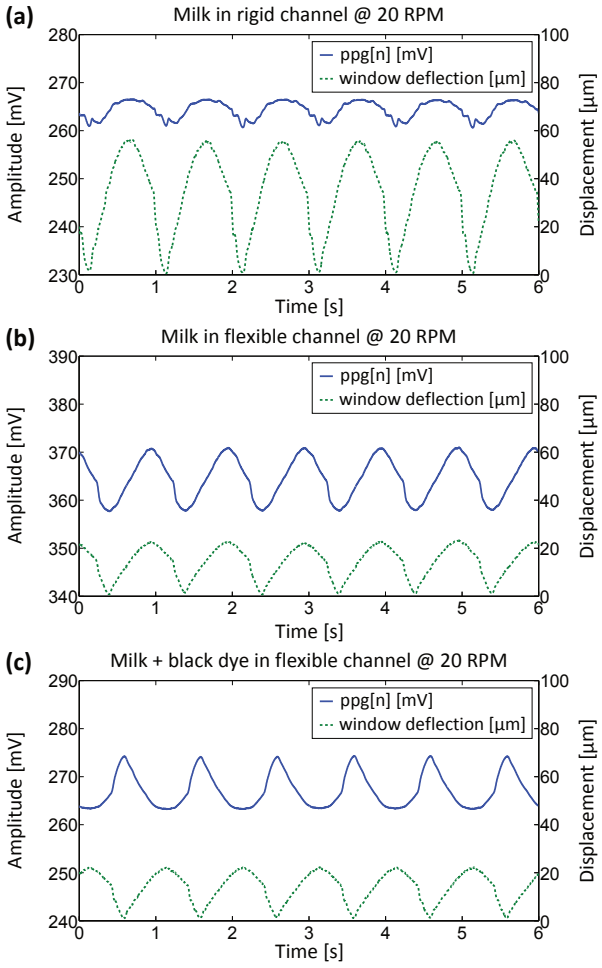

Figure 2.6: PPG signals (solid curves) measured in the flow cell (Fig. 2.1 and 2.2) with the roller pump set at 20 RPM to simulate pulses at a rate of 60 BPM. The deflection of the POM window (dashed curves) was measured via SMI with $\theta = 30°$. (a) Pulsatile milk flow through the rigid channel. (b) Pulsatile milk flow through the channel with the silicone membranes. (c) Pulsatile milk flow through the channel with the silicone membranes, with the milk containing a water-soluble black dye. BPM: beats per minute; POM: polyoxymethylene (Delrin®); PPG: photoplethysmography; RPM: rounds per minute; SMI: self-mixing interferometry.

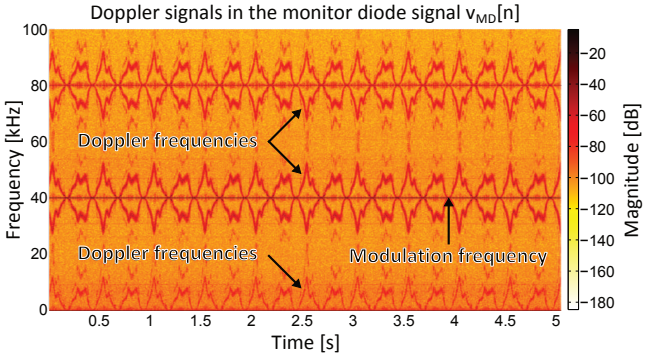

Figure 2.7: Spectrogram of monitor signal $v_{\mathrm{MD}}[n]$. Doppler signals as a result of laser motion occurred in the baseband, around the modulation frequency at 40 kHz, and around the second harmonic at 80 kHz.

2.5.2 Displacement measurement

When the laser beam was focused on the POM window, the displacement of the laser could be measured using SMI, by processing the monitor diode signal as outlined in Fig. 2.4. In this section, the measured Doppler signals, the effects of speckle and the accuracy of the displacement measurement are presented.

2.5.2.1 Doppler signals

Figure 2.7 shows the spectrogram of the monitor diode signal, $v_{\mathrm{MD}}[n]$, when the shaker was driven by a 2-Hz sinusoid with an amplitude such that the peak-to-peak displacement was approximately 1 mm. Doppler signals as a result of laser motion occurred in the baseband, around the modulation frequency at 40 kHz, and the second harmonic at 80 kHz. In each of these three frequency bands, weak second harmonics of the Doppler frequencies themselves could be observed, indicating weak optical feedback and an interference pattern which was not perfectly sinusoidal [55, 85]. Furthermore, the spectrogram shows that the used modulation depth of the laser injection current effectively reduced the magnitude of the Doppler signals in the baseband, and resulted in Doppler signals of comparable magnitude in the frequency bands around 40 kHz and 80 kHz, as explained at the end of Section 2.3.1, and by (2.11) and (2.14).

Demodulation of the monitor diode signal $v_{\mathrm{MD}}[n]$, as described by (2.15) and (2.16), resulted in the baseband Doppler signals $v_y[n]$ and $v_x[n]$, as exemplified by the dashed blue and solid red curves in Fig. 2.8, respectively. The strong variation of the amplitude of the signals was caused by speckle effects. The local minima resulted from destructive speckle interference. The segment in Fig. 2.8 shows a change in the direction of motion of the laser diode. At first the speed of motion decreased, as indicated by the decreasing Doppler frequency. Motion

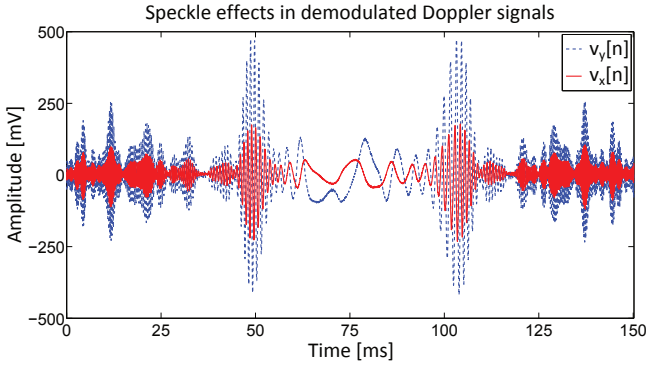

Figure 2.8: Segment of the baseband Doppler signals $v_y[n]$ and $v_x[n]$ obtained by demodulation of the monitor diode signal $v_{\mathrm{MD}}[n]$. The strong variation of the amplitude of the signals was caused by speckle effects.

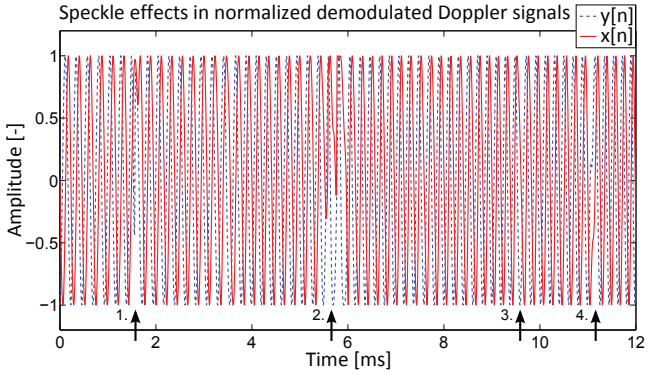

Figure 2.9: Segment of the normalized baseband Doppler signals $y[n]$ and $x[n]$. Arrows 1 and 2 indicate ineffective normalization, which was due to destructive speckle interference which strongly decreased the amplitude of the original Doppler signals. Arrows 3 and 4 indicate a jump of π rad in the phase of the Doppler signals, which was also due to speckle interference. This is a different segment than shown in Fig. 2.8.

stopped at about halfway the segment. Then the speed of motion increased again, as indicated by the increasing Doppler frequency in the right half of the figure. Furthermore, in the right half of the figure the order of the local extremes of $v_y[n]$ and $v_x[n]$ is opposite compared to the left half of the figure. This indicates that the direction of motion changed, and this is the information in the demodulated Doppler signals which was used to determine the direction of motion.

The normalized Doppler signals $y[n]$ and $x[n]$, as we obtained by using the phase of the Hilbert transform in (2.19) and (2.20), are shown by the dashed blue and solid red curves in Fig. 2.9, respectively (this is a different segment than

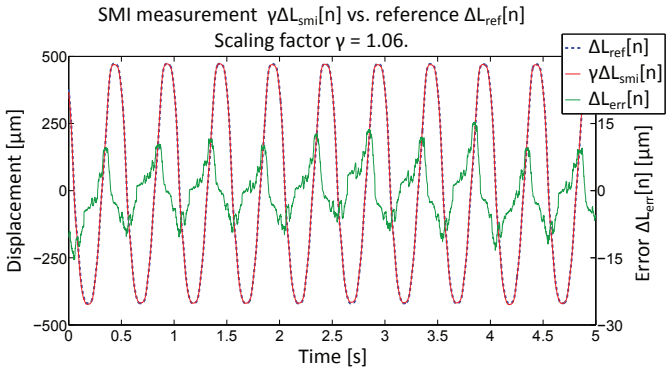

Figure 2.10: The laser diode displacement measured via SMI, $\Delta L_{\mathrm{smi}}[n]$, was scaled by $\gamma = 1.06$ (heavy solid red curve) to correct for any scaling error with the reference LDV measurement, $\Delta L_{\mathrm{ref}}[n]$ (heavy dashed blue curve). Their difference, $\Delta L_{\mathrm{err}}[n] = \gamma \Delta L_{\mathrm{smi}}[n] - \Delta L_{\mathrm{ref}}[n]$ (thin green curve), is shown explicitly, because the SMI and LDV displacement measurements were almost identical. LDV: laser Doppler vibrometer; SMI: self-mixing interferometry.

shown in Fig. 2.8). Overall, effective normalization was obtained via the Hilbert transform, although effects of interference by speckle were also apparent. When destructive speckle interference strongly reduced the amplitude of the Doppler signals, proper normalization was no longer possible, which is indicated by arrows 1 and 2. In addition, speckle interference could cause jumps of π rad in the phase of the Doppler signals, as indicated by arrows 3 and 4.

The SNRs of the baseband Doppler signals $v_y[n]$ and $v_x[n]$ were determined according to (2.30) and (2.31), respectively. The SNRs were determined in recordings with a duration of about 30 s. The SNRs of $v_y[n]$ and $v_x[n]$ were comparable: $\mathrm{SNR}_y = 23.9$ dB on average in a range from -53.6 dB to 38.2 dB, and $\mathrm{SNR}_x = 23.0$ dB on average in a range from -45.6 dB to 38.3 dB. SNR < 0 dB of either of the baseband Doppler signals occurred only during approximately 1% of the recording.

2.5.2.2 Accuracy

The heavy solid red curve in Fig. 2.10 is the displacement $\gamma \Delta L_{\mathrm{smi}}[n]$. $\Delta L_{\mathrm{smi}}[n]$ was obtained via (2.21) with $\theta = 60°$. The scaling factor $\gamma = 1.06$ minimized the scaling error between the SMI-derived measurement, $\Delta L_{\mathrm{smi}}[n]$, and the LDV reference measurement, $\Delta L_{\mathrm{ref}}[n]$ (heavy dashed blue curve). The difference $\Delta L_{\mathrm{err}}[n] = \gamma \Delta L_{\mathrm{smi}}[n] - \Delta L_{\mathrm{ref}}[n]$ (thin solid green curve) is shown explicitly, because the SMI and LDV displacement measurements were almost identical. The baseline of $\Delta L_{\mathrm{smi}}[n]$ was removed by applying an 0.3-Hz HPF ($\omega_{\mathrm{ppg\,min}}$ in Fig. 2.4). The remaining error $\Delta L_{\mathrm{err}}[n]$ was 0.09 ± 6 μm (mean $\pm$ standard deviation).

2.5.3 In-vitro artifact reduction

Figure 2.11 illustrates the reduction of optical motion artifacts using LMS with the SMI displacement measurement $\Delta L_{\mathrm{smi}}[n]$ as an artifact reference. These results were obtained by applying the scheme in Fig. 2.5.

First, the reduction of pure optical motion artifacts was considered. Pure artifacts were obtained by translating the laser diode, but keeping the milk volume in the channel constant (roller pump switched off). So here we had $ppg_{\mathrm{ac}}[n] = ma[n] + r[n]$. The reduction of a pure artifact is illustrated by the three PPG signals shown in Fig. 2.11a. The thin blue curve shows the pure optical motion artifacts, $ppg_{\mathrm{ac}}[n]$, and the heavy red curve shows the result of LMS motion artifact reduction, $ppg_{\mathrm{ar}}[n]$. The dashed dark curve shows the reference PPG signal, $ppg_{\mathrm{ref-ac}}[n] = r[n]$, as measured while the laser diode was stationary, and which was the background noise $r[n]$ in the PPG signal. An artifact reduction of $Q = -17.5$ dB was achieved. Figure 2.11c shows the laser displacement that resulted in the pure optical motion artifact in Fig. 2.11a. The heavy solid red and dashed blue curves in Fig. 2.11c show the SMI and LDV displacement measurements, respectively. The thin green curve is their difference, which is shown explicitly because the SMI and LDV measurements were almost identical. Note that the scaling factor γ was not determined here, i.e., we used $\gamma = 1$.

Second, the reduction of an optical motion artifact corrupting a simulated pulse was considered. Corrupted PPG signals were obtained by translating the laser diode, while the roller pump generated a pulsatile flow. So here we had $ppg_{\mathrm{ac}}[n] = sp[n] + ma[n] + r[n]$. The reduction of a motion artifact corrupting a simulated pulse is illustrated by the three PPG signals in Fig. 2.11b. The thin blue curve shows the corrupted PPG signal, $ppg_{\mathrm{ac}}[n]$, and the heavy red curve shows the result of LMS motion artifact reduction, $ppg_{\mathrm{ar}}[n]$. The dashed dark curve shows the reference PPG signal, $ppg_{\mathrm{ref-ac}}[n] = sp[n] + r[n]$, as measured by illuminating the pulsating milk volume by a stationary laser. The artifact reduction decreased to $Q = -9.9$ dB. Figure 2.11d shows the laser displacement that caused the corrupted PPG signal in Fig. 2.11b. The heavy solid red and dashed blue curves in Fig. 2.11d show the SMI and LDV displacement measurements, respectively. The thin green curve is their difference, which is shown explicitly because the SMI and LDV measurements were almost identical.

Figure 2.12 illustrates the fast convergence of the LMS algorithm. Filter weight $h_0[n]$ (dashed blue curve) and the output power $ppg^2_{\mathrm{ar}}[n]$ (solid red curve) converged within 0.5 s. Furthermore, $h_0[n]$ fluctuated little when reducing pure artifacts (Fig. 2.12a), whereas it fluctuated strongly when reducing artifacts corrupting a simulated pulse (Fig. 2.12b).

For the measurements performed to assess the artifact reduction performance, visual inspection of the baseline of the monitor diode signal showed that the optical output power of the laser diode remained constant during motion.

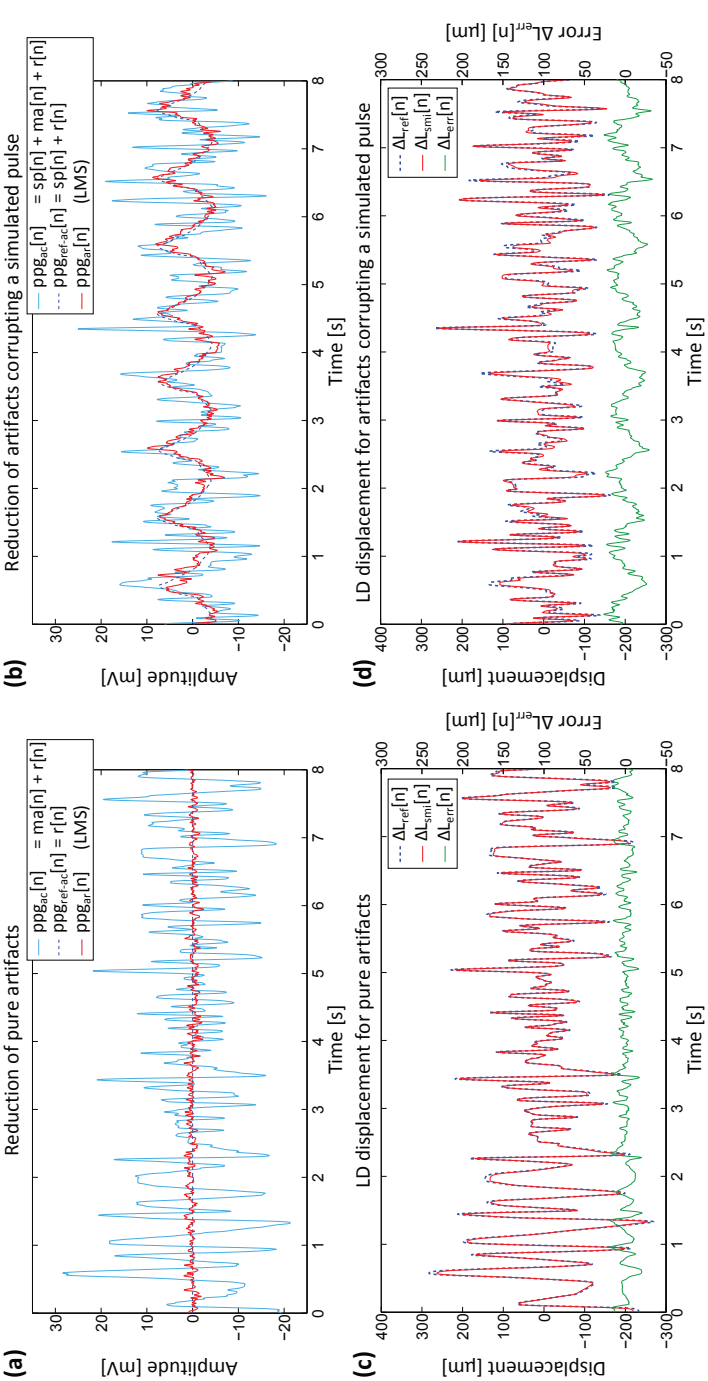

Figure 2.11: (a) Reduction of pure motion artifacts. (b) Reduction of motion artifacts corrupting a simulated pulse in the PPG signal. In (a) and (b), the thin blue curve is the motion corrupted signal, $ppg_{\mathrm{ac}}[n]$, the heavy solid red curve is the LMS output, $ppg_{\mathrm{ar}}[n]$, and the heavy dashed dark curve is the reference PPG signal, $ppg_{\mathrm{ref-ac}}[n]$ measured with a stationary laser diode. (c) Laser displacement causing the pure artifacts in (a). (d) Laser displacement causing the motion artifacts in (b). In (c) and (d), the heavy solid red and dashed blue curves are the displacement measured via SMI and the LDV reference measurement, respectively, and the thin green curve is their difference $\Delta L_{\mathrm{err}}[n] = \Delta L_{\mathrm{smi}}[n] - \Delta L_{\mathrm{ref}}[n]$. The difference is shown explicitly, because the SMI and LDV displacement measurements were almost identical. Note that the scaling factor γ was not determined here, i.e., we used $\gamma = 1$. LD: laser diode; LDV: laser Doppler vibrometer; LMS: least mean-squares; PPG: photoplethysmography; SMI: self-mixing interferometry.

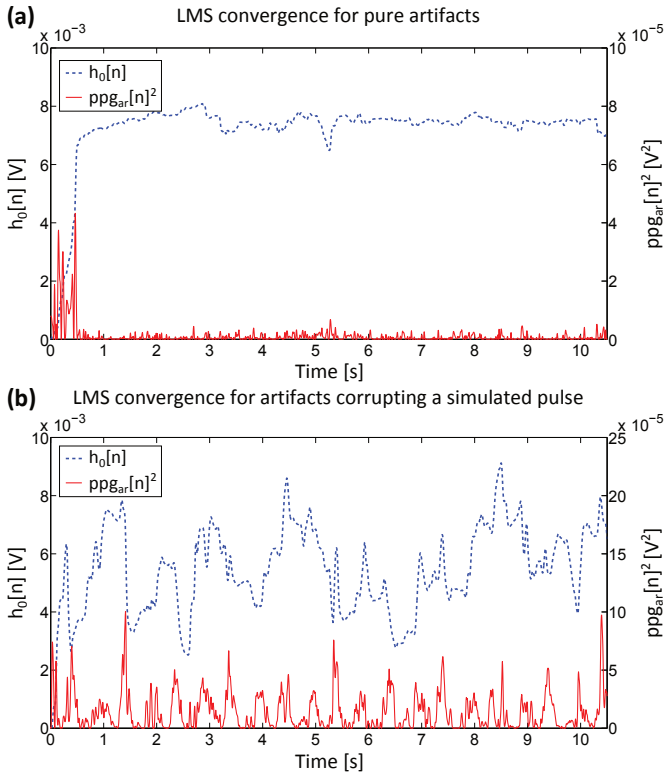

Figure 2.12: Convergence of the LMS algorithm. The dashed blue and solid red curves show the convergence of the filter weight $h_0[n]$ and the output power $ppg_{\mathrm{ar}}^2[n]$, respectively. (a) Convergence for pure artifacts. (b) Convergence for artifacts corrupting a simulated pulse. LMS: least mean-squares.

2.6 Discussion

2.6.1 In-vitro PPG measurements

Although the channel was rigid, the weak PPG signal measured in case one (solid curve in Fig. 2.6a) was still a result of the increase in milk volume in the channel. Milk volume increased in the channel because of upward deflection of the window as measured via SMI, thus increasing the amount of backscattered light that reached the detector.

When comparing case two (Fig. 2.6b) to case one, the PPG waveform was more smooth and its amplitude increased by a factor of 2.4, while the window deflection decreased by a factor of 2.4. The upward motion of the window decreased, because the increased channel compliance decreased the pressure in the channel. Furthermore, the silicone membranes caused the periodic increases in channel volume to

be larger compared to the rigid channel. And as in case one, the PPG signal was in phase with the window deflection. Therefore, we conclude that the increased PPG signal amplitude has to be attributed to the stronger backscattering as a result of the larger increase in milk volume in the flexible channel. Furthermore, in case two the DC level of the PPG signal increased by approximately 100 mV, because light reached the detector that tunneled through the silicone membrane and was reflected back from the base, as indicated by the third and fourth exponents in (2.32). These light paths contributed to the increased PPG amplitude as well. However, because the PPG amplitude was mostly a result of increased backscattering in the milk, the most direct paths via the milk volume provided the largest contribution to the PPG signal pulse amplitude.

When using milk as a blood phantom, the PPG signal amplitude was in phase with the deflection of the window, i.e., an increase in milk volume lead to an increase in the PPG signal. This was opposite to most in-vivo reflectance PPG signals, which show a decrease upon an increase in blood volume, as a result of increased absorption [58,146]. In case three, a PPG signal was measured of which the amplitude was in antiphase with the window deflection (Fig. 2.6c), i.e., as a result of the added absorption, an increase in milk volume now lead to a decrease in the PPG signal. Furthermore, the resulting PPG signal amplitude was about 4% of the PPG signal baseline, which is comparable to the relative amplitude of in-vivo PPG signals [24, 105, 123]. Therefore, we concluded that in case three an in-vitro PPG signal representative of an in-vivo PPG signal was obtained by adding a water-soluble black dye to the milk, although the shape of the in-vitro PPG signal was not necessarily similar to the shape of an in-vivo PPG signal. In particular, in-vivo PPG signals show a faster systolic decrease and a slower diastolic increase (see Fig. 1.2), while the in-vitro PPG signal showed a slower "systolic" decrease and a faster "diastolic" increase. Lastly, we considered the deflection of the window which we observed in-vitro a relevant effect, because skin pulsates in-vivo as a result of pulsations of the arterial blood.

In the perfusion phantom, a small laser displacement of 100 μm - 200 μm resulted in optical motion artifacts with a magnitude comparable to the PPG signal magnitude (Fig. 2.11b). However, the skin-perfusion phantom only modeled the basic optical effects qualitatively. It is for instance not known whether the optical shunt through the POM window had a realistic contribution to the measured PPG signal. Therefore, no conclusion can be drawn from the in-vitro model regarding the magnitude of motion artifacts expected in-vivo as a result of relative sensor motion.

Finally, the measurements with pure milk illustrate the limitations of the Beer-Lambert model for strongly scattering media [58,105]. Increases in detected light intensity caused by increases in milk volume resulted from an increased light scattering (Fig. 2.6a and 2.6b). This effect cannot be described by the Beer-Lambert law, which only takes into account light absorption. Therefore, it should be noted that the model proposed in Section 2.4.1 can only be interpreted as a coarse description of the detected light intensity.

2.6.2 Displacement measurement

Comparing the displacement measured via SMI to the LDV reference shows that both displacement measurements are equal in shape (Fig. 2.10). Moreover, motion towards the LDV gives a positive sign, which confirms that motion towards the laser beam of the VCSEL indeed resulted in a positive displacement measured via SMI, as indicated by (2.1) and (2.22).

The precision of the SMI displacement measurement can predominantly be ascribed to speckle interference [55]. As shown in Fig. 2.8, destructive speckle interference repeatedly caused the amplitude of the Doppler signals to fade. As a result of destructive speckle interference, normalization of the Doppler signals was ineffective and interference fringes were missed on a structural basis, as indicated by arrows 1 and 2 in Fig. 2.9. Furthermore, speckle interference lead to jumps of π rad in the phase of the Doppler signals, as indicated by arrows 3 and 4 in Fig. 2.9, or other irregularities in the phase of the Doppler signals. These effects of speckle interference lead to structural inaccuracies in the displacement measurement, which resulted in a baseline drift in the displacement measurement. The slope of the drift depends on the number of speckle interference events per unit of time, and thus on the surface roughness and the speed of motion. Baseline drift occurred in this recording, even though SNR < 1 of either of the baseband Doppler signals occurred only during about 1% of the recording time. However, the baseline drift was effectively removed by the 0.3-Hz HPF ($\omega_{\text{ppg min}}$ in Fig. 2.4).

Furthermore, γ indicated a constant scaling error of about 6% between the SMI displacement measurement, $\Delta L_{\text{smi}}[n]$, and the LDV reference measurement, $\Delta L_{\text{ref}}[n]$. This can be explained by an error of approximately 1° in the angle between the laser beam and the direction of motion. However, it is likely that the inaccuracy in the angle θ was smaller than 1°, and that γ corrected for the inaccuracy in wavelength λ_0 as well. In addition, we expect that the effects of speckle interference also lead to a structural error in the amplitude of the displacement measurement, for which γ partly corrected too.

The error in the final displacement measurement was on the order of 10^{-6} m (Fig. 2.10). A precision of 10^{-6} m is sufficient, because we expect sensor motion to be on the order of 10^{-4} - 10^{-3} m. Therefore, this measurement shows that translation of the laser over a diffusely-scattering POM-window can be reconstructed with sufficient accuracy using SMI by applying the theory outlined in Section 2.3.

In-vivo experiments are required to determine the influence of speckle on the Doppler signals when measuring on real skin. Moreover, during in-vivo experiments the laser diode will move more irregularly with respect to the skin, during which the distance L_o between the laser diode and the skin will vary over time as well. The variation of this distance can also adversely affect the amplitude of the Doppler signals ((2.11) and (2.14)). Furthermore, in this case the displacement can no longer be measured in absolute units, because a three-dimensional motion is projected onto a single axis, and the angle between the laser beam and the direction of motion is unknown.

2.6.3 In-vitro artifact reduction

Figures 2.11a and 2.11b show that the optical motion artifacts are in phase with the laser displacement, i.e., when the laser moves towards the PPG photodiode (positive displacement), the measured light intensity increases. This is in accordance with the Taylor approximation of the PPG signal in (2.33): a decrease in emitter-detector distance increases the light intensity received. Figures 2.11a and 2.11b furthermore show a significant reduction of optical motion artifacts via an LMS algorithm that adaptively scales the laser displacement to estimate the artifacts. This indicates a strong correlation between the laser displacement and the artifacts, thus confirming our hypothesis in-vitro. The fast convergence in Fig. 2.12 indicates feasibility of a real-time implementation.

Figures 2.11a and 2.11b illustrate that the proposed algorithm does not fully suppress the motion artifacts. This resulted from fast fluctuating artifacts which were beyond the adaptation speed of the algorithm. Increasing step-size parameter μ would increase the adaptation speed, but this cannot be done to assure stability. The pure motion artifacts in Fig. 2.11a furthermore show fast fluctuations which were not present in the displacement in Fig. 2.11c, e.g., at 0.3 s. These fast fluctuations were a result of small inhomogeneities in the skin-perfusion phantom and were multiplicative effects on the pure displacement artifact. Because visual inspection of the baseline of the monitor diode signal showed that the optical output power of the laser diode remained constant during motion, we conclude that these fast fluctuations were not the result of fluctuations in the optical power. These multiplicative artifacts as a result of inhomogeneities were not estimated accurately, because they were beyond the adaptation speed of the algorithm. In addition, the LMS algorithm may have to correct for the inaccuracies in the SMI displacement measurement as a result of speckle. This would be done by adjusting $h_0[n]$, which slows down the process of estimating the motion artifacts.

Figures 2.11a and 2.11b show that artifacts corrupting a simulated pulse were suppressed to a smaller extent compared to pure artifacts. Three complicating factors occur in this situation. First, in this situation a motion artifact component arises, which is proportional to the product of variation in source-detector distance and variation in milk volume, as shown by the fourth term in the Taylor-approximation of the PPG signal in (2.33). That is, in this case the artifact amplitude also depends on milk volume variations, which results in additional fluctuations over time which complicate correct estimation of $h_0[n]$. Second, the adaptation of $h_0[n]$ is influenced by the simulated pulse $sp[n]$ in $ppg_{\mathrm{ar}}[n]$ via the cross-correlation in the weight update rule (2.38). These two factors may contribute to the larger fluctuation of $h_0[n]$ over time, as can be seen in Fig. 2.12b. Third, the reduction in performance can be attributed to the window deflection component in $\Delta L_{\mathrm{smi}}[n]$, as shown by $\Delta L_{\mathrm{err}}[n]$ (thin curve in Fig. 2.11d). Window deflection is correlated with $sp[n]$. The window deflection component in the SMI

measurement probably leaks into the motion artifact estimate, $h_0[n]\Delta l_{\mathrm{ma}}[n]$, and thereby affects the signal of interest, $sp[n]$.

In-vivo measurements are necessary to determine the true potential of the proposed method. In this case, SMI with one laser diode will provide a one-dimensional reference of three-dimensional sensor-tissue motion. The usefulness of such a reference is to be determined. Furthermore, more complex motion artifacts will be observed in the PPG signals in-vivo, which presumably result from optical coupling effects, sloshing of blood and deformation of the skin. In-vivo results will demonstrate whether sensor-tissue motion as measured via SMI also correlates to other artifacts than optical artifacts. Lastly, it is likely that pulsations of the skin at the PR will be measured via SMI, which can affect the cardiac pulse component in the PPG signal when removing motion artifacts based on correlation cancellation. Furthermore, as the laser light will be focused onto the skin, we expect that the contribution of laser light directly backscattered by the pulsating skin will dominate the contribution of laser light backscattered by the randomly moving red blood cells in the dermis. Therefore, we expect a negligible contribution by moving red blood cells to the relative motion signal.

2.7 Conclusions

We hypothesized that optical motion artifacts in a PPG signal as a result of sensor motion or deformation correlate with movement of the PPG sensor relative to the skin. This hypothesis has been proven true in a laboratory setup. We developed a skin-perfusion phantom with a diffusely scattering skin phantom to measure in-vitro PPG signals. Optical motion artifacts were generated in the in-vitro PPG signal by translating the PPG light source with respect to the PPG photodiode. The PPG light source was a laser diode, with which we could measure the light source displacement via SMI. This allowed us to use a single component as light source as well as artifact reference measurement. Translation of the laser diode over the diffusely-scattering skin-phantom was accurately measured via SMI. We achieved a significant reduction of the optical motion artifacts in the in-vitro PPG signals, by using the SMI-derived light source displacement as an artifact reference in a correlation canceler. The correlation canceler scaled the laser displacement by only a single coefficient to estimate and remove the motion artifacts, which proved good correlation between the laser displacement and the optical motion artifacts in-vitro. Although good results have been obtained using the in-vitro setup, in-vivo measurements are required to determine the true potential of the use of sensor displacement as a means to reduce motion artifacts in PPG signals.

CHAPTER 3

Generic algorithm for reduction of quasi-periodic motion artifacts in photoplethysmography

This chapter is based on

R.W.C.G.R. Wijshoff, M. Mischi, and R.M. Aarts, "Reduction of periodic motion artifacts in photoplethysmography," accepted for publication in *IEEE Transactions on Biomedical Engineering*.

Abstract

Introduction: Quasi-periodic motion artifacts can affect photoplethysmography (PPG) signals in activities of daily living (ADL), cardiopulmonary exercise testing (CPX), and cardiopulmonary resuscitation (CPR). This hampers measurement of inter-beat-intervals (IBIs) and oxygen saturation (SpO_2). Our objective was to develop a generic algorithm to remove quasi-periodic motion artifacts, and thereby recover artifact-reduced PPG signals for further beat-to-beat analysis.

Methods: The algorithm was retrospectively evaluated on red and infrared forehead PPG signals, which were acquired from six healthy volunteers while they were walking on a treadmill. The step rate was tracked in a motion reference signal via a second-order generalized-integrator with a frequency-locked loop. Two reference signals were compared: sensor motion relative to the skin ($\Delta x[n]$) measured via self-mixing interferometry (SMI), and head motion ($a_v[n]$) measured via accelerometry. A quadrature harmonic model with frequencies related to the tracked step-rate was used to estimate the artifacts. Quadrature components need only two coefficients per frequency leading to a short filter, and prevent undesired frequency-shifted components in the artifact estimate. The coefficients of the quadrature harmonic model were determined via a least mean-squares algorithm. Subtracting the artifact estimate from the measured PPG signal reduced the artifacts.

Results: Compared to relative sensor motion $\Delta x[n]$, head motion $a_v[n]$ had a better signal-to-noise ratio and more consistently contained a component at the step rate. The inferior quality of $\Delta x[n]$ in a number of measurements may have been the result of limited relative sensor motion. Artifact reduction was effective for distinct step rate and pulse rate, since the artifact-reduced PPG signals provided more stable IBI and SpO_2 measurements.

Conclusions: Accelerometry provided a more reliable motion reference signal than SMI. The proposed algorithm can be of significance for monitoring in ADL, CPX or CPR, by providing artifact-reduced PPG signals for improved IBI and SpO_2 measurements during quasi-periodic motion.

3.1 Introduction

Photoplethysmography (PPG) is a non-invasive easy-to-use optical technology, widely applied to monitor the cardiovascular and respiratory systems [6, 10, 146, 156, 177]. PPG measures local changes in blood volume by emitting light through tissue [72]. PPG can be used to measure cardiac pulse rate (PR) and peripheral arterial functional-hemoglobin oxygen-saturation (SpO_2) [10, 108, 156, 177]. PR can be derived from the cardiac-induced variations in a PPG signal, either in the time domain [118] or the frequency domain [155]. An empirical calibration relates SpO_2 to the ratio of the baseline-normalized cardiac-induced variations in two PPG signals obtained at different wavelengths, typically red and near-infrared [11, 105, 108, 124, 140, 191].

PPG signals are highly susceptible to motion which hampers their use in, e.g., activities of daily living (ADL) [10, 14, 177], cardiopulmonary exercise testing (CPX) [16, 49], or cardiopulmonary resuscitation (CPR) [202, 203]. In ADL, the use of PPG is for instance researched to detect PR changes in patients with epilepsy [183], as this can indicate seizures [184]. Susceptibility to motion hampers beat-to-beat analysis, e.g., to obtain pulse rate variability (PRV) [159], or to detect atrial fibrillation [23, 45]. Motion can also affect SpO_2 measurements, e.g., causing false positive desaturations during CPX [16, 49]. During CPR, motion artifacts due to chest compressions complicate detection of a cardiac pulse in the signal [202, 203]. In this chapter, we will focus on quasi-periodic motion artifacts, which is one type of motion artifact that can occur in ADL, CPX and CPR. Quasi-periodic artifacts are furthermore relevant because algorithms may falsely detect them as a PR component [34].

Removal of motion artifacts to recover artifact-reduced PPG signals has been researched extensively. Various generic approaches exist for removal of additive periodic motion artifacts using correlation cancellation with an accelerometer as a motion reference [34, 51, 64, 90, 138, 205]. In these approaches the artifact is estimated by applying a finite impulse response (FIR) filter to a single reference signal and updating all FIR-coefficients over time. However, quadrature reference signals would be preferred here, because then only two coefficients are needed per frequency and undesired frequency-shifted components cancel in the estimate [56, 193]. Wavelength-independent multiplicative optical-coupling artifacts can be removed from a PPG signal by normalization by a second PPG signal obtained at a different wavelength [65, 66, 135]. However, this requires a revised calibration for SpO_2. Artifact-reduced PPG signals can also be recovered using a synthetic reference for the cardiac pulse waveform [33], deriving artifact references from the measured PPG signals [144, 212], applying a signal decomposition method [83, 87], or averaging several consecutive pulses [91]. However, the approaches without an additional motion measurement provide a segmented recovery of the artifact-reduced PPG signal, require a reliable PR measurement prior to artifact removal, or need to detect the individual cardiac pulses in the corrupted PPG signal.

Methods have also been developed focussing on the extraction of averaged physiological parameters from motion-corrupted PPG signals. PR has been determined from the PPG signal frequency spectrum using an accelerometer to identify the motion frequencies [50, 158, 215, 216]. In [158], an artifact-reduced PPG time-trace is also reconstructed, but the reconstruction is window-based, and uses per window a single PR selected from the PPG frequency spectrum. PR has also been determined from the PPG signal frequency spectrum after artifact removal with a notch filter at the motion frequency as measured via the photodiode with the light emitting diodes (LEDs) switched off [188]. Motion-robust SpO_2 measurements have been obtained by discriminating cardiac-induced arterial and motion-induced venous components based on their different amplitude ratios in the red and near-infrared PPG signals [57, 211]. PR and SpO_2 can also be measured more reliably by using the smoothed pseudo Wigner-Ville distribution [210].

In this chapter, we focus on a generic approach to remove quasi-periodic motion artifacts to recover artifact-reduced PPG signals for beat-to-beat analysis. We determined the fundamental motion frequency from a motion reference signal via a second-order generalized integrator (SOGI) with a frequency-locked loop (FLL) [152]. We described the motion artifact by a harmonic model of quadrature components with frequencies related to the fundamental motion frequency. With quadrature components only two coefficients need to be estimated per frequency component, leading to a short filter. We estimated the coefficients via a least mean-squares (LMS) algorithm. Quadrature components also prevent undesired frequency-shifted components in the artifact estimate. The motion artifact was removed by subtracting the harmonic model from the measured PPG signal. Furthermore, we compare two motion reference signals: sensor motion relative to the skin and body motion. Motion relative to the skin is an origin of artifacts in PPG [10, 33, 65, 66, 108, 205]. We measured relative sensor motion by augmenting the PPG sensor with a laser diode and using self-mixing interferometry (SMI) [196, 197, 201]. The objective was to gain insight in the amount of relative sensor motion. We measured body motion with an accelerometer. Red and near-infrared (IR) PPG signals were measured on the forehead while walking on a treadmill to generate quasi-periodic motion artifacts. We used a reflective PPG sensor, because measurement of relative motion is more convenient compared to a transmissive sensor. Furthermore, a reflective sensor is more widely applicable than a transmissive sensor [63, 110, 177, 191]. We performed a preliminary validation of the algorithm only, using a limited data set of thirty measurements obtained from six healthy volunteers.

3.2 Methods A: Experiment and measurements

Thirty measurements were performed on six healthy male volunteers, following the protocol in Fig. 3.1a. Each subject walked on a treadmill at speeds of 4, 5, 6, 7 and 8 km/h to generate quasi-periodic motion artifacts. Each speed was

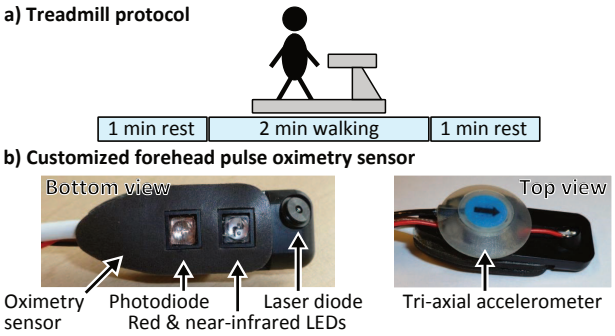

Figure 3.1: (a) Treadmill protocol to generate periodic motion artifacts. (b) Forehead pulse oximetry sensor with laser diode and tri-axial accelerometer as motion references. LED: light emitting diode.

maintained for 2 min, and was preceded and followed by 1-min of rest with the subject standing still. The institutional review board approved the study. All subjects signed informed consent.

Figure 3.1b shows the customized forehead sensor. Raw red (660 nm) and near-infrared (900 nm) PPG signals were obtained with a forehead reflectance pulse oximetry sensor (Nellcor™ Oxisensor II RS-10, Covidien-Nellcor™, Dublin, Ireland), controlled by a custom-built photoplethysmograph. The headband delivered with the oximetry sensor was used to exert pressure on the sensor. An 850-nm vertical-cavity surface-emitting laser diode with an internal monitor diode (ULM-Photonics GmbH, Philips, Ulm, Germany) was positioned next to the oximetry sensor to measure sensor motion relative to the skin. As Fig. 3.1b shows, the laser diode was positioned at an angle of 45° in the plane of the oximetry sensor and at an angle of 30° with respect to the surface normal, to allow measuring vertical and horizontal relative sensor motion. The laser light was focused onto the skin via a ball lens integrated into the laser diode package. A tri-axial accelerometer (LIS344ALH, STMicroelectronics, Geneva, Switzerland) was positioned on top of the oximetry sensor to measure head motion. A lead I electrocardiography (ECG) signal was recorded as a reference, using a custom-built ECG module. The PPG, accelerometry, monitor diode and ECG signals were simultaneously recorded using a 16-bit digital data acquisition card (DAQ) (NI USB-6259, National Instruments, Austin, TX, USA). A LabVIEW (National Instruments, Austin, TX, USA) program controlled the DAQ. A finger clip pulse oximetry sensor (M1191B, Philips Medizin Systeme Boeblingen GmbH, Boeblingen, Germany) was used with a commercial pulse oximetry OEM board to obtain SpO_2 measurements for comparison.

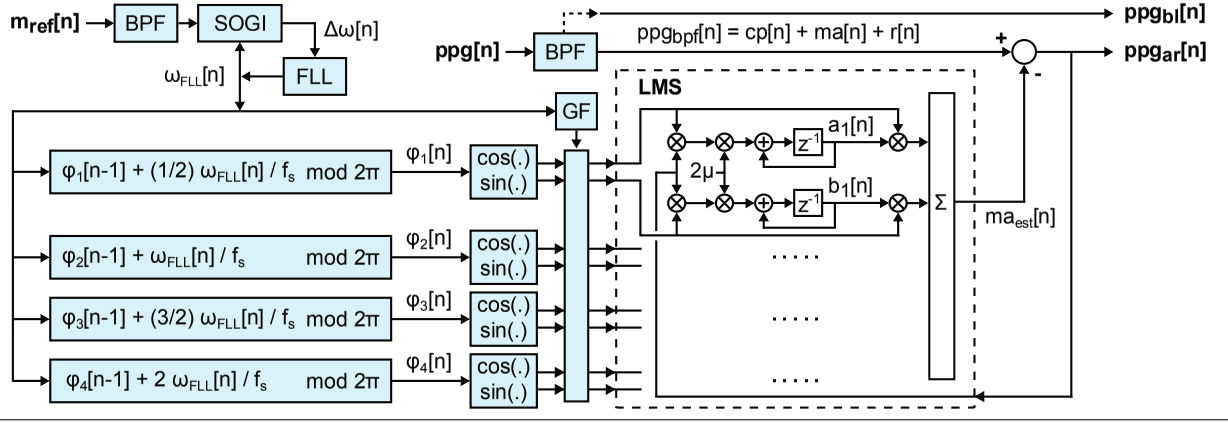

a_1, b_1	coefficients of artifact model	FLL	frequency-locked loop	ma	motion artifact	ppg_{bl}	baseline of PPG signal
BPF	band-pass filter	$\varphi_{1\text{-}4}$	phases of artifact model	ma_{est}	motion artifact estimate	ppg_{bpf}	band-pass filtered PPG signal
cp	cardiac pulse	GF	gating function	μ	LMS step-size parameter	r	residual noise
Δω	FLL frequency error	LMS	least mean-squares	ppg	photoplethysmography signal	SOGI	second-order generalized integrator
f_s	sampling rate	m_{ref}	motion reference	ppg_{ar}	artifact-reduced PPG signal	ω_{FLL}	motion frequency tracked by FLL

Figure 3.2: Overview of the motion artifact reduction algorithm. The primary input is the red or near-infrared PPG signal, $ppg[n]$. The algorithm runs once for each of the PPG signals. The secondary input is the motion reference signal, $m_{\mathrm{ref}}[n]$. The primary and secondary inputs are preprocessed with a BPF. After the BPF, the PPG signal $ppg_{\mathrm{bpf}}[n]$ is assumed a sum of a cardiac pulse component, $cp[n]$, a motion artifact, $ma[n]$, and residual noise, $r[n]$. The BPF also extracts the baseline of the PPG signal, $ppg_{\mathrm{bl}}[n]$. A SOGI-based structure with an FLL tracks the fundamental frequency of motion, $\omega_{\mathrm{FLL}}[n]$, in $m_{\mathrm{ref}}[n]$. This frequency is used to construct the phases $\phi_{1-4}[n]$ of four cosine and sine quadrature components, which are the basis of the artifact model. An LMS algorithm with step-size parameter μ determines the amplitudes $a_{1-4}[n]$ and $b_{1-4}[n]$ of the cosine and sine quadrature components, respectively, and sums these components to construct the motion artifact estimate, $ma_{\mathrm{est}}[n]$. Subtracting $ma_{\mathrm{est}}[n]$ from $ppg_{\mathrm{bpf}}[n]$ yields the artifact-reduced output signal, $ppg_{\mathrm{ar}}[n]$. The artifact removal stage is switched on by the GF only if the tracked motion frequency $\omega_{\mathrm{FLL}}[n]$ is considered stable. BPF: band-pass filter; FLL: frequency-locked loop; GF: gating function; LMS: least mean-squares; PPG: photoplethysmography; SOGI: second-order generalized integrator.

3.3 Methods B: Artifact reduction algorithm

Figure 3.2 shows the generic motion artifact reduction algorithm which ran at a sampling rate of $f_s = 250$ Hz. The primary input was the measured red or near-IR PPG signal, $ppg[n]$ [V], with sample index n. The algorithm was run once for the red PPG signal, and once for the near-IR PPG signal. The secondary input was the motion reference signal, $m_{\text{ref}}[n]$, used to track the fundamental frequency of motion, which was the step rate. We compared two motion reference signals: sensor motion relative to the skin measured via SMI (Section 3.3.1), and head motion derived from the accelerometer (Section 3.3.2). The primary and secondary input signals were preprocessed by a band-pass filter (BPF) (Section 3.3.3). The fundamental motion frequency, $\omega_{\text{FLL}}[n]$ [rad/s], was estimated from $m_{\text{ref}}[n]$ using a SOGI-based structure with an FLL (Section 3.3.4). The motion artifact was subsequently estimated and removed by constructing quadrature reference signals and applying an LMS algorithm (Section 3.3.5). The algorithm output was the artifact-reduced PPG signal, $ppg_{\text{ar}}[n]$.

3.3.1 Relative sensor motion

We measured motion of the oximetry sensor relative to the skin, because we expected that relative sensor motion would change the tissue volume which is illuminated by the LEDs, resulting in a motion artifact. Therefore, we expected a good correlation between relative sensor motion and motion artifacts in the PPG signals.

Relative sensor motion was measured with the laser diode using SMI. Relative sensor motion caused a Doppler shift in the emitted laser light. The monitor diode of the laser diode measured a signal at the Doppler frequency when back-scattered laser light entered the laser cavity and interfered with the standing wave. We determined a measure of sensor motion relative to the skin from the monitor diode signal.

A DC laser current of about 1.63 mA generated about 0.5 mW of optical output power. The laser current was sinusoidally modulated at a frequency of 40 kHz with an amplitude of 158 μA. The modulation resulted in quadrature Doppler frequency components around the modulation frequency and its second harmonic, respectively, as was measured by the monitor diode. The DAQ sampled the 100 kHz band-limited monitor diode signal at a sampling rate of 200 kHz.

The remainder of this section summarizes the determination of relative sensor motion. More details can be found in Chapter 2 and [201].

Baseband quadrature Doppler signals were obtained by translating the Doppler signals around the modulation frequency and its second harmonic to baseband and applying a 15-kHz low-pass filter (LPF) and a 10-Hz high-pass filter (HPF). The baseband Doppler signals were normalized via the Hilbert transform, by using the Doppler phase of the resulting analytical signals, $\phi_d[n]$ [rad], in a sine and a

cosine. This resulted in the normalized Doppler signals $y[n]$ and $x[n]$:

$$y[n] = \sin\left(\phi_d[n]\right), \tag{3.1}$$

$$x[n] = \cos\left(\phi_d[n]\right). \tag{3.2}$$

Relative sensor motion, $\Delta x[n]$, was then obtained via

$$\Delta x[n] = \frac{1}{2\pi}\text{unwrap}\left[\text{atan2}\left(\frac{y[n]}{x[n]}\right)\right], \tag{3.3}$$

where unwrap$[\cdot]$ removes discontinuities in the radian phase by adding multiples of $\pm 2\pi$, and atan2$(\cdot)$ is a four-quadrant arctangent implementation. After the preprocessing LPF (Section 3.3.3), $\Delta x[n]$ was down-sampled to $f_s = 250$ Hz.

The unit of $\Delta x[n]$ was the number of Doppler cycles. The absolute unit could not be determined because the angle between the laser beam and the skin was unknown and because a three-dimensional motion was mapped onto a single axis.

3.3.2 Accelerometry

The tri-axial accelerometer measured head motion. From the three axes, the head-vertical axis $a_v[n]$ contained the strongest fundamental motion-frequency component, and was therefore used as motion reference $m_{\text{ref}}[n]$.

3.3.3 Preprocessing

As preprocessing, the same BPF was applied to $ppg[n]$ and $m_{\text{ref}}[n]$. The BPF was an LPF followed by a linear-phase HPF. A sixth-order Butterworth 4-Hz LPF removed high-frequency noise. To construct the HPF, the low-frequency baseline was first extracted via a filter with impulse response

$$h_{\text{bl}}[n] = \frac{\sin\left(2\pi f_c\left(n - N_{\text{bl}}\right)/f_s\right)}{2\pi f_c\left(n - N_{\text{bl}}\right)/f_s}\frac{w_H[n]}{S_{\text{hbl}}},\ n = 0, ..., 2N_{\text{bl}}, \tag{3.4}$$

with cut-off frequency $f_c = 0.5$ Hz, Hamming window $w_H[n]$ centered at $n = N_{\text{bl}}$, normalization factor S_{hbl} to have $h_{\text{bl}}[n]$ sum to 1, and $N_{\text{bl}} = f_s/f_c = 500$ samples. The HPF was obtained by subtracting the baseline from the original signal delayed by N_{bl} samples. The sinc-function in (3.4) assured a linear phase-response. The Hamming window reduced overshoot and ringing in the magnitude frequency-response. The extracted PPG signal baselines, $ppg_{\text{bl}}[n]$, were used to determine pulsatility (Section 3.4.3) and SpO_2 (Section 3.4.5).

3.3.4 Measurement of the step rate

Figure 3.3 shows the SOGI-based structure with the FLL [31, 114, 152] used to track the step rate in $m_{\text{ref}}[n]$ on a sample-to-sample basis. The SOGI has two

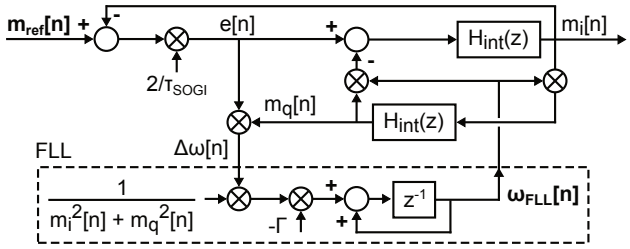

Figure 3.3: The motion frequency, $\omega_{\mathrm{FLL}}[n]$, is tracked in the motion reference signal, $m_{\mathrm{ref}}[n]$, via a SOGI-based structure with an FLL. The integrators $H_{\mathrm{int}}(z)$ of the SOGI filter from the input $m_{\mathrm{ref}}[n]$ the outputs $m_i[n]$ and $m_q[n]$, the in-phase and quadrature signals at $\omega_{\mathrm{FLL}}[n]$, respectively. The time-constant τ_{SOGI} [s] sets the filter bandwidth. The FLL input, $\Delta\omega[n] = e[n] \cdot m_q[n]$ with $e[n] = 2(m_{\mathrm{ref}}[n] - m_i[n])/\tau_{\mathrm{SOGI}}$, is a measure of the FLL frequency error and is used to adjust the FLL output $\omega_{\mathrm{FLL}}[n]$. The FLL gain Γ [-] sets the FLL bandwidth. FLL: frequency-locked loop; SOGI: second-order generalized integrator.

integrators, $H_{\mathrm{int}}(z)$, which filtered from the input $m_{\mathrm{ref}}[n]$ the outputs $m_i[n]$ and $m_q[n]$, the in-phase and quadrature signals at FLL frequency $\omega_{\mathrm{FLL}}[n]$ [rad/s], respectively. The FLL used $m_i[n]$ and $m_q[n]$ to estimate the frequency error between $\omega_{\mathrm{FLL}}[n]$ and the step rate, $\Delta\omega[n]$, and to make the FLL adaptation speed independent of the magnitude of the tracked frequency component. We assumed step rates between 1 and 3 Hz.

The transfer functions from $m_{\mathrm{ref}}[n]$ to $m_i[n]$ and $m_q[n]$ are, respectively, using continuous-time for simplicity,

$$H_i(s) = \frac{(2/\tau_{\mathrm{SOGI}})s}{s^2 + (2/\tau_{\mathrm{SOGI}})s + \omega_{\mathrm{FLL}}^2}, \tag{3.5}$$

$$H_q(s) = \frac{(2/\tau_{\mathrm{SOGI}})\omega_{\mathrm{FLL}}}{s^2 + (2/\tau_{\mathrm{SOGI}})s + \omega_{\mathrm{FLL}}^2}, \tag{3.6}$$

with $s = j\omega$, frequency ω [rad/s], time-constant τ_{SOGI} [s], and FLL frequency ω_{FLL} [rad/s] which has been assumed constant here. Frequency ω_{FLL} is the resonance of (3.5) and (3.6), where the input appears unchanged at $m_i[n]$ and with a 90° lag at $m_q[n]$. The zero of the transfer function from $m_{\mathrm{ref}}[n]$ to $e[n]$ shows that loop input $e[n]$ contains no component at ω_{FLL}:

$$H_e(s) = \frac{H_q(s)}{\omega_{\mathrm{FLL}}}\left(s^2 + \omega_{\mathrm{FLL}}^2\right). \tag{3.7}$$

The 3-dB frequencies f_{cSOGI} [Hz] around the resonances of (3.5) and (3.6) describe the bandwidth of the filter:

$$f_{\mathrm{cSOGI}} = \frac{1}{2\pi}\sqrt{\omega_{\mathrm{FLL}}^2 + \frac{2}{\tau_{\mathrm{SOGI}}^2} \pm \frac{2}{\tau_{\mathrm{SOGI}}}\sqrt{\omega_{\mathrm{FLL}}^2 + \frac{1}{\tau_{\mathrm{SOGI}}^2}}}. \tag{3.8}$$

We used $\tau_{\mathrm{SOGI}} = 0.7$ s, giving a 3-dB width of about 0.5 Hz.

We implemented $H_{\mathrm{int}}(z)$ as a second-order integrator [31] to accurately approximate an ideal integrator $1/(j\omega)$ for the assumed motion frequencies up to 3 Hz:

$$H_{\mathrm{int}}(z) = \frac{T_s}{2}\frac{3z^{-1} - z^{-2}}{1 - z^{-1}}. \tag{3.9}$$

Compared to an ideal integrator for frequencies up to 3 Hz, the deviation in magnitude and phase frequency response of (3.9) was at most 0.24% and $-0.006°$, respectively. The delays in the numerator of (3.9) prevented an algebraic loop.

The FLL adjusted $\omega_{\mathrm{FLL}}[n]$ to track the frequency $\omega_{\mathrm{ref}}[n]$ in $m_{\mathrm{ref}}[n]$. The FLL input, $\Delta\omega[n] = e[n] \cdot m_q[n]$, is an instantaneous measure of the frequency error $\omega_{\mathrm{FLL}}[n] - \omega_{\mathrm{ref}}[n]$. Equation (3.7) shows that $H_e(s)$ is a scaled version of $H_q(s)$, where the scaling factor is positive when $\omega_{\mathrm{FLL}}[n] > \omega_{\mathrm{ref}}[n]$, and where the scaling factor is negative when $\omega_{\mathrm{FLL}}[n] < \omega_{\mathrm{ref}}[n]$. Equation (3.7) thus shows that $e[n]$ and $m_q[n]$ have the same phase when $\omega_{\mathrm{FLL}}[n] > \omega_{\mathrm{ref}}[n]$ and opposite phase when $\omega_{\mathrm{FLL}}[n] < \omega_{\mathrm{ref}}[n]$. Therefore, $\Delta\omega[n]$ is on average positive when $\omega_{\mathrm{FLL}}[n]$ should decrease, and on average negative when $\omega_{\mathrm{FLL}}[n]$ should increase. Multiplying $\Delta\omega[n]$ by the negative FLL gain $-\Gamma$ [-] resulted in a frequency correction which steered $\omega_{\mathrm{FLL}}[n]$ towards $\omega_{\mathrm{ref}}[n]$. The input $\Delta\omega[n]$ was normalized by $m_i^2[n] + m_q^2[n]$ to make the adaptation speed independent of the magnitude of the tracked frequency component. When $m_i^2[n]+m_q^2[n] = 0$, normalization was not performed and $\omega_{\mathrm{FLL}}[n]$ was not updated. When $m_i^2[n] + m_q^2[n] > 0$, $\omega_{\mathrm{FLL}}[n]$ was adjusted according to the following approximation for $\omega_{\mathrm{FLL}}[n] \approx \omega_{\mathrm{ref}}[n]$, by using $\omega_{\mathrm{FLL}}^2[n] - \omega_{\mathrm{ref}}^2[n] \approx 2\omega_{\mathrm{FLL}}[n](\omega_{\mathrm{FLL}}[n] - \omega_{\mathrm{ref}}[n])$ in (3.7):

$$\omega_{\mathrm{FLL}}[n+1] = (1 - \Gamma)\,\omega_{\mathrm{FLL}}[n] + \Gamma\omega_{\mathrm{ref}}[n], \tag{3.10}$$

where we neglected the double-frequency component in $\Delta\omega[n]$. The relationship between FLL gain Γ, time-constant τ_{FLL} [s], and 3-dB cut-off frequency f_{cFLL} [Hz] follows from (3.10):

$$\Gamma = 1 - \exp\left(\frac{-1}{\tau_{\mathrm{FLL}} f_s}\right) = 1 - \exp\left(\frac{-2\pi f_{\mathrm{cFLL}}}{f_s}\right). \tag{3.11}$$

We used $f_{\mathrm{cFLL}} = 0.1$ Hz ($\tau_{\mathrm{FLL}} \approx 1.6$ s) so (3.10) suppressed the minimum 2-Hz double-frequency component by a factor of twenty. We initiated the FLL at $\omega_{\mathrm{FLL}}[0]/(2\pi) = 1.5$ Hz.

The SOGI-based structure in Fig. 3.3 locked to the frequency in $m_{\mathrm{ref}}[n]$ which was closest to $\omega_{\mathrm{FLL}}[n]$ at start-up or after a temporary loss of signal in $m_{\mathrm{ref}}[n]$. It could therefore lock to a (sub-)harmonic of the step rate. To ascertain locking to the step rate, $\omega_{\mathrm{FLL}}[n]$ was for each n compared to the frequency $f_{\max}$ of the largest local maximum between 1 and 3 Hz in the magnitude frequency spectrum of $m_{\mathrm{ref}}[n]$. Once per second, a coarse spectrum of $m_{\mathrm{ref}}[n]$ was determined via the Fast Fourier Transform of a 5-s window and $f_{\max}$ was updated. If $\omega_{\mathrm{FLL}}[n]/(2\pi)$

deviated by more than 0.5 Hz from $f_{\max}$, then $\omega_{\mathrm{FLL}}[n]$ was replaced by $2\pi f_{\max}$ to lock to the step rate, otherwise $\omega_{\mathrm{FLL}}[n]$ remained unchanged. Frequency $f_{\max}$ was updated as unavailable if no local maximum was found, and then $\omega_{\mathrm{FLL}}[n]$ remained unchanged too.

3.3.5 Estimation and reduction of motion artifacts

We described the band-pass filtered signal, $ppg_{\mathrm{bpf}}[n]$, obtained by applying the BPF in Section 3.3.3 to the measured signal $ppg[n]$, as a sum of a cardiac pulse component, $cp[n]$, a motion artifact, $ma[n]$, and residual noise, $r[n]$:

$$ppg_{\mathrm{bpf}}[n] = cp[n] + ma[n] + r[n]. \tag{3.12}$$

We chose an additive model, because spectral analysis of $ppg_{\mathrm{bpf}}[n]$ showed that walking introduced frequency components at the step rate and its (sub-)harmonics in $ppg_{\mathrm{bpf}}[n]$ in addition to frequency components at the PR and its harmonics. Subtracting the motion artifact estimate $ma_{\mathrm{est}}[n]$ from $ppg_{\mathrm{bpf}}[n]$ gave the artifact-reduced signal $ppg_{\mathrm{ar}}[n]$:

$$ppg_{\mathrm{ar}}[n] = ppg_{\mathrm{bpf}}[n] - ma_{\mathrm{est}}[n]. \tag{3.13}$$

We obtained $ma_{\mathrm{est}}[n]$ via a quadrature harmonic model:

$$\mathrm{ma}_{\mathrm{est}}[n] = G[n] \sum_{k=1}^{4} \left[a_k[n] \cos\left(\phi_k[n]\right) + b_k[n] \sin\left(\phi_k[n]\right) \right], \tag{3.14}$$

with gating function $G[n]$ [-], amplitudes $a_k[n]$ and $b_k[n]$ [V] and motion phases $\phi_k[n]$ [rad]. Motion artifact $ma_{\mathrm{est}}[n]$ was separately estimated for the red and near-IR PPG signal. $G[n]$ assessed the stability of $\omega_{\mathrm{FLL}}[n]$. $G[n]$ equaled one when $\omega_{\mathrm{FLL}}[n]$ was considered stable, and equaled zero otherwise. $G[n]$ forced $ma_{\mathrm{est}}[n]$ to zero when no stable motion frequency was detected. We determined $G[n]$ via hysteresis detection:

$$df_{\mathrm{FLL}}[n] = \frac{f_s}{2\pi} H_G(z) \left| \omega_{\mathrm{FLL}}[n] - \omega_{\mathrm{FLL}}[n-1] \right|, \tag{3.15}$$

$$G_h[n] = \begin{cases} 0 \rightarrow 1 \text{ if } df_{\mathrm{FLL}}[n] < 0.1 \text{ Hz/s} \\ 1 \rightarrow 0 \text{ if } df_{\mathrm{FLL}}[n] > 0.5 \text{ Hz/s} \end{cases}, \tag{3.16}$$

$$G[n] = H_G(z) G_h[n], \tag{3.17}$$

$$H_G(z) = \frac{1 - \exp(-1/(\tau_G f_s))}{z - \exp(-1/(\tau_G f_s))}, \tag{3.18}$$

with $\tau_G = 0.2$ s. $H_G(z)$ tracked the envelope in (3.15) and smoothed in (3.17). We initialized $G_h[n]$ at 0. The phases $\phi_k[n]$ [rad] were determined as:

$$\phi_k[n] = \phi_k[n-1] + \frac{k}{2} \frac{\omega_{\mathrm{FLL}}[n]}{f_s} \bmod 2\pi, k = 1, 2, 3, 4, \tag{3.19}$$

where mod is the modulo operation. Phases were reset to $\phi_k[n] = 0$ when $G[n] < 0.005$. The amplitudes $a_k[n]$ and $b_k[n]$ were estimated via an LMS algorithm [193, 207]:

$$a_k[n+1] = a_k[n] + 2\mu G[n] ppg_{\mathrm{ar}}[n] \cos\left(\phi_k[n]\right), \tag{3.20}$$

$$b_k[n+1] = b_k[n] + 2\mu G[n] ppg_{\mathrm{ar}}[n] \sin\left(\phi_k[n]\right), \tag{3.21}$$

with step-size parameter μ. Coefficients were reset to $a_k[n] = 0$ and $b_k[n] = 0$ when $G[n] < 0.005$. The LMS-filter transfer-function between $ppg_{\mathrm{bpf}}[n]$ and $ppg_{\mathrm{ar}}[n]$ can be approximated by a cascade of notch filters at $(k/2)\omega_{\mathrm{FLL}}$ [193,207], where each notch has a 3-dB bandwidth W [Hz] of about [193]

$$W \approx \frac{\mu f_s}{\pi}. \tag{3.22}$$

Furthermore, μ determined the convergence time T_{cv} [s] to a fraction $0 < v < 1$ of the targeted values for a_k and b_k via

$$T_{cv} = \frac{1}{f_s} \frac{\ln(1-v)}{\ln(1-\mu)}. \tag{3.23}$$

Removal of pulses with a PR close to the step rate was limited to ranges of about $(k\omega_{\mathrm{FLL}})/(4\pi) \pm 1/24$ Hz by using $\mu = 0.001$, so $W \approx 0.08$ Hz ≈ 4.8 min^{-1}, and $T_{c0.95} \approx 12$ s.

3.4 Methods C: Performance evaluation

The performance of the artifact reduction was assessed for both relative sensor motion $\Delta x[n]$ and head motion $a_v[n]$. The adequacy as motion reference was assessed by the signal-to-noise ratio (SNR) and the stability of the extracted motion frequency (Section 3.4.1). The artifact-reduced PPG signal was assessed for accuracy of the inter-beat intervals (IBIs) compared to the ECG R-peak intervals (Section 3.4.2, 3.4.3 and 3.4.4), and for the spread in SpO_2 (Section 3.4.5).

3.4.1 Motion references

The SNR of the motion references was determined as the ratio of the root mean-square (RMS) amplitude during walking and rest. The RMS amplitude was determined from $\Delta x_{\mathrm{bpf}}[n]$ and $a_{v\_\mathrm{bpf}}[n]$, as obtained by applying the BPF in Section 3.3.3 to $\Delta x[n]$ and $a_v[n]$, respectively. Episodes with outliers in $\Delta x_{\mathrm{bpf}}[n]$ and $a_{v\_\mathrm{bpf}}[n]$, caused by touching the head band, were excluded. The stability of $f_{\mathrm{FLL}}[n] = \omega_{\mathrm{FLL}}[n]/(2\pi)$ was assessed for $\Delta x[n]$ and $a_v[n]$ in each 2 min walking period by the standard deviation (SD) of $f_{\mathrm{FLL}}[n]$ excluding the first 10 s, and the mean and SD of $df_{\mathrm{FLL}}[n]$ (3.15) and $G[n]$ (3.17).

3.4.2 R-peak detection

As a reference for the IBIs we used the R-peak to R-peak intervals (RRIs) in the ECG signal, which was sampled at 250 Hz and band-limited between 0.5 and 20 Hz. We detected the steepest ascent and descent of the QR and RS slopes, respectively, by applying positive and negative thresholds to the ECG signal time-derivative. The initial R-peak was found as the maximum in the ECG signal between the QR and RS slopes. The time instant of the i^{th} R-peak, $t_R[i]$ [s], was found by interpolating the initial R-peak and its neighbouring samples with a second-order polynomial. All detected R-peaks were visually inspected. The RRI was determined from the interpolated time instants as

$$RRI[i] = t_R[i] - t_R[i-1] \ \text{[s]}. \tag{3.24}$$

3.4.3 Pulse detection

Pulses were detected in the red and near-IR band-pass filtered signal $ppg_{\mathrm{bpf}}[n]$ and artifact-reduced signal $ppg_{\mathrm{ar}}[n]$. In the following list we use $ppg_{\mathrm{bp}}[n]$ to represent one of these four signals. Pulse detection comprised of the following steps:

1) The index of the systolic slope n_{sl} was found as the positive-to-negative zero-crossing in $ppg_{\mathrm{bp}}[n]$.

2) The index of the diastolic level n_{dias} was found as the positive-to-negative zero-crossing in the time-derivative of $ppg_{\mathrm{bp}}[n]$ directly preceding n_{sl}.

3) The index of the systolic level n_{sys} was found as the negative-to-positive zero-crossing in the time-derivative of $ppg_{\mathrm{bp}}[n]$ directly following n_{sl}.

4) A set of pulse candidates was formed for all n_{sl} which had both an associated n_{dias} and n_{sys}.

5) Pulse candidates with a pulsatility plt smaller than a threshold plt_{thr} were omitted. For each pulse, we defined

$$plt = 10^3 \cdot \left(\frac{ppg_{\mathrm{bp}}[n_{\mathrm{dias}}]}{ppg_{\mathrm{bl}}[n_{\mathrm{dias}}]} - \frac{ppg_{\mathrm{bp}}[n_{\mathrm{sys}}]}{ppg_{\mathrm{bl}}[n_{\mathrm{sys}}]} \right). \tag{3.25}$$

   The threshold plt_{thr} was empirically chosen as 70% of the average pulsatility of all pulse candidates detected in the 10 s prior to the walking period, i.e., plt_{thr} was adapted to each individual measurement.

6) From the remaining pulse candidates we only kept pairs of red and near-IR pulses which we could associate with an R-peak. We associated a pulse pair with an R-peak at time instant $t_R[i]$, if the time instants of their diastolic levels were between $t_R[i]$ and $t_R[i+1]$. If multiple red or near-IR pulses occurred between $t_R[i]$ and $t_R[i+1]$, the one closest to $t_R[i]$ was selected and the others were omitted. An R-peak at $t_R[i]$ had no associated pulse pair if the red or near-IR pulse was missing between $t_R[i]$ and $t_R[i+1]$.

7) The systolic and diastolic levels and their time instants of the pulses associated with R-peaks were finally found by interpolating the initial detections and their neighbouring samples with a second-order polynomial.

We assessed pulse detection during walking by the percentage p_A of initial pulse candidates that was associated with an R-peak. We compared p_A before and after artifact reduction.

3.4.4 Inter-beat intervals

The artifact-reduced signal $ppg_{\mathrm{ar}}[n]$ was assessed for IBI accuracy. IBIs were determined as the time difference between the interpolated systolic points of subsequent near-IR PPG pulses which were associated with R-peaks. For R-peaks without associated pulse pair, the involved IBIs were ignored. The IBI accuracy was determined as the difference with the associated RRI:

$$\Delta IBI[i] = IBI[i] - RRI[i] \ \ [\mathrm{s}], \tag{3.26}$$

with i referring to the i^{th} IBI. We assessed the algorithm performance by the 10^{th} to 90^{th} percentile range of ΔIBI for each measurement during rest, walking, and after artifact reduction. The interpolation in the R-peak and pulse detection assured that ΔIBI was not restricted to integer multiples of 4 ms.

3.4.5 Oxygen saturation

The artifact-reduced signal $ppg_{\mathrm{ar}}[n]$ was also assessed for the spread in $\mathrm{SpO_2}$. For pulse pairs associated with an R-peak, $\mathrm{SpO_2}$ was obtained via the calibration curve of the oximetry sensor:

$$\mathrm{SpO_2} = a\rho^2 + b\rho + c, \tag{3.27}$$

with calibration coefficients a [%], b [%] and c [%], and ratio-of-ratios ρ [-]. The ratio-of-ratios was determined as

$$\rho = \left(AC_{\mathrm{rd}}/DC_{\mathrm{rd}}\right) / \left(AC_{\mathrm{ir}}/DC_{\mathrm{ir}}\right), \tag{3.28}$$

in which pulse magnitude AC [V] was the difference between the interpolated diastolic and systolic levels, pulse mean DC [V] was the average of $ppg_{\mathrm{bl}}[n]$ between the interpolated time instants of the diastolic and systolic points, and subscripts rd and ir refer to the red and near-IR PPG signal, respectively. An 0.1 change in ρ corresponded to a 3-4% change in $\mathrm{SpO_2}$.

We assessed the algorithm performance by the 10^{th} to 90^{th} percentile range of $\mathrm{SpO_2}$ during rest, walking, and after artifact reduction. We compared the median $\mathrm{SpO_2}$ obtained from (3.27) during rest and after artifact reduction to the median $\mathrm{SpO_2}$ obtained during rest with the commercial device. No beat-to-beat comparison was made, because of differences in circulation transit time from the lungs to the forehead and the finger, and because of low-pass filtering in the commercial device.

3.5 Results

3.5.1 Motion artifact references

Inspection of the spectrograms of the monitor diode signal showed that a frequency range of 15 kHz was insufficient for the Doppler signals measured for subjects 1 and 5 when walking at speeds of 7 and 8 km/h. In the other measurements, the 15 kHz Doppler frequency range was sufficient.

The relative sensor motion $\Delta x[n]$ and the head motion $a_v[n]$ are evaluated in Fig. 3.4 and Table 3.1. Figures 3.4a and 3.4b show the RMS-amplitudes of $\Delta x_{\mathrm{bpf}}[n]$ and $a_{v\_\mathrm{bpf}}[n]$, respectively, for each measurement during rest (dots) and walking (circles). Across the subjects, $a_{v\_\mathrm{bpf}}[n]$ behaved more consistently than $\Delta x_{\mathrm{bpf}}[n]$, and $a_{v\_\mathrm{bpf}}[n]$ had a better SNR than $\Delta x_{\mathrm{bpf}}[n]$. Table 3.1 quantifies the SNR as the ratio of the RMS-amplitudes during walking and rest. The average ratio was about 82 for $a_{v\_\mathrm{bpf}}[n]$, and about 6 for $\Delta x_{\mathrm{bpf}}[n]$.

Figures 3.4c and 3.4d show the mean (open triangle / square) and SD (filled triangle / square) of $df_{\mathrm{FLL}}[n]$ (3.15) for $\Delta x[n]$ and $a_v[n]$, respectively. These are smaller and more consistent for $a_v[n]$. Table 3.1 shows the SD of $f_{\mathrm{FLL}}[n]$. This is also smaller and more consistent for $a_v[n]$. The mean SD of $f_{\mathrm{FLL}}[n]$ was about 2 min^{-1} for $a_v[n]$ and about 17 min^{-1} for $\Delta x[n]$. The FLL thus tracked the step rate more steadily in $a_v[n]$ than in $\Delta x[n]$.

Figures 3.4e and 3.4f show the mean (open triangle / square) and SD (filled triangle / square) of $G[n]$ for $\Delta x[n]$ and $a_v[n]$, respectively. The mean was consistently about 1 for $a_v[n]$, whereas it fluctuated for $\Delta x[n]$. For $\Delta x[n]$, a decrease in mean and an increase in SD of $G[n]$ was due to unstable tracking of the step rate, as shown by an increase in $df_{\mathrm{FLL}}[n]$. In these cases, the most prominent spectral component over time in $\Delta x[n]$ did not occur at the step rate. Instead, the most prominent spectral component varied between the step rate and its (sub)harmonic, or the spectral activity was unstructured.

Table 3.1 also shows for $a_v[n]$ that subject 3 has an approximately twofold SD of $f_{\mathrm{FLL}}[n]$ compared to the other subjects, indicating a larger step rate variation for subject 3.

3.5.2 Motion artifact reduction

The time traces in Fig. 3.5 exemplify the effect of walking and artifact reduction on the PPG signal, IBIs, and SpO_2. Walking caused $ppg_{\mathrm{bpf}}[n]$ in Fig. 3.5a to vary periodically, where destructive interference by the artifact caused fading of the signal. The artifact estimate $ma_{\mathrm{est}}[n]$ in Fig. 3.5b was obtained via head motion $a_v[n]$. Subtracting $ma_{\mathrm{est}}[n]$ from $ppg_{\mathrm{bpf}}[n]$ gave the stable-amplitude artifact-reduced signal $ppg_{\mathrm{ar}}[n]$ in Fig. 3.5c. Figures 3.5d and 3.5e respectively show that the IBIs and SpO_2 derived from the motion-affected signals varied periodically (diamonds). The IBIs and SpO_2 after artifact reduction (squares) did not show this variation any longer, and were closer to the ECG-derived IBIs (crosses in

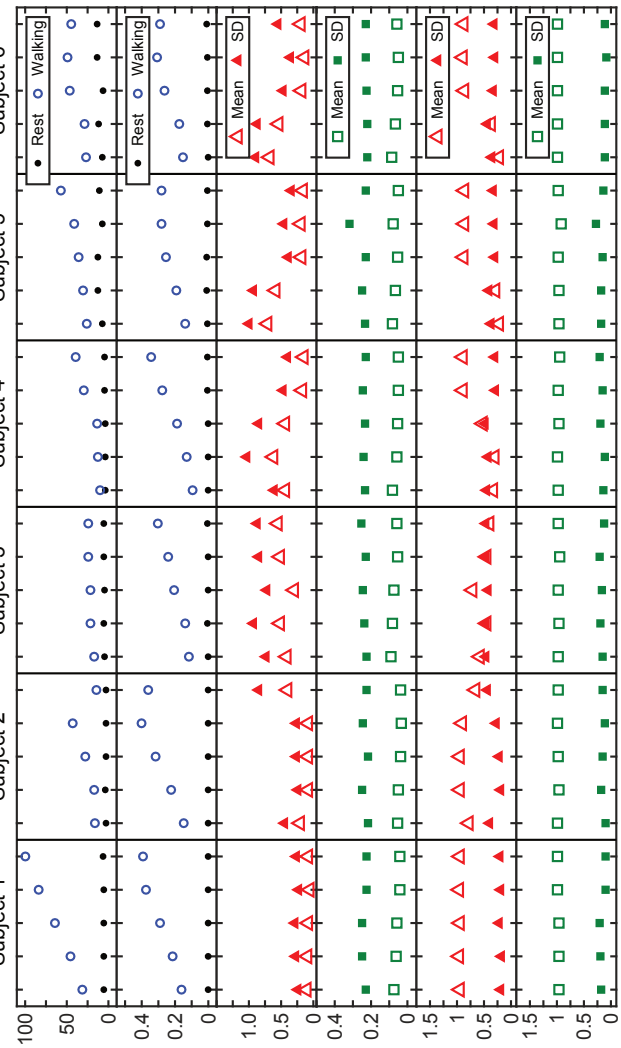

Figure 3.4: (a) RMS-amplitude of relative sensor motion $\Delta x_{\mathrm{bpf}}[n]$ during rest (dots) and walking (circles). (b) RMS-amplitude of head motion $a_{v\_\mathrm{bpf}}[n]$ during rest and walking. (c) Mean (open triangle) and SD (filled triangle) of FLL-frequency time-derivative $df_{\mathrm{FLL}}[n]$ during walking for $\Delta x[n]$. (d) Mean and SD of $df_{\mathrm{FLL}}[n]$ during walking for $a_v[n]$. (e) Mean and SD of gating function $G[n]$ during walking for $\Delta x[n]$. (f) Mean and SD of $G[n]$ during walking for $a_v[n]$. bpf: band-pass filtered; FLL: frequency-locked loop; RMS: root mean-square; SD: standard deviation.

Table 3.1: Evaluation of relative sensor motion Δx and head motion a_v.

	Measure	Subject 1	Subject 2	Subject 3	Subject 4	Subject 5	Subject 6	Average
Δx	RMS Δx_{bpf} walking/rest [-]	10.9±4.4	7.8±4.3	4.2±0.5	4.6±2.3	3.9±1.4	4.0±1.6	5.9±3.7
	SD f_{FLL} [min^{-1}]	1.3±0.1	10.5±12.6	29.7±5.5	23.4±11.7	16.4±11.3	19.6±9.7	16.8±12.7
a_v	RMS a_{v_bpf} walking/rest [-]	119.9±36.6	166.2±57.0	66.5±25.3	56.1±10.0	35.6±18.7	48.2±18.6	82.1±55.0
	SD f_{FLL} [min^{-1}]	1.2±0.1	1.4±0.6	4.7±1.9	2.0±1.4	1.7±0.7	2.7±1.1	2.3±1.6

Results in mean ± standard deviation. RMS walking/rest: ratio of the root mean-square amplitudes during walking and rest; SD f_{FLL}: standard deviation of the frequency tracked by the frequency-locked loop after the initial 10 s transient.

Table 3.2: Evaluation of motion artifact reduction using relative sensor motion Δx and head motion a_v.

	Measure	Subject 1	Subject 2	Subject 3	Subject 4	Subject 5	Subject 6	Average
Δx	ΔIBI 10-90 perc. [%]	-40±9	-51±14	2±16	4±21	-14±19	-18±23	-20±26
	ΔIBI vs rest [-]	2.8±0.4	2.6±0.8	2.5±0.4	1.1±0.2	1.5±0.3	3.5±0.7	2.3±0.9
	SpO_2 10-90 perc. [%]	-42±6	-52±16	-1±7	-5±20	-33±32	-16±14	-25±25
	SpO_2 vs rest [-]	1.3±0.2	1.3±0.2	1.6±0.3	1.0±0.2	1.4±0.3	1.7±0.2	1.4±0.3
a_v	ΔIBI 10-90 perc. [%]	-40±11	-59±13	-9±28	16±38	-22±11	-42±16	-26±32
	ΔIBI vs rest [-]	2.8±0.5	2.2±0.6	2.2±0.6	1.2±0.2	1.3±0.2	2.5±0.5	2.0±0.7
	SpO_2 10-90 perc. [%]	-43±7	-62±9	-9±12	-8±14	-51±14	-37±16	-35±24
	SpO_2 vs rest [-]	1.2±0.3	1.1±0.2	1.5±0.3	1.0±0.2	1.1±0.3	1.3±0.3	1.2±0.3

Results in mean ± standard deviation. ΔIBI / SpO_2 10-90 perc.: reduction in 10^{th} to 90^{th} percentile range of the IBI error / spread in SpO_2 achieved by artifact reduction; ΔIBI / SpO_2 vs rest: 10^{th} to 90^{th} percentile range of the IBI error / spread in SpO_2 after artifact reduction relative to this range at rest; IBI: inter-beat interval; SpO_2: oxygen saturation.

Fig. 3.5d) and commercial device SpO_2 (crosses in Fig. 3.5e), respectively. The exclusion of pulses with too small pulsatility (3.25) caused the gaps in the IBIs and SpO_2 before artifact reduction. After artifact reduction, no pulses were excluded in Figs. 3.5d and 3.5e.

The spectrograms in Fig. 3.6 further illustrate the effect of walking and artifact reduction. Figure 3.6a shows that step-rate-related frequency components appeared in $ppg_{\mathrm{bpf}}[n]$ during walking in addition to the PR related frequency components. The component at half the step rate was due to guiding the sensor wire behind the left ear, which caused pulling of the sensor each time the head turned right. Figure 3.6b shows that $ma_{\mathrm{est}}[n]$ captured all step-rate related components, with slight leakage of PR related components. Figure 3.6c shows that subtracting $ma_{\mathrm{est}}[n]$ from $ppg_{\mathrm{bpf}}[n]$ effectively removed the artifacts.

Figure 3.7 shows the effect of artifact reduction on pulse detection. It shows the percentage p_{A_rd} of candidate pulses in the red PPG signal which was associated with an R-peak before artifact reduction (diamonds), and after artifact reduction using $\Delta x[n]$ (triangles) and $a_v[n]$ (squares). For subject 1 at 5 and 6 km/h, subject 2 at all speeds, and subject 6 at 6-8 km/h, artifact reduction increased p_{A_rd} because the algorithm removed destructive interference by the artifact, so more pulses exceeded plt_{thr}. This effect is illustrated in Fig. 3.5. For subject 4 at all speeds, artifact reduction decreased p_{A_rd} because the algorithm partly removed cardiac pulses with a PR close to the step rate, so less pulses exceeded plt_{thr}. For subject 4 at 4-6 km/h, the decrease in p_{A_rd} was smaller for $\Delta x[n]$ than for $a_v[n]$, because $G[n]$ was less active for $\Delta x[n]$ than for $a_v[n]$ (Figs. 3.4e and 3.4f). For subject 1 at 4 km/h, subjects 3 and 5 at all speeds, and subject 6 at 4 km/h, artifact reduction affected p_{A_rd} little, because destructive interference was not pronounced, and step rate and PR were distinct. For subject 1 at 7 and 8 km/h, and subject 6 at 5 km/h, artifact reduction affected p_{A_rd} little, because the improvement by removal of destructive interference balanced the deterioration due to comparable step rate and PR. For subject 6 at 4 and 5 km/h, spurious detection of dicrotic notches lowered p_{A_rd} overall. Results were similar for the near-IR PPG signal.

Figure 3.8 gives an overview of ΔIBI for PPG signals at rest (R), with motion artifacts (M), and after artifact reduction using $\Delta x[n]$ and $a_v[n]$. The middle line is the median, the box extends from the 25^{th} to the 75^{th} percentile, and the whiskers from the 10^{th} to the 90^{th} percentile. Motion artifacts increased the spread in ΔIBI to various degrees. Motion hardly affected ΔIBI for subject 4, because step rate and PR were comparable. The percentages with Δx and a_v in Fig. 3.8 are the changes in the 10^{th} to the 90^{th} percentile range after artifact reduction compared to M. The numbers with Δx and a_v in Fig. 3.8 are the 10^{th} to the 90^{th} percentile ranges after artifact reduction divided by this range at R. Table 3.2 gives the averages. Artifact reduction reduced the spread in ΔIBI for subjects 1 and 2. For subject 1, artifact reduction was less at 7 and 8 km/h compared to 4-6 km/h, because step rate and PR partly coincided. For subject 2, a less active $G[n]$ for $\Delta x[n]$ at 4 and 8 km/h affected artifact reduction compared

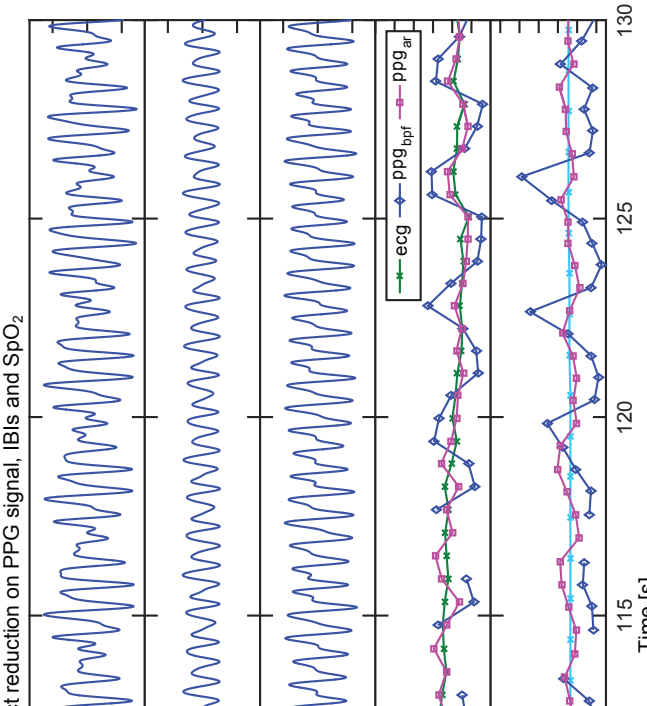

Figure 3.5: Example time-traces of the near-infrared PPG signal, IBIs, and SpO_2 from subject 6 while walking at 6 km/h. (a) Walking causes periodic variation in $ppg_{\mathrm{bpf}}[n]$. (b) Motion artifact estimate $ma_{\mathrm{est}}[n]$ obtained via head motion $a_v[n]$. (c) Artifact-reduced signal $ppg_{\mathrm{ar}}[n] = ppg_{\mathrm{bpf}}[n] - ma_{\mathrm{est}}[n]$. (d) IBIs from $ppg_{\mathrm{bpf}}[n]$ vary periodically (diamonds). IBIs from $ppg_{\mathrm{ar}}[n]$ (squares) are closer to ECG RRIs (crosses). (e) SpO_2 from $ppg_{\mathrm{bpf}}[n]$ varies periodically (diamonds). SpO_2 from $ppg_{\mathrm{ar}}[n]$ (squares) is closer to commercial device SpO_2 (crosses). Gaps in IBIs and SpO_2 for $ppg_{\mathrm{bpf}}[n]$ are excluded pulses with too small pulsatility. ECG: electrocardiography; IBI: inter-beat interval; PPG: photoplethysmography; RRI: R-peak to R-peak interval; SpO_2: oxygen saturation.

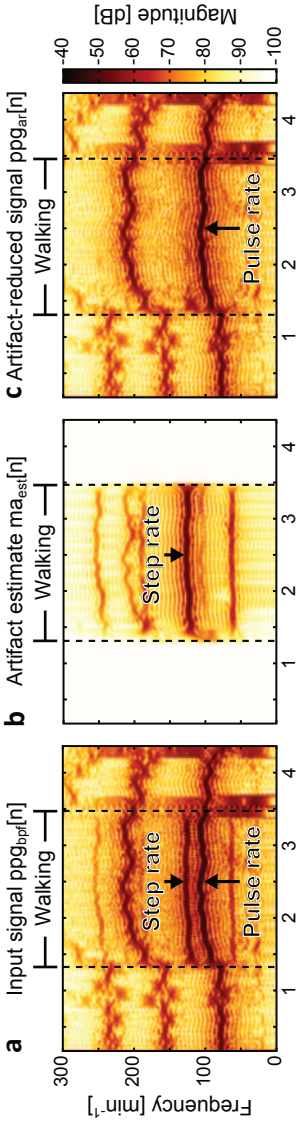

Figure 3.6: Example spectrograms of the near-infrared PPG signal from subject 6 while walking at 6 km/h. (a) The measured PPG signal $ppg_{\mathrm{bpf}}[n]$ contains artifacts at step-rate related frequencies during walking. (b) The artifact estimate $ma_{\mathrm{est}}[n]$ contains all step-rate related frequency components. (c) Subtracting $ma_{\mathrm{est}}[n]$ from $ppg_{\mathrm{bpf}}[n]$ effectively removes the motion artifacts in $ppg_{\mathrm{ar}}[n]$. PPG: photoplethysmography.

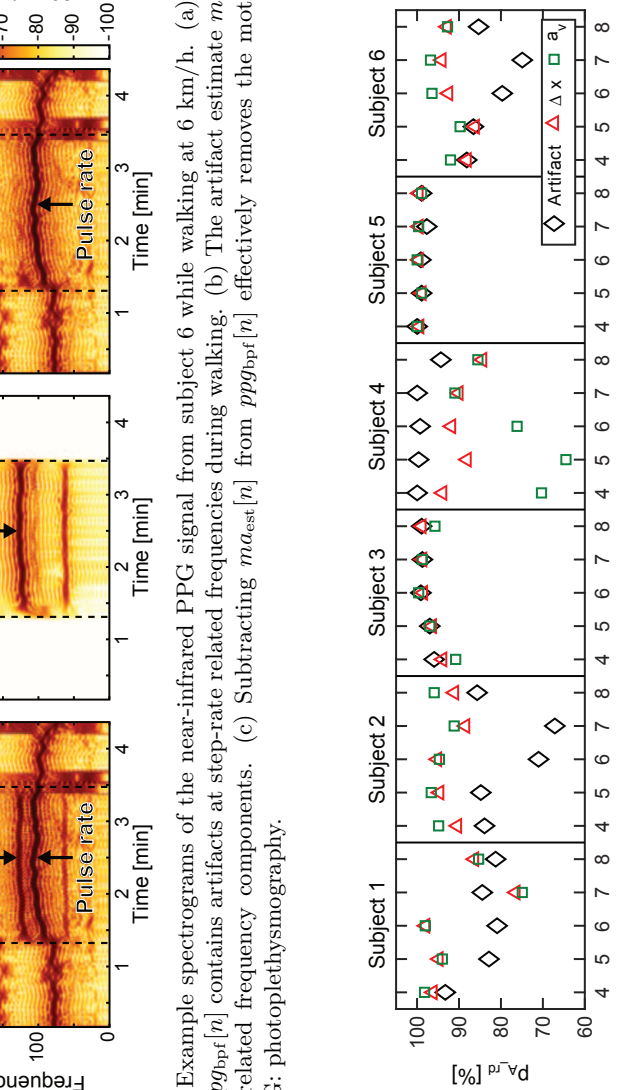

Figure 3.7: Percentage of candidate pulses in the red PPG signal which is associated with an R-peak. The percentages were determined in the walking intervals before artifact reduction (diamonds), and after artifact reduction using relative sensor motion $\Delta x[n]$ (triangles) and head motion $a_v[n]$ (squares). Results were similar for the near-infrared PPG signal. PPG: photoplethysmography.

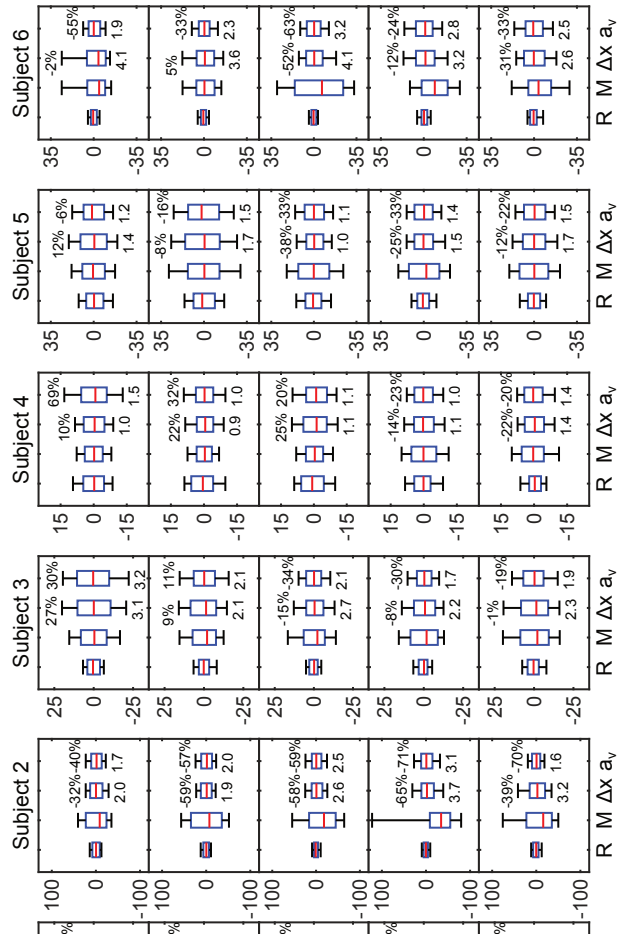

Figure 3.8: ΔIBIs from near-infrared PPG signals at rest (R), with motion artifacts (M), and after artifact reduction using relative sensor motion (Δx) and head motion (a_v). From top to bottom, walking speed increases from 4 to 8 km/h. The middle line is the median, the box extends from the 25^{th} to the 75^{th} percentile, and the whiskers from the 10^{th} to the 90^{th} percentile. The percentages with Δx and a_v are the changes in the whisker range after artifact reduction compared to this range at M. The numbers with Δx and a_v are the ratios of the whisker ranges after artifact reduction and at R. IBI = inter-beat interval; PPG: photoplethysmography.

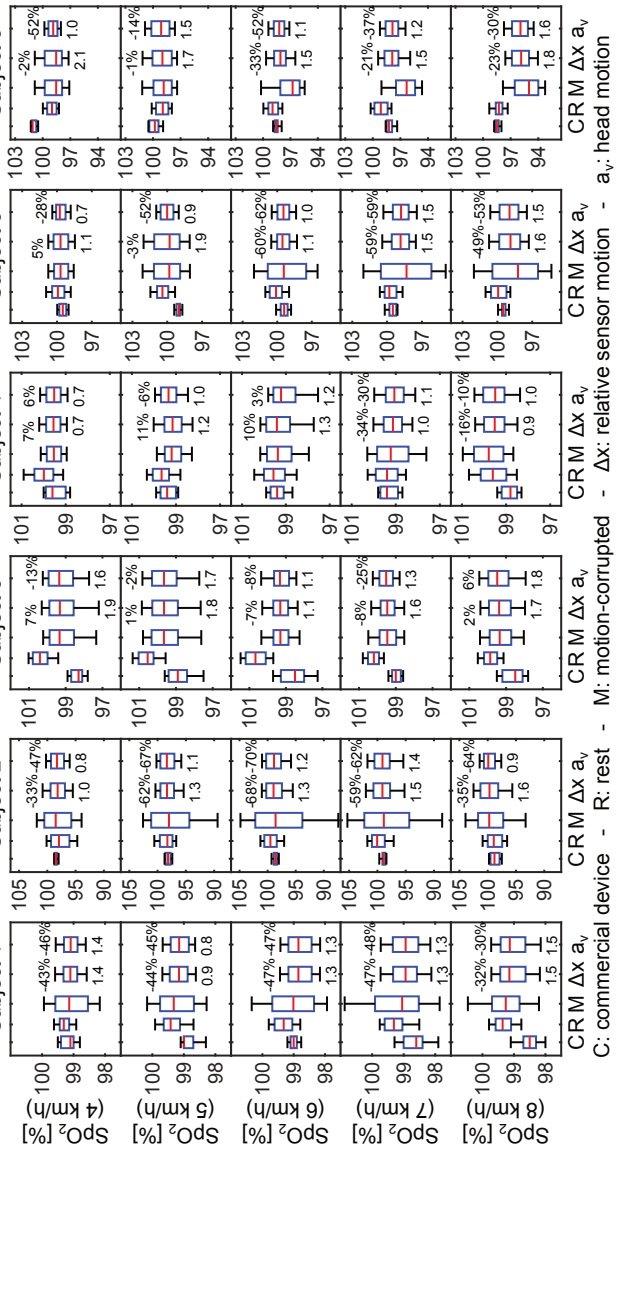

Figure 3.9: SpO_2 from the commercial device at rest (C), and from red and near-infrared PPG signals at rest (R), with motion artifacts (M), and after artifact reduction using relative sensor motion (Δx) and head motion (a_v). From top to bottom, walking speed increases from 4 to 8 km/h. The middle line is the median, the box extends from the 25^{th} to the 75^{th} percentile, and the whiskers from the 10^{th} to the 90^{th} percentile. The percentages with Δx and a_v are the changes in the whisker range after artifact reduction compared to this range at M. The numbers with Δx and a_v are the ratios of the whisker ranges after artifact reduction and at R. PPG: photoplethysmography; SpO_2: oxygen saturation.

to 5-7 km/h (Fig. 3.4e). For subject 3, using $\Delta x[n]$ reduced ΔIBI by at most 15% at 6 km/h. The poor quality of $\Delta x[n]$ hampered tracking of the step rate, as shown by $df_{\mathrm{FLL}}[n]$ and $G[n]$ in Figs. 3.4c and 3.4e, respectively. Using $a_v[n]$ only improved ΔIBI at 6-8 km/h. The larger step-rate variation of subject 3 presumably affected the artifact reduction (Table 3.1). For subject 4 at 4-6 km/h, ΔIBI increased after artifact reduction, because of coinciding step rate and PR. At 7 and 8 km/h, some reduction in ΔIBI was achieved, because step rate and PR coincided less during walking. For subjects 5 and 6, reduction in ΔIBI was achieved at 6-8 km/h for $\Delta x[n]$, and at all speeds for $a_v[n]$. At 4 and 5 km/h, improvement in ΔIBI was affected by a poor quality of $\Delta x[n]$, which hampered tracking of the step rate, as shown by $df_{\mathrm{FLL}}[n]$ and $G[n]$ in Figs. 3.4c and 3.4e, respectively. The 10^{th} to 90^{th} percentile range of ΔIBI after artifact reduction was mostly 1 to 3 times this range at rest.

Figure 3.9 gives an overview of the spread in SpO_2 measured by the commercial device during rest (C), and derived from the PPG signals at rest (R), with motion artifacts (M), and after artifact reduction (Δx and a_v). The ranges and numbers shown in Fig. 3.9 are obtained in the same way as in Fig. 3.8. Table 3.2 gives the averages. For subject 2, the 10^{th} to 90^{th} percentile range of SpO_2 obtained via (3.27) was about 4-5% at rest, whereas this was about 1-2% for the other subjects. This was caused by the lower SNR of the PPG signals of subject 2. Motion increased the spread in SpO_2 to various degrees. Artifact reduction decreased the spread in SpO_2 for subjects 1 and 2. For subject 1, step rate and PR partly coincided at 7 and 8 km/h, but only at 8 km/h artifact reduction was affected. For subject 2, a less active $G[n]$ for $\Delta x[n]$ at 4 and 8 km/h affected artifact reduction compared to 5-7 km/h (Fig. 3.4e). For subject 3, spread in SpO_2 was only slightly reduced at 6 and 7 km/h for $\Delta x[n]$. The poor quality of $\Delta x[n]$ hampered tracking of the step rate, as shown by $df_{\mathrm{FLL}}[n]$ and $G[n]$ in Figs. 3.4c and 3.4e, respectively. For $a_v[n]$, a relatively small reduction of the spread in SpO_2 was achieved at 4-7 km/h. The irregular step rate of subject 3 presumably affected the reduction of the spread in SpO_2 (Table 3.1). For subject 4 at 4-6 km/h, the coinciding step rate and PR hampered artifact reduction for $\Delta x[n]$ and $a_v[n]$. At 7 and 8 km/h, some reduction of the spread in SpO_2 was achieved, because step rate and PR coincided less during walking. For subjects 5 and 6, reduction of the spread in SpO_2 was achieved at 6-8 km/h for $\Delta x[n]$, and at all speeds for $a_v[n]$. At 4 and 5 km/h, reduction of the spread in SpO_2 was affected by a poor quality of $\Delta x[n]$, which hampered tracking of the step rate, as shown by $df_{\mathrm{FLL}}[n]$ and $G[n]$ in Figs. 3.4c and 3.4e, respectively. The 10^{th} to 90^{th} percentile range of SpO_2 after artifact reduction was mostly 1 to 2 times the range at rest. The median SpO_2 obtained via (3.27) at rest and after artifact reduction did not differ more than 2.6% from the median SpO_2 measured by the commercial device at rest.

3.6 Discussion

We developed a generic algorithm to remove periodic motion artifacts from PPG signals (Fig. 3.2). The algorithm recovered an artifact-reduced PPG signal for further time-domain beat-to-beat analysis in addition to, e.g., spectral analysis. We described the motion artifact using a quadrature basis so only two coefficients are needed per frequency component and the artifact estimate contains no undesired frequency-shifted components [56, 193]. These advantages are not offered by approaches directly estimating FIR filter coefficients [56, 193]. We retrospectively evaluated the algorithm on forehead PPG signals which were measured on healthy volunteers while they were walking on a treadmill (Fig. 3.1a). As motion references we compared sensor motion relative to the skin, $\Delta x[n]$, measured via SMI, and head motion, $a_v[n]$, measured with an accelerometer (Fig. 3.1b). We used a SOGI-based structure with an FLL to track the step rate in the reference signals (Fig. 3.3). We showed that $a_v[n]$ had a better SNR than $\Delta x[n]$, and that the FLL tracked the step rate more consistently in $a_v[n]$ than in $\Delta x[n]$ (Fig. 3.4 and Table 3.1). Therefore, $a_v[n]$ outperformed $\Delta x[n]$ as motion reference. The FLL frequency was used in a quadrature harmonic model to describe the motion artifact (3.14). An LMS algorithm estimated the amplitudes of the quadrature components. Subtracting the artifact estimate from the measured PPG signal effectively reduced the artifact in the resulting artifact-reduced PPG signal, $ppg_{\mathrm{ar}}[n]$ (Figs. 3.5 and 3.6). When the step rate was stable and different than the PR, the proposed algorithm reduced ΔIBI and the spread in SpO_2 by 30-70% (Figs. 3.8 and 3.9, and Table 3.2). When step rate and PR were comparable, the algorithm partly removed cardiac pulses too. This was detected by thresholding the magnitude of the baseline-normalized pulses in the artifact-reduced PPG signal, to exclude too small pulses for further analysis (Fig. 3.7).

Degradation of the algorithm performance occurred in three occasions. Motion artifacts were removed to a lesser extent when, firstly, a low-quality motion reference signal hampered tracking of the step rate or, secondly, the step rate varied faster than the algorithm could track. Thirdly, cardiac pulses were partly removed when step rate and PR were comparable. However, when the step rate was stable and distinct from the PR, and the motion reference signal consistently contained a component at the step rate, the proposed algorithm considerably reduced ΔIBI and the spread in SpO_2. Therefore, the proposed algorithm can facilitate analysis of IBIs and SpO_2 during periodic motion in, e.g., ADL, sports, CPX, or CPR. Coinciding motion frequency and PR can furthermore be identified when pulses in the artifact-reduced PPG signal become too small.

The relative sensor motion $\Delta x[n]$ was not a stable motion reference signal. The FLL did not steadily track the step rate in $\Delta x[n]$ in 14 out of 30 measurements (Fig. 3.4). This may indicate limited relative sensor motion in these cases. Poor quality of the signal $\Delta x[n]$ may also result from insufficient optical feedback into the laser diode due to a sub-optimal focal distance of the ball lens. However, Fig. 3.4e shows that for subjects 4, 5 and 6 the step rate could be tracked in

$\Delta x[n]$ at higher speeds of walking, but not at lower speeds of walking. This may indicate that there was sufficient optical feedback at lower speeds of walking, but that the relative sensor motion was limited. On the other hand, the actual movement of the sensor presumably depends on the impact of the feet on the treadmill and therefore on the speed of walking. The actual movement of the sensor may also influence the amount of optical feedback. This prevents drawing a solid conclusion, although it is plausible that relative sensor motion indeed was limited when the step rate could not be tracked in $\Delta x[n]$. Because the accelerometry-derived reference signal outperformed the SMI-derived reference signal, we recommend the use of an accelerometer to generate a motion reference for (quasi-)periodic motion.

After successful artifact reduction, the spread in ΔIBI was larger compared to measurements at rest (Fig. 3.8 and Table 3.2). This may result from residual motion artifacts, or from physiological fluctuations in IBIs during walking caused by variations in pre-ejection time and pulse transit time [159]. Inaccuracies in the ECG signal during walking may also contribute, resulting from electrode-skin motion, and the electromyogram [190].

The spread in SpO_2 after artifact reduction was about 1 to 2 times the spread at rest, and was therefore smaller than the spread in ΔIBI after artifact reduction, which was about 1 to 3 times the spread at rest (Figs. 3.8 and 3.9, and Table 3.2). This is presumably caused by the different nature of the performance measures. We only considered the spread in SpO_2 without direct comparison to a reference, and we therefore do not have a measure of the SpO_2 accuracy. In contrast, ΔIBI was a beat-to-beat comparison of IBIs and ECG-derived RRIs. Consequently, although the spread in SpO_2 after artifact reduction is more comparable to the spread at rest, this does not indicate a better performance for SpO_2 than for IBIs.

The proposed solution has some limitations. The algorithm can only deal with slowly-varying periodic motion artifacts. When the motion frequency and PR coincide, no improvement can be obtained. In a real-world application, an additional algorithm may be required which first assesses presence and periodicity of motion to determine whether the proposed algorithm should be initiated. Furthermore, a limited number of measurements have been performed on a limited number of subjects, resulting in only a preliminary validation of the algorithm. Also, the periodic motion artifacts generated on the treadmill may be more periodic than encountered in ADL. SpO_2 accuracy has not been assessed. Only the variation in SpO_2 has been quantified, assuming a relatively constant SpO_2 for healthy subjects.

3.7 Conclusions

The proposed generic algorithm can effectively remove periodic motion artifacts from PPG signals measured while walking on a treadmill. A SOGI-based structure with an FLL can track the step rate in a motion reference signal. An accelerometry-derived motion reference signal outperforms an SMI-derived motion reference signal, which measures sensor motion relative to the skin. This may have been the result of limited relative sensor motion in a number of measurements. Periodic motion artifacts can be described by a harmonic model of quadrature components with frequencies related to the tracked step rate. Subtracting the harmonic model from the measured PPG signal effectively removes the motion artifacts. More stable IBI and SpO_2 measurements can be derived from the resulting artifact-reduced PPG signals if the step rate and PR are distinct. If step rate and PR are comparable, also cardiac pulses are partly removed, which can be detected by thresholding the magnitude of the baseline-normalized pulses in the artifact-reduced PPG signal.

Part II

Photoplethysmography

in cardiopulmonary resuscitation

CHAPTER 4

Detection of a spontaneous pulse via photoplethysmography during pre-clinical automated cardiopulmonary resuscitation

This chapter is based on

R.W.C.G.R. Wijshoff, T. van der Sar, W.H. Peeters, R. Bezemer, P. Aelen, I.W.F. Paulussen, S.C.M.A. Ordelman, A. Venema, P.F.J. van Berkom, R.M. Aarts, P.H. Woerlee, G.-J. Scheffer, and G.J. Noordergraaf, "Detection of a spontaneous pulse in photoplethysmograms during automated cardiopulmonary resuscitation in a porcine model," *Resuscitation*, vol. 84, no. 11, pp. 1625-1632, Nov. 2013.

Abstract

Introduction: Reliable, non-invasive detection of return of spontaneous circulation (ROSC) with minimal interruptions to chest compressions would be valuable for high-quality cardiopulmonary resuscitation (CPR). Our objective was to determine the potential of photoplethysmography (PPG) to detect the presence of a spontaneous pulse during automated CPR in an animal study.

Methods: Twelve anesthetized pigs were instrumented to monitor circulatory and respiratory parameters. Here we present the simultaneously recorded PPG and arterial blood pressure (ABP) signals. Ventricular fibrillation was induced, followed by twenty minutes of automated CPR and subsequent defibrillation. After defibrillation, pediatric-guidelines-style life support was given in cycles of two minutes. PPG and ABP waveforms were recorded during all stages of the protocol. Raw PPG waveforms were acquired with a custom-built photoplethysmograph controlling a commercial reflectance pulse oximetry probe attached to the nose. ABP was measured in the aorta. PPG and ABP signals were retrospectively visually analyzed in the time and frequency domains for the presence of a spontaneous pulse.

Results: In nine animals ROSC was achieved. Throughout the protocol, PPG and ABP frequency content showed strong resemblance. We demonstrate that (1) the PPG waveform allows for the detection of a spontaneous pulse during ventilation pauses, and that (2) frequency analysis of the PPG waveform allows for the detection of a spontaneous pulse and the determination of the pulse rate, even during ongoing chest compressions, if the pulse and compression rates are sufficiently distinct.

Conclusions: These results demonstrate the potential of PPG as a non-invasive means to detect pulse presence or absence, as well as pulse rate during CPR. PPG may therefore potentially support clinicians in detecting ROSC.

4.1 Introduction

High-quality cardiopulmonary resuscitation (CPR) requires minimizing interruptions to chest compressions [41, 120]. Pulse checks, even during potentially perfusing rhythms, may lead to prolonged interruptions which can negatively impact outcome [21, 30, 36, 204]. In particular, manual palpation can be time-consuming and is known to be unreliable even if performed by expert clinicians [43,113,129,178]. Therefore, a rapid, objective method to detect the return of spontaneous circulation (ROSC) would be a valuable asset.

Monitoring of end-tidal CO_2 [39,60,69,139], invasive blood pressure [133,151], or central venous oxygen saturation [150] allows for a more objective assessment of ROSC, but requires a secured airway or placement of catheters. Transthoracic impedance (TTI) measurements [100, 149, 172] and near-infrared spectroscopy (NIRS) [8, 79, 117, 134, 148, 160] are non-invasive, but TTI is strongly influenced by chest compressions [100, 149, 172] and NIRS may respond slowly upon ROSC [8, 117, 148, 160]. Doppler ultrasound is being researched as a non-invasive method to detect pulse absence and presence in the carotid artery, but this technique is sensitive to a correct placement over the carotid artery and is strongly influenced by chest compressions [89, 213]. Despite the challenges, and even though determining whether an observed rhythm is life-supporting remains a clinical, situational assessment, such techniques can provide valuable support.

CPR guidelines mention the potential of photoplethysmography (PPG) to support ROSC detection [120]. A PPG sensor, such as the well-known finger clip commonly used to monitor arterial oxygen saturation, measures transmission of light through tissue to detect cardiac-induced pulses in tissue blood volume [191]. PPG is generally an easy-to-use and non-invasive technique to measure spontaneous pulse and other hemodynamic parameters [10,146,163,191], but using PPG to detect spontaneous pulse during CPR is not common clinical practice [208]. Interpretation of the PPG signal can be compromised by low perfusion, temperature effects, delays by signal processing, and motion artifacts [112, 120, 171]. It may also be difficult to determine if pulses in the PPG signal should be attributed to chest compressions or to spontaneous cardiac activity [112].

In this study, we investigated the potential of PPG to detect the presence and rate of a spontaneous pulse during CPR. We retrospectively analyzed PPG and arterial blood pressure (ABP) signals, simultaneously recorded in pigs undergoing automated CPR. PPG-based detection of a spontaneous pulse during CPR is a first step towards determining the potential use of PPG to support ROSC detection.

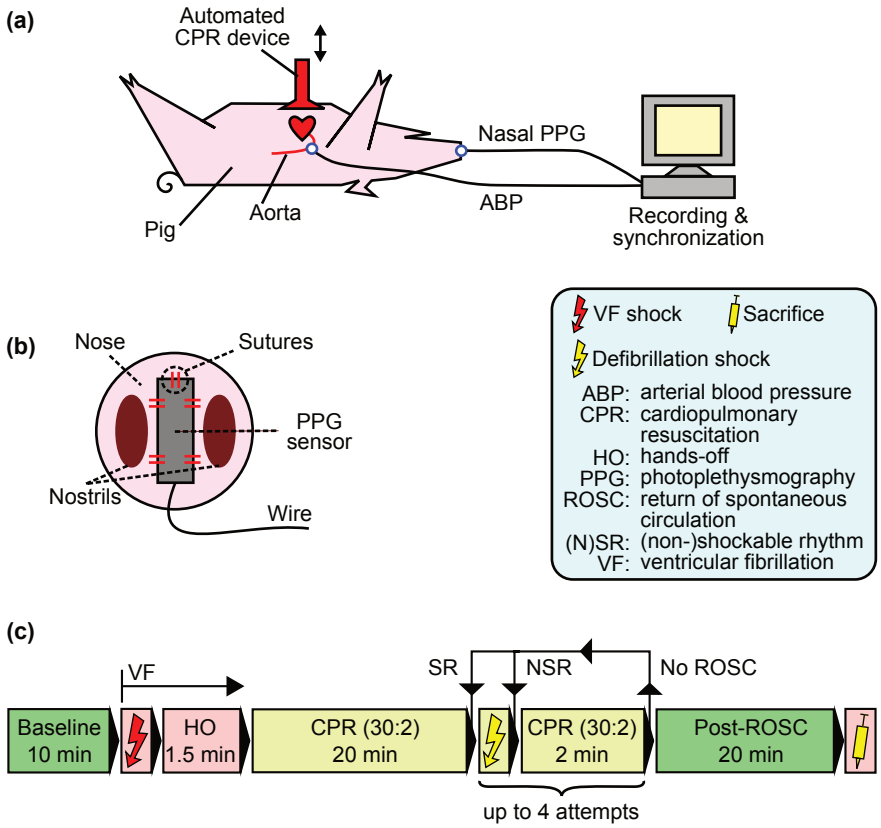

Figure 4.1: Simultaneous acquisition of PPG and ABP waveforms during automated CPR in a pig model. (a) Experimental setting. PPG signals have been acquired from the nose. ABP has been measured in the thoracic aorta using a Millar catheter. (b) Attachment of the PPG sensor to the nose. (c) Summary of the experimental protocol. See text for further details. ABP: arterial blood pressure; CPR: cardiopulmonary resuscitation; PPG: photoplethysmography.

4.2 Methods

4.2.1 Study design

An automated-CPR animal study was conducted on 16 pathogen-free female Yorkshire pigs, with an average age of 10.7 weeks (range 7-12 weeks) and an average weight of 30 kg (range 25-36 kg) (Fig. 4.1a). All animals received care in compliance with the Dutch Animal Experimentation Law and the Standard Operation Procedures of the Central Animal Laboratory of the Radboud University Nijmegen Medical Center, where the experiments were conducted. The Radboud

University Animal Ethical Committee approved the protocol[1]. The experiments were designed and executed using the Utstein-style guidelines [75]. PPG-based detection of a spontaneous pulse during CPR was a secondary objective of the animal experiments, which were designed to study characteristics of automated CPR and their relationship to ROSC as primary objective. Only data pertinent to the PPG study are reported here.

PA, IP, SO, PW, and GN designed the experiments for the primary objective of the study, and determined the study protocol and the number of animals involved in the study. PPG measurements were added to these experiments for the secondary objective, which extended the amount of useful data obtainable from this study.

4.2.2 Anesthesia and management

Animals received intramuscular (IM) premedication with ketamine (10 mg/kg), midazolam (1 mg/kg), and atropine (50 μg/kg). After intravenous (IV) access was gained, propofol (2-3 mg/kg) was administered, and the animals were orally intubated and moved to the operating table. Anesthesia was maintained with isoflurane (0.5-1% end-tidal) via a SmartVent 7900 Anesthesia Ventilator (Datex-Ohmeda, Finland), and by IV infusions of midazolam (0.6 mg/kg/hr), sufentanyl (5 μg/kg and 10 μg/kg/hr), and vecuronium (0.2 mg/kg and 0.4 mg/kg/hr). Amoxicilline (20 mg/kg) was administered IV.

Animals were ventilated through a bacteria-virus filter using an FiO_2 of 0.4 and 6-7 cmH_2O PEEP, with tidal volumes of 275-300 mL at a rate of about 20 min^{-1} to achieve end-tidal CO_2 partial pressures of 30-40 mmHg. Five minutes before induction of cardiac arrest, FiO_2 was increased to 1.0. Following cardiac arrest, ventilation was continued manually with an FiO_2 of 1.0 via a pediatric 500 mL self-inflating bag, without isoflurane, and sufentanyl infusion was stopped.

During instrumentation, warm normal saline (0.9% NaCl) was administered to maintain a mean right-atrial pressure of 6-10 mmHg. Blood loss was compensated for by IV boli of Voluven. Temperature was controlled with a water-filled mattress. Euthanasia was performed with 500 mg pentobarbital (IV bolus).

4.2.3 Instrumentation and monitoring

Instrumentation and monitoring was performed once the animal was installed on the operating table. End-tidal CO_2 partial pressure, and airway pressure, flow and volume were monitored using spirometry (IntelliVue MP50 Patient Monitor, Philips, Andover, MA, USA). Via cutdown, a 20 G 16 cm cannula was placed in the left ileo-femoral artery for sampling purposes. Mikro-Tip® Pressure Catheters (Model SPC-360S, Millar Instruments, Houston, TX, USA) connected to a PCU-2000 Pressure Control Unit (Millar Instruments, Houston, TX, USA) were placed

[1]Protocol number of the Animal Ethical Committee of the Radboud University Nijmegen Medical Center: RU-DEC 2011-188.

via the right femoral artery and vein, such that their tips lay just distal to the aortic arch (to measure arterial blood pressure, ABP) and in the inferior vena cava just proximal to the right atrium (to measure central venous pressure), respectively. Via cutdown to the right internal jugular vein, a Swan-Ganz catheter (Edwards Lifesciences, Irvine, CA, USA) was positioned in the pulmonary artery such that wedge was achieved. A flow sensor (Transonic® Animal Research Flowmeter T206, Transonic Systems Inc., Ithaca, NY, USA) was placed around the right common carotid artery. Catheter positions were confirmed by visual inspection at autopsy.

Raw red (660 nm) and near-infrared (900 nm) PPG signals were obtained using a forehead reflectance pulse oximetry probe (Nellcor™ Oxisensor II RS-10, Covidien-Nellcor™, Dublin, Ireland), controlled by a custom-built photoplethysmograph. The probe was customized to enable placement by suturing between the nostrils (Fig. 4.1b), because it is a relatively stable measurement site in terms of motion, and it allows tight fixation of the probe to the skin.

PPG and ABP waveforms were recorded simultaneously using a 16-bit digital data acquisition card (DAQ) (NI USB-6259, National Instruments, Austin, TX, USA). A LabVIEW® (National Instruments, Austin, TX, USA) program controlled the DAQ.

4.2.4 Experimental protocol

The experimental protocol is outlined in Fig. 4.1c. After instrumentation, a ten minute baseline period, including blood gas analysis, documented the physiological condition of the animal. Subsequently, cardiac arrest was induced with a trans-thoracic electrical shock (90 V, 50 Hz for 3 s, using a proprietary fibrillation device), followed by a 90 s hands-off period. CPR was then performed for twenty minutes, using a rhythm of thirty compressions alternated by two ventilations (30:2 ratio). Chest compressions were delivered by a LUCAS™2 Chest Compression System [173] (Physio-Control Inc. / Jolife AB, Lund, Sweden) or by a custom-built automated CPR device, which was randomly assigned. The compression rate was 100 min^{-1}, and the ventilation pause lasted 3.8 s. No vasoactive medication was given during this period. After twenty minutes of CPR, rhythm analysis was performed and defibrillation attempted at 4 J/kg if appropriate, using the HeartStart MRx Monitor/Defibrillator (Philips, Andover, MA, USA) with Adult Plus Multifunction Electrode Pads M3713A (Philips, Andover, MA, USA). CPR was then immediately reinstituted for two minutes, after which the next rhythm analysis and pulse check were performed. If ROSC was diagnosed, CPR was stopped. If ROSC was not achieved, up to three additional two-minute cycles were performed. Starting after the first rhythm analysis, pediatric advanced life-support guidelines were used for medication, volume management, and critical care interventions [84]. Infusion of sufentanyl was also restarted. Measurements were continued up to twenty minutes post-ROSC. After that, or if ROSC was not

achieved after four two-minute cycles, the experiment was ended, the animal was euthanized, and an autopsy was performed.

Blood gases were analyzed from samples drawn simultaneously from the left femoral artery and the right atrium. Blood samples were drawn after five minutes of baseline, at the beginning and end of CPR, two minutes after a second and fourth defibrillation attempt, and at the beginning and end of the post-ROSC period. Samples were analyzed on-site via two i-STAT® Blood Gas Analyzers (Abbott Point of Care Inc., Princeton, NJ, USA).

4.2.5 Data analysis

The PPG signal, reported in Volt, is proportional to the detected light intensity, i.e., an increase in blood volume in the sampled tissue results in a decrease in the PPG signal. The PPG signal was limited in frequency to 11 Hz to reduce the influence of noise. Only the near-infrared PPG signal has been analyzed, because it had a better signal-to-noise ratio than the red PPG signal [66].

Both PPG and ABP signals were analyzed retrospectively with special interest in the period before and after ROSC. The PPG time traces were analyzed to detect the presence of a spontaneous cardiac pulse. The observations were validated by comparing the PPG signal to the ABP signal. Furthermore, to gain more insight in the origin of the signals, spectrograms were plotted, which show which frequencies are present in the signals as a function of time. These spectrograms were obtained via Fourier transformation of consecutive segments of the time traces.

4.3 Results

We used PPG and ABP data from 12 out of 16 animals. PPG signals from the first four animals were excluded because of interference between the study probe and the clinical saturation probes. This was resolved by increasing the distance between the probes. Table 4.1 presents baseline and CPR data of the 12 animals included in our analysis, and the post-ROSC data of the nine animals with ROSC in this group.

4.3.1 Spontaneous pulse during ventilation pauses

Figure 4.2 illustrates the different morphologies of the PPG and ABP signals during the CPR protocol. During baseline, cardiac pulses were visible in the PPG and ABP waveforms (Fig. 4.2a). After induction of cardiac arrest, automated chest compressions caused oscillations in PPG and ABP signals (Fig. 4.2b), and no spontaneous pulsations could be observed consistent with persisting cardiac arrest. Following successful defibrillation, subsequent ventilation pauses showed spontaneous pulses at an increasing rate (Fig. 4.2c).

Table 4.1: Physiological variables of the 12 animals included in the study. Pulse rate, arterial blood pressure, and end-tidal CO_2 were determined during the last thirty seconds of baseline, 20 minutes CPR, and 20 minutes post-ROSC.

	Baseline (12 animals)				20 minutes CPR (12 animals)				20 minutes post-ROSC (9 animals)			
	Mean	SD	Min	Max	Mean	SD	Min	Max	Mean	SD	Min	Max
PR [BPM]	93	17	64	124	-	-	-	-	113	19	86	155
ABP [mmHg]												
Mean	107	10	97	132	33	7	24	46	93	23	64	124
Systolic	122	14	109	157	59	16	36	89	102	25	69	135
Diastolic	94	10	80	114	18	6	10	31	84	21	58	114
Arterial blood												
PaO_2 [kPa]	60	17	27	77	22	17	8	54	48	17	19	70
$PaCO_2$ [kPa]	6	0.3	5	6	8	2	5	11	7	0.5	6	7
pH	7.50	0.04	7.44	7.60	7.22	0.09	7.12	7.39	7.34	0.06	7.22	7.41
Lactate [mmol/L]	0.8	0.4	0.4	1.8	5	2	3	8	4	1	3	5
Hb [mmol/L]	4	0.6	3	5	-	-	-	-	5	0.7	4	6
SaO_2 [%]	100	0	100	100	94	6	83	100	100	0	99	100
Venous blood												
PvO_2 [kPa]	11	6	5	29	3	0.4	3	4	7	2	6	12
$PvCO_2$ [kPa]	6	0.8	4	7	10	1	8	12	8	0.8	6	9
pH	7.44	0.03	7.38	7.50	7.19	0.05	7.10	7.29	7.26	0.05	7.17	7.32
Lactate [mmol/L]	0.8	0.4	0.4	2	4	1	3	6	4	1	3	6
SvO_2 [%]	91	8	72	100	30	7	18	39	73	26	8	96
$ETCO_2$ [mmHg]	38	2	35	43	39	8	27	48	41	3	36	45

ABP: arterial blood pressure; BPM: beats per minute; CPR: cardiopulmonary resuscitation; $ETCO_2$: end-tidal CO_2; Max: maximum; Min: minimum; PR: pulse rate; ROSC: return of spontaneous circulation; SD: standard deviation. Arterial blood pressure was measured with a Millar catheter in the thoracic aorta. Units are indicated in square brackets.

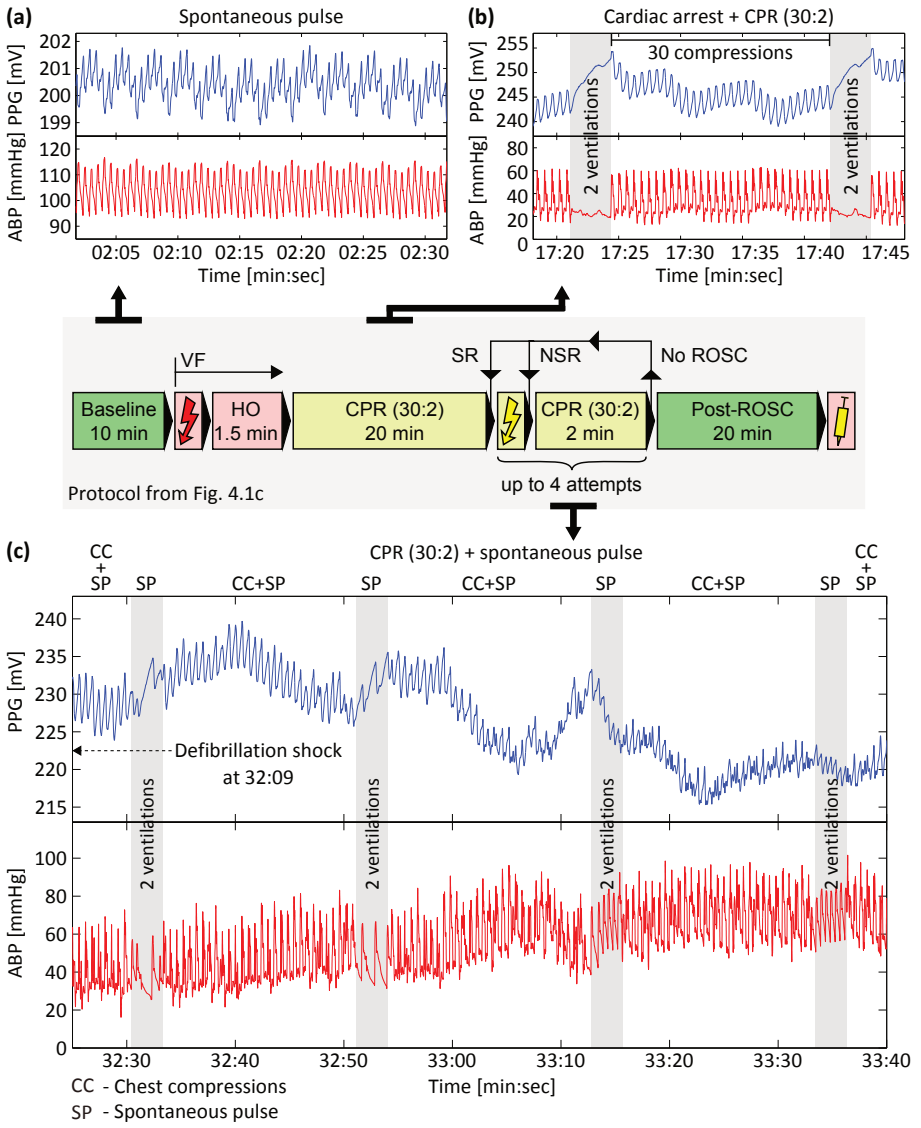

Figure 4.2: Distinct morphologies of the PPG and ABP waveforms during different stages of the experiment. (a) Baseline. PPG and ABP waveforms show a spontaneous pulse rate of approximately 110 beats per minute. Continuous ventilation causes slow variations in the baseline of both PPG and ABP waveforms. (b) CPR during cardiac arrest (ventricular fibrillation). (c) CPR after defibrillation. Traces start 16 s after the shock. As early as the first ventilation pause following successful defibrillation, spontaneous cardiac output can be seen in both PPG and ABP waveforms. This is the same animal (R1) as in Fig. 4.3 and Fig. 4.4d. ABP: arterial blood pressure; CPR: cardiopulmonary resuscitation; PPG: photoplethysmography.

4.3.2 Spontaneous pulse during chest compressions

After successful defibrillation, increasing irregularity could be observed in the PPG waveform resulting from the influence of both chest compressions and spontaneous cardiac output (Fig. 4.2c). Spectrograms of the PPG and ABP signals show the chest compressions at a rate of 100 min^{-1} before and after defibrillation (Fig. 4.3). In addition, after defibrillation, a disorganized spectral activity appeared, filling the frequency band from 0 to 200 min^{-1}. About one minute after the shock, a distinct spectral component appeared at about 125 min^{-1}, increasing to about 140 min^{-1}, and continuing when compressions were stopped. In this controlled setting, this component could only be a spontaneous pulse.

For all 12 animals, the PPG and ABP frequency spectra showed strong resemblance (Fig. 4.4). For animals without return of spontaneous pulse, the spectra only contained components due to the automated chest compressions (Fig. 4.4a-4.4c). For animals with ROSC, the spontaneous pulse resulted in one or more additional components in the spectra (Fig. 4.4d-4.4l). The pulse rate could be readily identified in the frequency spectra in eight out of nine cases. In Fig. 4.4f, the pulse rate was close to the compression rate and was only observable as a small broadening in the right flanks of the chest compression components.

4.3.3 Trend of relative PPG amplitude

In a case of transient ROSC (Fig. 4.5), CPR was stopped when ROSC was diagnosed, and restarted when the circulation was considered inadequate. During the period without compressions, the spectrograms of the PPG and ABP signals (Fig. 4.5a-4.5b) showed a spontaneous pulse. The pulse amplitude in the PPG signal time-trace decreased in this period and had almost disappeared when compressions were restarted (Fig. 4.5c).

4.4 Discussion

The aim of the present study was to investigate whether PPG signals can be used to detect the presence or absence of spontaneous cardiac-induced pulsations during CPR. This could be a first step towards objectifying and shortening ROSC determination. Raw PPG data acquired with a custom-built photoplethysmograph were analyzed retrospectively in both time and frequency domains, using the ABP as a reference.

Although PPG and ABP waveforms have comparable morphology, it is important to note that ABP represents the blood pressure in the macrovasculature, while PPG reflects the blood volume pulse in the microvasculature [10, 146]. As such, besides ABP, also arteriolar vasomotor tone and microvascular shunting affect the PPG waveform [10,146,163]. Therefore, during CPR, decreased ABP and increased vasomotor tone might significantly reduce the pulsatility in the PPG

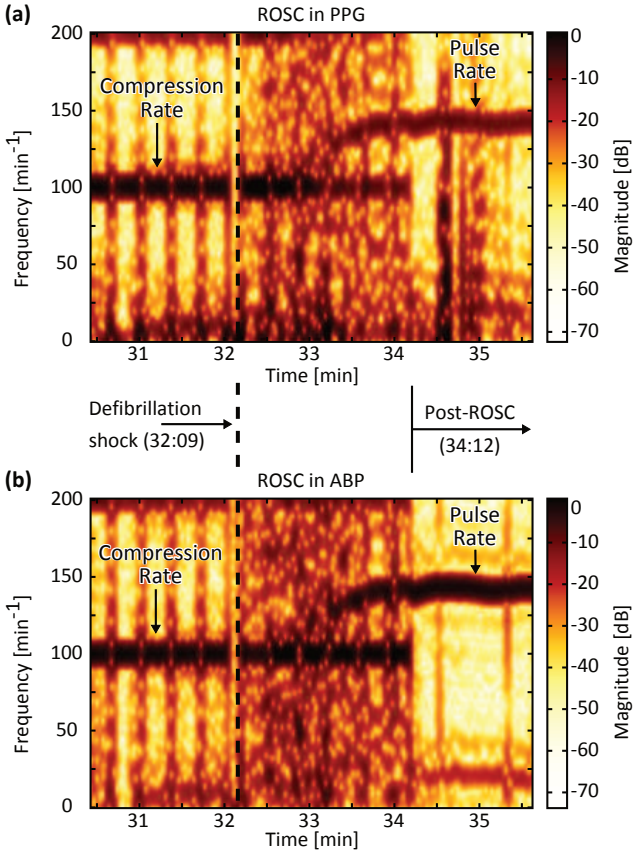

Figure 4.3: Spectrograms of the PPG and ABP signals in a peri-arrest period. The defibrillation shock was applied at 32:09 (dashed line). Chest compressions were stopped at 34:12. (a) Spectrogram of the PPG signal. At 34:30 the ventilation bag is uncoupled and the ventilator is attached, which results in a broad spectral motion artifact. (b) Spectrogram of the ABP signal. The spectrograms were obtained by partitioning the 0.1-Hz high-pass filtered signals in segments of 10 seconds with 90% overlap and applying a Hamming window. For convenient time referencing, the time axis corresponds to the center of each segment. The spectrograms have been normalized by the magnitude of the spectral compression component in the signal at the beginning of the trace shown. This is the same animal (R1) as in Fig. 4.2 and Fig. 4.4d. ABP: arterial blood pressure; PPG: photoplethysmography; ROSC: return of spontaneous circulation.

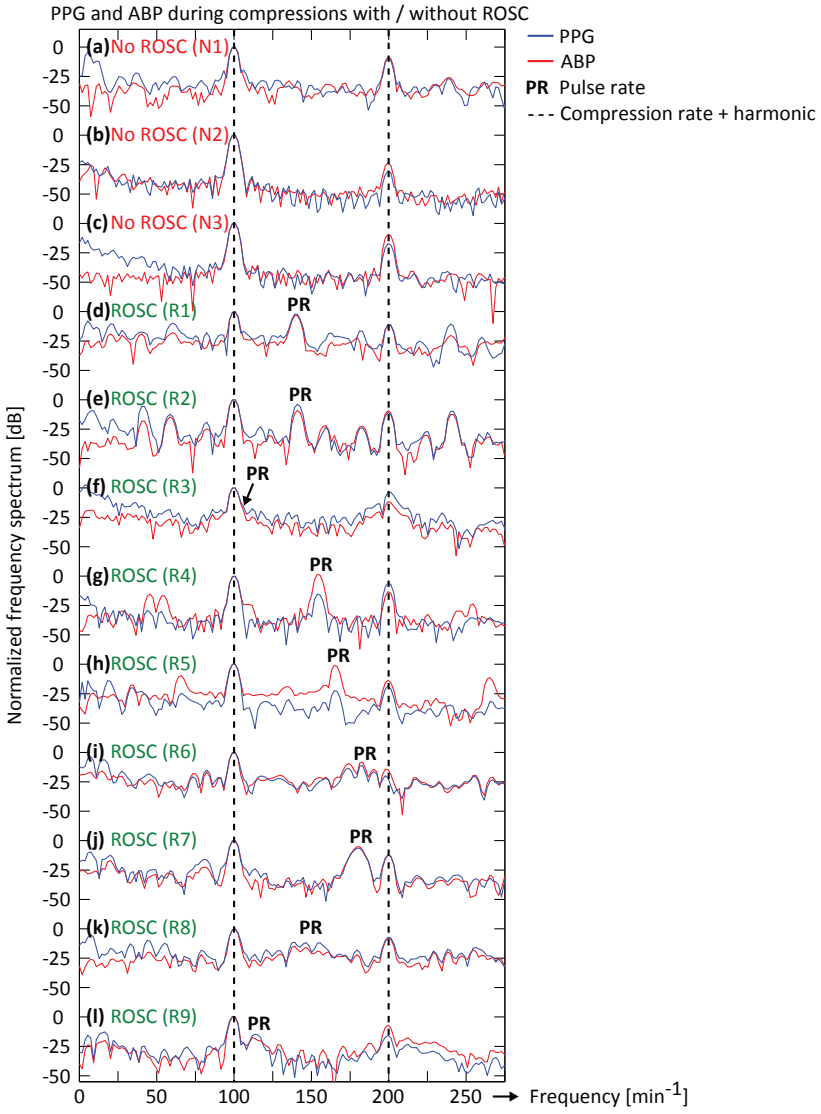

Figure 4.4: PR behavior during CPR in PPG and ABP spectra of various animals. Dashed lines indicate the automated chest compression rate at 100 min^{-1} and its harmonic at 200 min^{-1}. (a)-(c) Animals without ROSC. (d)-(l) Animals with ROSC. The PR has been determined by visually inspecting the corresponding spectrograms. Spectra (a)-(l) have been determined from a segment of 20 s containing the last series of 30 chest compressions in each experiment. An 0.1-Hz high-pass filter and a Hamming window were applied before determining the spectra via Fourier transformation. Each spectrum has been normalized by the magnitude of the 100 min^{-1} spectral compression component in the signal. ABP: arterial blood pressure; CPR: cardiopulmonary resuscitation; PPG: photoplethysmography; PR: pulse rate; ROSC: return of spontaneous circulation.

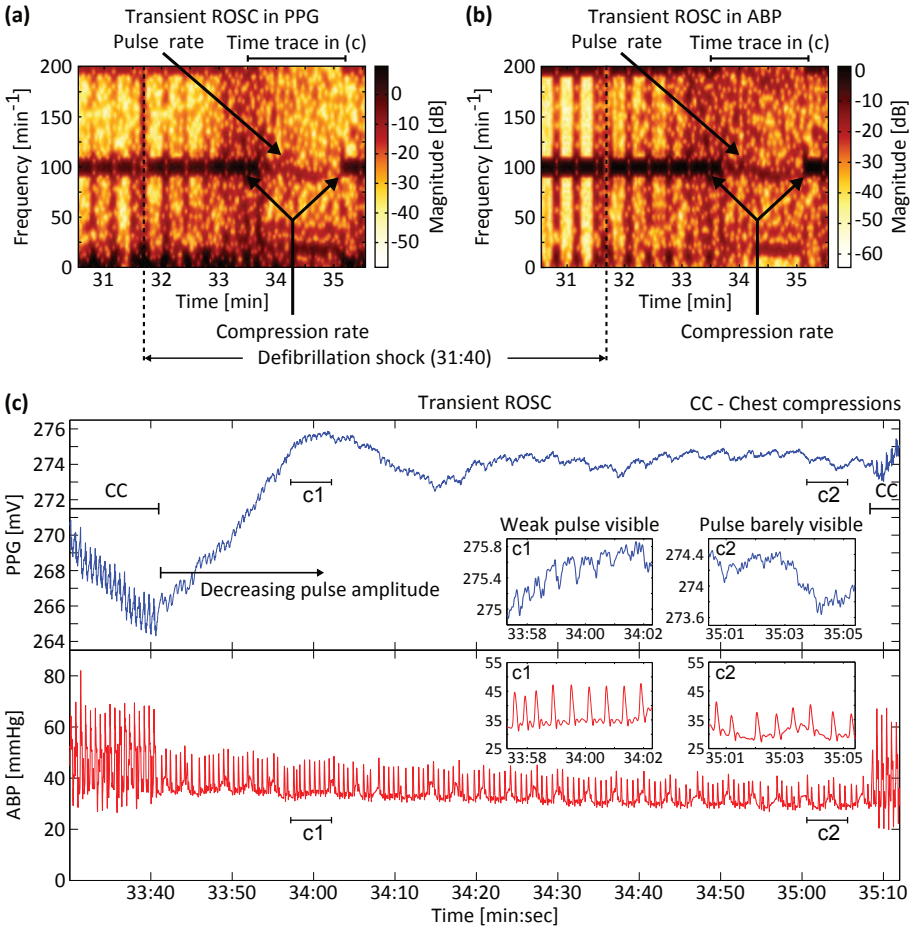

Figure 4.5: Decreasing pulse amplitude observable in PPG signal during transient ROSC. The defibrillation shock was applied at 31:40 (dashed line). CPR was stopped at 33:41, and restarted at 35:08. (a) Spectrogram of the PPG signal. (b) Spectrogram of the ABP signal. (c) Time traces of the PPG and ABP signals. The insets show two close-ups of the PPG and ABP waveforms. The spectrograms were obtained by partitioning the 0.1-Hz high-pass filtered signals in segments of 10 seconds with 90% overlap and applying a Hamming window. For convenient time referencing, the time axis corresponds to the center of each segment. The spectrograms have been normalized by the magnitude of the spectral compression component in the signal at the beginning of the trace shown. This is the same animal (N1) as in Fig. 4.4a. ABP: arterial blood pressure; CC: chest compressions; PPG: photoplethysmography; ROSC: return of spontaneous circulation.

waveform while ABP pulsatility remains. Nevertheless, the data show that presence and rate of a spontaneous cardiac pulse could be determined from a PPG signal during CPR. A PPG time trace could be used to detect spontaneous pulses during ventilation pauses, as illustrated in Fig. 4.2c. However, Fig. 4.2c also illustrates that it can be challenging to directly identify the spontaneous pulses in the PPG time trace during compressions. To resolve this, a spectral analysis was performed, which facilitates the identification of a spontaneous pulse and its rate during chest compressions, as shown by Figs. 4.3, 4.4d, 4.4e, and 4.4g-4.4l.

During CPR, a PPG measurement performed at a stable site has the advantage of being less sensitive to motion artifacts than a TTI measurement, which is performed at the chest. Furthermore, PPG shows pulse presence faster than NIRS. However, the frequency spectra also show that real-time identification of a spontaneous cardiac pulse in the PPG signal during automated CPR may not be straightforward in all cases. Three complicating situations can occur, the first two being specifically related to ongoing chest compressions. First, the presence of spectral components in addition to the pulse and compression rates (and their harmonics) can complicate the identification of the spontaneous pulse component (Figs. 4.4d, 4.4e, and 4.4h-4.4l). As these additional spectral components seem to arise at rates equal to the sum and difference of the compression and pulse rates, they may indicate an interaction between the chest compressions and the spontaneous cardiac activity. Second, when the pulse rate is close to the compression rate, the spontaneous pulse is difficult to identify in the spectrum (Figs. 4.4f, 4.5a, and 4.5b). And third, in general it can be technically challenging to identify a rapidly varying pulse rate in the spectrum, because variations in the rate result in a less well-defined, broadened peak in the spectrum (Figs. 4.4i and 4.4k). Furthermore, in case of manual CPR where the compression rate may fluctuate, an independent measurement of the manual compression rate [30, 120, 204] can potentially be used to identify the chest compression rate in the spectrum and distinguish it from a spontaneous pulse rate.

In addition to using PPG signals to obtain feedback on manual chest compression rates as described by Xu et al. [208] and Spittal [171], our data show that PPG signals can offer information about the presence or absence of a spontaneous cardiac pulse during CPR, making it potentially useful to support ROSC detection. Via PPG-based screening for pulse during ongoing compressions, absence of spontaneous cardiac activity can be noted which may prevent unnecessary or lengthy pauses in chest compressions for examination of ROSC. Preventing pauses in compressions increases the chest compression fraction during CPR, which may increase the probability of achieving ROSC [181]. Furthermore, detection of return of spontaneous pulse during ongoing compressions may guide administration of vasopressors, as vasopressors may have detrimental effects when administered following a shock that has resulted in a perfusing rhythm [41, 120]. The broad spectral activity in the PPG signal spectrogram during CPR following the defibrillation shock (Figs. 4.3 and 4.5) may provide an early indication of start-up of spontaneous cardiac output, or other muscular activity. Reinstitution of CPR

may be guided by fading of a spontaneous pulse in the PPG signal, which may indicate loss of a perfusing rhythm (Fig. 4.5c). These observations warrant further research on the potential of PPG as a ROSC indicator.

This study, however, has some limitations. First, an animal model is never fully representative of clinical scenarios, but it allowed comparison between PPG signals and invasively measured ABP in a controlled environment. Second, suturing the PPG sensor to the nose to limit excessive motion artifacts is not representative of good clinical practice. However, the goal of this study was determining the feasibility of identifying a spontaneous pulse in a PPG signal during CPR, and not dealing with the technical solution for corrupting motion. Finally, to be able to detect a spontaneous pulse in humans during CPR in clinical practice, a central-site PPG measurement (e.g. from the facial region) may be preferred over a peripheral site, as centralization and the associated vasoconstriction can severely compromise peripheral pulsatile blood flow [24, 120, 132].

4.5 Conclusions

After ROSC, cardiac pulses could be observed in the nasal PPG waveform during ventilation pauses. During chest compressions the contribution of spontaneous cardiac activity could be identified by analyzing the PPG frequency spectrum, when the pulse and compression rates were sufficiently distinct. We conclude that PPG has potential to support detection of ROSC during CPR.

CHAPTER 5

Photoplethysmography-based algorithm for detection of cardiogenic output during cardiopulmonary resuscitation

This chapter is based on

R.W.C.G.R. Wijshoff, A.M.T.M. van Asten, W.H. Peeters, R. Bezemer, G.J. Noordergraaf, M. Mischi, and R.M. Aarts, "Photoplethysmography-based algorithm for detection of cardiogenic output during cardiopulmonary resuscitation," *IEEE Transactions on Biomedical Engineering*, vol. 62, no. 3, pp. 909-921, March 2015.

R.W.C.G.R. Wijshoff, W.H. Peeters, G.J. Noordergraaf, M. Mischi, and R.M. Aarts, "Photoplethysmographic detection of a spontaneous pulse during cardiopulmonary resuscitation," *5th Dutch Bio-Medical Engineering Conference (BME)*, Egmond aan Zee, the Netherlands, Jan. 22-23, 2015.

R.W.C.G.R. Wijshoff, W.H. Peeters, G.J. Noordergraaf, M. Mischi, and R.M. Aarts, "Detection of a spontaneous pulse by photoplethysmography during experimental automated cardiopulmonary resuscitation," *49th Annual Conference of the Deutsche Gesellschaft für Biomedizinische Technik (DGBMT)*, Lübeck, Germany, Sep. 16-18, 2015.

Abstract

Introduction: Detecting return of spontaneous circulation (ROSC) during cardiopulmonary resuscitation (CPR) is challenging, time-consuming, and interrupts the chest compressions. Our objective was to develop an algorithm which can support ROSC detection during ongoing chest compressions, by detecting cardiogenic output in a near-infrared photoplethysmography (PPG) signal. The algorithm can detect palpable and impalpable spontaneous pulses.

Methods: We based the algorithm development on pre-clinical automated-CPR data. The algorithm consisted of two stages. The first stage filtered out the compression component to obtain a compression-reduced PPG signal, which could show an estimate of the underlying spontaneous pulse waveform. The compression component was modeled by a harmonic series. The fundamental frequency of this series was the compression rate which we derived from the trans-thoracic impedance signal that was measured between the defibrillation pads. The amplitudes of the harmonic components were obtained via a least mean-squares algorithm. Subtracting the compression estimate from the measured PPG signal reduced the compression component. The second stage of the algorithm determined the status of an indicator of cardiogenic output. Cardiogenic output was indicated when a pulse rate (PR) or a redistribution of blood volume to the periphery was detected. The PR was determined from the frequency spectrum of the compression-reduced PPG signal, which was estimated via an autoregressive model. The relationship between the spectral peaks was analyzed to identify the PR. Resumed cardiogenic output could also be detected from a decrease in the baseline of the PPG signal, which was presumably caused by a redistribution of blood volume to the periphery. The indicator was validated by a comparison to the annotation of ROSC as retrospectively provided by nine clinicians.

Results: The first stage of the algorithm reduced the root mean-square amplitude of the compression component by about 79%, as measured during cardiac arrest phases. The second stage of the algorithm indicated cardiogenic output with 94% specificity and 69% sensitivity compared to the ROSC annotation.

Conclusions: Results showed that ROSC detection can be supported by combining the compression-reduced PPG signal with an indicator of cardiogenic output based on the detected PR and redistribution of blood volume.

5.1 Introduction

High-quality cardiopulmonary resuscitation (CPR) requires minimizing interruptions of chest compressions, as interruptions reduce compression-generated blood flow and thus the chance of achieving return of spontaneous circulation (ROSC) [21,30,36,41,120,126]. International guidelines state that interruptions for ROSC assessment should last at most 10 s [41, 120]. ROSC is assessed by analyzing the electrocardiographic rhythm and checking for a palpable circulatory pulse. In practice, however, pulse checks by manual palpation can take significantly longer than 10 s, especially when a spontaneous pulse is absent [43, 178]. Furthermore, the interpretation of manual palpation is known to be unreliable, even when performed by expert clinicians [43, 178]. Therefore, an objective method to detect presence or absence of a spontaneous pulse, especially during compressions, would be valuable to support ROSC detection.

Monitoring of end-tidal CO_2 [39, 139], invasive blood pressure [133, 151], or central venous oxygen saturation [150] allows for a more objective assessment of ROSC, also during compressions, but requires a secured airway or placement of catheters. Trans-thoracic impedance (TTI) measurements [100, 149, 153] and near-infrared spectroscopy (NIRS) [79, 134, 160] are non-invasive methods, but TTI is strongly influenced by compressions and NIRS may respond slowly upon ROSC. Doppler ultrasound is being researched as a non-invasive method to detect pulse absence and presence in the carotid artery, but this technique is sensitive to a correct placement over the carotid artery and is strongly influenced by chest compressions [89, 213]. Generally, photoplethysmography (PPG) is an easy-to-use and non-invasive technique to continuously measure a spontaneous pulse [10, 146]. Its potential to measure a spontaneous pulse during compressions has been observed in an automated-CPR animal study [203]. When the complexity of the PPG signal increased during compressions, the invasive blood pressure indicated presence of a spontaneous pulse. Furthermore, frequency spectra of the PPG signals showed that the spontaneous pulse rate (PR) and compression rate could be distinguished. Although these methods can provide valuable support, ROSC detection remains a clinical situational assessment, because it involves determining whether a perfusing rhythm is life-sustaining.

This chapter describes a PPG-based algorithm that detects cardiogenic output during chest compressions to support ROSC detection, developed based on pre-clinical data from [203]. Cardiogenic output was detected using the compression-reduced PPG signal and the baseline of the PPG signal. The compression-reduced PPG signal was obtained by subtracting the compression component from the PPG signal, to estimate the spontaneous pulse waveform. We defined a spontaneous pulse in the PPG signal as a (quasi-)periodic feature resulting from cardiac contractions. The spontaneous pulse can be palpable or impalpable. The compression component subtracted from the PPG signal was determined via a harmonic series. The fundamental compression rate of this series was derived from the TTI signal. The TTI signal had been measured between the defibrillation pads, as

is common in defibrillators. The frequency spectrum of the compression-reduced PPG signal was analyzed to detect the PR. When cardiogenic output resumed, the baseline of the PPG signal decreased, presumably caused by a redistribution of blood volume to the periphery. The algorithm indicated cardiogenic output when a PR or a decrease in the baseline of the PPG signal was detected.

5.2 Methods

5.2.1 Experimental measurements

An automated-CPR study was conducted on 16 pigs [203]. All animals received care compliant with the Dutch Animal Experimentation Law and the Standard Operation Procedures of the Central Animal Laboratory of the Radboud University Nijmegen Medical Center, where the experiments were conducted. The Radboud University Animal Ethical Committee approved the protocol[1]. The experiments, protocol and physiological data are described in detail in Chapter 4 and [203].

After a 10 min baseline recording, cardiac arrest was induced via an electrical shock, followed by 20 min of CPR in a rhythm of thirty compressions alternated by two ventilations (30:2 rhythm). Chest compressions were delivered by an automated CPR device at a rate of 100 min^{-1}. After 20 min of CPR, 2-min cycles were initiated to achieve ROSC, each starting with defibrillation if appropriate, followed by 30:2 CPR. If ROSC was achieved after one of the cycles, CPR stopped and measurements continued for 20 min post-ROSC. Otherwise the experiment ended after the fourth 2-min cycle. Animals were euthanized at the end of the experiment.

All animals were monitored by electrocardiography (ECG), capnography, and pulse oximetry, and by measuring arterial blood pressure (ABP) just distal to the aortic arch, and carotid artery blood flow. Near-infrared (IR) (900 nm) PPG signals [Volt] were obtained using a forehead reflectance pulse oximetry probe (Nellcor™ Oxisensor II RS-10, Covidien-Nellcor™, Dublin, Ireland), controlled by a custom-built photoplethysmograph. The probe was customized to enable placement by suturing between the nostrils, because this site is relatively stable in terms of motion, and allows for tight fixation of the probe to the skin. Transthoracic impedance (TTI) [Ohm] between Adult Plus Multifunction Electrode Pads M3713A (Philips, Andover, MA, USA) was recorded via the HeartStart MRx Monitor/Defibrillator (Philips, Andover, MA, USA).

PPG and ABP waveforms were recorded simultaneously using a 16-bit digital data acquisition card (DAQ) (NI USB-6259, National Instruments, Austin, TX, USA). The DAQ was controlled by dedicated software implemented in LabVIEW® (National Instruments, Austin, TX, USA).

[1]Protocol number of the Animal Ethical Committee of the Radboud University Nijmegen Medical Center: RU-DEC 2011-188.

All waveforms were sampled at $f_s = 250$ Hz. The TTI signal was synchronized to the PPG signal by resampling and translating the TTI signal such that correlation was maximal between the fundamental compression frequency components in the TTI and ABP signals. Resampling was done at rates between 249.91 Hz and 250.09 Hz in steps of 0.01 Hz.

5.2.2 Overview of the algorithm

Figure 5.1 outlines the algorithm that indicated cardiogenic output during CPR. The algorithm contained three modules: one for reduction of the compression component and PR detection (purple and green blocks in Fig. 5.1, Sections 5.2.3 to 5.2.6), one for analysis of the PPG signal baseline (yellow blocks in Fig. 5.1, Section 5.2.7), and one for the indicator of cardiogenic output (blue blocks in Fig. 5.1, Sections 5.2.8 and 5.2.9).

The primary input of the algorithm was the raw measured near-IR PPG signal, $ppg[n]$, with sample index n. A band-pass filtered PPG signal, $ppg_{\mathrm{ac}}[n]$, was obtained via a first-order Butterworth low-pass filter with a 12-Hz cut-off and a fourth-order Butterworth high-pass filter with a 0.3-Hz cut-off. By using the compression rate derived from the auxiliary TTI signal $Z[n]$ (Section 5.2.3), the compression component was reduced in $ppg_{\mathrm{ac}}[n]$ to obtain the compression-reduced PPG signal $ppg_{\mathrm{cr}}[n]$ (Section 5.2.4). The frequency spectrum of $ppg_{\mathrm{cr}}[n]$ was determined via an autoregressive (AR) model (Section 5.2.5). The PR was identified in the spectrum, if it contained a signal with sufficient high-frequency content (Section 5.2.6). In parallel, the baseline of the near-IR PPG signal, $ppg_{\mathrm{bl\_d}}[n]$, was obtained via a 0.5-Hz low-pass filter. A presumable redistribution of blood volume to the periphery could be detected from a decrease in $ppg_{\mathrm{bl\_d}}[n]$ (Section 5.2.7). The algorithm indicated cardiogenic output when a PR or a decrease in the baseline was detected (Sections 5.2.8 and 5.2.9). In this study, we have not extensively optimized the algorithm parameter values, because of the small pre-clinical data set.

5.2.3 Determination of compression characteristics

The instantaneous compression frequency and phase were determined from the TTI signal, for which it has been used before [13,15]. To extract the fundamental compression frequency component, the TTI signal $Z[n]$ was band-limited by a fourth-order Butterworth filter with a pass-band between 1 and 3 Hz. This accommodates for the range of manual chest compression frequencies between about 60 and 180 min^{-1} as observed in clinical practice [13,15,154].

The band-limited TTI signal, indicated by $Z_f[n]$, had a sinusoidal-like-shape, with local minima occurring at the end of a compression. Compressions were detected by finding consecutive sequences of a local maximum $(n_l, Z_{f\max l})$, a local minimum $(n_c, Z_{f\min c})$, and a local maximum $(n_r, Z_{f\max r})$. The local extremes were found from the zero-crossings in the time-derivative of $Z_f[n]$. It was required

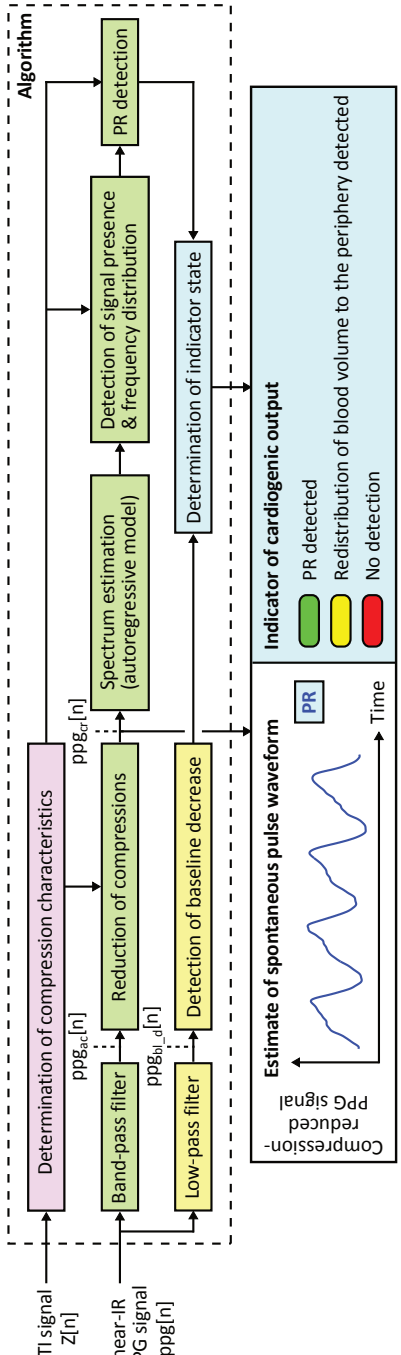

Figure 5.1: Overview of the PPG-based algorithm that indicated cardiogenic output during CPR. A compression-reduced near-IR PPG signal, $ppg_{\mathrm{cr}}[n]$, containing an estimate of the spontaneous pulse waveform, was obtained by reducing the compression component. The compression reduction stage used the compression rate determined from the auxiliary TTI signal $Z[n]$. The frequency spectrum of $ppg_{\mathrm{cr}}[n]$ was estimated via an AR model. The PR was determined in this spectrum, if it contained a signal with sufficient high-frequency content. A presumable redistribution of blood volume to the periphery was detected by a decrease in the baseline of the near-IR PPG signal $ppg_{\mathrm{bl\_d}}[n]$. Cardiogenic output was indicated if a PR or a decrease in baseline was detected. AR: autoregressive; CPR: cardiopulmonary resuscitation; IR: infrared; PPG: photoplethysmography; PR: pulse rate; TTI: trans-thoracic impedance.

that $Z_{f\max l,r} \geq 0$ and $Z_{f\min c} < 0$. To avoid detecting ventilations, motion artifacts or noise, a sequence of three local extremes had to meet four criteria to be associated with a compression:

- The peak-to-valley amplitude was within a specified range:

$$Z_{lb} \leq \frac{Z_{f\max l} + Z_{f\max r}}{2} - Z_{f\min c} \leq Z_{ub}, \tag{5.1}$$

  with limits $Z_{lb} = 0.2\ \Omega$ and $Z_{ub} = 10\ \Omega$ [153].

- The distance $n_r - n_l$ was within a specified range:

$$n_{lb} \leq n_r - n_l \leq n_{ub}, \tag{5.2}$$

  with initially $n_{lb} = n_{lb0} = 0.3\text{s} \cdot f_s$ and $n_{ub} = n_{ub0} = 1\text{s} \cdot f_s$ to allow for compression rates of 60 to 200 min^{-1}. After detection of at least N_D compressions, the bounds changed to $n_{lb,i} = (1 - k_D)n_{D,i}$ and $n_{ub,i} = (1 + k_D)n_{D,i}$, with $0 < k_D < 1$ setting the allowed deviation from $n_{D,i} = N_D^{-1} \sum_{i'=i-N_D+1}^{i} (n_{r,i'} - n_{l,i'})$, with i indicating the most recently detected compression. If $n_{lb,i}$ or $n_{ub,i}$ became incompliant with compression rates of 60 to 200 min^{-1}, or if N_D sequential sequences failed this criterion, the bounds were reset to n_{lb0} and n_{ub0}.

- The sequence was sufficiently symmetric in time:

$$\frac{1}{k_T} \leq \frac{n_c - n_l}{n_r - n_c} \leq k_T, \tag{5.3}$$

  where parameter $k_T > 1$ set the allowed asymmetry.

- The sequence was sufficiently symmetric in amplitude:

$$\frac{1}{k_A} \leq \frac{-Z_{f\min c}}{(Z_{f\max l} + Z_{f\max r})/2} \leq k_A, \tag{5.4}$$

  where parameter $k_A > 1$ set the allowed asymmetry. This criterion was only met if $Z_{f\max l} + Z_{f\max r} > 0$.

After identifying the individual compressions, first the instantaneous chest compression frequency $f_{\text{cc,i}}$ associated with compression i was determined from the distance between two consecutive local minima. If the local minima were at most 1 s apart,

$$f_{\text{cc,i}} = \frac{f_s}{n_{c,i} - n_{c,i-1}}. \tag{5.5}$$

If a local minimum was not preceded by another local minimum within 1 s, a new sequence of chest compressions was assumed to have started. In that case, the

compression frequency associated with the second compression of the sequence was also associated with the first compression of the sequence. This implies an inherent delay in the algorithm of at least two compressions. Compressions more than 1 s apart from both neighboring compressions were ignored.

Second, the onset $n_{o,i}$ of compression i was determined as

$$n_{o,i} = n_{c,i} - \frac{f_s}{f_{\mathrm{cc,i}}}. \tag{5.6}$$

Third, by starting at the onset of compression i, the compression phase $\phi_{\mathrm{cc}}[n]$ [rad] was determined as

$$\phi_{\mathrm{cc}}[n] = \phi_{\mathrm{cc}}[n-1] + 2\pi\frac{f_{\mathrm{cc,i}}}{f_s}, \quad n_{o,i} \leq n < n_{o,i+1}. \tag{5.7}$$

Compression phase $\phi_{\mathrm{cc}}[n]$ was initialized at 0 rad, and was reset to 0 rad when a new compression sequence started.

Fourth, a smooth envelope function $A[n]$ [-] was constructed, indicating presence of compressions. $A[n]$ equaled 1 during a compression that was not the first of a sequence. For the first compression of a sequence, $A[n]$ smoothly increased from 0 to 1 in $N_{o,i} = \mathrm{round}\,(f_s/(4f_{\mathrm{cc,i}}))$ samples via

$$\frac{1}{2}\left(1 - \cos\left(\pi\frac{n - n_{o,i}}{N_{o,i}}\right)\right), \quad n_{o,i} \leq n \leq n_{o,i} + N_{o,i}, \tag{5.8}$$

after which $A[n]$ equaled 1 during the remaining compression period. After the last compression of a sequence, $A[n]$ smoothly decreased from 1 to 0 in $N_{o,i}$ samples via

$$\frac{1}{2}\left(1 + \cos\left(\pi\frac{n - n_{c,i}}{N_{o,i}}\right)\right), \quad n_{c,i} \leq n \leq n_{c,i} + N_{o,i}. \tag{5.9}$$

Otherwise $A[n]$ equaled 0.

Based on the measured TTI signals, $N_D = 5$, $k_D = 0.35$, and $k_T = k_A = 3$ were used for all animals.

5.2.4 Reduction of the compression component

5.2.4.1 Harmonic model

To estimate the spontaneous pulse waveform, that can support the clinician in detecting ROSC, a harmonic series was employed to model and reduce the chest compression component in the PPG signal. A harmonic series has been employed successfully before to model and reduce the chest compression component in the ECG signal [13, 76, 154].

The primary input of the compression reduction stage was the band-pass filtered PPG signal, $ppg_{\mathrm{ac}}[n]$, that we assumed to be a sum of a spontaneous pulse

component, $sp[n]$, a compression component, $cmp[n]$, and remaining noise components, $r[n]$ [203]:

$$ppg_{\mathrm{ac}}[n] = sp[n] + cmp[n] + r[n]. \tag{5.10}$$

We observed that the PPG signal measured during CPR could contain frequency components at the sum and the difference of the compression rate and the PR and their harmonics [203] (Fig. 4.4). These components may be interaction frequencies resulting from interaction between spontaneous cardiac activity and compressions [203]. These components may possibly result from, e.g., amplitude modulation of the spontaneous pulse component. We considered these interaction frequencies to be part of the spontaneous pulse component, $sp[n]$. A compression-reduced PPG signal, $ppg_{\mathrm{cr}}[n]$, containing an estimate of the spontaneous pulse component, was obtained by subtracting the estimate of the compression component, $cmp_{\mathrm{est}}[n]$:

$$ppg_{\mathrm{cr}}[n] = ppg_{\mathrm{ac}}[n] - cmp_{\mathrm{est}}[n]. \tag{5.11}$$

The estimate $cmp_{\mathrm{est}}[n]$ was modeled by a harmonic series of K in-phase and quadrature components with fundamental frequency $f_{\mathrm{cc,i}}$ determined from the TTI signal [76, 154]:

$$cmp_{\mathrm{est}}[n] = A[n] \sum_{k=1}^{K} \left[a_k[n] \cos\left(k\phi_{\mathrm{cc}}[n]\right) + b_k[n] \sin\left(k\phi_{\mathrm{cc}}[n]\right) \right], \tag{5.12}$$

with envelope function $A[n]$ (Section 5.2.3), compression phase $\phi_{\mathrm{cc}}[n]$ (5.7), and $a_k[n]$ and $b_k[n]$ [Volt] the amplitudes of the in-phase and quadrature components of the k^{th} harmonic, respectively. $A[n]$ quickly forced $cmp_{\mathrm{est}}[n]$ to 0 during interruptions of compressions, so that input $ppg_{\mathrm{ac}}[n]$ stayed unaffected in these interruptions. Amplitudes $a_k[n]$ and $b_k[n]$ were estimated via a least mean-squares (LMS) algorithm [76, 193, 207]:

$$a_k[n+1] = a_k[n] + 2\mu A[n] ppg_{\mathrm{cr}}[n] \cos\left(k\phi_{\mathrm{cc}}[n]\right), \tag{5.13}$$

$$b_k[n+1] = b_k[n] + 2\mu A[n] ppg_{\mathrm{cr}}[n] \sin\left(k\phi_{\mathrm{cc}}[n]\right), \tag{5.14}$$

for $k = 1, ..., K$, and with step-size parameter μ.

The transfer function $H(z)$ of the LMS filter between $ppg_{\mathrm{ac}}[n]$ and $ppg_{\mathrm{cr}}[n]$ can be approximated by a cascade of K notch filters having the notch centered at kf_{cc}, $k = 1, ..., K$, when the estimate of the compression frequency is stable at f_{cc}, $A[n] = 1$, and the step-size parameter $\mu < 1$ [193, 207]:

$$H(z) \approx \prod_{k=1}^{K} \frac{z^2 - 2z\cos\left(2\pi\frac{kf_{\mathrm{cc}}}{f_s}\right) + 1}{z^2 - 2(1-\mu)z\cos\left(2\pi\frac{kf_{\mathrm{cc}}}{f_s}\right) + (1-2\mu)}. \tag{5.15}$$

Each notch has a 3-dB bandwidth W [Hz] of about [76, 193]

$$W \approx \frac{\mu f_s}{\pi}. \tag{5.16}$$

Furthermore, μ determined the convergence time T_{cv} [s] to a fraction $0 < v < 1$ of the targeted values for a_k and b_k via

$$T_{cv} = \frac{1}{f_s} \frac{\ln(1-v)}{\ln(1-\mu)}. \tag{5.17}$$

We used $K = 9$ to reduce all compression harmonics from $ppg_{\mathrm{ac}}[n]$ which remained in the frequency-band that was to be analyzed for PR detection. High harmonics could result from probe motion relative to the skin. To limit the removal of spontaneous pulses with PRs close to the compression rate to ranges of about $95 - 105$ min^{-1} and $195 - 205$ min^{-1}, we set $\mu = 0.002$, resulting in $W \approx 10$ min^{-1}, and $T_{c0.95} \approx 6$ s.

5.2.4.2 Evaluation

The effectiveness of the reduction of the compression component was evaluated during phases of CPR on cardiac arrest. The reduction of the compression component was determined per series of thirty compressions, was based on the root mean-square (RMS) value, and was expressed as a percentage. For each compression series κ consisting of $N_{cs,\kappa}$ samples and starting at $N_{cs0,\kappa}$ samples, the reduction of the compression component, $\Delta cmp[\kappa]$ [%], was determined as the ratio of RMS values of the PPG signal before and after reduction of the compression component:

$$\Delta cmp[\kappa] = 100 \times \left(1 - \frac{\sqrt{\frac{1}{N_{cs,\kappa}} \sum_{k=0}^{N_{cs,\kappa}-1} ppg_{\mathrm{cr}}[N_{cs0,\kappa}+k]^2}}{\sqrt{\frac{1}{N_{cs,\kappa}} \sum_{k=0}^{N_{cs,\kappa}-1} ppg_{\mathrm{ac}}[N_{cs0,\kappa}+k]^2}} \right). \tag{5.18}$$

Series of compressions were identified by selecting all segments during cardiac arrest where the envelope function $A[n] > 0$. For each animal, the effectiveness of the reduction of the compression component was determined as the average and standard deviation of $\Delta cmp[\kappa]$ over all identified series of compressions on arrest.

5.2.5 Spectrum estimation

5.2.5.1 Autoregressive (AR) model

Frequency spectra of the compression-reduced PPG signal $ppg_{\mathrm{cr}}[n]$ were determined over time via AR models. Because $ppg_{\mathrm{cr}}[n]$ was non-stationary, spectra could only be estimated from short time-windows. AR models provide a better frequency resolution on short time-windows compared to the Fast Fourier Transform [81, 98, 106].

Prior to determining the AR models, $ppg_{\mathrm{cr}}[n]$ was down-sampled to $f_{s\_d} = 31.25$ Hz. Down-sampling increases the phase angle of the poles in the data, resulting in more reliable estimation of the AR coefficients [46]. Down-sampling

was done in three consecutive steps to avoid numerical issues. First, a third-order Butterworth low-pass filter with a 12-Hz cut-off was applied, followed by down-sampling to 125 Hz. Second, a 6^{th}-order Butterworth low-pass filter with a 12-Hz cut-off was applied, followed by down-sampling to 62.5 Hz. Third, a 6^{th}-order Butterworth low-pass filter with a 12-Hz cut-off was applied, followed by down-sampling to $f_{s\_d} = 31.25$ Hz.

The AR models were then estimated from the down-sampled compression-reduced PPG signal $ppg_{\mathrm{cr\_d}}[n]$ [81]:

$$ppg_{\mathrm{cr\_d}}[n] = -\sum_{k=1}^{N_{\mathrm{AR}}} \alpha_k ppg_{\mathrm{cr\_d}}[n-k] + e[n], \tag{5.19}$$

with AR coefficients α_k, model order N_{AR}, and prediction error $e[n]$. If model order N_{AR} is sufficiently large, all correlations in the data are described by the linear prediction in (5.19) and the prediction error $e[n]$ is white noise [81]. For each AR model, the power spectral density (PSD) is obtained as a continuous function of frequency f [Hz] [81]:

$$P_{\mathrm{AR}}(f) = \frac{\sigma_e^2 / f_{s\_d}}{\left|1 + \sum_{k=1}^{N_{\mathrm{AR}}} \alpha_k \exp\left(-j2\pi k f / f_{s\_d}\right)\right|^2}, \tag{5.20}$$

with prediction error power σ_e^2. The AR coefficients α_k were obtained from time-windows of $T_w = 5$ s using the forward-backward approach [81]. The AR coefficients were computed once per second by translating these windows by 1 s. $P_{\mathrm{AR}}(f)$ was evaluated on a 1 min^{-1} resolution.

5.2.5.2 Model order

The AR model order N_{AR} should be sufficiently large to capture the strongest frequency components present in $ppg_{\mathrm{cr\_d}}[n]$. N_{AR} was determined empirically using the prediction error power. As a function of model order, the prediction error power was determined relative to the total signal power in the window from which the AR model was estimated. N_{AR} was selected as the smallest order with the mean plus two standard deviations of the relative prediction error power at most 5%.

Model orders between 2 and 50 with increments of 2 were considered. AR models were estimated from $T_w = 5$ s sliding windows, with 4 s overlap. For all animals with ROSC, AR models were estimated in the 2-min cycle between successful defibrillation and the end of CPR. Therefore, for each model order the relative prediction error power was determined for 115 AR models. In [67], Ulrych and Ooe suggest that satisfactory results are often obtained if the model order does not exceed 1/3 to 1/2 of the available data points. This criterion was met by considering model orders of at most 50 for $T_w = 5$ s windows at a sampling rate of $f_{s\_d} = 31.25$ Hz.

5.2.6 Spectral analysis

If a signal with sufficient high-frequency content was detected in $ppg_{\mathrm{cr\_d}}[n]$ (Section 5.2.6.1), an iterative algorithm identified the PR among the peaks in $P_{\mathrm{AR}}(f)$ (Section 5.2.6.2). The PR detection was evaluated via the ABP (Section 5.2.6.3).

5.2.6.1 Signal presence

To detect presence of a potential spontaneous pulse in compression-reduced PPG signal $ppg_{\mathrm{cr\_d}}[n]$, we defined two criteria. One criterion required the prediction error power $P_e[n]$ to be smaller than a fraction $R_P \ll 1$ of the total signal power $P_s[n]$. The other criterion required the power of the low frequencies to be smaller than a fraction $R_D < 1$ of the total signal power. Both criteria were evaluated in each window from which the AR model in (5.19) had been determined. Specifically, we considered a signal present if

$$\frac{P_e[n]}{P_s[n]} < R_P, \tag{5.21}$$

and if

$$\frac{\sum_{0 \le f' < f_l} P_{\mathrm{AR}}(f')}{\sum_{0 \le f' \le f_{s\_d}/2} P_{\mathrm{AR}}(f')} < R_D, \tag{5.22}$$

with $f_l = 40$ min^{-1} the lower PR limit, below the bradycardia limit at 50 min^{-1} [120], and considered a minimum rate predictive of a potential ROSC [39]. If (5.21) or (5.22) did not hold, no signal was considered present. If both held, the peaks in $P_{\mathrm{AR}}(f)$ were analyzed to identify the PR.

In (5.21), the prediction error power was computed as

$$P_e[n] = \frac{1}{N_w - N_{\mathrm{AR}}} \sum_{k=n-N_w+1+N_{\mathrm{AR}}}^{n} \mathrm{e}^2[k], \tag{5.23}$$

and the total signal power was computed as

$$P_s[n] = \frac{1}{N_w - N_{\mathrm{AR}}} \sum_{k=n-N_w+1+N_{\mathrm{AR}}}^{n} ppg^2_{\mathrm{cr\_d}}[k], \tag{5.24}$$

with AR model order N_{AR} and window length $N_w = \lceil T_w \cdot f_{s\_d} \rceil$. The first N_{AR} samples were omitted, as there is no prediction.

If (5.21) held, $ppg_{\mathrm{cr\_d}}[n]$ contained periodic components. In that case, correlations in the signal resulted in a large contribution of the linear prediction in (5.19) to $ppg_{\mathrm{cr\_d}}[n]$, causing the prediction error power to be much smaller than the total signal power. If periodic components were absent, $ppg_{\mathrm{cr\_d}}[n]$ mainly contained noise, resulting in a smaller contribution of the linear prediction to $ppg_{\mathrm{cr\_d}}[n]$, and a larger ratio between prediction error power and total signal power.

Low-frequency oscillations could cause (5.21) to hold, whereas $ppg_{\mathrm{cr\_d}}[n]$ contained no frequencies potentially corresponding to a PR. We observed such low-frequency oscillations during compressions or interruptions of compressions. Therefore, (5.22) required a limited contribution of low frequencies to the signal power, to ascertain that $ppg_{\mathrm{cr\_d}}[\mathrm{n}]$ contained frequencies potentially corresponding to a PR. Equation (5.22) was only considered, if the TTI signal contained compressions in the window from which the AR model had been estimated.

$R_P = 0.05$ was used, because the AR model order N_{AR} was selected such that the mean plus two standard deviations of the relative prediction error power was at most 5%. The spectral distribution observed in the PSDs determined $R_D = 0.5$.

5.2.6.2 PR detection

To identify the PR, the relationship was determined between the frequencies of the peaks in $P_{\mathrm{AR}}(f)$. All spectral peaks were found by using the zero-crossings from positive to negative in the derivative of $P_{\mathrm{AR}}(f)$. From all peaks found, a set of N_{pks} peaks $\{f_{\mathrm{pks}}\}$ was formed, where all frequencies were at least 18 min^{-1}, and deviated more than 5 min^{-1} from all compression rates $f_{\mathrm{cc,i}}$ and harmonics $2 \cdot f_{\mathrm{cc,i}}$ found in the window from which $P_{\mathrm{AR}}(f)$ was estimated.

Figure 5.2 outlines the iterative algorithm that determined the relationship between the frequencies in $\{f_{\mathrm{pks}}\}$ to identify the PR. The frequency corresponding to the largest peak in $P_{\mathrm{AR}}(f)$ was not necessarily the PR, as measurements showed that the largest peak during compressions could correspond to an interaction frequency equal to the sum or the difference of the compression rate and the PR. Therefore, the iterative algorithm determined the presence of interaction frequencies to identify the PR among the peaks.

The frequencies in $\{f_{\mathrm{pks}}\}$ were analyzed by iteratively creating subsets $\{f_i\}$ corresponding to the N_i largest peaks in the PSD. N_i was initialized at 3 and incremented by 1 until the PR had been identified or all N_{pks} frequencies had been analyzed. In each iteration, a set of PR candidates $\{f_{\mathrm{cnd}}\}$ was derived from $\{f_i\}$ by selecting the frequencies between 40 min^{-1} [39] and 250 min^{-1} [192]. For each PR candidate, three related frequencies were searched for in $\{f_i\}$ and collected in the set $\{f_{\mathrm{cnd,rel}}\}$: the harmonic $f_{\mathrm{hrm}} = 2 \cdot f_{\mathrm{cnd}}$, the sum interaction frequency $f_{\mathrm{sum}} = f_{\mathrm{cnd}} + f_{\mathrm{cca}}$, and the difference interaction frequency $f_{\mathrm{diff}} = |f_{\mathrm{cnd}} - f_{\mathrm{cca}}|$. Interaction frequencies were considered only if the TTI signal contained compressions in the window from which $P_{\mathrm{AR}}(f)$ had been determined. Compression rate f_{cca} was the average of the rates $f_{\mathrm{cc,i}}$ detected in this window. Frequencies were considered related if deviating at most Δf from the expected value. To identify the PR, a score was assigned to each candidate with related frequencies, by summing the corresponding peak values:

$$\mathrm{Score}(f_{\mathrm{cnd}}) = \sum_{f' \in \{f_{\mathrm{cnd}}, \{f_{\mathrm{cnd,rel}}\}\}} P_{\mathrm{AR}}(f'). \tag{5.25}$$

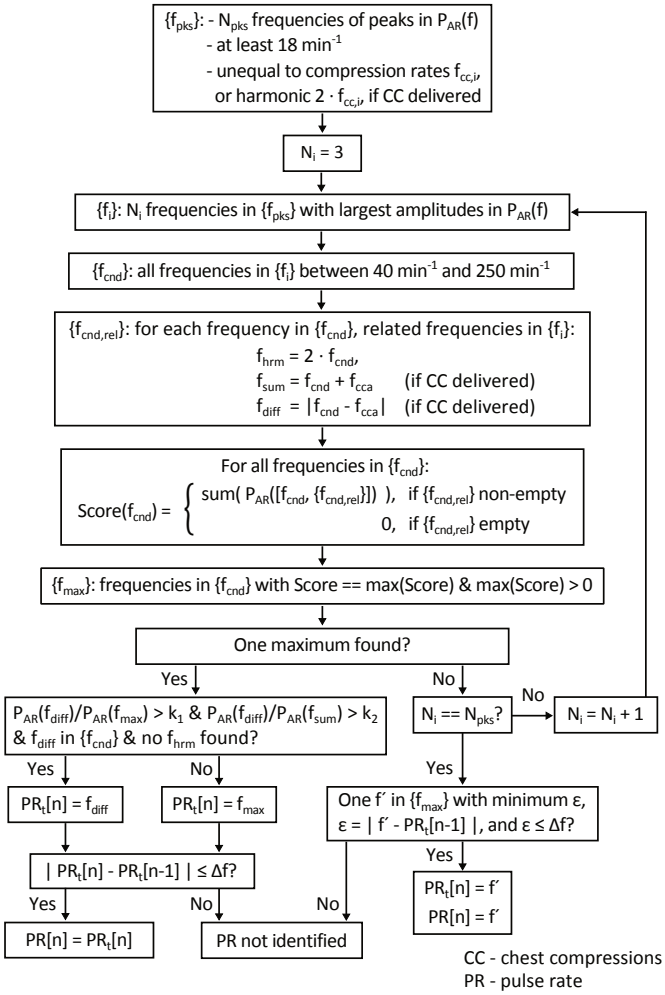

Figure 5.2: Flow chart of the iterative algorithm that identified the PR among the peaks in the PSD $P_{\mathrm{AR}}(f)$, by searching for one harmonic frequency f_{hrm}, one sum interaction frequency f_{sum}, and one difference interaction frequency f_{diff}. Sets of frequencies are shown between curly brackets. Frequency is in min^{-1}. CC: chest compressions; PR: pulse rate; PSD: power spectral density.

PR candidates without related frequencies had score zero. The scoring mechanism is related to Hinich's harmogram, where harmonics are added to detect a frequency [73]. PR candidates with a score equal to the strictly positive maximum of all scores were collected in the set $\{f_{\max}\}$. If there was one maximum with frequency $f_{\max}$, iterations stopped and a tentative identification $\mathrm{PR}_t[n]$ was obtained. If $f_{\max}$ had no associated harmonic f_{hrm}, but did have associated interaction frequencies f_{sum} and f_{diff}, with $P_{\mathrm{AR}}(f_{\mathrm{diff}})/P_{\mathrm{AR}}(f_{\max}) > k_1 > 1$ and $P_{\mathrm{AR}}(f_{\mathrm{diff}})/P_{\mathrm{AR}}(f_{\mathrm{sum}}) > k_2 > k_1$, with f_{diff} in $\{f_{\mathrm{cnd}}\}$, then $\mathrm{PR}_t[n] = f_{\mathrm{diff}}$. That is, based on the decreasing spectral amplitudes, f_{diff} was considered the PR, and both $f_{\max}$ and f_{sum} were considered sum interaction frequencies. However, if one of these conditions was not met, $\mathrm{PR}_t[n] = f_{\max}$. Next, if the difference between the current and previous tentative identifications was at most Δf, the final identification was $\mathrm{PR}[n] = \mathrm{PR}_t[n]$. Otherwise, $\mathrm{PR}[n]$ could not be identified. If there was not one strictly positive maximum score, $\{f_{\max}\}$ was either empty, occurring when there were no related frequencies, or $\{f_{\max}\}$ contained multiple frequencies, occurring, e.g., when $\{f_i\}$ only contained the PR and one interaction frequency. In this case, the next iteration was performed. If $\{f_{\max}\}$ contained multiple frequencies when all N_{pks} peaks had been analyzed, it was determined whether $\{f_{\max}\}$ contained one frequency f' with minimum deviation $\epsilon = |\mathrm{PR}_t[n-1] - f'|$, with $\epsilon \leq \Delta f$. If so, $\mathrm{PR}[n] = \mathrm{PR}_t[n] = f'$, otherwise $\mathrm{PR}[n]$ and $\mathrm{PR}_t[n]$ could not be identified.

Parameters $k_1 = 3$ and $k_2 = 10$ were determined from the amplitude ratio observed between the associated peaks in the PSDs. Parameter $\Delta f = 15$ min^{-1} was determined from the frequency deviations observed in the PSDs.

5.2.6.3 Evaluation

The PR detection was evaluated in the 2-min cycle before the post-ROSC phase. Detection was considered correct if a PR was observed in the ABP, and if the detected PR was within 15 min^{-1} of the PR observed in the ABP spectrogram, and in the ABP signal during ventilations. The number of correct PR detections over the total number of PR detections was determined per animal and overall. The evaluation shows whether the detected PR can qualify the cardiac condition, but does not give the quantitative accuracy of the detected PR. From ABP signals identically high-pass filtered as PPG signals (Section 5.2.2) spectrograms were obtained using 10 s windows, translated by 1 s, and zero-padded to 60 s.

5.2.7 Detection of blood volume redistribution to the periphery

When PR and compression rate coincide, the compression reduction stage also reduces the spontaneous pulse component, making the compression-reduced PPG signal unusable. However, when cardiogenic output resumed, a transient change in skin color could be observed, presumably caused by a redistribution of blood

volume to the periphery and leading to a sudden decrease in the baseline of the near-IR PPG signal. We used the sudden decrease in baseline as an extra parameter to detect cardiogenic output, to accommodate for coinciding PR and compression rate.

The baseline of the near-IR PPG signal, $ppg_{\mathrm{bl\_d}}[n]$, was obtained by a cascade of three first-order Butterworth low-pass filters with a 0.5-Hz cut-off applied to the raw signal $ppg[n]$. Each filtering operation was followed by down-sampling by a factor of two. Therefore, $ppg_{\mathrm{bl\_d}}[n]$ was sampled at $f_{s\_d} = 31.25$ Hz.

To detect a sudden decrease in $ppg_{\mathrm{bl\_d}}[n]$, a least-squares regression line ρ_n was fitted in a window of N_{bl} (odd) samples:

$$\rho_n[n-m] = \beta_n \left[\frac{N_{bl}-1}{2} - m \right] + \gamma_n, \quad m = 0, ..., N_{bl}-1. \tag{5.26}$$

A sudden decrease in $ppg_{\mathrm{bl\_d}}[n]$ was detected if the normalized rate of change

$$\Delta_{bl}[n] = \beta_n (N_{bl}-1)/\gamma_n < \Delta_{BL}, \tag{5.27}$$

with threshold $\Delta_{BL} < 0$ [$(N_{bl}$ samples$)^{-1}$]. Equation (5.27) was evaluated once per second. N_{bl} and Δ_{BL} were determined by inspecting the decrease in baseline for the animals with ROSC.

5.2.8 Indicator of cardiogenic output

To support ROSC assessment and interpretation of the compression-reduced PPG signal, the algorithm determined the state of an indicator of cardiogenic output, S_{ICO}:

- $S_{\mathrm{ICO}} = 0$: no PR and no decrease in $ppg_{\mathrm{bl\_d}}[n]$ were detected, i.e., "No detection" (red) in Fig. 5.1.
- $S_{\mathrm{ICO}} = 1$: a decrease in $ppg_{\mathrm{bl\_d}}[n]$ was detected, i.e., "Redistribution of blood volume to the periphery detected" (yellow) in Fig. 5.1.
- $S_{\mathrm{ICO}} = 2$: a PR was detected in $P_{\mathrm{AR}}(f)$, i.e., "PR detected" (green) in Fig. 5.1.
- $S_{\mathrm{ICO}} = 3$: a PR and a decrease in $ppg_{\mathrm{bl\_d}}[n]$ were detected, i.e., states 1 and 2 held simultaneously (yellow and green in Fig. 5.1).

The state of the indicator S_{ICO} was determined once per second.

5.2.9 Validation of the indicator

To validate whether the indicator can support ROSC assessment, the indicator S_{ICO} was compared to the retrospective ROSC assessment of nine clinicians, who worked in the emergency department, operating room, intensive care unit or

quick response team of the St. Elisabeth hospital in Tilburg, the Netherlands. The clinicians were requested to assess at what time instant ROSC occurred in each experiment, so they would stop CPR. For this assessment, we provided the ECG, ABP, capnography, and carotid artery blood flow signals, as recorded over the entire experiment. We indicated upfront that the animals achieved ROSC. A ROSC annotation trace, indicating the number of clinicians having detected ROSC over time, was constructed from the provided time instants.

We used five parameters to quantify the performance of the indicator S_{ICO}. In the 2-min cycle before the post-ROSC phase, the time difference $\Delta T = T_I - T_C$ [s] was determined. We defined T_I as the time instant after which S_{ICO} contained no further episodes of $S_{\mathrm{ICO}} = 0$ which lasted 5 s or longer. We interpreted T_I as the start of consistent detection of cardiogenic output by S_{ICO}. We defined T_C as the median of the time instants at which the clinicians detected ROSC, to exclude early and late detections. Specificity and sensitivity were determined for S_{ICO} and the PR detection. Comparing the specificities and sensitivities shows the contribution to S_{ICO} by the detection of decreases in $ppg_{\mathrm{bl\_d}}[n]$. The specificity $SpICO$ was defined as the percentage of correct cardiac arrest detections by $S_{\mathrm{ICO}} = 0$ in the 20-min CPR period during cardiac arrest. The specificity $SpPR$ was defined as the percentage of non-identified PRs in this period. The sensitivity $SeICO$ was defined as the percentage of correct detections of cardiogenic output by $S_{\mathrm{ICO}} \neq 0$ between T_C and the start of the post-ROSC phase. The sensitivity $SePR$ was defined as the percentage of identified PRs in this period.

5.3 Results

For consistency, the animal numbering from Chapter 4 and [203] has been adopted. Animals N1 - N3 had no sustained ROSC. Animals R1 - R9 had sustained ROSC. Animal N1 briefly had ROSC, but deteriorated to cardiac arrest again. For unambiguous annotation, the brief post-ROSC phase and the preceding 2-min cycle have been excluded from the data of animal N1.

To develop the algorithm, we used data from 10 out of 16 animals. As in Chapter 4 and [203], four animals were excluded because the pulse oximeter probe interfered with the study PPG probe. This was resolved by increasing the distance between the probes. Further, animals R5 and R9 were excluded, because the snout of R5 was poorly perfused due to complications with the carotid arteries, and because for R9 no TTI signal was recorded.

5.3.1 Determination of compression characteristics

Figure 5.3 illustrates filtering of the measured TTI signal $Z[n]$ (Fig. 5.3a) to obtain the fundamental compression component in $Z_f[n]$ (Fig. 5.3b). Local extremes were detected in $Z_f[n]$ (blue circles) to identify the onsets of the individual compressions (red squares). Ventilation effects were partly suppressed in $Z_f[n]$.

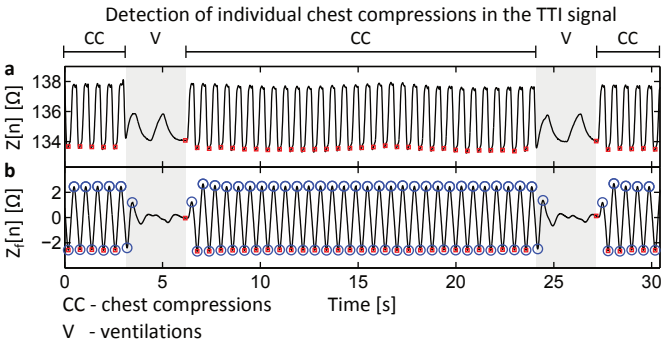

Figure 5.3: (a) Measured TTI signal $Z[n]$. (b) Band-pass filtered TTI signal $Z_f[n]$ showing the fundamental compression component. Via the local extremes (blue circles) in $Z_f[n]$, the onsets of the individual compressions (red squares) are found. CC: chest compressions; TTI: trans-thoracic impedance; V: ventilations.

Table 5.1: Results of compression rate detection and compression component reduction.

Animal	$f_{cc,i}$ [min^{-1}]	Δcmp [%]
N1	100.0±1.2	76.8±4.6
N2	99.7±1.2	83.2±4.1
N3	100.0±4.0	77.4±12.5
R1	100.0±0.9	78.1±6.6
R2	99.8±0.6	69.6±8.8
R3	99.8±0.6	72.6±7.8
R4	99.9±1.2	85.7±4.3
R6	99.8±1.3	80.8±3.8
R7	100.0±0.6	82.7±2.3
R8	99.9±1.4	78.1±11.4
Mean	99.9±1.7	78.6±8.7

No ROSC: N1-3. ROSC: R1-4, R6-8. $f_{cc,i}$: compression rate. Δcmp: compression component reduction during cardiac arrest. Results in mean ± standard deviation. ROSC: return of spontaneous circulation.

The compression rate $f_{cc,i}$ and phase $\phi_{cc}[n]$ ((5.5) and (5.7)), and the envelope function $A[n]$ were determined from the onsets. Compression rate $f_{cc,i}$ was found accurately, fluctuating slightly around 100 min^{-1} (Table 5.1). Only for animal N3 fluctuations in $f_{cc,i}$ were larger, due to a lower-quality TTI signal.

5.3.2 Reduction of the compression component

Figure 5.4 illustrates reduction of the compression component by a representative example. The defibrillation shock (dashed line) ended cardiac arrest, after which a spontaneous pulse appeared. During arrest, the PPG signal $ppg_{\mathrm{ac}}[n]$ in Fig. 5.4a showed the 30:2 CPR rhythm. When a spontaneous pulse appeared, the complexity of $ppg_{\mathrm{ac}}[n]$ increased during compressions. During arrest, the compression estimate $cmp_{\mathrm{est}}[n]$ in Fig. 5.4b was almost identical to the compressions in $ppg_{\mathrm{ac}}[n]$. When a spontaneous pulse appeared, $cmp_{\mathrm{est}}[n]$ changed shape. This was due to the harmonic of the PR at about 300 min^{-1}, which was close to a harmonic of the compression rate. Figure 5.4c shows the compression-reduced PPG signal $ppg_{\mathrm{cr}}[n]$ obtained by subtracting $cmp_{\mathrm{est}}[n]$ from $ppg_{\mathrm{ac}}[n]$. The compression component was strongly reduced in $ppg_{\mathrm{cr}}[n]$, although a decaying residual was present in $ppg_{\mathrm{cr}}[n]$ at the start of a new compression sequence. During ventilations, the envelope function $A[n]$ forced $cmp_{\mathrm{est}}[n]$ to zero, leaving $ppg_{\mathrm{ac}}[n]$ unaffected in $ppg_{\mathrm{cr}}[n]$. During arrest, $ppg_{\mathrm{cr}}[n]$ showed absence of a spontaneous pulse. During the first compression sequence after the shock, a spontaneous pulse appeared in $ppg_{\mathrm{cr}}[n]$. During compressions, the difference interaction frequency between the PR and the compression rate could be recognized as a low-frequency oscillation in $ppg_{\mathrm{cr}}[n]$, which disappeared when compressions stopped.

The spectrograms in Fig. 5.5 illustrate the effective reduction of the compressions. The PPG signal $ppg_{\mathrm{ac}}[n]$ (Fig. 5.5a) contained components at the compression rate and its harmonics during CPR, and components at the PR and its harmonics after successful defibrillation. The compression estimate $cmp_{\mathrm{est}}[n]$ (Fig. 5.5b) mainly contained the compression frequency components, but could also contain frequency components related to the spontaneous pulse when these were close to the compression components (shortly after 33:00). The components at the compression rate and its harmonics were strongly reduced in the compression-reduced PPG signal $ppg_{\mathrm{cr}}[n]$ (Fig. 5.5c). The interaction frequencies, however, remained present in $ppg_{\mathrm{cr}}[n]$. The spectra of $ppg_{\mathrm{ac}}[n]$ and $ppg_{\mathrm{cr}}[n]$ contained interaction frequencies between the defibrillation shock and 32:30.

Table 5.1 shows the reduction of the compression component, Δcmp. Overall, the algorithm achieved an average reduction of about 79%, where the average reduction per animal varied between about 70% and 86%. Two effects contributed to the variations in Δcmp across the animals. First, $ppg_{\mathrm{cr}}[n]$ contained a residual compression component which decayed throughout a compression series, as is illustrated in Fig. 5.4c. The residual compression component was larger at the beginning of a compression series, due to the deviation of the compression components at the beginning of a series compared to those at the end of the preceding series. The deviation in compression components at the beginning and end of a series varied across the animals, contributing to variations in Δcmp. Second, in some animals low-frequency oscillations with a period on the order of seconds were observed in $ppg_{\mathrm{ac}}[n]$ during compressions. These oscillations remained unaffected in $ppg_{\mathrm{cr}}[n]$ and decreased the measured reduction of the compression component.

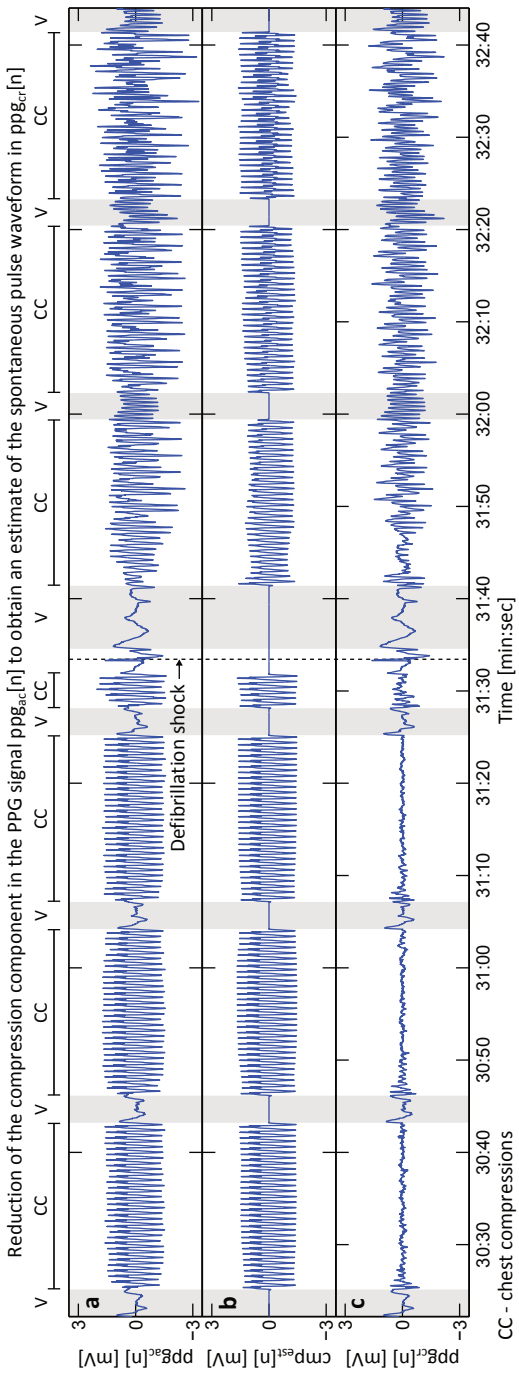

Figure 5.4: (a) Band-pass filtered PPG signal $ppg_{\mathrm{ac}}[n]$. (b) Compression estimate $cmp_{\mathrm{est}}[n]$. (c) Compression-reduced PPG signal $ppg_{\mathrm{cr}}[n]$ obtained by subtracting $cmp_{\mathrm{est}}[n]$ from $ppg_{\mathrm{ac}}[n]$. Before the defibrillation shock (dashed line), a spontaneous pulse is absent in $ppg_{\mathrm{cr}}[n]$. During the first compression sequence after the shock, a spontaneous pulse appears in $ppg_{\mathrm{cr}}[n]$. This episode is part of the spectrograms in Fig. 5.5. CC: chest compressions; PPG: photoplethysmography; V: ventilations.

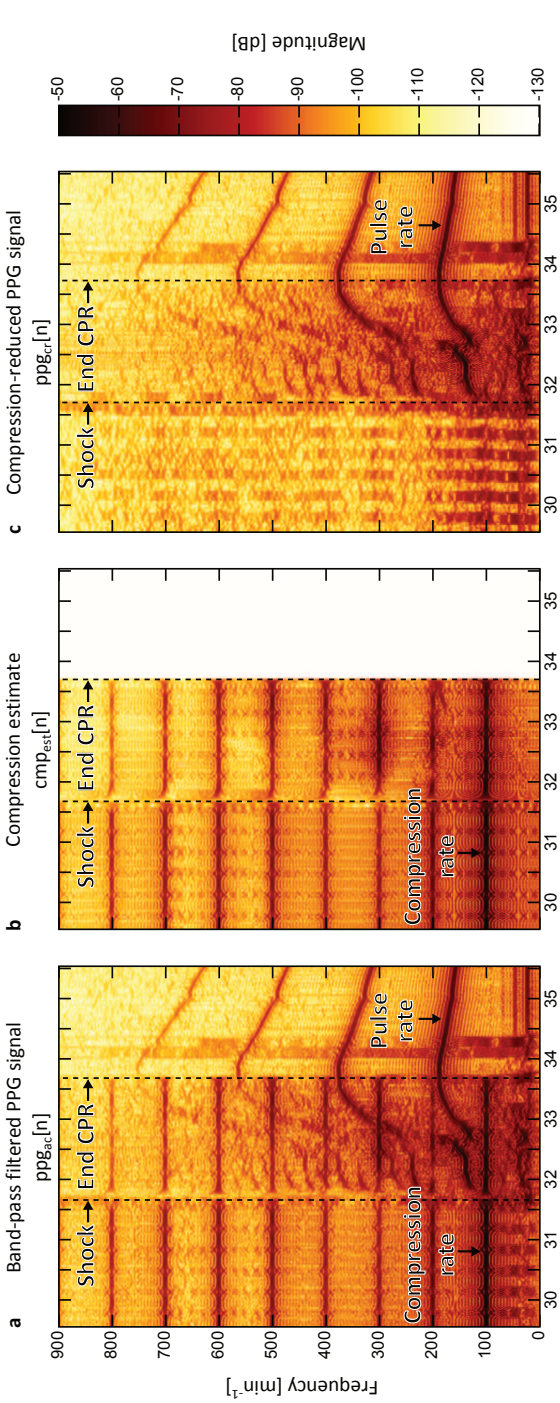

Figure 5.5: Spectrograms of (a) the PPG signal $ppg_{\mathrm{ac}}[n]$, (b) the compression estimate $cmp_{\mathrm{est}}[n]$, and (c) the compression-reduced PPG signal $ppg_{\mathrm{cr}}[n]$ show effective reduction of the components at the compression rate and its harmonics in $ppg_{\mathrm{cr}}[n]$, by subtracting $cmp_{\mathrm{est}}[n]$ from $ppg_{\mathrm{ac}}[n]$. After the defibrillation shock (first dashed line) a spontaneous pulse appears, which continues when CPR stops (second dashed line). The spectrograms have been obtained from 10 s windows, translated by 1 s, and zero-padded to 60 s. They contain the episode of Fig. 5.4. CPR: cardiopulmonary resuscitation; PPG: photoplethysmography.

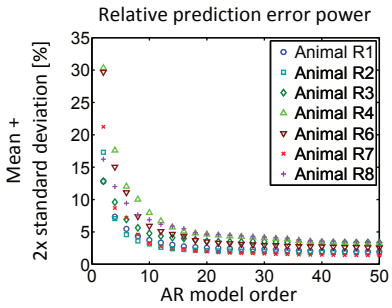

Figure 5.6: Mean plus two standard deviations of the prediction error power relative to the compression-reduced PPG signal power as a function of AR model order for all animals with ROSC. AR: autoregressive; PPG: photoplethysmography; ROSC: return of spontaneous circulation.

5.3.3 AR model order

Figure 5.6 shows the mean plus two standard deviations of the relative prediction error power as a function of AR model order N_{AR}, which was at most 5% by selecting $N_{\mathrm{AR}} = 18$.

5.3.4 Spectral analysis

Figure 5.7 illustrates the spectral analysis. The PR detection algorithm (Fig. 5.2) analyzed the peaks in the PSD $P_{\mathrm{AR}}(f)$ ((5.20), Fig. 5.7a) to identify the PR, if a signal was detected in the compression-reduced PPG signal $ppg_{\mathrm{cr\_d}}[n]$ ((5.21), SIG in Fig. 5.7b), with sufficient high-frequency content ((5.22), FD in Fig. 5.7b). The SIG and FD conditions prevented analyzing most PSDs before the defibrillation shock (dashed line), when the animal was in cardiac arrest. When a PR was identified (black dots in Fig. 5.7c), typically 3-4 peaks had been analyzed (purple dots in Fig. 5.7c) out of all peaks (blue circles in Fig. 5.7c). During cardiac arrest, false PR detections occurred due to peaks deviating more than 5 min^{-1} from the compression rate or its second harmonic, as illustrated in Fig. 5.7c. When the heart resumed cardiogenic output, 86% of the detected PRs was within 15 min^{-1} of the PRs observed in the ABP and was therefore considered correct (PR in Table 5.2). Comparing Fig. 5.7c to the ABP spectrogram in Fig. 5.7d shows 11 incorrect detections after the shock. Incorrect detections of the PR harmonic or a residual compression component at about 200 min^{-1} occurred from 31:37 to 31:39, from 32:04 to 32:08, and at 32:16. Two more incorrect detections occurred at 32:44 and 32:45. The remaining detected PRs were recognized as a PR in the ABP spectrogram, and were therefore considered correct. Between 32:09 and 32:23 no PR was detected, except for one false detection, when no relationships were found between the peaks.

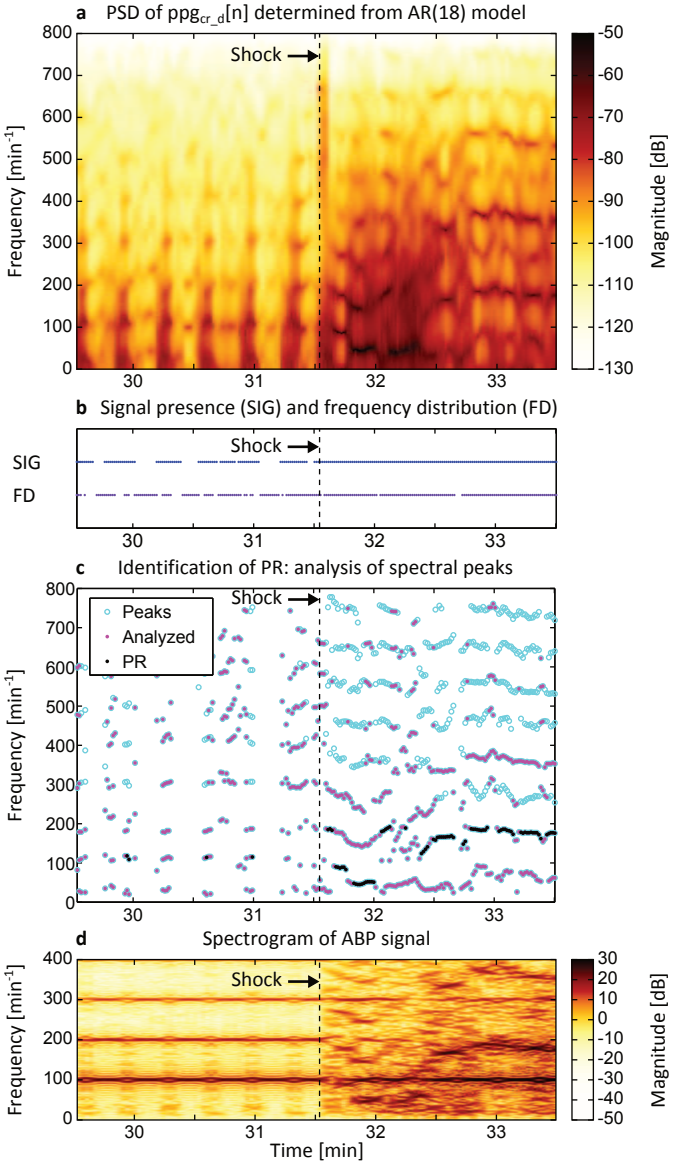

Figure 5.7: (a) The PSD $P_{\mathrm{AR}}(f)$ of the compression-reduced PPG signal $ppg_{\mathrm{cr\_d}}[n]$, obtained from an order-18 AR-model. (b) Dots indicate detection of a signal in $ppg_{\mathrm{cr\_d}}[n]$ (SIG, (5.21)) having sufficient high-frequency content (FD, (5.22)). If both conditions hold, PR detection is performed. (c) The PR detection algorithm analyzes a number (purple dots) of all peaks in the PSD (blue circles) to identify the PR (black dots). (d) The spectrogram of the ABP signal is used to evaluate the PR detection. The dashed line indicates the defibrillation shock. ABP: arterial blood pressure; AR: autoregressive; PR: pulse rate; PPG: photoplethysmography; PSD: power spectral density.

Table 5.2: Evaluation of the PR detection and the indicator of cardiogenic output.

Animal	PR		ΔT [s]	*SpPR*		*SpICO*		*SePR*		*SeICO*	
N1	n.a.	n.a.	n.a.	100%	(1669/1669)	100%	(1664/1669)	n.a.	n.a.	n.a.	n.a.
N2	n.a.	n.a.	n.a.	100%	(1821/1825)	99%	(1815/1825)	n.a.	n.a.	n.a.	n.a.
N3	n.a.	n.a.	n.a.	95%	(1685/1766)	95%	(1676/1766)	n.a.	n.a.	n.a.	n.a.
R1	77%	(49/64)	25	92%	(1125/1226)	88%	(1081/1226)	70%	(55/79)	72%	(57/79)
R2	85%	(66/78)	46	91%	(1056/1161)	87%	(1006/1161)	74%	(74/100)	77%	(77/100)
R3	56%	(9/16)	96	97%	(1271/1311)	96%	(1254/1311)	14%	(14/101)	22%	(22/101)
R4	82%	(40/49)	69	97%	(1117/1151)	94%	(1083/1151)	52%	(49/94)	76%	(71/94)
R6	86%	(65/76)	69	90%	(1080/1206)	89%	(1078/1206)	64%	(63/98)	64%	(63/98)
R7	98%	(100/102)	-16	97%	(1169/1207)	95%	(1150/1207)	96%	(89/93)	96%	(89/93)
R8	91%	(40/44)	3	99%	(1196/1214)	90%	(1098/1214)	75%	(44/59)	83%	(49/59)
Mean	86%	(369/429)	42±40	96%	(13189/13736)	94%	(12905/13736)	62%	(388/624)	69%	(428/624)

No ROSC: N1-3. ROSC: R1-4, R6-8. Mean ΔT in mean ± standard deviation. Correct detections over occurrences in parentheses. $\Delta T = T_I - T_C$, $T_{I,C}$: detection moment of ICO (I) and clinicians (C); *SpPR*: specificity PR detection; *SpICO*: specificity ICO; *SePR*: sensitivity PR detection; *SeICO*: sensitivity ICO. ICO: indicator of cardiogenic output; n.a.: not applicable; PR: pulse rate; ROSC: return of spontaneous circulation.

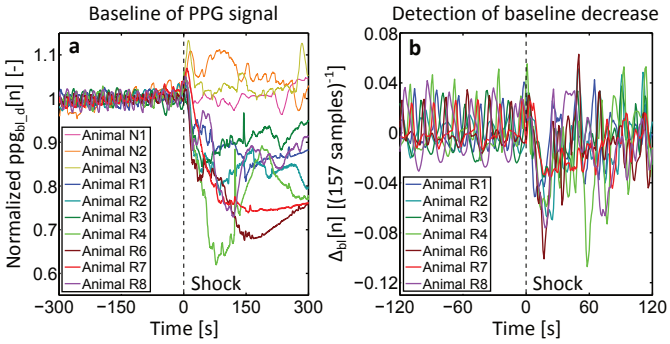

Figure 5.8: (a) In animals with ROSC (thick lines), the baseline of the PPG signal shows a pronounced decrease when cardiogenic output resumes. Without ROSC (thin lines), such decrease is absent. The spikes in the traces of R3 and R4 are motion artifacts caused by changing the ventilator. Each baseline has been normalized by its mean over the 5 min preceding the shock. (b) The baseline decrease can be detected when $\Delta_{bl}[n]$ decreases below -0.03 when using 5 s windows. All signals have been aligned with respect to the defibrillation shock at 0 s. PPG: photoplethysmography; ROSC: return of spontaneous circulation.

5.3.5 Detection of blood volume redistribution to the periphery

Figure 5.8a shows that a pronounced decrease in the baseline of the PPG signal occurred, lasting at least 10 s, when cardiogenic output resumed in the animals with ROSC (thick lines). In contrast, this decrease was absent in animals without ROSC (thin lines). The decrease observed when cardiogenic output resumed could be detected by using $N_{bl} = \lceil 5 \cdot f_{s\_d} \rceil = 157$ and $\Delta_{BL} = -0.03$ (Fig. 5.8b). With these parameters, most fluctuations in baseline during cardiac arrest were not detected.

5.3.6 Validation of the indicator

Figure 5.9 presents the compression-reduced PPG signal $ppg_{\mathrm{cr\_d}}[n]$ (blue traces) of the animals with ROSC, the state of the indicator of cardiogenic output S_{ICO} (dots) and the ROSC annotation trace (black traces). The waveform and indicator showed good agreement with the annotations. When clinicians detected ROSC, a spontaneous pulse was often present in $ppg_{\mathrm{cr\_d}}[n]$ and blood volume redistribution was detected. In animal R3, the spontaneous pulse occasionally had a PR of about 100 min^{-1} and was therefore removed in $ppg_{\mathrm{cr\_d}}[n]$ by the compression reduction stage, although $ppg_{\mathrm{cr\_d}}[n]$ then still showed presence of a spontaneous pulse during the ventilation periods. In animal R8 the spontaneous pulse appeared clearly only after the majority of clinicians detected ROSC. In animals R1, R4 and R8 blood volume redistribution had been detected before the first clinician detected ROSC.


Detection of cardiogenic output via the PPG signal during CPR after a successful defibrillation shock
Animal R1
Animal R2
Animal R3
Animal R4
Animal R6
Animal R7
Animal R8
Annot
Time [min:sec]
ppg_cr: compression-reduced PPG signal, ppg_cr_d[n] [mV], containing an estimate of the spontaneous pulse waveform.
S_ICO: indicator of cardiogenic output (dots): (0) no detection (1) decrease in PPG baseline detected (2) PR detected (3) PR and decrease in PPG baseline detected.
Annot: ROSC annotation trace (black line) showing the number of clinicians having detected ROSC over time.

Figure 5.9 ***(previous page)*****:** The compression-reduced PPG signal $ppg_{\mathrm{cr\_d}}[n]$ (blue traces) (a,c,e,g,i,k,m) combined with the indicator of cardiogenic output S_{ICO} (dots) (b,d,f,h,j,l,n) can potentially support ROSC detection, given the good agreement with the annotations of the clinicians (black traces) (b,d,f,h,j,l,n). Solid green lines mark T_C, the median time instant at which clinicians detected ROSC. Dashed green lines mark T_I, the moment after which interruptions in S_{ICO} are shorter than 5 s. Traces start at the defibrillation shock. The first five oscillations in (a) are unfiltered compressions, due to incorrect detections in the TTI signal. CPR: cardiopulmonary resuscitation; PPG: photoplethysmography; PR: pulse rate; ROSC: return of spontaneous circulation; TTI: trans-thoracic impedance.

For all animals in Fig. 5.9, the indicator showed presence of cardiogenic output before the majority of the clinicians detected ROSC at time instant T_C, although consistent detection, on average, occurred only 42 s after T_C (ΔT in Table 5.2). By combining the detection of PR with decreases in PPG signal baseline in the indicator, the average specificity decreased from $SpPR = 96\%$ to $SpICO = 94\%$, but the average sensitivity increased from $SePR = 62\%$ to $SeICO = 69\%$ (Table 5.2). False detections of cardiogenic output by the indicator occurred in nine animals when CPR was started after cardiac arrest induction, when redistributing blood volume caused a decrease in the PPG signal baseline. False detections of cardiac arrest by the indicator were due to undetected PRs, caused by coinciding of the compression rate and the PR or their harmonics, $ppg_{\mathrm{cr\_d}}[n]$ not meeting the conditions on signal presence (Section 5.2.6.1), or irregularity of $ppg_{\mathrm{cr\_d}}[n]$. However, when no PR was detected and the fundamental PR component had not been removed, $ppg_{\mathrm{cr\_d}}[n]$ could still show presence of a spontaneous pulse, and whether the spontaneous pulse had a regular or an irregular rhythm.

5.4 Discussion

Based on automated-CPR porcine data, we developed an algorithm that detected cardiogenic output in a near-IR PPG signal during chest compressions (Fig. 5.1). A compression-reduced PPG signal was obtained by subtracting the compression component as modeled by a harmonic series. The fundamental frequency of the series was the compression rate, which could be accurately derived from good-quality TTI signals (Fig. 5.3 and Table 5.1). During automated CPR, when compression rate and depth are controlled, the RMS amplitude of the compression component was effectively reduced by about 79% (Figs. 5.4 and 5.5, and Table 5.1). Via an AR model, the PSD of the compression-reduced PPG signal $ppg_{\mathrm{cr\_d}}[n]$ could be accurately obtained (Fig. 5.6). The AR model allowed for detecting signal presence, and the PR could be identified in the PSD by searching for a harmonic of the PR and sum and difference interaction frequencies (Figs. 5.2 and 5.7). When cardiogenic output resumed, the detected PR agreed for 86% with

the PR observed in the ABP (Table 5.2). Incorrect PR detections resulted from residual compression components, inadvertent removal of frequencies related to the spontaneous pulse, or irregularities in $ppg_{\mathrm{cr\_d}}[n]$. The spontaneous pulse was removed from $ppg_{\mathrm{cr\_d}}[n]$ when the PR was close to the compression rate (Fig. 5.9e). To accommodate for coinciding PR and compression rate, decreases in the baseline of the PPG signal were detected. Decreases in baseline occurred when cardiogenic output resumed (Fig. 5.8), presumably caused by a redistribution of blood volume to the periphery. The indicator of cardiogenic output had a good specificity of 94% and a reasonable sensitivity of 69% (Table 5.2).

The compression-reduced PPG signal and the indicator of cardiogenic output can potentially support ROSC detection during compressions, as is illustrated by the good agreement with the ROSC annotation trace (Fig. 5.9 and Table 5.2). The 94% specificity suggests that a PPG-based indicator can support detecting absence of cardiogenic output during compressions. In addition, Fig. 5.9 shows that the indicator could detect presence of cardiogenic output before the majority of the clinicians detected ROSC, which suggests that a PPG-based indicator could also provide an early indication of ROSC or its development. Furthermore, Fig. 5.9 illustrates that the compression-reduced PPG signal can be more valuable to the clinician than the indicator alone. For example, the waveform can show presence of a spontaneous pulse when the PR cannot be determined, and allows for assessing the regularity of the spontaneous pulse during compressions. Therefore, this algorithm could support the clinician in deciding when it is appropriate to further assess a potential ROSC after a 2-min CPR cycle, although a single PPG signal does not provide quantitative information on blood pressure [146].

Detecting cardiogenic output during compressions can also support decision making in the CPR protocol. Information on cardiogenic output may support tailoring the duration of the compression sequence and medication choices to the clinical state of the patient [128]. Detecting absence of cardiogenic output during compressions may prevent interrupting compressions for futile and lengthy pulse checks [199]. Preventing unnecessary interruptions in compressions increases the chest compression fraction during CPR, which may increase the probability of achieving ROSC [181]. Detecting presence of cardiogenic output during compressions may possibly guide stopping compressions to reduce the risk of refibrillation, which is associated with sustained compressions on a beating heart [20,86,130,131,164]. Furthermore, detecting cardiogenic output during compressions may guide administration of vasopressors, which may have detrimental effects if administered when the heart has just resumed cardiogenic output [120].

The algorithm needs further improvement for clinical application, although 94% specificity is promising. Reduction of the compression component was feasible in automated-CPR data, achieving a reduction in the RMS amplitude of about 79% (Table 5.1). However, Fig. 5.4 also shows a slowly-decaying residual compression component in $ppg_{\mathrm{cr}}[n]$ at the beginning of a compression series, which indicates that the algorithm cannot track rapid variations in the compression component. Therefore, the varying compression rate and depth in manual CPR

can require faster adaptation to changes in the PPG compression component, and also adaptive thresholds for TTI-based compression detection [13, 15, 154]. In the small pre-clinical data set, parameter values were not extensively optimized. In a large clinical data set, optimization can be performed and adaptive thresholds further investigated, to improve the algorithm performance as required for clinical application. The algorithm could operate in real-time, despite that compression detection is delayed by two compressions, and AR and regression analysis operate on 5-s windows. Real-time operation can require an efficient implementation of AR analysis.

This study has limitations. First, we used porcine data obtained during automated CPR in a controlled laboratory environment. A clinical CPR study should show the ability of central and peripheral PPG signals to indicate cardiogenic output in humans during CPR [24, 120], and the suitability of the baseline of the PPG signal to support ROSC detection. Second, compressions and ventilations were alternated. The influence of ventilations during compressions on TTI-based compression detection should be further investigated [15].

5.5 Conclusions

Detecting cardiogenic output during chest compressions using a PPG-based algorithm is feasible in automated-CPR porcine data with a high specificity (94%). The compression component in the PPG signal can be effectively reduced (79%), by subtracting an estimate of the compression component as modeled by a harmonic series. The compression rate, which is the fundamental frequency of the harmonic series, can be accurately derived from the TTI signal. The resulting compression-reduced PPG signal contains an estimate of the underlying spontaneous pulse waveform. The PR can be detected in the AR spectrum of the compression-reduced PPG signal by identifying a harmonic and interaction frequencies. Resumed cardiogenic output can also be detected from a decrease in the baseline of the PPG signal, presumably caused by a redistribution of blood volume to the periphery. ROSC detection can potentially be supported by combining the compression-reduced PPG signal with an indicator of cardiogenic output based on the detected PR and redistribution of blood volume.

CHAPTER 6

General discussion and future directions for research

6.1 Artifact reduction in PPG

Photoplethysmography (PPG) measurements have been widely applied in hospital settings [10,88], mostly via the application of pulse oximetry to measure pulse rate (PR) and peripheral arterial functional-hemoglobin oxygen-saturation (SpO_2). Pulse oximetry has been standard of care in the operating room since 1990 and in the recovery room since 1992 [19]. Currently, PPG is getting more widely applied in ambulatory settings. For instance, PPG has been integrated in sports watches to measure PR during exercise [170,177]. These watches are also being researched for medical applications. PPG-based measurement of changes in PR could for instance indicate epileptic seizures [183]. And beat-to-beat analysis of ambulatory measured PPG signals could be relevant for the detection of atrial fibrillation [23, 45]. Furthermore, ambulatory pulse oximetry monitoring can be important in the context of long-term oxygen therapy and titration of supplemental oxygen to the needs of the patient [44].

PPG signals are highly susceptible to motion [10,14,140,177]. Motion artifacts in PPG signals are spurious fluctuations which complicate the detection of the cardiac component. Motion artifacts can be caused by motion of the PPG sensor relative to the skin [10, 33, 65, 66, 72, 108], acceleration-induced sloshing of blood [33, 57, 109, 137, 140, 211], and deformation of the illuminated tissue volume by dynamic variations in sensor contact-pressure [14, 33, 65, 66, 109, 140, 177, 179]. Furthermore, motion can cause the PPG sensor to variably loose contact with the skin, which can cause variations in the amount of ambient light reaching the photodiode [14, 65, 188].

In this thesis, we investigated motion artifacts caused by motion of the PPG sensor relative to the skin, as described in Chapter 2. First, a convenient method was developed to measure relative sensor motion via a laser diode and self-mixing interferometry (SMI) [201]. Via SMI, the monitor diode of the laser diode could measure the Doppler frequency-shift of laser-light which was back-scattered from a moving object and re-entered the laser cavity. The displacement of the laser diode could be derived from the measured Doppler frequencies. Via SMI we could use a single component as a light source for the PPG measurement and as a sensor for the relative motion measurement. Second, an in-vitro skin perfusion phantom was developed to investigate the effect of relative sensor motion on PPG signals [201]. In-vitro PPG signals were measured by using the laser diode as a PPG light source. Artifacts were generated by dynamically varying the distance between the laser diode and the PPG photodiode. SMI could accurately measure displacement of the laser diode relative to the diffusely-scattering skin phantom. Good correlation was found between the laser displacement and the resulting artifacts in the in-vitro PPG signals [201].

The developed skin perfusion phantom was basic, including only optical effects. The effect of skin deformation was not included in the perfusion phantom, which is expected to occur concurrently when a PPG sensor moves relative to the skin. Furthermore, the laser diode was translated over the perfusion phantom to vary the distance between the PPG light source and the PPG photodiode to generate motion artifacts. Therefore, the laser diode made a one-dimensional motion with respect to the photodiode in the laboratory setup. When a PPG sensor moves relative to the skin, motion will be three-dimensional. When using a single laser diode to measure relative motion, this three-dimensional motion will be projected onto a single axis, which complicates the relationship between the SMI-derived relative motion measurement and the resulting artifact. Therefore, when using SMI-derived relative sensor motion for artifact reduction in PPG measurements on humans, we would expect a decreased performance compared to the results obtained in the laboratory.

A study was performed on healthy volunteers to test the performance of the SMI-derived relative sensor motion in a more realistic scenario, as described in Chapter 3. Red and near-infrared PPG signals were measured on the forehead with a commercially available PPG sensor. The PPG sensor was augmented with a laser diode to measure motion relative to the skin. An accelerometer was positioned on top of the PPG sensor to measure head motion. Quasi-periodic motion artifacts were generated by walking on a treadmill at various speeds. Although we recognize that motion is mostly irregular in clinical practice [179], we decided to study the effect of quasi-periodic motion because it can be of relevance in activities of daily living, and it is relevant during cardiopulmonary exercise testing (CPX) and cardiopulmonary resuscitation (CPR). Furthermore, algorithms may falsely detect a quasi-periodic motion artifact as a PR component [34].

Based on the data collected from the healthy volunteers, we developed an algorithm to estimate and remove motion artifacts from measured PPG signals

[200]. This algorithm is described in Chapter 3. Because quasi-periodic motion artifacts can occur in different applications of PPG, we decided to design an algorithm which is generic in nature. This algorithm tracked the step rate in a motion reference signal. The motion artifact was estimated via a harmonic series with frequencies related to the tracked step rate. Reduction of the motion artifacts was achieved by subtracting the estimated artifact from the measured PPG signal. The resulting artifact-reduced PPG signals provided more stable measurements of inter-beat-intervals and SpO_2.

The coefficients of the components of the harmonic series which modeled the motion artifacts were estimated from the measured motion-corrupted PPG signal. Therefore, only the measured signal was modeled, and no transfer function was estimated between the motion reference signal and the motion artifacts in the PPG signal. The motion reference signal was only used to determine the fundamental frequency of motion. This has the advantage that any desired number of harmonics can be generated in the harmonic series, and that the algorithm does not depend on the harmonic content of the motion reference signal and any (time-varying) difference in harmonics which possibly exists between the motion reference signal and the measured PPG signal.

In Chapter 3, we compared the relative sensor motion determined via SMI with the head motion determined via accelerometry as motion reference signals for the artifact reduction algorithm. We found that the accelerometry-derived reference signal was superior to the SMI-derived reference signal in terms of signal-to-noise ratio and in terms of the consistency in providing to the algorithm a frequency component at the step rate. In about half of the measurements, the SMI-derived reference signal did not consistently contain a frequency component at the step rate. It is plausible that this was caused by limited motion of the PPG sensor relative to the skin, although insufficient optical feedback into the laser diode may have contributed as well. Optical feedback was influenced by the subject-dependent distance between the laser diode and the skin, because a ball lens integrated into the laser diode package focused the laser light at a fixed distance. In the context of quasi-periodic motion artifacts we only needed to measure the fundamental frequency of motion, because we modeled the artifacts as harmonic series. Because the fundamental frequency of motion was reliably measured by the accelerometer, we recommend to use an accelerometer to obtain a motion reference measurement in this context.

The algorithm in Chapter 3 has been tested for slow and moderate speeds of walking between 4 and 8 km/h. Furthermore, the speeds of walking were imposed by a treadmill and therefore relatively constant. Further testing and development of the algorithm is needed to make it better suited for dealing with more variable periodic motion as can be expected in ambulatory settings, and for running where much more severe motion artifacts are expected. This could be done by acquiring PPG data during natural walking and running scenarios where the speed is not mechanically imposed.

The algorithms presented in Chapters 3 and 5 estimated the motion and compression artifacts by fitting a harmonic series with frequencies related to the step rate and the compression rate, respectively. The main difference in the approaches is in the determination of the step rate and the compression rate. In Chapter 3, the step rate was tracked via a frequency-locked loop (FLL). In Chapter 5, the compression rate was derived by detecting the individual compressions in the trans-thoracic impedance (TTI) signal. The overall detection of individual compressions was accurate in the TTI signals measured during the pre-clinical experiments, because the waveform typically had a good signal-to-noise ratio and the automated compressions produced reproducible fluctuations in the TTI signals. The compression reduction algorithm could also be quickly switched off, when no compressions were detected. However, this approach has a number of disadvantages. First, there is an intrinsic delay of two compressions, which need to be detected to make an estimate of the compression rate. Second, the detection of individual compressions was based on a number of criteria with empirically determined thresholds, which complicates the adjustment of the algorithm. Third, the adopted criteria make the algorithm sensitive to missing individual compressions which do not meet the empirically determined thresholds. The last disadvantage is especially relevant in the case of manual CPR, where a strong variation in wave shape of the TTI signal can make robust detection of all compressions and their onsets challenging. Therefore, we expect that using an FLL would be advantageous. The FLL can provide an estimate of the compression rate on a sample-to-sample basis without an inherent delay of two compressions, although the initial convergence to the actual compression rate can be slow. Furthermore, the proposed FLL with the second-order generalized integrator has only two parameters (Fig. 3.3), which makes adjustment easier. And lastly, we expect the FLL to be less sensitive to missing individual compressions due to variations in the compression duration, and due to variations in the shape of the compressions in the reference signal. On the other hand, we expect the FLL to provide an averaged compression rate, instead of a rate with compression-to-compression variations as obtained when detecting the individual compressions. Therefore, further research concerning the algorithm proposed in Chapter 3 could focus on adjusting the algorithm to remove the compression component from PPG signals measured during automated and manual CPR.

6.2 PPG in CPR

This thesis has also addressed the use of PPG during CPR intended to support clinicians with the detection of return of spontaneous circulation (ROSC). In current clinical practice, detection of ROSC typically involves pulse checks by manual palpation. The interpretation of manual palpation is unreliable and time-consuming [43, 113, 129, 178], and manual palpation requires interruption of the chest compressions [120]. Pulse checks by manual palpation may therefore lead

to long interruptions in the chest compressions, which reduce blood flow and can thereby negatively impact CPR outcome [21, 30, 36, 204].

Methods exist for more objective and more continuous assessment of ROSC. These methods are for instance monitoring of end-tidal CO_2 [39, 139], invasive blood pressure [133,151], or central venous oxygen saturation [150], which can also be applied during compressions. However, measurement of end-tidal CO_2 requires intubation, and measurement of invasive blood pressure and central venous oxygen saturation require placement of catheters with associated risks for the patient. Trans-thoracic impedance (TTI) measurements [100, 149, 153] and near-infrared spectroscopy (NIRS) [79, 134, 160] are non-invasive methods, but TTI is strongly influenced by compressions and NIRS may respond slowly upon ROSC. Doppler ultrasound is being researched as a non-invasive method to detect pulse absence and presence in the carotid artery, but this technique is sensitive to a correct placement over the carotid artery and is strongly influenced by chest compressions [89, 213]. The more objective methods are therefore less practical in use during CPR or cannot be used during ongoing compressions.

Generally, PPG is an easy-to-use and non-invasive technique to continuously measure a spontaneous pulse [10, 146], mostly applied in pulse oximetry systems in hospitals [88]. Initial attempts to use the pulse oximeter during CPR mostly aimed at obtaining feedback on the rate at which the chest compressions were delivered [208].

As described in Chapters 4 and 5, we demonstrated with data from a pre-clinical automated-CPR study that PPG can detect a spontaneous pulse during CPR, both in few-second pauses in compressions and during ongoing compressions [203]. When the spontaneous pulse rate and compression rate were different, PPG could also be used to detect the spontaneous pulse rate during compressions [203].

Based on our pre-clinical data, we developed an algorithm to detect cardiogenic output in a PPG signal during CPR, intended to support clinicians in the detection of ROSC [202], as described in Chapter 5. For automated CPR, the algorithm could estimate and reduce the compression component in the PPG signal. The resulting compression-reduced PPG signal contained an estimate of the underlying spontaneous pulse component. The algorithm also determined an indicator of cardiogenic output by detecting a spontaneous pulse rate, or a pronounced decrease in the baseline of the PPG signal. The algorithm could track the spontaneous pulse rate by analyzing the relationship between the spectral components of the compression-reduced PPG signal. Pronounced decreases in the baseline of the PPG signal were detected when the heart resumed beating and were presumably caused by a redistribution of blood volume to the periphery. The indicator of cardiogenic output showed good agreement with the occurrence of ROSC as annotated by clinicians. Therefore, we concluded that the proposed algorithm may support clinicians in the detection of ROSC during CPR.

Support in the detection of ROSC by PPG may have several advantages during CPR. First, an objective detection of absence of a spontaneous pulse may already offer benefits. During a pause in compressions, absence of a spontaneous

pulse in the PPG signal may be rapidly recognized, thereby potentially shortening unnecessary interruptions in compressions for the assessment of ROSC [199]. Already detecting absence of a spontaneous pulse during ongoing compressions may potentially prevent interrupting compressions for unnecessary and lengthy pulse checks [199]. Shortening or preventing unnecessary interruptions in compressions increases the chest compression fraction during CPR, which may increase the probability of achieving ROSC [181]. Second, an objective detection of presence of cardiogenic output via spontaneous pulses in the PPG signal or decreases in the baseline of the PPG signal may also bring several benefits, even without providing quantitative information on blood pressure or flow [146]. Detecting presence of cardiogenic output via PPG during compressions can support decision making in the CPR protocol. Information on cardiogenic output may support tailoring the duration of the compression sequence and the medication choices to the clinical state of the patient [128]. Detecting presence of cardiogenic output via PPG during compressions may possibly guide stopping compressions. A clinician may for instance decide to stop compressions when a stable and sufficiently high spontaneous pulse rate has been measured via PPG for a sufficiently long period of time. This may reduce the risk of refibrillation, which is associated with sustained compressions on a beating heart [20, 86, 130, 131, 164]. Detecting cardiogenic output during compressions may also guide administration of vasopressors, which may have detrimental effects if administered when the heart has just resumed beating [120].

The use of PPG during CPR has a fundamental limitation. PPG does not provide a quantitative (absolute) measure of blood pressure or flow [146]. PPG can only provide a measure related to local variations in blood volume in the illuminated tissue [10, 105, 146]. PPG has furthermore been shown to be very sensitive, which can be both an advantage and a disadvantage. In our pre-clinical study, PPG could already detect spontaneous pulses at blood pressure levels which could be considered sub-life-supporting [195]. Here, PPG-based detection of resumed beating of the heart can have the advantage of being early, but the disadvantage of occurring when the circulation is not life-sustaining. Therefore, PPG can only show whether the heart has resumed beating and, if so, what the associated pulse rate is. Further, a PPG signal in which the compression component has been strongly reduced could directly show whether the heart is beating regularly or irregularly. However, ROSC detection cannot be based on PPG measurements alone. In any case, ROSC detection remains a clinical situational assessment, because it involves determining whether a perfusing rhythm is life-sustaining.

As follow-up, a clinical study would be needed to determine whether PPG can support detection of ROSC in humans during CPR. In this study, central and peripheral sites should be assessed for the adequacy of PPG-based detection of cardiogenic output during CPR. A central site measurement could for instance be performed on the forehead, the nose or the ear, and a peripheral site measurement could be performed on the finger. A central-site PPG measurement may be preferred over a peripheral site, as centralization and the associated vasoconstriction

can severely compromise peripheral pulsatile blood flow [24,120,132]. The clinical study should also assess the ease of use of various PPG sensors and assess their compatibility with the current clinical workflow during CPR.

Recently, the use of PPG during CPR has received more attention. In [93], a pre-clinical study is described that is similar to our pre-clinical study in [203] and confirms our findings. A retrospective investigation of the PPG waveforms acquired by pulse oximeters in patients undergoing CPR showed that the morphology and frequency content of the PPG signal changed during compressions when the heart resumed beating [94], which confirms the findings in our pre-clinical studies. A case report of a patient undergoing extracorporeal life support describes that PPG signals measured centrally on the nasal septum and the ear pinna directly showed spontaneous pulses when the heart resumed beating, and that the PPG signal measured peripherally on the finger showed spontaneous pulses with a delay of about 50 s [74]. This suggests that a central-site PPG measurement in, e.g., the facial region, may be preferred over a peripheral-site PPG measurement on, e.g., the finger, for rapidly detecting presence of a spontaneous pulse. On the other hand, this may also suggest that the combination of a central-site and a peripheral-site PPG measurement may be beneficial, where the peripheral site may show presence of a spontaneous pulse once some level of spontaneous circulation has been achieved. The first clinical results are promising, but a more extensive clinical study on patients undergoing CPR with chest compressions is still warranted. Such a study can be designed to determine which site is most suited for PPG measurements during CPR. For various sites and PPG sensors, one could assess presence of a spontaneous pulse in the PPG signal or a lack of vasoconstriction, presence of severe motion artifacts which cannot be compensated for and render the PPG measurements useless, and the ease of use and compatibility with the current clinical workflow.

In the pre-clinical study we conducted, PPG was assessed during automated CPR, where chest compressions were delivered by an automated mechanical device at a constant rate and with a controlled depth. In these conditions, reduction of the compression component was feasible [202]. During manual CPR, the compression rate and depth vary over time. Therefore, the compression component will also show more variations over time, which will complicate the estimation and reduction of the compression component in the PPG signal. The algorithm presented in Chapter 5 is expected to be unsuitable to accurately estimate a compression component during manual CPR. The algorithm to reduce the compression component is based on the assumption that subsequent compressions are comparable in shape and amplitude, which holds for automated CPR. However, this assumption will not hold when compressions are delivered manually. Whether reduction of the compression component in the PPG signal is feasible during manual CPR, is a topic for further research. First results obtained in a pre-clinical manual-CPR study do indicate that the spontaneous pulse rate and the manual chest compression rate can be distinguished via spectral analysis of the PPG signal, when compressions are delivered by a person trained in CPR [198].

Reduction of the compression component in the PPG signal may even not be necessary for PPG to add value during CPR. When delivering CPR following the 30:2 protocol (see Figs. 1.4, 4.2 and 5.4a), there are natural pauses every thirty compressions which can be used for rapid analysis of the uncorrupted PPG signal. In these few-second pauses for the ventilations, absence or presence of a spontaneous pulse in the PPG signal can be directly observed. Also, inspection of the morphology of the measured PPG signal during compressions may already indicate whether there is an underling spontaneous pulse. We observed a change in the morphology of the PPG signal during compressions, once the heart resumed beating, as illustrated in Fig. 4.2b and 4.2c, and in Fig. 5.4a. Delivering compressions during cardiac arrest resulted in a PPG signal with a periodic and stable appearance. On the other hand, delivering compressions while the heart had resumed beating resulted in a PPG signal with a more complex time-varying morphology. This was also confirmed in a pre-clinical manual-CPR study [198]. However, a change in morphology does not provide information about the rate and the regularity of the contractions of the heart.

The algorithm presented in Chapter 5 for the detection of cardiogenic output in the PPG signal during CPR only demonstrates basic feasibility during automated CPR. In addition to the challenges posed by manual CPR regarding the estimation and reduction of the compression component in the PPG signal, two more aspects should be further considered. First, the computational complexity of the algorithm should be reduced to make it better suited for battery-powered monitor-defibrillators. For instance, spectral estimation was performed by autoregressive modeling of the PPG data on 5-s time-windows. The autoregressive coefficients may be estimated more efficiently via an online-method which tracks the coefficients over time. Second, the algorithm detected decreases in the baseline of the PPG signal to indicate cardiogenic output when the spontaneous pulse rate and compression rate were comparable. This was successful in a controlled laboratory environment, where the animals were stably positioned in a trough. In clinical practice, changes in the baseline of the PPG signal may also occur when the patient is moved. Therefore, further research is needed to determine to which extent decreases in the baseline of the PPG signal can reliably indicate cardiogenic output during CPR in a clinical scenario.

Bibliography

[1] J. Abdul Sukor, S. J. Redmond, and N. H. Lovell, "Signal quality measures for pulse oximetry through waveform morphology analysis," *Physiological Measurement*, vol. 32, no. 3, pp. 369–384, March 2011.

[2] U. R. Acharya, K. P. Joseph, N. Kannathal, C. M. Lim, and J. S. Suri, "Heart rate variability: A review," *Medical & Biological Engineering & Computing*, vol. 44, no. 12, pp. 1031–1051, Dec. 2006.

[3] G. A. Acket, D. Lenstra, A. J. Den Boef, and B. H. Verbeek, "The influence of feedback intensity on longitudinal mode properties and optical noise in index-guided semiconductor lasers," *IEEE Journal of Quantum Electronics*, vol. 20, no. 10, pp. 1163–1169, Oct. 1984.

[4] P. S. Addison and J. N. Watson, "Oxygen saturation determined using a novel wavelet ratio surface," *Medical Engineering & Physics*, vol. 27, no. 3, pp. 245–248, April 2005.

[5] P. S. Addison, J. N. Watson, M. L. Mestek, and R. S. Mecca, "Developing an algorithm for pulse oximetry derived respiratory rate (RR_{oxi}): A healthy volunteer study," *Journal of Clinical Monitoring and Computing*, vol. 26, no. 1, pp. 45–51, Feb. 2012.

[6] P. S. Addison, J. N. Watson, M. L. Mestek, J. P. Ochs, A. A. Uribe, and S. D. Bergese, "Pulse oximetry-derived respiratory rate in general care floor patients," *Journal of Clinical Monitoring and Computing*, vol. 29, no. 1, pp. 113–120, Feb. 2014.

[7] P. Agache and P. Humbert, Eds., *Measuring the skin.* Berlin, Germany: Springer, 2004.

[8] A. Ahn, J. Nolan, and S. Parnia, "Cerebral oximetry in cerebral resuscitation after cardiac arrest," in *Annual Update in Intensive Care and Emer-*

gency Medicine 2013, J.-L. Vincent, Ed. Berlin, Heidelberg: Springer, 2013, pp. 337–345.

[9] S. Akselrod, D. Gordon, F. A. Ubel, D. C. Shannon, A. C. Berger, and R. J. Cohen, "Power spectrum analysis of heart rate fluctuation: A quantitative probe of beat-to-beat cardiovascular control," *Science*, vol. 213, no. 4504, pp. 220–222, July 1981.

[10] J. Allen, "Photoplethysmography and its application in clinical physiological measurement," *Physiological Measurement*, vol. 28, no. 3, pp. R1–R39, March 2007.

[11] T. Aoyagi, "Pulse oximetry: Its invention, theory, and future," *Journal of Anesthesia*, vol. 17, no. 4, pp. 259–266, Jan. 2003.

[12] T. Aoyagi, M. Fuse, N. Kobayashi, K. Machida, and K. Miyasaka, "Multiwavelength pulse oximetry: Theory for the future," *Anesthesia & Analgesia*, vol. 105, no. 6 Suppl, pp. S53–S58, Dec. 2007.

[13] E. Aramendi, U. Ayala, U. Irusta, E. Alonso, T. Eftestøl, and J. Kramer-Johansen, "Suppression of the cardiopulmonary resuscitation artefacts using the instantaneous chest compression rate extracted from the thoracic impedance," *Resuscitation*, vol. 83, no. 6, pp. 692–698, June 2012.

[14] H. H. Asada, P. Shaltis, A. Reisner, S. Rhee, and R. C. Hutchinson, "Mobile monitoring with wearable photoplethysmographic biosensors," *IEEE Engineering in Medicine and Biology Magazine*, vol. 22, no. 3, pp. 28–40, July 2003.

[15] U. Ayala, T. Eftestøl, E. Alonso, U. Irusta, E. Aramendi, S. Wali, and J. Kramer-Johansen, "Automatic detection of chest compressions for the assessment of CPR-quality parameters," *Resuscitation*, vol. 85, no. 7, pp. 957–963, July 2014.

[16] G. J. Balady, R. Arena, K. Sietsema, J. Myers, L. Coke, G. F. Fletcher, D. Forman, B. Franklin, M. Guazzi, M. Gulati, S. J. Keteyian, C. J. Lavie, R. Macko, D. Mancini, and R. V. Milani, "Clinician's guide to cardiopulmonary exercise testing in adults: A scientific statement from the American Heart Association," *Circulation*, vol. 122, no. 2, pp. 191–225, July 2010.

[17] C. W. Barratt, H. Vyas, B. R. Hayes-Gill, J. A. Crowe, and D. Flatman, "Detection of previously unrecognized daytime desaturation in children with chronic lung disease," *Journal of Medical Engineering & Technology*, vol. 31, no. 2, pp. 101–108, March 2007.

[18] A. Bauer, M. Malik, G. Schmidt, P. Barthel, H. Bonnemeier, I. Cygankiewicz, P. Guzik, F. Lombardi, A. Müller, A. Oto, R. Schneider, M. Watanabe, D. Wichterle, and W. Zareba, "Heart rate turbulence: Standards of measurement, physiological interpretation, and clinical use," *Journal of the American College of Cardiology*, vol. 52, no. 17, pp. 1353–1365, Oct. 2008.

[19] G. D. Baura, *System theory and practical applications of biomedical signals*, M. Akay, Ed. Piscataway, NJ, USA: Wiley-IEEE Press, 2002.

[20] J. Berdowski, J. G. P. Tijssen, and R. W. Koster, "Chest compressions cause recurrence of ventricular fibrillation after the first successful conversion by defibrillation in out-of-hospital cardiac arrest," *Circulation, Arrhythmia and Electrophysiology*, vol. 3, no. 1, pp. 72–78, Feb. 2010.

[21] R. Berg, A. B. Sanders, K. B. Kern, R. W. Hilwig, J. W. Heidenreich, M. E. Porter, and G. A. Ewy, "Adverse hemodynamic effects of interrupting chest compressions for rescue breathing during cardiopulmonary resuscitation for ventricular fibrillation cardiac arrest," *Circulation*, vol. 104, no. 20, pp. 2465–2470, Nov. 2001.

[22] P. F. Binkley, "Predicting the potential of wearable technology," *IEEE Engineering in Medicine and Biology Magazine*, vol. 22, no. 3, pp. 23–27, May 2003.

[23] A. G. Bonomi, F. Schipper, L. M. Eerikäinen, J. Margarito, R. Aarts, S. Babaeizadeh, H. de Morree, and L. Dekker, "Atrial fibrillation detection using photo-plethysmography and acceleration data at the wrist," in *Computing in Cardiology*. Vancouver, Canada: IEEE, Sep. 2016.

[24] R. D. Branson and P. D. Mannheimer, "Forehead oximetry in critically ill patients: The case for a new monitoring site," *Respiratory Care Clinics of North America*, vol. 10, no. 3, pp. 359–367, Sep. 2004.

[25] I. M. Braverman, "The cutaneous microcirculation," *The Journal of Investigative Dermatology Symposium Proceedings*, vol. 5, no. 1, pp. 3–9, Dec. 2000.

[26] A. J. Camm, P. Kirchhof, G. Y. Lip, U. Schotten, I. Savelieva, S. Ernst, I. C. Van Gelder, N. Al-Attar, G. Hindricks, B. Prendergast, H. Heidbuchel, O. Alfieri, A. Angelini, D. Atar, P. Colonna, R. De Caterina, J. De Sutter, A. Goette, B. Gorenek, M. Heldal, S. H. Hohloser, P. Kolh, J.-Y. Le Heuzey, P. Ponikowski, and F. H. Rutten, "Guidelines for the management of atrial fibrillation," *European Heart Journal*, vol. 31, no. 19, pp. 2369–2429, Oct. 2010.

[27] C. Casanova, M. C. Hernández, A. Sánchez, I. García-Talavera, J. P. de Torres, J. Abreu, J. M. Valencia, A. Aguirre-Jaime, and B. R. Celli, "Twenty-four-hour ambulatory oximetry monitoring in COPD patients with moderate hypoxemia," *Respiratory Care*, vol. 51, no. 12, pp. 1416–1423, Dec. 2006.

[28] S. J. Choi, H. J. Ahn, M. K. Yang, C. S. Kim, W. S. Sim, J. A. Kim, J. G. Kang, J. K. Kim, and J. Y. Kang, "Comparison of desaturation and resaturation response times between transmission and reflectance pulse oximeters," *Acta Anaesthesiologica Scandinavica*, vol. 54, no. 2, pp. 212–217, Feb. 2010.

[29] J. W. Chong, D. K. Dao, S. M. A. Salehizadeh, D. D. McManus, C. E. Darling, K. H. Chon, and Y. Mendelson, "Photoplethysmograph signal reconstruction based on a novel hybrid motion artifact detection-reduction approach. Part I: Motion and noise artifact detection." *Annals of Biomedical Engineering*, vol. 42, no. 11, pp. 2238–2250, Nov. 2014.

[30] J. Christenson, D. Andrusiek, S. Everson-Stewart, P. Kudenchuk, D. Hostler, J. Powell, C. W. Callaway, D. Bishop, C. Vaillancourt, D. Davis, T. P. Aufderheide, A. Idris, J. A. Stouffer, I. Stiell, and R. Berg, "Chest compression fraction determines survival in patients with out-of-hospital ventricular fibrillation," *Circulation*, vol. 120, no. 13, pp. 1241–1247, Sep. 2009.

[31] M. Ciobotaru, R. Teodorescu, and F. Blaabjerg, "A new single-phase PLL structure based on second order generalized integrator," in *Proceedings of the 37th Conference of the IEEE Power Electronics Specialists Conference (PESC)*. Jeju, South Korea: IEEE, June 2006, pp. 1–6.

[32] A. P. Clark, K. Giuliano, and H.-M. Chen, "Pulse oximetry revisited: "But his O2 sat was normal!"," *Clinical Nurse Specialist*, vol. 20, no. 6, pp. 268–272, Nov. 2006.

[33] F. M. Coetzee and Z. Elghazzawi, "Noise-resistant pulse oximetry using a synthetic reference signal," *IEEE Transactions on Biomedical Engineering*, vol. 47, no. 8, pp. 1018–1026, Aug. 2000.

[34] G. Comtois, Y. Mendelson, and P. Ramuka, "A comparative evaluation of adaptive noise cancellation algorithms for minimizing motion artifacts in a forehead-mounted wearable pulse oximeter," in *Proceedings of the 29th Annual International Conference of the IEEE EMBS*. Lyon, France: IEEE, Jan. 2007, pp. 1528–1531.

[35] R. Couceiro, P. Carvalho, R. P. Paiva, J. Henriques, and J. Muehlsteff, "Detection of motion artifact patterns in photoplethysmographic signals based on time and period domain analysis," *Physiological Measurement*, vol. 35, no. 12, pp. 2369–2388, Dec. 2014.

[36] L. M. Cunningham, A. Mattu, R. E. O'Connor, and W. J. Brady, "Cardiopulmonary resuscitation for cardiac arrest: The importance of uninterrupted chest compressions in cardiac arrest resuscitation," *American Journal of Emergency Medicine*, vol. 30, no. 8, pp. 1630–1638, Oct. 2012.

[37] M. Cutaia, "Ambulatory monitoring of oxygen saturation in chronic lung disease: Optimizing long-term oxygen therapy," *Clinical Pulmonary Medicine*, vol. 9, no. 6, pp. 297–305, Nov. 2002.

[38] A. Cuyt, V. B. Petersen, B. Verdonk, H. Waadeland, and W. B. Jones, *Handbook of continued fractions for special functions*. Berlin, Germany: Springer, 2008.

[39] D. P. Davis, R. E. Sell, N. Wilkes, R. Sarno, R. D. Husa, E. M. Castillo, B. Lawrence, R. Fisher, C. Brainard, and J. V. Dunford, "Electrical and mechanical recovery of cardiac function following out-of-hospital cardiac arrest," *Resuscitation*, vol. 84, no. 1, pp. 25–30, Jan. 2013.

[40] P. J. de Groot, G. M. Gallatin, and S. H. Macomber, "Ranging and velocimetry signal generation in a backscatter-modulated laser diode," *Applied Optics*, vol. 27, no. 21, pp. 4475–4480, Nov. 1988.

[41] C. D. Deakin, J. P. Nolan, J. Soar, K. Sunde, R. W. Koster, G. B. Smith, and G. D. Perkins, "European Resuscitation Council guidelines for resuscitation 2010 Section 4. Adult advanced life support," *Resuscitation*, vol. 81, no. 10, pp. 1305–1352, Oct. 2010.

[42] M. K. Diab, E. Kiani-Azarbayjany, I. M. Elfadel, R. J. McCarthy, W. M. Weber, and R. A. Smith, "Signal processing apparatus," U.S. Patent 6,745,060 B2, June 1, 2004.

[43] B. Eberle, W. F. Dick, T. Schneider, G. Wisser, S. Doetsch, and I. Tzanova, "Checking the carotid pulse check: Diagnostic accuracy of first responders in patients with and without a pulse," *Resuscitation*, vol. 33, no. 2, pp. 107–116, Dec. 1996.

[44] I. Faria, C. Gaspar, M. Zamith, I. Matias, R. C. das Neves, F. Rodrigues, and C. Bárbara, "TELEMOLD project: Oximetry and exercise telemonitoring to improve long-term oxygen therapy," *Telemedicine and e-Health*, vol. 20, no. 7, pp. 626–632, July 2014.

[45] L. Ferranti and R. Laureanti, "Atrial fibrillation detection in PPG signal recorded through a wristband device," Master's thesis, Dept. of Electronics, Information and Bioengineering, Politecnico di Milano, Milan, Italy, Dec. 2015.

[46] S. G. Fleming and L. Tarassenko, "A comparison of signal processing techniques for the extraction of breathing rate from the photoplethysmogram," *International Journal of Biological and Medical Sciences*, vol. 4, no. 2, pp. 232–236, Oct. 2007.

[47] J. Y. A. Foo, "Use of independent component analysis to reduce motion artifact in pulse transit time measurement," *IEEE Signal Processing Letters*, vol. 15, no. 1, pp. 124–126, Jan. 2008.

[48] J. Y. A. Foo and C. S. Lim, "Pulse transit time as an indirect marker for variations in cardiovascular related reactivity," *Technology and Health Care*, vol. 14, no. 2, pp. 97–108, Jan. 2006.

[49] D. E. Forman, J. Myers, C. J. Lavie, M. Guazzi, B. Celli, and R. Arena, "Cardiopulmonary exercise testing: Relevant but underused," *Postgraduate Medicine*, vol. 122, no. 6, pp. 68–86, Nov. 2010.

[50] H. Fukushima, H. Kawanaka, M. S. Bhuiyan, and K. Oguri, "Estimating heart rate using wrist-type photoplethysmography and acceleration sen-

sor while running," in *34th Annual International Conference of the IEEE EMBS*. San Diego, CA, USA: IEEE, Aug. 2012, pp. 2901–2904.

[51] P. Gibbs and H. Asada, "Reducing motion artifact in wearable bio-sensors using MEMS accelerometers for active noise cancellation," in *Proceedings of the American Control Conference*. Portland, OR, USA: IEEE, June 2005, pp. 1581–1586.

[52] P. T. Gibbs, L. B. Wood, and H. H. Asada, "Active motion artifact cancellation for wearable health monitoring sensors using collocated MEMS accelerometers," M. Tomizuka, Ed., vol. 5765. San Diego, CA, USA: SPIE, March 2005, pp. 811–819.

[53] E. Gil, M. Orini, R. Bailón, J. M. Vergara, L. Mainardi, and P. Laguna, "Photoplethysmography pulse rate variability as a surrogate measurement of heart rate variability during non-stationary conditions," *Physiological Measurement*, vol. 31, no. 9, pp. 1271–1290, Sep. 2010.

[54] E. Gil, P. Laguna, J. P. Martínez, O. Barquero-Pérez, A. García-Alberola, and L. Sörnmo, "Heart rate turbulence analysis based on photoplethysmography," *IEEE Transactions on Biomedical Engineering*, vol. 60, no. 11, pp. 3149–3155, Nov. 2013.

[55] G. Giuliani, M. Norgia, S. Donati, and T. Bosch, "Laser diode self-mixing technique for sensing applications," *Journal of Optics A: Pure and Applied Optics*, vol. 4, no. 6, pp. S283–S294, Nov. 2002.

[56] J. R. Glover, "Adaptive noise cancelling applied to sinusoidal interferences," *IEEE Transactions on Acoustics, Speech and Signal Processing*, vol. ASSP-25, no. 6, pp. 484–491, Dec. 1977.

[57] J. M. Goldman, M. T. Petterson, R. J. Kopotic, and S. J. Barker, "Masimo signal extraction pulse oximetry," *Journal of Clinical Monitoring and Computing*, vol. 16, no. 7, pp. 475–483, Jan. 2000.

[58] R. Graaff, A. C. M. Dassel, W. G. Zijlstra, F. F. M. de Mul, and J. G. Aarnoudse, "How tissue optics influences reflectance pulse oximetry," in *Oxygen Transport to Tissue XVII (Advances in Experimental Medicine and Biology Vol. 388)*, C. Ince, J. Kesecioglu, L. Telci, and K. Akpir, Eds., vol. 388. New York, NY, USA: Plenum Press, 1996, pp. 117–132.

[59] M. Griffin and C. Cooney, "Pulse oximetry during cardiopulmonary resuscitation," *Anaesthesia*, vol. 50, no. 11, p. 1008, Nov. 1995.

[60] Š. Grmec, M. Križmarič, Š. Mally, A. Koželj, M. Špindler, and B. Lešnik, "Utstein style analysis of out-of-hospital cardiac arrest – Bystander CPR and end expired carbon dioxide," *Resuscitation*, vol. 72, no. 3, pp. 404–414, March 2007.

[61] D. Guo and M. Wang, "Self-mixing interferometry based on a double-modulation technique for absolute distance measurement," *Applied Optics*, vol. 46, no. 9, pp. 1486–1491, March 2007.

[62] A. C. Guyton and J. E. Hall, *Textbook of medical physiology.* Philadelphia, PA, USA: Saunders, 2000.

[63] R. G. Haahr, S. B. Duun, M. H. Toft, B. Belhage, J. Larsen, K. Birkelund, and E. V. Thomsen, "An electronic patch for wearable health monitoring by reflectance pulse oximetry," *IEEE Transactions on Biomedical Circuits and Systems*, vol. 6, no. 1, pp. 45–53, Feb. 2012.

[64] H. Han and J. Kim, "Artifacts in wearable photoplethysmographs during daily life motions and their reduction with least mean square based active noise cancellation method," *Computers in Biology and Medicine*, vol. 42, no. 4, pp. 387–393, April 2012.

[65] M. J. Hayes and P. R. Smith, "Artifact reduction in photoplethysmography," *Applied Optics*, vol. 37, no. 31, pp. 7437–7446, Nov. 1998.

[66] M. J. Hayes and P. R. Smith, "A new method for pulse oximetry possessing inherent insensitivity to artifact," *IEEE Transactions on Biomedical Engineering*, vol. 48, no. 4, pp. 452–461, April 2001.

[67] S. Haykin, Ed., *Nonlinear methods of spectral analysis.* New York, NY, USA: Springer-Verlag, 1979.

[68] S. Haykin, *Adaptive filter theory*, T. Kailath, Ed. Upper Saddle River, NJ, USA: Information and System Sciences Series, Prentice-Hall, 1996.

[69] B. E. Heradstveit, K. Sunde, G.-A. Sunde, T. Wentzel-Larsen, and J.-K. Heltne, "Factors complicating interpretation of capnography during advanced life support in cardiac arrest – A clinical retrospective study in 575 patients," *Resuscitation*, vol. 83, no. 7, pp. 813–818, July 2012.

[70] A. B. Hertzman, "Photoelectric plethysmography of the fingers and toes in man," *Experimental Biology and Medicine*, vol. 37, no. 3, pp. 529–534, Dec. 1937.

[71] A. B. Hertzman, "Photoelectric plethysmography of the nasal septum in man," *Experimental Biology and Medicine*, vol. 37, no. 2, pp. 290–292, Nov. 1937.

[72] A. B. Hertzman, "The blood supply of various skin areas as estimated by the photoelectric plethysmograph," *American Journal of Physiology*, vol. 124, no. 2, pp. 328–340, July 1938.

[73] M. J. Hinich, "Detecting a hidden, periodic signal when its period is unknown," *IEEE Transactions on Acoustics, Speech and Signal Processing*, vol. ASSP-30, no. 5, pp. 747–750, Oct. 1982.

[74] P. Hubner, J. Muehlsteff, R. Wijshoff, J. K. Russell, K. Nammi, and F. Sterz, "Pulse appearance in photoplethysmography signals obtained from finger, nose and ear during extracorporeal life support," *Resuscitation*, vol. 96, no. Suppl. 1, p. 44, Nov. 2015.

[75] A. H. Idris, L. B. Becker, J. P. Ornato, J. R. Hedges, N. G. Bircher, N. C. Chandra, R. O. Cummins, W. Dick, U. Ebmeyer, H. R. Halperin, M. F. Hazinski, R. E. Kerber, K. B. Kern, P. Safar, P. A. Steen, M. M. Swindle, J. E. Tsitlik, I. von Planta, M. von Planta, R. L. Wears, and M. H. Weil, "Utstein-style guidelines for uniform reporting of laboratory CPR research," *Circulation*, vol. 94, no. 9, pp. 2324–2336, Nov. 1996.

[76] U. Irusta, J. Ruiz, S. R. de Gauna, T. Eftestøl, and J. Kramer-Johansen, "A least mean-square filter for the estimation of the cardiopulmonary resuscitation artifact based on the frequency of the compressions," *IEEE Transactions on Biomedical Engineering*, vol. 56, no. 4, pp. 1052–1062, April 2009.

[77] A. Jubran, "Pulse oximetry," *Critical Care*, vol. 19, no. 1, pp. 272:1–7, July 2015.

[78] S. Kaestle, H. Block, and M. Block, "Method and apparatus for determining the concentration of a component," U.S. Patent 6,122,535, Sep. 19, 2000.

[79] A. Kämäräinen, M. Sainio, K. T. Olkkola, H. Huhtala, J. Tenhunen, and S. Hoppu, "Quality controlled manual chest compressions and cerebral oxygenation during in-hospital cardiac arrest," *Resuscitation*, vol. 83, no. 1, pp. 138–142, Jan. 2012.

[80] S. Kästle, "Recognition of a useful signal in a measurement signal," U.S. Patent 6,631,281 B1, Oct. 7, 2003.

[81] S. M. Kay and S. L. Marple, "Spectrum analysis – A modern perspective," *Proceedings of the IEEE*, vol. 69, no. 11, pp. 1380–1419, Nov. 1981.

[82] E. Khan, F. Al Hossain, S. Z. Uddin, S. K. Alam, and M. K. Hasan, "A robust heart rate monitoring scheme using photoplethysmographic signals corrupted by intense motion artifacts," *IEEE Transactions on Biomedical Engineering*, vol. 63, no. 3, pp. 550–562, March 2016.

[83] B. S. Kim and S. K. Yoo, "Motion artifact reduction in photoplethysmography using independent component analysis," *IEEE Transactions on Biomedical Engineering*, vol. 53, no. 3, pp. 566–568, March 2006.

[84] M. E. Kleinman, L. Chameides, S. M. Schexnayder, R. A. Samson, M. F. Hazinski, D. L. Atkins, M. D. Berg, A. R. de Caen, E. L. Fink, E. B. Freid, R. W. Hickey, B. S. Marino, V. M. Nadkarni, L. T. Proctor, F. A. Qureshi, K. Sartorelli, A. Topjian, E. W. van der Jagt, and A. L. Zaritsky, "Pediatric advanced life support: 2010 American Heart Association guidelines for cardiopulmonary resuscitation and emergency cardiovascular care," *Pediatrics*, vol. 126, no. 5, pp. e1361–e1399, Nov. 2010.

[85] M. H. Koelink, M. Slot, F. F. de Mul, J. Greve, R. Graaff, A. C. Dassel, and J. G. Aarnoudse, "Laser Doppler velocimeter based on the self-mixing effect in a fiber-coupled semiconductor laser: Theory," *Applied Optics*, vol. 31, no. 18, pp. 3401–3408, June 1992.

[86] R. W. Koster, "Refibrillation during out-of-hospital arrest: A frequent event with clinical consequences," *Signa Vitae*, vol. 5, no. Suppl 1, pp. 66–68, 2010.

[87] R. Krishnan, B. B. Natarajan, and S. Warren, "Two-stage approach for detection and reduction of motion artifacts in photoplethysmographic data," *IEEE Transactions on Biomedical Engineering*, vol. 57, no. 8, pp. 1867–1876, Aug. 2010.

[88] P. A. Kyriacou, "Pulse oximetry in the oesophagus," *Physiological Measurement*, vol. 27, no. 1, pp. R1–R35, Jan. 2006.

[89] T. M. Larabee, C. M. Little, B. I. Raju, E. Cohen-Solal, R. Erkamp, S. Wuthrich, J. Petruzzello, M. Nakagawa, and S. Ayati, "A novel hands-free carotid ultrasound detects low-flow cardiac output in a swine model of pulseless electrical activity arrest," *American Journal of Emergency Medicine*, vol. 29, no. 9, pp. 1141–1146, Nov. 2011.

[90] B. Lee, J. Han, H. J. Baek, J. H. Shin, K. S. Park, and W. J. Yi, "Improved elimination of motion artifacts from a photoplethysmographic signal using a Kalman smoother with simultaneous accelerometry," *Physiological Measurement*, vol. 31, no. 12, pp. 1585–1603, Dec. 2010.

[91] H.-W. Lee, J.-W. Lee, W.-G. Jung, and G.-K. Lee, "The periodic moving average filter for removing motion artifacts from PPG signals," *International Journal of Control, Automation, and Systems*, vol. 5, no. 6, pp. 701–706, Dec. 2007.

[92] M. N. Levy and A. J. Pappano, *Cardiovascular physiology.* Philadelphia, PA, USA: Mosby Elsevier, 2007.

[93] C. Li, J. Xu, F. Han, L. Zheng, Y. Fu, D. Yao, X. Zhang, H. Zhu, S. Guo, and X. Yu, "The role of pulse oximetry plethysmographic waveform monitoring as a marker of restoration of spontaneous circulation: A pilot study," *Chinese Critical Care Medicine*, vol. 27, no. 3, pp. 203–208, March 2015.

[94] C. Li, J. Xu, H. Zhu, and X. Yu, "Pulse oximetry plethysmographic waveform: A new method to identify ROSC during CPR," *Circulation*, vol. 132, no. A15002, Nov. 2015.

[95] Q. Li and G. D. Clifford, "Dynamic time warping and machine learning for signal quality assessment of pulsatile signals," *Physiological Measurement*, vol. 33, no. 9, pp. 1491–1501, Sep. 2012.

[96] L.-G. Lindberg and P. Å. Öberg, "Optical properties of blood in motion," *Optical Engineering*, vol. 32, no. 2, pp. 253–257, Feb. 1993.

[97] M. S. Link, L. C. Berkow, P. J. Kudenchuk, H. R. Halperin, E. P. Hess, V. K. Moitra, R. W. Neumar, B. J. O'Neil, J. H. Paxton, S. M. Silvers, R. D. White, D. Yannopoulos, and M. W. Donnino, "Part 7: Adult advanced cardiovascular life support: 2015 American Heart Association guidelines update for cardiopulmonary resuscitation and emergency cardiovascular care," *Circulation*, vol. 132, no. 18 Suppl 2, pp. S444–S464, Nov. 2015.

[98] D. A. Linkens, "Short-time-series spectral analysis of biomedical data," *IEE Proc.*, vol. 129 Pt. A, no. 9, pp. 663–672, Dec. 1982.

[99] R. Lohwasser and G. Soelkner, "Experimental and theoretical laser-Doppler frequency spectra of a tissuelike model of a human head with capillaries," *Applied Optics*, vol. 38, no. 10, pp. 2128–2137, April 1999.

[100] H. Losert, M. Risdal, F. Sterz, J. Nysaether, K. Köhler, T. Eftestøl, C. Wandaller, H. Myklebust, T. Uray, S. O. Aase, and A. N. Laggner, "Thoracic-impedance changes measured via defibrillator pads can monitor signs of circulation," *Resuscitation*, vol. 73, no. 2, pp. 221–228, May 2007.

[101] G. Lu and F. Yang, "Limitations of oximetry to measure heart rate variability measures," *Cardiovascular Engineering*, vol. 9, no. 3, pp. 119–125, Sep. 2009.

[102] S. Lu, H. Zhao, K. Ju, K. Shin, M. Lee, K. Shelley, and K. H. Chon, "Can photoplethysmography variability serve as an alternative approach to obtain heart rate variability information?" *Journal of Clinical Monitoring and Computing*, vol. 22, no. 1, pp. 23–29, Feb. 2008.

[103] M. Malik, J. T. Bigger, A. J. Camm, R. E. Kleiger, A. Malliani, A. J. Moss, and P. J. Schwartz, "Heart rate variability standards of measurement, physiological interpretation, and clinical use," *Circulation*, vol. 93, no. 5, pp. 1043–1065, March 1996.

[104] P. D. Mannheimer, J. R. Casciani, M. E. Fein, and S. L. Nierlich, "Wavelength selection for low-saturation pulse oximetry," *IEEE Transactions on Biomedical Engineering*, vol. 44, no. 3, pp. 148–158, March 1997.

[105] P. D. Mannheimer, "The light-tissue interaction of pulse oximetry," *Anesthesia & Analgesia*, vol. 105, no. 6 Suppl, pp. S10–S17, Dec. 2007.

[106] S. L. J. Marple, "Corrections to "Spectrum analysis – A modern perspective"," *Proceedings of the IEEE*, vol. 70, no. 10, p. 1238, Oct. 1982.

[107] F. Massé, M. van Bussel, A. Serteyn, J. Arends, and J. Penders, "Miniaturized wireless ECG monitor for real-time detection of epileptic seizures," *ACM Transactions on Embedded Computing Systems*, vol. 12, no. 4, pp. 102:1–21, June 2013.

[108] Y. Mendelson, "Pulse oximetry: Theory and applications for noninvasive monitoring," *Clinical Chemistry*, vol. 38, no. 9, pp. 1601–1607, Sep. 1992.

[109] Y. Mendelson, D. K. Dao, and K. H. Chon, "Multi-channel pulse oximetry for wearable physiological monitoring," in *IEEE International Conference on Body Sensor Networks*. Cambridge, MA, USA: IEEE, May 2013, pp. 1–6.

[110] Y. Mendelson and B. D. Ochs, "Noninvasive pulse oximetry utilizing skin reflectance photoplethysmography," *IEEE Transactions on Biomedical Engineering*, vol. 35, no. 10, pp. 798–805, Oct. 1988.

[111] M.-C. Michalski, V. Briard, and F. Michel, "Optical parameters of milk fat globules for laser light scattering measurements," *Lait*, vol. 81, no. 6, pp. 787–796, Nov. 2001.

[112] S. Moorthy, S. Dierdorf, and S. Schmidt, "Erroneous pulse oximeter data during CPR," *Anesthesia & Analgesia*, vol. 70, no. 3, pp. 334–341, March 1990.

[113] P. Moule, "Checking the carotid pulse: Diagnostic accuracy in students of the healthcare professions," *Resuscitation*, vol. 44, no. 3, pp. 195–201, May 2000.

[114] K. Możdżyński, K. Rafał, and M. Bobrowska-Rafał, "Application of the second order generalized integrator in digital control systems," *Archives of Electrical Engineering*, vol. 63, no. 3, pp. 423–437, Sep. 2014.

[115] J. Muehlsteff, O. Such, M. Kelm, and C. Meyer, "Phase-space representation of photoplethysmography signals as visualization concept," in *Proceedings of BMT 2010, 44. Jahrestagung der Deutschen Gesellschaft für Biomedizinische Technik*, vol. 55, no. Suppl. 1. Berlin, New York: Walter de Gruyter, Oct. 2010.

[116] W. B. Murray and P. A. Foster, "The peripheral pulse wave: Information overlooked," *Journal of Clinical Monitoring*, vol. 12, no. 5, pp. 365–377, Sep. 1996.

[117] N. Nagdyman, T. P. K. Fleck, P. Ewert, H. Abdul-Khaliq, M. Redlin, and P. E. Lange, "Cerebral oxygenation measured by near-infrared spectroscopy during circulatory arrest and cardiopulmonary resuscitation," *British Journal of Anaesthesia*, vol. 91, no. 3, pp. 438–442, Sep. 2003.

[118] K. Nakajima, T. Tamura, and H. Miike, "Monitoring of heart and respiratory rates by photoplethysmography using a digital filtering technique," *Medical Engineering & Physics*, vol. 18, no. 5, pp. 365–372, Jul. 1996.

[119] V. P. S. Narang, "Utility of the pulse oximeter during cardiopulmonary resuscitation," *Anesthesiology*, vol. 65, no. 2, pp. 239–240, Aug. 1986.

[120] R. W. Neumar, C. W. Otto, M. S. Link, S. L. Kronick, M. Shuster, C. W. Callaway, P. J. Kudenchuk, J. P. Ornato, B. McNally, S. M. Silvers, R. S. Passman, R. D. White, E. P. Hess, W. Tang, D. Davis, E. Sinz, and L. J. Morrison, "Part 8: Adult advanced cardiovascular life support: 2010 American Heart Association guidelines for cardiopulmonary resuscitation and emergency cardiovascular care," *Circulation*, vol. 122, no. 18 Suppl 3, pp. S729–S767, Nov. 2010.

[121] P. M. Nilsson, P. Boutouyrie, and S. Laurent, "Vascular aging: A tale of EVA and ADAM in cardiovascular risk assessment and prevention," *Hypertension*, vol. 54, no. 1, pp. 3–10, July 2009.

[122] M. Nitzan, A. Babchenko, and B. Khanokh, "Very low frequency variability in arterial blood pressure and blood volume pulse," *Medical & Biological Engineering & Computing*, vol. 37, no. 1, pp. 54–58, Jan. 1999.

[123] M. Nitzan, A. Babchenko, B. Khanokh, and D. Landau, "The variability of the photoplethysmographic signal – A potential method for the evaluation of the autonomic nervous system," *Physiological Measurement*, vol. 19, no. 1, pp. 93–102, Feb. 1998.

[124] M. Nitzan, A. Romem, and R. Koppel, "Pulse oximetry: Fundamentals and technology update," *Medical Devices (Auckland, N.Z.)*, vol. 7, pp. 231–239, Jan. 2014.

[125] M. Nitzan, S. Turivnenko, A. Milston, A. Babchenko, and Y. Mahler, "Low-frequency variability in the blood volume and in the blood volume pulse measured by photoplethysmography," *Journal of Biomedical Optics*, vol. 1, no. 2, pp. 223–229, April 1996.

[126] J. P. Nolan, "High-quality cardiopulmonary resuscitation," *Current Opinion in Critical Care*, vol. 20, no. 3, pp. 227–233, June 2014.

[127] J. P. Nolan, J. Soar, G. B. Smith, C. Gwinnutt, F. Parrott, S. Power, D. A. Harrison, E. Nixon, and K. Rowan, "Incidence and outcome of in-hospital cardiac arrest in the United Kingdom National Cardiac Arrest Audit," *Resuscitation*, vol. 85, no. 8, pp. 987–992, Aug. 2014.

[128] T. Nordseth, D. P. Edelson, D. Bergum, T. M. Olasveengen, T. Eftestøl, R. Wiseth, J. T. Kvaløy, B. S. Abella, and E. Skogvoll, "Optimal loop duration during the provision of in-hospital advanced life support (ALS) to patients with an initial non-shockable rhythm," *Resuscitation*, vol. 85, no. 1, pp. 75–81, Jan. 2014.

[129] F. J. Ochoa, E. Ramalle-Gómara, J. M. Carpintero, A. García, and I. Saralegui, "Competence of health professionals to check the carotid pulse," *Resuscitation*, vol. 37, no. 3, pp. 173–175, June 1998.

[130] J. Osorio, D. J. Dosdall, R. P. Robichaux, P. B. Tabereaux, and R. E. Ideker, "In a swine model, chest compressions cause ventricular capture and, by means of a long-short sequence, ventricular fibrillation," *Circulation, Arrhythmia and Electrophysiology*, vol. 1, no. 4, pp. 282–289, Oct. 2008.

[131] J. Osorio, D. J. Dosdall, P. B. Tabereaux, R. P. Robichaux, S. Stephens, J. D. Kerby, R. E. Stickney, S. Pogwizd, and R. E. Ideker, "Effect of chest compressions on ventricular activation," *The American Journal of Cardiology*, vol. 109, no. 5, pp. 670–674, March 2012.

[132] H. Pälve, "Reflection and transmission pulse oximetry during compromised peripheral perfusion," *Journal of Clinical Monitoring and Computing*, vol. 8, no. 1, pp. 12–15, Jan. 1992.

[133] N. Paradis, G. Martin, E. Rivers, M. Goetting, T. Appleton, M. Feingold, and R. Nowak, "Coronary perfusion pressure and the return of spontaneous

circulation in human cardiopulmonary resuscitation," *Journal of the American Medical Association*, vol. 263, no. 8, pp. 1106–1113, Feb. 1990.

[134] S. Parnia, A. Nasir, C. Shah, R. Patel, A. Mani, and P. Richman, "A feasibility study evaluating the role of cerebral oximetry in predicting return of spontaneous circulation in cardiac arrest," *Resuscitation*, vol. 83, no. 8, pp. 982–985, Aug. 2012.

[135] J. A. C. Patterson and G. Z. Yang, "Ratiometric artifact reduction in low power reflective photoplethysmography," *IEEE Transactions on Biomedical Circuits and Systems*, vol. 5, no. 4, pp. 330–338, July 2011.

[136] K. Petermann, *Laser diode modulation and noise*. Dordrecht, the Netherlands: Kluwer Academic Publishers, 1988.

[137] M. T. Petterson, V. L. Begnoche, and J. M. Graybeal, "The effect of motion on pulse oximetry and its clinical significance," *Anesthesia & Analgesia*, vol. 105, no. 6 Suppl, pp. S78–S84, Dec. 2007.

[138] M.-Z. Poh, N. C. Swenson, and R. W. Picard, "Motion-tolerant magnetic earring sensor and wireless earpiece for wearable photoplethysmography," *IEEE Transactions on Information Technology in Biomedicine*, vol. 14, no. 3, pp. 786–794, Feb. 2010.

[139] M. Pokorná, E. Nečas, J. Kratochvíl, R. Skřipský, M. Andrlík, and O. Franěk, "A sudden increase in partial pressure end-tidal carbon dioxide ($P_{ET}CO_2$) at the moment of return of spontaneous circulation," *The Journal of Emergency Medicine*, vol. 38, no. 5, pp. 614–621, June 2010.

[140] J. Pologe, "Pulse oximetry: Technical aspects of machine design," *International Anesthesiology Clinics*, vol. 25, no. 3, pp. 137–153, Feb. 1987.

[141] J. Qin and R. Lu, "Measurement of the absorption and scattering properties of turbid liquid foods using hyperspectral imaging," *Applied Spectroscopy*, vol. 61, no. 4, pp. 388–396, April 2007.

[142] L. R. Rabiner and B. Gold, *Theory and application of digital signal processing*. Englewood Cliffs, NJ, USA: Prentice-Hall, 1975.

[143] J. M. Raja, A. Mary, and A. Kishore, "Heart rate variability a cardiac indicator in diabetic autonomic neuropathy: A systematic review," *International Journal of Medical Research*, vol. 1, no. 2, pp. 13–16, April 2013.

[144] M. R. Ram, K. V. Madhav, E. H. Krishna, N. R. Komalla, and K. A. Reddy, "A novel approach for motion artifact reduction in PPG signals based on AS-LMS adaptive filter," *IEEE Transactions on Instrumentation and Measurement*, vol. 61, no. 5, pp. 1445–1457, May 2012.

[145] T. D. Rea, A. J. Cook, I. G. Stiell, J. Powell, B. Bigham, C. W. Callaway, S. Chugh, T. P. Aufderheide, L. Morrison, T. E. Terndrup, T. Beaudoin, L. Wittwer, D. Davis, A. Idris, and G. Nichol, "Predicting survival after out-of-hospital cardiac arrest: Role of the Utstein data elements," *Annals of Emergency Medicine*, vol. 55, no. 3, pp. 249–257, March 2010.

[146] A. Reisner, P. Shaltis, D. McCombie, and H. Asada, "Utility of the photoplethysmogram in circulatory monitoring," *Anesthesiology*, vol. 108, no. 5, pp. 950–958, May 2008.

[147] J. L. Reuss and D. Siker, "The pulse in reflectance pulse oximetry: Modeling and experimental studies," *Journal of Clinical Monitoring and Computing*, vol. 18, no. 4, pp. 289–299, Aug. 2004.

[148] J. C. Reynolds, D. Salcido, A. C. Koller, M. L. Sundermann, A. Frisch, B. P. Suffoletto, and J. J. Menegazzi, "Tissue oximetry by near-infrared spectroscopy in a porcine model of out-of-hospital cardiac arrest and resuscitation," *Resuscitation*, vol. 84, no. 6, pp. 843–847, Dec. 2013.

[149] M. Risdal, S. O. Aase, J. Kramer-Johansen, and T. Eftestøl, "Automatic identification of return of spontaneous circulation during cardiopulmonary resuscitation," *IEEE Transactions on Biomedical Engineering*, vol. 55, no. 1, pp. 60–68, Jan. 2008.

[150] E. P. Rivers, G. B. Martin, H. Smithline, M. Y. Rady, C. H. Schultz, M. G. Goetting, T. J. Appleton, and R. M. Nowak, "The clinical implications of continuous central venous oxygen saturation during human CPR," *Annals of Emergency Medicine*, vol. 21, no. 9, pp. 1094–1101, Sep. 1992.

[151] E. Rivers, J. Lozon, E. Enriquez, S. Havstad, G. Martin, C. Lewandowski, M. Goetting, J. Rosenberg, N. Paradis, and R. Nowak, "Simultaneous radial, femoral, and aortic arterial pressures during human cardiopulmonary resuscitation," *Critical Care Medicine*, vol. 21, no. 6, pp. 878–883, June 1993.

[152] P. Rodríguez, A. Luna, I. Candela, R. Mujal, R. Teodorescu, and F. Blaabjerg, "Multiresonant frequency-locked loop for grid synchronization of power converters under distorted grid conditions," *IEEE Transactions on Industrial Electronics*, vol. 58, no. 1, pp. 127–138, Jan. 2011.

[153] J. Ruiz, E. Alonso, E. Aramendi, J. Kramer-Johansen, T. Eftestøl, U. Ayala, and D. González-Otero, "Reliable extraction of the circulation component in the thoracic impedance measured by defibrillation pads," *Resuscitation*, vol. 84, no. 10, pp. 1345–1352, Oct. 2013.

[154] J. Ruiz, U. Irusta, S. Ruiz de Gauna, and T. Eftestøl, "Cardiopulmonary resuscitation artefact suppression using a Kalman filter and the frequency of chest compressions as the reference signal," *Resuscitation*, vol. 81, no. 9, pp. 1087–1094, Sep. 2010.

[155] T. Rusch, R. Sankar, and J. Scharf, "Signal processing methods for pulse oximetry," *Computers in Biology and Medicine*, vol. 26, no. 2, pp. 143–159, March 1996.

[156] R. Sahni, "Noninvasive monitoring by photoplethysmography," *Clinics in Perinatology*, vol. 39, no. 3, pp. 573–583, Sep. 2012.

[157] S. M. A. Salehizadeh, D. K. Dao, J. W. Chong, D. McManus, C. Darling, Y. Mendelson, and K. H. Chon, "Photoplethysmograph signal reconstruction based on a novel motion artifact detection-reduction approach. Part II: Motion and noise artifact removal." *Annals of Biomedical Engineering*, vol. 42, no. 11, pp. 2251–2263, Nov. 2014.

[158] S. Salehizadeh, D. Dao, J. Bolkhovsky, C. Cho, Y. Mendelson, and K. Chon, "A novel time-varying spectral filtering algorithm for reconstruction of motion artifact corrupted heart rate signals during intense physical activities using a wearable photoplethysmogram sensor," *Sensors*, vol. 16, no. 10, pp. 1–20, Jan. 2016.

[159] A. Schäfer and J. Vagedes, "How accurate is pulse rate variability as an estimate of heart rate variability? A review on studies comparing photoplethysmographic technology with an electrocardiogram," *International Journal of Cardiology*, vol. 166, no. 1, pp. 15–29, June 2013.

[160] J.-C. Schewe, M. O. Thudium, J. Kappler, F. Steinhagen, L. Eichhorn, F. Erdfelder, U. Heister, and R. Ellerkmann, "Monitoring of cerebral oxygen saturation during resuscitation in out-of-hospital cardiac arrest: A feasibility study in a physician staffed emergency medical system," *Scandinavian Journal of Trauma, Resuscitation and Emergency Medicine*, vol. 22, no. 1, pp. 58:1–8, Oct. 2014.

[161] J. W. Severinghaus and P. B. Astrup, "History of blood gas analysis. VI. Oximetry." *Journal of Clinical Monitoring*, vol. 2, no. 4, pp. 270–288, Oct. 1986.

[162] J. W. Severinghaus and Y. Honda, "History of blood gas analysis. VII. Pulse oximetry." *Journal of Clinical Monitoring*, vol. 3, no. 2, pp. 135–138, April 1987.

[163] K. H. Shelley, "Photoplethysmography: Beyond the calculation of arterial oxygen saturation and heart rate," *Anesthesia & Analgesia*, vol. 105, no. 6 Suppl, pp. S31–S36, Dec. 2007.

[164] A. Shiyovich, A. Gerovich, and A. Katz, "Recurrence of ventricular fibrillation after successful conversion, may be associated with immediate post-shock chest compressions: A case report," vol. 3, no. 3, pp. 722–726, Feb. 2013.

[165] J. Soar, J. P. Nolan, B. W. Böttiger, G. D. Perkins, C. Lott, P. Carli, T. Pellis, C. Sandroni, M. B. Skrifvars, G. B. Smith, K. Sunde, C. D. Deakin, R. W. Koster, K. G. Monsieurs, and N. I. Nikolaou, "European Resuscitation Council guidelines for resuscitation 2015 Section 3. Adult advanced life support," *Resuscitation*, vol. 95, no. 10, pp. 100–147, Oct. 2015.

[166] J. Solà, O. Chételat, C. Sartori, Y. Allemann, and S. F. Rimoldi, "Chest pulse-wave velocity: A novel approach to assess arterial stiffness," *IEEE Transactions on Biomedical Engineering*, vol. 58, no. 1, pp. 215–223, Jan. 2011.

[167] J. Solà, M. Proenca, D. Ferrario, J.-A. Porchet, A. Falhi, O. Grossenbacher, Y. Allemann, S. F. Rimoldi, and C. Sartori, "Noninvasive and nonocclusive blood pressure estimation via a chest sensor," *IEEE Transactions on Biomedical Engineering*, vol. 60, no. 12, pp. 3505–3513, Dec. 2013.

[168] J. Solà, S. F. Rimoldi, and Y. Allemann, "Ambulatory monitoring of the cardiovascular system: The role of pulse wave velocity," in *New Developments in Biomedical Engineering*, D. Campolo, Ed. InTech, Jan. 2010, pp. 391–424.

[169] J. Solà, R. Vetter, P. Renevey, O. Chételat, C. Sartori, and S. F. Rimoldi, "Parametric estimation of pulse arrival time: A robust approach to pulse wave velocity." *Physiological Measurement*, vol. 30, no. 7, pp. 603–615, July 2009.

[170] D. K. Spierer, Z. Rosen, L. L. Litman, and K. Fujii, "Validation of photoplethysmography as a method to detect heart rate during rest and exercise," *Journal of Medical Engineering & Technology*, vol. 39, no. 5, pp. 264–271, June 2015.

[171] M. J. Spittal, "Evaluation of pulse oximetry during cardiopulmonary resuscitation," *Anaesthesia*, vol. 48, no. 8, pp. 701–703, Aug. 1993.

[172] F. S. Stecher, J.-A. Olsen, R. E. Stickney, and L. Wik, "Transthoracic impedance used to evaluate performance of cardiopulmonary resuscitation during out of hospital cardiac arrest," *Resuscitation*, vol. 79, no. 3, pp. 432–437, Dec. 2008.

[173] S. Steen, Q. Liao, L. Pierre, A. Paskevicius, and T. Sjöberg, "Evaluation of LUCAS, a new device for automatic mechanical compression and active decompression resuscitation," *Resuscitation*, vol. 55, no. 3, pp. 285–299, Dec. 2002.

[174] J. M. Steinke and A. P. Shepherd, "Role of light scattering in whole body oximetry," *IEEE Transactions on Biomedical Engineering*, vol. BME-33, no. 3, pp. 294–301, March 1986.

[175] O. Such and J. Muehlsteff, "The challenge of motion artifact suppression in wearable monitoring solutions," in *Proceedings of the 3rd IEEE-EMBS International Summer School and Symposium on Medical Devices and Biosensors*. Boston, MA, USA: IEEE, Sep. 2006, pp. 49–52.

[176] Y. Sun and N. Thakor, "Photoplethysmography revisited: From contact to noncontact, from point to imaging," *IEEE Transactions on Biomedical Engineering*, vol. 63, no. 3, pp. 463–477, March 2016.

[177] T. Tamura, Y. Maeda, M. Sekine, and M. Yoshida, "Wearable photoplethysmographic sensors – Past and present," *Electronics*, vol. 3, no. 2, pp. 282–302, April 2014.

[178] J. Tibballs and P. Russell, "Reliability of pulse palpation by healthcare personnel to diagnose paediatric cardiac arrest," *Resuscitation*, vol. 80, no. 1, pp. 61–64, Jan. 2009.

[179] R. M. Tobin, J. A. Pologe, and P. B. Batchelder, "A characterization of motion affecting pulse oximetry in 350 patients," *Anesthesia & Analgesia*, vol. 94, no. 1 Suppl, pp. S54–S61, Feb. 2002.

[180] H. Tsuji, M. G. Larson, F. J. Venditti, Jr., E. S. Manders, J. C. Evans, C. L. Feldman, and D. Levy, "Impact of reduced heart rate variability on risk for cardiac events. The Framingham heart study." *Circulation*, vol. 94, no. 11, pp. 2850–2855, Dec. 1996.

[181] C. Vaillancourt, S. Everson-Stewart, J. Christenson, D. Andrusiek, J. Powell, G. Nichol, S. Cheskes, T. P. Aufderheide, R. Berg, and I. G. Stiell, the Resuscitation Outcomes Consortium Investigators, "The impact of increased chest compression fraction on return of spontaneous circulation for out-of-hospital cardiac arrest patients not in ventricular fibrillation," *Resuscitation*, vol. 82, no. 12, pp. 1501–1507, Dec. 2011.

[182] C. Valdez-Lowe, S. A. Ghareeb, and N. T. Artinian, "Pulse oximetry in adults," *American Journal of Nursing*, vol. 109, no. 6, pp. 52–59, June 2009.

[183] J. van Andel, C. Ungureanu, R. Aarts, F. Leijten, and J. Arends, "Using photoplethysmography in heart rate monitoring of patients with epilepsy," *Epilepsy & Behavior*, vol. 45, no. 4, pp. 142–145, April 2015.

[184] W. J. van Elmpt, T. M. Nijsen, P. A. Griep, and J. B. Arends, "A model of heart rate changes to detect seizures in severe epilepsy," *Seizure*, vol. 15, no. 6, pp. 366–375, June 2006.

[185] D. K. Vanderveen, T. A. Mansfield, and E. C. Eichenwald, "Lower oxygen saturation alarm limits decrease the severity of retinopathy of prematurity," *Journal of the American Association for Pediatric Ophthalmology and Strabismus*, vol. 10, no. 5, pp. 445–448, Oct. 2006.

[186] M. Vegfors, L.-G. Lindberg, P. Å. Öberg, and C. Lennmarken, "Accuracy of pulse oximetry at various haematocrits and during haemolysis in an in vitro model," *Medical & Biological Engineering & Computing*, vol. 31, no. 2, pp. 135–141, March 1993.

[187] W. Verkruysse, L. O. Svaasand, and J. S. Nelson, "Remote plethysmographic imaging using ambient light," *Optics Express*, vol. 16, no. 26, pp. 21 434–21 445, Dec. 2008.

[188] L. Wang, B. P. L. Lo, and G.-Z. Yang, "Multichannel reflective PPG earpiece sensor with passive motion cancellation," *IEEE Transactions on Biomedical Circuits and Systems*, vol. 1, no. 4, pp. 235–241, Dec. 2007.

[189] K. M. Warren, J. R. Harvey, K. H. Chon, and Y. Mendelson, "Improving pulse rate measurements during random motion using a wearable multichan-

nel reflectance photoplethysmograph," *Sensors*, vol. 16, no. 3, pp. 342:1–18, March 2016.

[190] J. G. Webster, "Reducing motion artifacts and interference in biopotential recording," *IEEE Transactions on Biomedical Engineering*, vol. BME-31, no. 12, pp. 823–826, Dec. 1984.

[191] J. G. Webster, Ed., *Design of pulse oximeters*. New York, NY, USA: Taylor & Francis Group, 1997.

[192] H. J. J. Wellens, K. I. Lie, and D. Durrer, "Further observations on ventricular tachycardia as studied by electrical stimulation of the heart: Chronic recurrent ventricular tachycardia and ventricular tachycardia during acute myocardial infarction," *Circulation*, vol. 49, no. 4, pp. 647–653, April 1974.

[193] B. Widrow, J. R. Glover, J. M. McCool, J. Kaunitz, C. S. Williams, R. H. Hearn, J. R. Zeidler, E. Dong, and R. C. Goodlin, "Adaptive noise cancelling: Principles and applications," *Proceedings of the IEEE*, vol. 63, no. 12, pp. 105–112, Dec. 1975.

[194] F. P. Wieringa, "Pulse oxigraphy: And other new in-depth perspectives through the near-infrared window," Ph.D. dissertation, Erasmus University, Rotterdam, the Netherlands, May 2007.

[195] R. Wijshoff, W. Peeters, A. Venema, R. Aarts, and G. Noordergraaf, "A photoplethysmography signal can show the presence of a spontaneous pulse at sub-life-supporting blood pressure during experimental cardiopulmonary resuscitation," *Circulation*, vol. 130, no. A137, Nov. 2014.

[196] R. W. C. G. R. Wijshoff, M. Mischi, P. H. Woerlee, and R. M. Aarts, "Improving pulse oximetry accuracy by removing motion artifacts from photoplethysmograms using relative sensor motion: A preliminary study," in *Oxygen Transport to Tissue XXXV (Advances in Experimental Medicine and Biology Vol. 789)*, S. Van Huffel, G. Naulaers, A. Caicedo, D. F. Bruley, and D. K. Harrison, Eds. New York, NY, USA: Springer Science+Business Media, 2013, pp. 411–417.

[197] R. W. C. G. R. Wijshoff, J. Veen, A. M. van der Lee, L. Mulder, J. M. A. Stijnen, S. van Tuijl, and R. M. Aarts, "PPG motion artifact handling using a self-mixing interferometric sensor," in *Proceedings of SPIE, Optical Fibers, Sensors, and Devices for Biomedical Diagnostics and Treatment XI*, I. Gannot, Ed., vol. 7894. San Francisco, CA, USA: SPIE, Jan. 2011, pp. 0F1–0F13.

[198] R. Wijshoff, J. Muehlsteff, M. Bartula, M. Fuller, D. Jorgenson, J. W. Lampe, and L. B. Becker, "Photoplethysmographic detection of a spontaneous pulse during manual experimental cardiopulmonary resuscitation," *Resuscitation*, vol. 96, no. Suppl. 1, p. 5, Nov. 2015.

[199] R. Wijshoff, T. van der Sar, R. Aarts, P. Woerlee, and G. Noordergraaf, "Potential of photoplethysmography to guide pulse checks during cardiopul-

monary resuscitation: Observations in an animal study," *Resuscitation*, vol. 84, no. 11, p. S1, Oct. 2013.

[200] R. W. C. G. R. Wijshoff, M. Mischi, and R. M. Aarts, "Reduction of periodic motion artifacts in photoplethysmography," *IEEE Transactions on Biomedical Engineering*, (accepted for publication) 2016.

[201] R. W. C. G. R. Wijshoff, M. Mischi, J. Veen, A. M. van der Lee, and R. M. Aarts, "Reducing motion artifacts in photoplethysmograms by using relative sensor motion: Phantom study," *Journal of Biomedical Optics*, vol. 17, no. 11, pp. 117 007–1–117 007–15, Nov. 2012.

[202] R. W. C. G. R. Wijshoff, A. M. T. M. van Asten, W. H. Peeters, R. Bezemer, G. J. Noordergraaf, M. Mischi, and R. M. Aarts, "Photoplethysmography-based algorithm for detection of cardiogenic output during cardiopulmonary resuscitation," *IEEE Transactions on Biomedical Engineering*, vol. 62, no. 3, pp. 909–921, March 2015.

[203] R. W. C. G. R. Wijshoff, T. van der Sar, W. H. Peeters, R. Bezemer, P. Aelen, I. W. F. Paulussen, S. C. M. A. Ordelman, A. Venema, P. F. J. van Berkom, R. M. Aarts, P. H. Woerlee, G.-J. Scheffer, and G. J. Noordergraaf, "Detection of a spontaneous pulse in photoplethysmograms during automated cardiopulmonary resuscitation in a porcine model," *Resuscitation*, vol. 84, no. 11, pp. 1625–1632, Nov. 2013.

[204] L. Wik, J. Kramer-Johansen, H. Myklebust, H. Sørebø, L. Svensson, B. Fellows, and P. A. Steen, "Quality of cardiopulmonary resuscitation during out-of-hospital cardiac arrest," *The Journal of the American Medical Association*, vol. 293, no. 3, pp. 299–304, Jan. 2005.

[205] L. Wood and H. Asada, "Low variance adaptive filter for cancelling motion artifact in wearable photoplethysmogram sensor signals," in *Proceedings of the 29th Annual International Conference of the IEEE EMBS*. Lyon, France: IEEE, Aug. 2007, pp. 652–655.

[206] M. W. Wukitsch, M. T. Petterson, D. R. Tobler, and J. A. Pologe, "Pulse oximetry: Analysis of theory, technology, and practice," *Journal of Clinical Monitoring*, vol. 4, no. 4, pp. 290–301, Oct. 1988.

[207] Y. Xiao and Y. Tadokoro, "LMS-based notch filter for the estimation of sinusoidal signals in noise," *Signal Processing*, vol. 46, no. 2, pp. 223–231, Oct. 1995.

[208] J. Xu, H. Zhu, Z. Wang, X. Yu, and J. Walline, "Why do not we use finger pulse oximeter plethysmograph waveform to monitor the effectiveness of cardiopulmonary resuscitation?" *Resuscitation*, vol. 82, no. 7, p. 959, July 2011.

[209] Y. Yamaya, H. J. Bogaard, P. D. Wagner, K. Niizeki, and S. R. Hopkins, "Validity of pulse oximetry during maximal exercise in normoxia, hypoxia,

and hyperoxia." *Journal of Applied Physiology*, vol. 92, no. 1, pp. 162–168, Jan. 2002.

[210] Y.-S. Yan, C. C. Poon, and Y.-T. Zhang, "Reduction of motion artifact in pulse oximetry by smoothed pseudo Wigner-Ville distribution," *Journal of Neuroengineering and Rehabilitation*, vol. 2, no. 1, pp. 3:1–9, March 2005.

[211] Y.-S. Yan and Y.-T. Zhang, "An efficient motion-resistant method for wearable pulse oximeter," *IEEE Transactions on Information Technology in Biomedicine*, vol. 12, no. 3, pp. 399–405, May 2008.

[212] R. Yousefi, M. Nourani, S. Ostadabbas, and I. Panahi, "A motion-tolerant adaptive algorithm for wearable photoplethysmographic biosensors," *IEEE Journal of Biomedical and Health Informatics*, vol. 18, no. 2, pp. 670–681, March 2014.

[213] A. C. H. Yu, E. Cohen-Solal, B. I. Raju, and S. Ayati, "An automated carotid pulse assessment approach using Doppler ultrasound," *IEEE Transactions on Biomedical Engineering*, vol. 55, no. 3, pp. 1072–1081, March 2008.

[214] G. Zhang, M. Gao, D. Xu, N. B. Olivier, and R. Mukkamala, "Pulse arrival time is not an adequate surrogate for pulse transit time as a marker of blood pressure," *Journal of Applied Physiology*, vol. 111, no. 6, pp. 1681–1686, Sep. 2011.

[215] Z. Zhang, "Photoplethysmography-based heart rate monitoring in physical activities via joint sparse spectrum reconstruction," *IEEE Transactions on Biomedical Engineering*, vol. 62, no. 8, pp. 1902–1910, Aug. 2015.

[216] Z. Zhang, Z. Pi, and B. Liu, "TROIKA: A general framework for heart rate monitoring using wrist-type photoplethysmographic signals during intensive physical exercise," *IEEE Transactions on Biomedical Engineering*, vol. 62, no. 2, pp. 522–531, Feb. 2015.

[217] C. Zhou, J. Feng, J. Hu, and X. Ye, "Study of artifact-resistive technology based on a novel dual photoplethysmography method for wearable pulse rate monitors," *Journal of Medical Systems*, vol. 40, no. 3, pp. 56:1–10, March 2016.

[218] Z. Zhu and R. K. Barnette, "Continuous oxygen monitoring – A better way to prescribe long-term oxygen therapy," *Respiratory Medicine*, vol. 99, no. 11, pp. 1386–1392, Nov. 2005.

Acknowledgements

This thesis has been written with the help, support and contributions of many people, either directly or indirectly. Without them, I would not have been able to write this thesis. I am very grateful for all their help, support and contributions.

First of all, I would like to sincerely thank my promotor, prof.dr. Ronald Aarts, and my copromotor, dr.ir. Massimo Mischi, for the continued guidance, advice, support, encouragements, patience and their confidence in me. I am grateful for all the open and positive discussions, and for your constructive feedback and new ideas, without which I could not have written this thesis. I am also thankful for the freedom you gave me in this project, to explore alternative directions than were initially planned. Thank you very much for all that you have done for me!

Second, I am grateful for the help, support, and advice of dr.ir. Jeroen Veen. Thank you for all the pleasant and constructive discussions, and for all your help in shaping this project! Many thanks go to dr. Alexander van der Lee for all the help with the laser diodes and the experimental work in the laboratory, and to dr.ir. Niek Lambert for all the valuable and critical discussions. Thank you for your guidance and the pleasant collaboration in this project!

Further, I would also like to thank prof.dr.ir. Jan Bergmans for giving me the opportunity to start this project, for the confidence in me, for the advice on signal processing, and for all the help organizationally.

Many thanks go to LifeTec Group for building an in-vitro skin perfusion phantom. I would especially like to thank ing. Sjoerd van Tuijl, dr.ir. Marco Stijnen, dr.ir. Lars Mulder, Luca Paroni MSc and dr.ir. Jurgen de Hart, for all the valuable and constructive discussions, for the interesting and inspiring demonstrations at their laboratory, and for the pleasant and positive working atmosphere. I also would like to thank dr.ir. Mahsa Nemati, dr. Nandini Bhattacharya and prof.dr. Paul Urbach for the pleasant collaboration, and the valuable and stimulating discussions.

I am very grateful that dr.ir. Pierre Woerlee gave me the opportunity to join the research project about CPR which has had an enormous impact on this research, and for all the valuable discussions and his guidance. I am also grateful for all the support by dr. Gerrit Jan Noordergraaf, for all the time he invested in me, and for his help to focus on the clinical applicability. I am very grateful for all the help of dr.ir. Toeno van der Sar, dr.ir. Wouter Peeters, and dr. Rick Bezemer whose energy and enthusiasm are inspiring and who have helped me to improve my research and communication skills. I would like to thank dr.-ing. Jens Mühlsteff for the valuable discussions, his inspiring enthusiasm and his confidence in me. I am grateful for the contribution of Toine van Asten MSc to this research and for the enjoyable collaboration we had during his MSc project. I would like to thank Alyssa Venema MPA, Paul van Berkom MSc, ir. Paul Aelen, ir. Igor Paulussen MPA, and dr.ir. Simone Ordelman for the valuable discussions and their help during the pre-clinical experiments.

Many thanks go to Mr Ben Wassink for building all the mechanical setups and adjustments we requested for, and to Mr Jos Bax for building all the electronics we needed. Your craftmanship, dedication and fast work have allowed us to actually conduct the experiments we had in mind.

In the past years, I have been given the opportunity to work in the very nice environments of the Biomedical Sensor Systems Group / Patient Care & Measurements Group of Philips Research, and in the Signal Processing Systems Group of the TU/e. I would like to thank all my colleagues for the very pleasant atmosphere they create.

I would like to thank the committee members, dr. John Allen, prof.dr.ir. Wiendelt Steenbergen, prof.dr.ir. Frans van de Vosse, prof.dr.ir. Pieter Wijn, dr. Gerrit Jan Noordergraaf, and prof.dr.ir. Bart Smolders, for reading, reviewing and assessing this thesis.

This research was part of the “Hemodynamics by Interferometric Photonics” project funded by NL Agency. I would like to thank the members of the user committee, ir. Jan Bosiers, dr. Bernhard Hoenders, ir. Jos Settels, and prof.dr.ir. Wiendelt Steenbergen, for the valuable discussions, feedback and advice.

I would like to thank all my friends for all the fun and the pleasant times we had. You have really helped me relax and find new energy to continue this research. Thank you for listening and your understanding during the times that this project was difficult!

I am very grateful for the continued support, understanding, and patience of my mother, my father, my sister and her husband. I definitely would not have been able to finish this project without your continued support, and I am especially grateful for all your understanding and patience during the difficult times of this project. Thank you very much!

About the author

Ralph Wijshoff was born in Sittard, the Netherlands, on June 24, 1984. In 2002 he finished grammar school at the Trevianum Scholengroep in Sittard, after which he studied Electrical Engineering at the Eindhoven University of Technology, in Eindhoven, the Netherlands. He received a B.Sc. as well as an M.Sc. degree at the Eindhoven University of Technology, both with honors. In 2009 he graduated on a project about motion artifact handling in photoplethysmography, which was performed in the Signal Processing Systems Group of the Eindhoven University of Technolgy, and in the Biomedical Sensor Systems Group of Philips Research, in Eindhoven, the Netherlands.

In 2009 Ralph started a PhD project within the Signal Processing Systems Group and the Biomedical Sensor Systems Group, continuing the topic of motion artifact handling in photoplethysmography. This project was part of the Hemodynamics by Interferometric Photonics project, which was funded by NL Agency. The results of the project about photoplethysmography are presented in this dissertation. These results have also been published in four journal papers and nine contributions to international conferences, and have lead to one patent application. Since July 2014, Ralph has been employed as a scientist in the Patient Care & Measurements Group of Philips Research, where he is working on the use of photoplethysmography in cardiopulmonary resuscitation and on pulse oximetry systems.

List of publications

Journal papers

J1 **R.W.C.G.R. Wijshoff**, M. Mischi, and R.M. Aarts, "Reduction of periodic motion artifacts in photoplethysmography," accepted for publication in *IEEE Transactions on Biomedical Engineering.* (Basis of Chapter 3.)

J2 **R.W.C.G.R. Wijshoff**, A.M.T.M. van Asten, W.H. Peeters, R. Bezemer, G.J. Noordergraaf, M. Mischi, and R.M. Aarts, "Photoplethysmography-based algorithm for detection of cardiogenic output during cardiopulmonary resuscitation," *IEEE Transactions on Biomedical Engineering*, vol. 62, no. 3, pp. 909-921, March 2015. (Basis of Chapter 5.)
(**Third place "Best paper published by IEEE-EMBS in 2014"** at the 5th Dutch Bio-Medical Engineering Conference, Egmond aan Zee, the Netherlands, Jan. 22-23, 2015. **Featured article of IEEE TBME in March 2015.**)

J3 **R.W.C.G.R. Wijshoff**, T. van der Sar, W.H. Peeters, R. Bezemer, P. Aelen, I.W.F. Paulussen, S.C.M.A. Ordelman, A. Venema, P.F.J. van Berkom, R.M. Aarts, P.H. Woerlee, G.-J. Scheffer, and G.J. Noordergraaf, "Detection of a spontaneous pulse in photoplethysmograms during automated cardiopulmonary resuscitation in a porcine model," *Resuscitation*, vol. 84, no. 11, pp. 1625-1632, Nov. 2013. (Basis of Chapter 4.)

J4 **R.W.C.G.R. Wijshoff**, M. Mischi, J. Veen, A.M. van der Lee, and R.M. Aarts, "Reducing motion artifacts in photoplethysmograms by using relative sensor motion: Phantom study," *Journal of Biomedical Optics*, vol. 17, no. 11, pp. 117007-1 - 117007-15, Nov. 2012. (Basis of Chapter 2.)

Conference contributions

1. **R.W.C.G.R. Wijshoff**, W.H. Peeters, G.J. Noordergraaf, M. Mischi, and R.M. Aarts, "Detection of a spontaneous pulse by photoplethysmography during experimental automated cardiopulmonary resuscitation," *49th Annual Conference of the Deutsche Gesellschaft für Biomedizinische Technik (DGBMT)*, Lübeck, Germany, Sep. 16-18, 2015.

2. **R.W.C.G.R. Wijshoff**, W.H. Peeters, G.J. Noordergraaf, M. Mischi, and R.M. Aarts, "Photoplethysmographic detection of a spontaneous pulse during cardiopulmonary resuscitation," *5th Dutch Bio-Medical Engineering Conference (BME)*, Egmond aan Zee, the Netherlands, Jan. 22-23, 2015.

3. **R.W.C.G.R. Wijshoff**, W.H. Peeters, A. Venema, R.M. Aarts, and G.J. Noordergraaf. "A photoplethysmography signal can show presence of a spontaneous pulse at sub-life-supporting blood pressure levels during experimental cardiopulmonary resuscitation," *Resuscitation Science Symposium (ReSS)*, Chicago, IL, USA, Nov. 15-16, 2014.

4. **R.W.C.G.R. Wijshoff**, T. van der Sar, R.M. Aarts, P.H. Woerlee, and G.J. Noordergraaf, "Potential of photoplethysmography to guide pulse checks during cardiopulmonary resuscitation: Observations in an animal study," *European Resuscitation Council Symposium*, Kraków, Poland, Oct. 25-26, 2013. **(Runner-up in the Best-of-the-Best competition)**

5. **R.W.C.G.R. Wijshoff**, M. Mischi, P.H. Woerlee, and R.M. Aarts, "Improving pulse oximetry accuracy by removing motion artifacts from photoplethysmograms using relative sensor motion: A preliminary study," in *Oxygen Transport to Tissue XXXV (Advances in Experimental Medicine and Biology Vol. 789)*, S. Van Huffel, G. Naulaers, A. Caicedo, D.F. Bruley, and D.K. Harrison, Eds. New York, NY, USA: Springer Science+Business Media, 2013, pp. 411-417.

6. **R.W.C.G.R. Wijshoff**, M. Mischi, A.M. van der Lee, P.H. Woerlee, P. Aelen, N. Lambert, and R.M. Aarts, "Correlation of relative and global sensor motion with motion artifacts in photoplethysmograms," *10th Belgian Day on Biomedical Engineering and the Annual Symposium of the IEEE EMBS Benelux Chapter*, Brussels, Belgium, Dec. 2, 2011.

7. **R.W.C.G.R. Wijshoff**, J. Veen, A.M. van der Lee, L. Mulder, J.M.A. Stijnen, S. van Tuijl, and R.M. Aarts, "Reducing motion artifacts in photoplethysmograms by using light source displacement as an artifact reference: Phantom study," *Biomedica Life Science Summit*, Eindhoven, the Netherlands, April 7-8, 2011.

8. **R.W.C.G.R. Wijshoff**, J. Veen, A.M. van der Lee, L. Mulder, J.M.A. Stijnen, S. van Tuijl, and R.M. Aarts, "PPG motion artifact handling

using a self-mixing interferometric sensor," in *Proceedings of SPIE, Optical Fibers, Sensors, and Devices for Biomedical Diagnostics and Treatment XI*, I. Gannot, Ed., vol. 7894, San Francisco, CA, USA, Jan. 2011, pp. 0F1-0F13.

9. **R.W.C.G.R. Wijshoff**, R.M. Aarts, J. Veen, A.M. van der Lee, and C. Presura, "Self-mixing interferometric sensor displacement reference for PPG motion artifact handling," *21st ProRISC Workshop of the STW.ICT Conference*, Veldhoven, the Netherlands, Nov. 18-19, 2010.

Patent application

1. W.H. Peeters, **R.W.C.G.R. Wijshoff**, A.M.T.M. van Asten, R. Bezemer, R.M. Aarts, and P.H. Woerlee, "Determining return of spontaneous circulation during CPR," Patent Application WO2015/121114 A1, Aug. 20, 2015.